Multistate Analysis and Design: Case Studies in Aerospace Design and Long Endurance Systems

by

Jeremy S. Agte

M.S., George Washington University (1999)
B.S., United States Air Force Academy (1997)

Submitted to the Department of Aeronautics and Astronautics
in partial fulfillment of the requirements for the degree of

Doctor of Philosophy

at the

MASSACHUSETTS INSTITUTE OF TECHNOLOGY

September 2011

©Jeremy S. Agte, all rights reserved.
The author hereby grants to MIT and Draper Laboratory permission to reproduce and to distribute publicly paper and electronic copies of the thesis document in whole or in part.

Author .....
Department of Aeronautics and Astronautics
August 18, 2011

Certified by .....
Olivier de Weck
Associate Professor of Aeronautics and Astronautics
Thesis Supervisor

Certified by .....
Nicholas Borer
System Design Engineer, The Charles Stark Draper Laboratory
Thesis Supervisor

Accepted by .....
Eytan H. Modiano
Professor of Aeronautics and Astronautics
Chair, Graduate Program Committee

Certified by . . . . . .
Brian Williams
Professor of Aeronautics and Astronautics
Committee Member

Certified by . . . . . .
Jaroslaw Sobieszczanski-Sobieski
Distinguished Research Associate, NASA Langley Research Center
Committee Member

Certified by . . . . . .
Karen Willcox
Associate Professor of Aeronautics and Astronautics
Thesis Reader

Certified by . . . . . .
Qiqi Wang
Assistant Professor of Aeronautics and Astronautics
Thesis Reader

Multistate Analysis and Design: Case Studies in Aerospace Design and Long Endurance Systems

by

Jeremy S. Agte

Submitted to the Department of Aeronautics and Astronautics
on August 18, 2011, in partial fulfillment of the
requirements for the degree of
Doctor of Philosophy

Abstract

This research contributes to the field of aerospace engineering by proposing and demonstrating an integrated process for the early-stage, multistate design of aerospace systems. The process takes into early consideration the many partially degraded states that real-world systems experience throughout their operation. Despite advancing efforts aimed at maintaining operation in a state of optimum performance, most systems spend very substantial amounts of time operating in degraded or off-nominal states (e.g. Hubble space telescope, Mars Spirit rover, or aircraft flying under minimum-equipment-list restrictions). There exist relatively few methods and tools to address this at the beginning of the design process. At one end of the spectrum is design optimization, but this typically concentrates on the system in its nominal state of operation, only infrequently considering failure states through piecemeal application of constraints. There is reliability analysis, which focuses on component failure rates and the benefits of redundancy but does not consider how well or poorly the system performs with partial failures. Finally, there is controls theory, where control laws are optimized but the plant is typically assumed to be given *a priori*. The methodology described within this thesis coordinates elements from each of these three areas into an effective integrated framework. It allows the designer deeper insight into the complex problem of designing cost effective systems that must operate for long durations with little or expensive opportunity for repair or intervention. Specific contributions include: 1) the above methodology, which evaluates responses in system expected performance and availability to changes in static design variables (geometry) and component failure rates, accounting for control design variables (gains) where appropriate, 2) the demonstration of the cost and benefits associated with a multistate design approach as compared to reliability analysis and the nominal design approach, and 3) a multilayer extension of Markov analysis, for translating single sortie vehicle level metrics into measures of multistate campaign performance.

The process is demonstrated through three application case studies. The first of

these establishes the feasibility of the approach through the multistate analysis of performance for an existing twin-engine aircraft. This analysis was enabled through the development of a multidisciplinary simulation based design model for evaluation of multistate aircraft performance. A medium-altitude long endurance unmanned aerial vehicle is designed in the second case study, first from a single-sortie, ultra long endurance perspective and then from a multiple sortie, mission campaign perspective. Finally, the third case study demonstrates applicability of the approach to a lower level subsystem, that of the lubrication system for a geared turbofan engine. Several major findings result from these case studies, including that: 1) multistate performance output spaces have distinctly unique shapes and boundaries, depending on whether formed through variation of component failure rates, static design variables (geometry), or a multistate combination of both, 2) a region of multistate performance results from the combined variation of failure rates and static design variables that is unachievable through the independent variation of either one, 3) small changes in static design variables may be used to significantly improve system availability, and 4) the general multistate design problem is one of competing objectives between system availability, expected performance, nominal performance, and cost.

Thesis Supervisor: Olivier de Weck
Title: Associate Professor of Aeronautics and Astronautics

Thesis Supervisor: Nicholas Borer
Title: System Design Engineer, The Charles Stark Draper Laboratory

Acknowledgments

This work was performed at the Charles Stark Draper Laboratory, where it was supported by Internal Research and Development funds.

There are many individuals without whose help this thesis would not have been possible, but foremost among these is my beautiful wife, Diana. I know that she suffered far more than I did during this past few years, but she was always there for me during the late nights and early mornings. I love you with all of my heart, and promise never to subject you to such craziness again.

To my 4-year old daughter, the one and only Eva, the provider of necessary distraction, the indisputable proof of perpetual motion, the radiant smile at the end of my day, I say, "Yes, honey, I can play now..." I am certain that someday your interminable will will guide you to much greater endeavors than this, and I rest assured that you will never forget to stop and smell the flowers along the way.

I also extend great gratitude to all of the members of my thesis committee, most notably Nick Borer and Oli de Weck, my dual advisers that provided much needed guidance throughout this work. Nick, thanks for always keeping me steered in the right direction. Oli, thank you for making sure to always move my deadlines forward by several weeks to ensure I finished this thing on time. I owe a great debt to both of you.

There is one committee member who deserves special mention. This is Jarek Sobieski, who has been a superb mentor and a great friend to me since he first introduced me to optimization nearly 15 years ago. Without a doubt, I would not be in this position without his direction over the years. He is an exceptionally brilliant researcher who sets the bar extremely high. Thank you, Jarek, I hope to continue to make you proud.

Finally, I dedicate this work to my father, Steve Agte, the one and only person that has always been there for me throughout my life, from the day of my birth to the bitter end, whenever that may be. He is a truly great man. As I write the final

words of this manuscript, he undergoes surgery for a massive heart attack suffered this morning.

Hang in there, Dad, I'm coming home.

****

In Loving Memory of

Steve D. Agte

12 November, 1947 – 18 August, 2011

May my daughter someday love me as much as I love you...

that I too, may go in Peace

Table of Contents

List of Figures

List of Tables

Nomenclature

Letters

b	wing span, [ft]
$\mathbf{c}$	vector of operational parameters
c	specific fuel consumption, [lbm/Hp/hr], [g/Kw/hr]
$C_{D\delta e}$	change in drag coeff. with elevator defl., [1/deg]
$C_{l\beta}$	change in roll moment coeff. with sideslip, [1/deg]
$C_{L\delta f}$	change in lift coeff. with flap deflection, [1/deg]
$C_{l\delta r}$	change in roll mom. coeff. with rudder defl., [1/deg]
C_{lp}	change in roll moment coeff. with roll rate, [1/deg]
$C_{m\alpha}$	change in pitch moment coeff. with AOA, [1/deg]
C_{mq}	change in pitch mom. coeff. with pitch rate, [1/deg]
$C_{n\beta}$	change in yaw moment coeff. with sideslip, [1/deg]
C_{nr}	change in yaw moment coeff. with yaw rate, [1/deg]
C_{Yr}	change in sideforce coeff. with yaw rate, [1/deg]
D_{CEMM}	degraded state in CEMM [1/hr]
E_A	expected system availability

E_G	expected performance
F_{CEMM}	failed state in CEMM [1/hr]
$\breve{\mathbf{g}}^{\mathbf{i}}$	set of element state performances, size k^i
$\breve{\mathbf{G}}^{\mathbf{s}}$	set of system state performances, size K^s
g_k^i	performance of element i, in element state k
G_K^s	system performance, in system state K
N_{CEMM}	nominal state in CEMM [1/hr]
$N_{engines}$	number of engines
$\breve{\mathbf{p}}^{\mathbf{i}}$	set of element state probabilities, size k^i
$\breve{\mathbf{P}}^{\mathbf{s}}$	set of system state probabilities, size K^s
P_s	(weight) specific excess power [fpm]
p_k^i	probability that element i occupies element state k
P_K^s	probability that system occupies system state K
P_{max}	maximum engine power, [Hp]
P_{pump}	max oil pump power, [kW]
Pr	probability
$\mathbf{r}$	vector of control variables
R	controller gain, or reliability, according to context
RPM_{HS}	high-spool RPM [rev/minute]
RPM_{LS}	low-spool RPM [rev/minute]
S	wing area, [ft^2]

SR	oil line size ratio
W	performance threshold
W_{empty}	aircraft empty weight, [lbs]
$\mathbf{x}$	vector of static design variables

— Symbols —

$\mathit{A\!R}$	wing aspect ratio
η_{prop}	propeller efficiency
Γ	wing dihedral, [deg]
$\boldsymbol{\lambda^s}$	set of system transition probabilities corresponding to failure rates, size n = number of elements in the system
Λ	wing sweep, [deg]
λ	taper ratio
λ_i	failure rate of ith component
$\lambda_{DAL,SEMM}$	equivalent SEMM transition rate, loss from abort from degraded [1/hr]
$\lambda_{DF,CEMM}$	equivalent transition rate from degraded to failed state in CEMM [1/hr]
$\lambda_{ND,CEMM}$	equivalent transition rate from nominal to degraded state in CEMM [1/hr]
$\lambda_{NDA,SEMM}$	equivalent SEMM transition rate, abort from degraded from nominal [1/hr]
$\lambda_{NF,CEMM}$	equivalent transition rate from nominal to failed state in CEMM [1/hr]
μ_{DN}	repair rate from degraded to nominal state in CEMM [1/hr]

μ_{FN}	repair rate from failed to nominal state in CEMM [1/hr]
$\tau_{FDGS,in}$	torque input to FDGS [N*m]

— Subscripts —

A	denotes abort, also used to denote specific element A
$c.g.$	denotes value at the center of gravity
cr	denotes value at cruise conditions
D	denotes degraded
d	denotes *derivative* gain
F	denotes value in failed state
i	denotes element i when used with μ or λ; with R it denotes controller *integral* gain
K	denotes system state K
k	denotes element state k
L	denotes state in which system is lost
LB	denotes lower bound value
LE	denotes value at the leading edge of the surface
LL	denotes *lead-lag* filter gain
M	total number of system states
m	total number of element states
N	denotes nominal

OP	denotes value in operational state
p	denotes *proportional* gain
s	used only as subscript on P to denote specific excess power
t	denotes value at time t
UB	denotes upper bound value
z	denotes value for the zth interval of time

— Superscripts —

i	denotes element i (used as subscript on only μ or λ to denote the same)
s	denotes a system level value, as opposed to an element level value
s, t	denotes truncated set of system values

— Acronyms —

FL	failure level (in Markov diagram)
AOHEX	air-oil heat exchanger
CEMM	Campaign Equivalent Markov Model
DAPCA	Development and Procurement Cost of Aircraft
DOE	Design of Experiments
FDGS	Fan-Drive Gear System
FOHEX	fuel-oil heat exchanger
LPC	low pressure compressor

LPT	low pressure turbine
MDAO	Multidisciplinary Design Analysis and Optimization
MTBF	mean-time-between-failure [hr]
MTTR	mean-time-to-repair [hr]
SEMM	Sortie Equivalent Markov Model
TSFC	thrust-specific fuel consumption
VMM	Vehicle Markov Model

Chapter 1

Introduction

Aggressive performance requirements and lifecycle cost constraints drive towards highly reliable or fail-safe systems. These are typically achieved through increased redundancy, expensive reduction in component failure rates, and heavier infrastructure. Despite these attempts to maintain a fully functional state of operation, most systems still spend very substantial amounts of time operating in degraded or off-nominal states. As a result, design efforts that focus on the optimization of performance for the nominal configuration overlook potential improvements to be made to the system's actual real-world performance. This thesis addresses the problem by exploring early-stage aerospace design from a multistate perspective, where multistate refers to a finite set of performance levels associated with distinct configurations of the system. The initial case study shows feasibility of this approach through the examination of a well known twin-engine aircraft, a Beechcraft Super King Air. A formalized methodology is then developed and applied to the case study design of an ultra long endurance unmanned aerial vehicle (UAV) and the design of the lubrication system for a geared turbofan engine.

This chapter begins with the motivation for the work, followed by the background research, and ends with a road map and chapter by chapter summary.

1.1 Motivation

There are two increasing trends in aerospace design that drive the need for an integrated multistate design approach early in the design process. The first of these is time, or more specifically, mission duration. The second is cost. While cost has been on a steep rise for two or three decades and numerous spacecraft have been fielded with very long mission durations, it is only in the past five to ten years that earth-bound aerial systems have been seriously considered with mission durations of months or even years. Thus, razor-thin margins for cost have converged with extraordinary demand for performance and reliability to form an extremely challenging design problem. Advancement in the tools of design optimization, reliability analysis, and parallel processing enable such a task to be accomplished today, whereas ten years ago it remained prohibitively challenging. What remains is to refine, integrate, and test these methodologies to provide an in-depth and comprehensive look into the multistate design space. This thesis sets the foundation for such an endeavor.

While past products have had the luxury of relatively short mission durations and frequent maintenance and repair opportunities, future mission scenarios will increasingly require extraordinary on-station times in often remote operating environments. Some examples of systems that fall into the above category include:

1. *Ultra long endurance unmanned aerial vehicles (UAVs)*: The Defense Advanced Research Projects Agency (DARPA) recently released a solicitation for proposals for its *Vulture* program, an UAV required to remain airborne for an uninterrupted period of five years. Top-level performance objectives for the system specify that it should carry a 1000 lb payload, have a 99% probability of station-keeping, and high probability of mission success [32].

2. *Reconfigurable rovers for planetary surface exploration*: One of two rovers currently on Mars was declared a "stationary research platform" early in 2010, after being stuck in a patch of soft soil for more than a year and a half [74]. This underscores the need for surface vehicles capable of operating under negative circumstances far away from any opportunity for maintenance. Here, the

desire for robust performance will become even more important in the face of NASA's recent shift in focus away from manned planetary landings [29, 94].

3. *Airships for use in long-term surveillance and reconnaissance*: NASA, as well as several militaries around the world, has been looking at the reemerging technology of airships for long-duration surveillance and reconnaissance. Several concepts have mission durations of several months to a year of continuous flight [30]. Another international group even makes a very persuasive case for using autonomous airships in the exploration of planetary bodies with atmosphere [48].

Systems such as these must operate in dynamic, heterogeneous environments for very long periods of time. A single point-design methodology is insufficient, as sub-optimal performance in any one of the many failure scenarios, ranging from fully operational to fully failed, will be unacceptable given the ultra long mission durations and cost of failure.

The above challenges pose a complex multistate design problem, the solution of which is critical for ensuring high probability of mission success. Many of these systems may experience off-nominal conditions that dominate their operational period. To gain an appreciation for this fact, consider the charts shown in Fig. 1-1. These are computed using the Markov analysis described in Chapter 2, Section 2.3.2, and show the probability that an aerial system will leave its nominal state of operation over a given mission duration. It assumes three levels of failure rates for critical flight control actuators and engines, which have been taken from several sources [36, 81, 84], and will be discussed in following chapters.

There are two important observations to take from Fig. 1-1. The first is that each of the three plots uses the same set of failure rates. When dealing with mission durations on the order of one or two days, as in the upper left chart, these rates result in very high probabilities of completing the mission without experiencing failures. In all but the lowest technology level, representative of component reliabilities used in UAV's of the 1990's, this probability is up near 99% or higher. For civil aviation, it

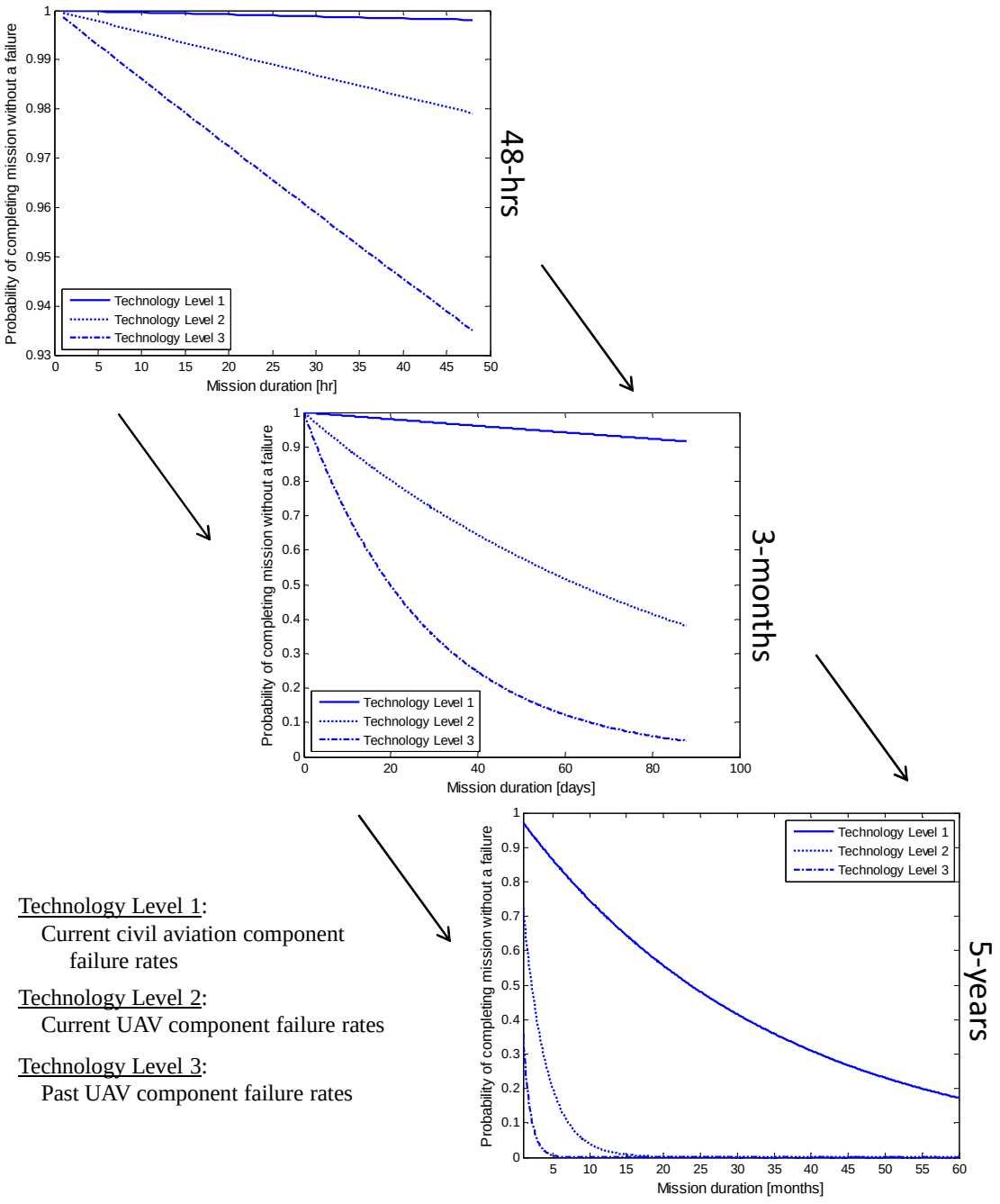

Figure 1-1: Increasing probability of failure with longer mission durations (6-component analysis); note zoomed-in y-axis on upper left chart

is where one would expect, in the range of 99.9%. As the mission duration increases, however, these same rates result in very poor probabilities of failure avoidance. In the case of the five year duration, such as that proposed by DARPA's *Vulture* program, even the highest technology levels used in current civil aviation fall far short of reasonable requirements. The development of such systems will require a paradigm shift in aerospace design methodology.

The direction in which this shift should head is underscored by the second important observation. Namely, that the charts in Fig. 1-1 comment only on whether or not the system will *experience* a failure of the engines or flight control actuators. They say nothing about the system's performance once that failure has occurred. Nevertheless, traditional reliability analysis focuses primarily on preventing this failure from occurring, after the system has been designed to maximize performance in the nominal state. As observed from the 5-year mission plot, the prevention of this failure will likely be a losing battle. The solution proposed here is to accept that failures will occur and integrate their performance into the early-phase design space. This represents a shift away from seeking perfection, to pursuing adequacy, a difficult paradigm shift for classically trained engineers.

A simple example hints at the potential effectiveness of using such an approach. Consider the case of a dual-engine aircraft, such as that shown in Fig. 1-2. A more

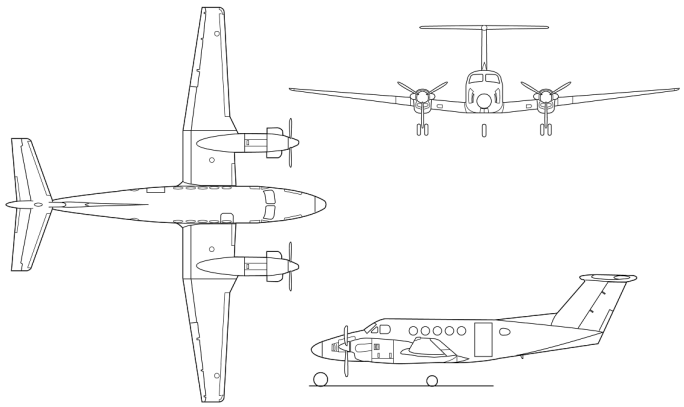

Figure 1-2: 3-view of a twin-engine aircraft

detailed development of the case is given in Chapter 3, but for now assume the aircraft

has a rudimentary three-axis control system, consisting under normal circumstances of a rudder, ailerons, and an elevator. In any particular state involving the failure of one of these components, the thrust of the engines becomes an additional factor in the failure scenario, one that can be used to improve control performance. Several different possibilities are outlined in Table 1.1.

Table 1.1: Engine effect scenarios in different states of control

State **State**	Rudder failure	Elevator failure	Aileron plus engine failure
Engine affects...	yaw through differential thrust	pitch through symmetric thrust	roll through torque (small effect through throttle change)

While this is not an all inclusive list, it serves to show the couplings that exist in vehicle states other than those in the nominal scenario. If one chooses to maximize the chances this aircraft will achieve a certain level of performance, given the likelihood that any one of these aircraft states may be entered at a given time on a given mission, there are several design choices at one's disposal. These may include:

- control surface size, location, or maximum effective deflection angle
- engine thrust, location from centerline, nacelle drag, or torque
- any one of the component reliabilities related to the control system

Several trade-offs may occur as well. While perhaps favorable in the engine-out scenario to have the engines further inboard to reduce the effect of yaw from differential thrust, in the case of rudder failure, one would desire the opposite. While these may seem trivial in the context of a well understood twin-engine aircraft design, such trade-offs may be successfully employed in designing systems with thin margins on performance across ultra long mission durations.

1.2 Summary of Relevant Research

The thesis approaches this problem by formulating it in terms of *expected*, or state averaged, performance, rather than nominal performance, and in terms of the system's availability across its planned mission duration. The focus is on accurately characterizing the multistate design space to ensure that the design/decision maker has the information necessary to make informed choices concerning the system's robust performance and to move this performance in a direction of improvement. The following is an overview of relevant research, which will followed by a more detailed review of literature in Chapter 2.

To date, the majority of design work done with regards to the robustness of multistate systems has occurred on three fronts, summarized here in the context of their relevance to the proposed research. The first deals with systems where a certain predictable structure applies to the various levels of state performance (typically, but not limited to, degraded performance in failure). This predictability allows performance levels to be modeled by a single, or set of, *structure functions* and optimized as described in Lisnianski [69]. Applicability is limited to simpler systems such as those related to flow (e.g. pumping stations) or data transmission (e.g. circuit boards). In aerospace systems, the complexity of interactions between disciplines and the much larger space of performance metrics makes usefulness of such methods limited. The second front focuses on control design and (dynamic) optimization to develop efficient methods for dynamically determining the system's state once in operation and effectively controlling it to maximize mission performance. Into this category fall the State Analysis methodology developed under NASA's Mission Data System Framework [66], work with hybrid systems, such as that at MIT described in [21], and a broad range of work in developing fault tolerant systems. While the research in this area is substantial and highly innovative, it deals predominantly with control, automation, and dynamic optimization as opposed to the parametric (static) optimization of the system's up-front design. The third front turns focus to the system's reliability as dependent on the failure rate (1/mean-time-between-failure) of its components and

subelements. Here, design has concentrated on analysis of how changes in these failure rates affect overall performance and system availability and adjusting them accordingly to maximize these two metrics. More recent work has concentrated on mapping the effect of system faults into the corresponding performance space and recognizes that reliability is an integrated systems problem, as described in Dominguez-Garcia [39] and Babcock [9]. In light of this integrated problem, the above mentioned research acknowledges the link between a system's core design parameters and expected performance in the face of degradation, but stops short of actually manipulating them in a comprehensive manner such that robustness is improved.

There are several reasons why the above solutions have not pushed beyond the described limitations. Many of these have to do with the effort of meeting the challenges presented by the multistate design problem, which includes: 1) multiple performance levels characterized by the duration of time the system spends in any particular state and their relative importance in terms of mission achievement, 2) competing trade-offs between states' maximum performance levels, and 3) potentially high dimensionality resulting from the evaluation of numerous states. With mission scenarios characterized by longer durations, more demanding environments, infrequent or costly maintenance opportunities, and tight fiscal constraints, the benefits of a more comprehensive and integrated approach to the early stage design become more attractive. Fortunately, each of the challenges are particularly suitable for the integrated analysis afforded by modern multidisciplinary analysis tools. These tools include various techniques for organizing coupled design problems of high dimensionality into smaller, more tractable sub-problems, as well as:

- Sensitivity analysis w.r.t. static design variables, both at the component/discipline level and at the coupled, system level
- Sensitivity analysis of optimum w.r.t. parameters
- Radical reduction of computational elapsed times by the use of surrogate models and parallel computing
- Many Design of Experiment (DOE) techniques for efficient sampling of the

design space and subsequent analysis of performance effects

This thesis extends the above sensitivity analyses to include the integrated effects of component failures rates, as well as static design variables. Where possible, it uses parallel computing for the evaluation of individual state performances, and adds to the surrogate modeling techniques a surrogate formulation for system availability. Finally, several DOE techniques are used throughout the case studies in the analysis and visualization of the multistate design space.

1.3 Thesis Contributions

As mentioned above, research into the design and optimization of multistate systems has typically focused on 1) systems with a predictable state performance structure, commonly referred to as *multistate coherent systems*, 2) control design and optimization, and 3) improvements in component failure rates and redundancy (reliability analysis). Fig 1-3 shows how the thesis fits within the current field of research defined in this context. Chapter 2 reviews the literature of multistate design in more detail as well as relevant research in multidisciplinary analysis and optimization.

The research goal is to propose and demonstrate an integrated multistate methodology early in the design process that improves expectation of the system's success over long mission durations. Key contributions of this work include:

- The development and demonstration of the central methodology, in the form of an integrated multistate design approach that formulates responses of system expected performance and availability as functions of static design variables (geometry) and component failure rates, accounting for control design variables (gains) where appropriate.

- Demonstration of the cost and benefits, in the form of design trade-offs, associated with a multistate design approach as compared to pure reliability analysis techniques and the nominal design approach.

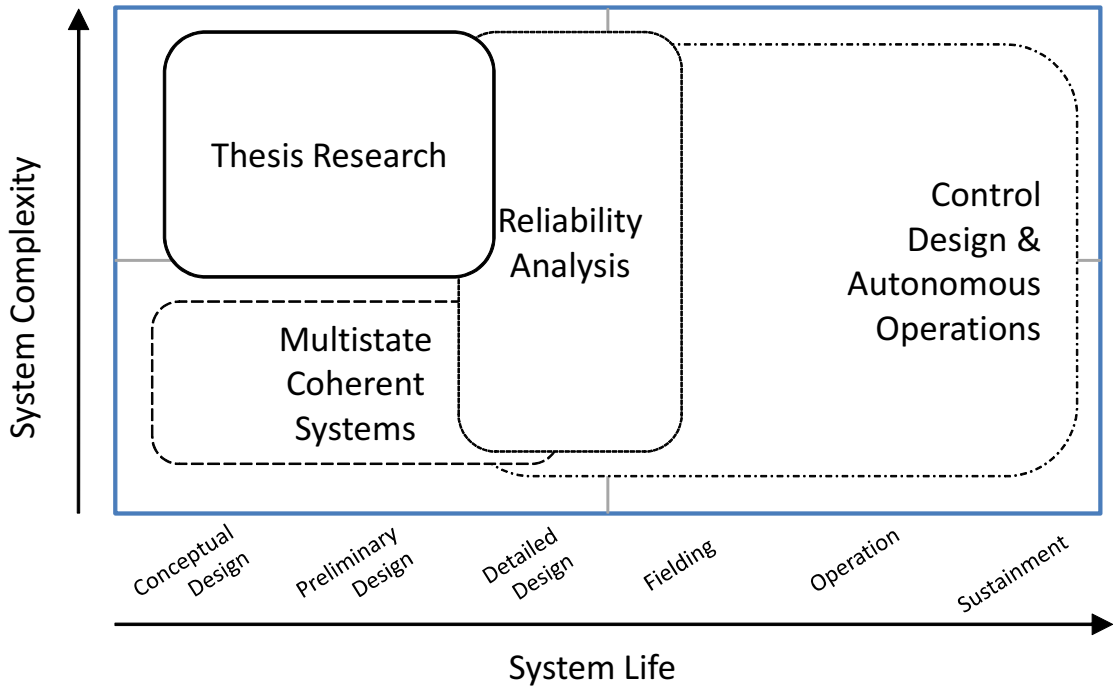

Figure 1-3: Fields related to multistate design

- A multilayer approach, using Markov analysis, for translating single sortie vehicle level metrics into measures of multistate campaign performance.[1]
- A surrogate function for system availability that allows the otherwise piecewise-constant metric to be optimized via gradient-based optimization algorithms.
- Major findings of the thesis, including evidence of:
  - multistate performance output spaces having distinctly unique shapes and boundaries, depending on whether formed through variation of component failure rates, static design variables (geometry), or a multistate combination of both,
  - a region of multistate performance resulting from the combined variation of failure rates and static design variables that is unachievable through the independent variation of either one,

[1] *Sortie* refers to a single operational return trip of the vehicle, while *campaign* refers to a collection of sortie operations for a single objective.

- small changes in static design variables that may be used to significantly improve system availability, and
- the general multistate design problem being one of competing objectives between system availability, expected performance, nominal performance, and cost.

In addition to the above contributions, the thesis develops some general principles concerning multistate analysis and design in the early-phase development of complex systems. These are described in detail in Chapter 7, and listed below for preliminary reference:

1. **The general multistate problem is a multi-objective one with competing trade-offs between nominal performance, system availability, expected performance, and cost.**

2. **The systems benefiting most from multistate analysis and design are systems with long operational durations and little opportunity for maintenance or repair, and systems involved in multi-system operations where costs of downtime and system loss are high.**

3. **Using component failure rates to increase availability or expected performance will tend to increase direct system cost, while using static design variables for the same can either increase or decrease this cost.**

4. **In multistate system design, time often plays the role of both objective and constraint.**

The last principle is especially true in the case of multistate long endurance systems, where the objective performance metric is to stay in operation as long as possible. As the improving design lengthens this period of operation, the probability distribution of performance begins migrating from the nominal state into the off-nominal states. Simply put, the longer the system's endurance, the longer the period

between maintenance opportunities, and the higher the chance of experiencing off-nominal states. Although the last principle seems to be common sense, it is a fact that many designers not familiar with reliability analysis might overlook. By the time the design makes it to the reliability engineers, it has already passed the point where useful improvement to the system's availability may be effected through static design variables. This is one of the key issues addressed by the thesis.

1.4 Thesis Overview

The research presented in this thesis began with a review of literature from several fields dealing with the topic of multistate design. Next, a well-known and validated aircraft design case was used to show the feasibility of using static design variables as an effective means of improving expected performance and system availability. A more formalized methodology was then developed, based on lessons from the first case study, and applied to the design of a long endurance UAV and the lubrication system for a geared turbofan engine.

Fig. 1-4 presents a comprehensive overview of the dissertation in the form of an Object-Process Diagram (OPD) [41]. Here, boxes depict objects (highlighted boxes are main objects, all others are supporting objects), ovals depict processes, unidirectional arrows indicate execution of a process resulting in an object, and circle-ended lines show linkages between processes and their supporting objects. Bidirectional arrows indicate two-way relationships between entities.

The following paragraphs give a detailed chapter-by-chapter summary:

Chapter 2. The main contributions of this chapter are the detailed presentation of the basic concepts and definitions in multistate design, and the extension of this from relatively simple systems to more complex aerospace systems. The chapter begins with a detailed review of literature, coming predominantly from the fields of design optimization, reliability analysis, and controls design. The remainder of Chapter 2 provides an in-depth discussion of multistate design. Some of this has been extracted

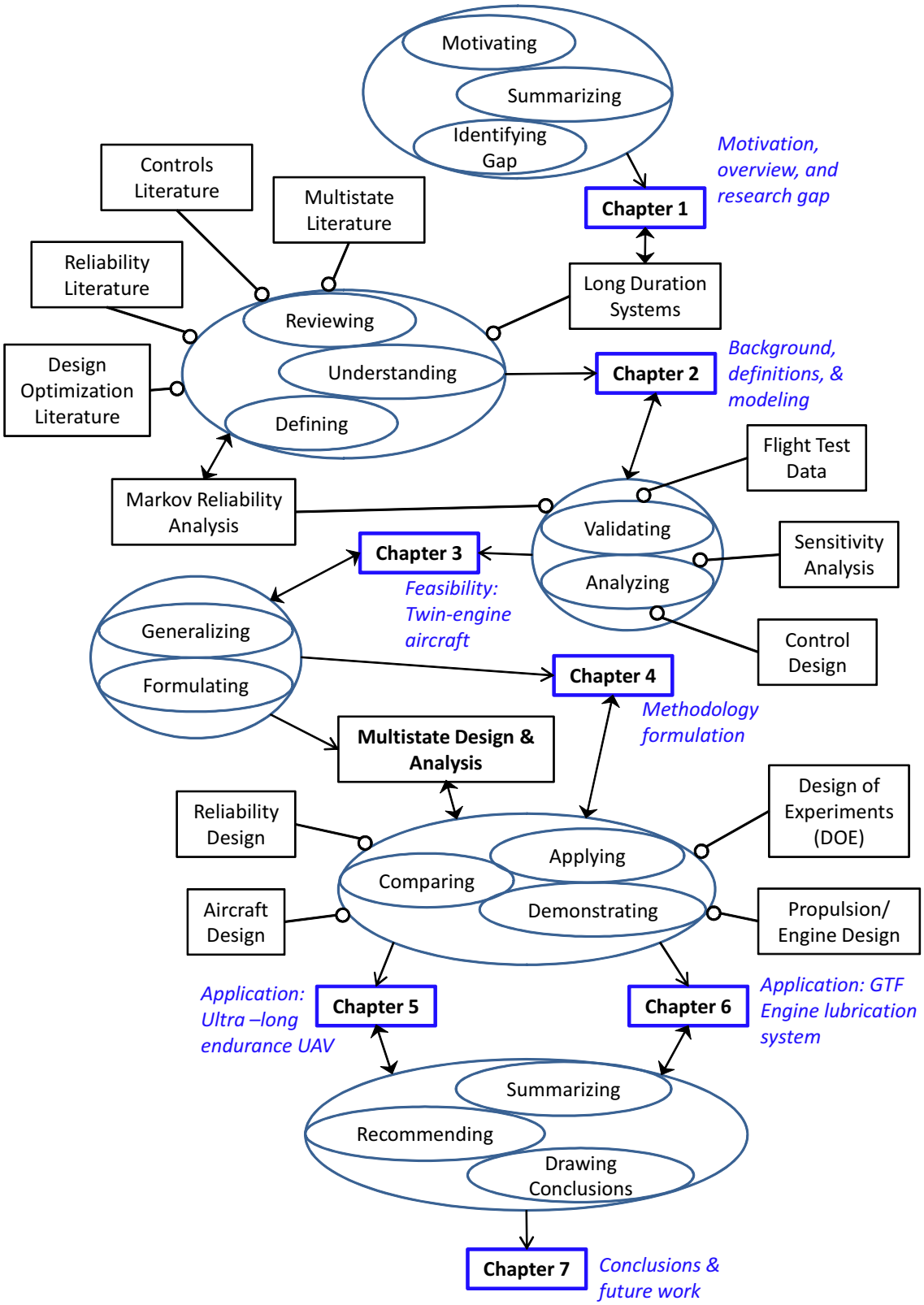

Figure 1-4: Object-Process Diagram presentation of thesis

from the very small body of formal multistate design literature, dealing with relatively simple systems, and much has been modified/extended to the case of more complex aerospace systems. Markov modeling, as it pertains to traditional reliability analysis, is discussed and its nomenclature integrated with that of the multistate processes described in the thesis.

Chapter 3. Chapter 3 demonstrates feasibility of the multistate approach through the design analysis of an existing twin-engine aircraft. The chapter begins to integrate elements for determining responses in expected performance and availability to changes in static design variables (geometry), control design variables (gains), and component failure rates, considered the three driving input categories affecting the aircraft's performance robustness. Key results from the twin-engine aircraft study show that, while many unsatisfactory geometry-state responses occur in the fully failed state and are expected, several occur in partially degraded states where the majority of geometries are able to meet performance requirements. This behavior clearly exhibits itself in the resulting design sensitivities, confirming that such an approach allows designers to identify elements that might drive system loss through analysis of performance changes across system states, and their respective response to changes in static design variables. The effectiveness of the basic methodology demonstrated in this chapter sets the stage for a more in-depth methodological formulation in Chapter 4, and the methodology's application to case studies in Chapters 5 and 6. A large part of the research and results from Chapter 3 have been recommended for publication in [1].

Chapter 4. The main contributions of this chapter include:

- A generalized methodology for multistate analysis and design, shown in Fig. 1-5.
- A multilayer extension of Markov analysis, for translating single sortie component and vehicle level availability to multiple sortie mission campaign robustness.
- The development and demonstration of a "surrogate" function for system avail-

ability.

The chapter begins with the development of the generalized methodology for multistate analysis and design, based upon its effectiveness as demonstrated in Chapter 3. In support of this framework, the chapter continues with the description of a multilayer Markov analysis technique that enables the calculation of campaign performance and vehicle attrition as a function of component failure rates and vehicle static design variables.

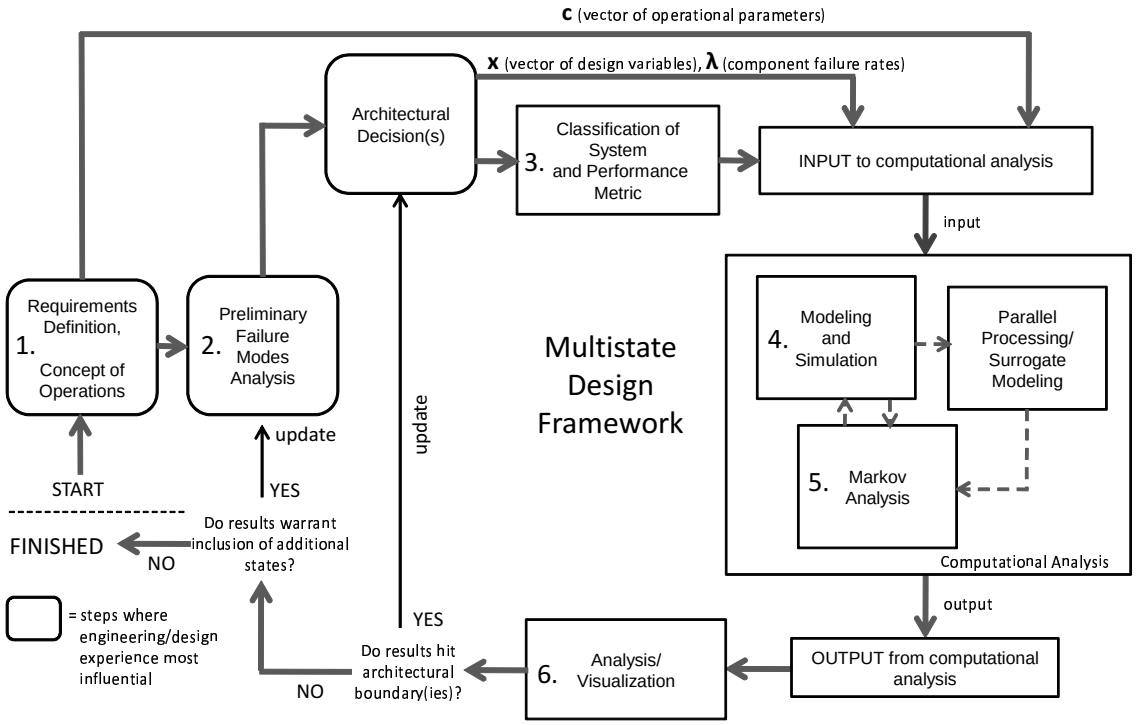

Figure 1-5: A framework outline for multistate design

Chapter 4 concludes with a discussion of issues in multistate optimization, which may occur as part of the computational analysis. This includes the special case of system availability, essentially a piecewise constant function in which improvement corresponds directly to increasing performance in off-nominal states above a certain threshold. A surrogate function is formulated that allows for the improvement of expected availability through gradient-based optimization methods.

Chapter 5. The methodologies formalized in Chapter 4 are applied to the design and analysis of a long endurance unmanned aerial vehicle in this chapter. Key findings from this case study show that:

- Each performance space stemming from three distinct design approaches (varying only failure rates, varying only static design variables, or combined multistate variation of both) has distinctly unique shapes and boundaries.
- The achievable improvement in system availability via static design variables is nearly as large as that made via component failure rates. From the perspective of reliability analysis, this is significant due to the fact that improvements in reliability are nearly always sought after through changes in component failure rates, rather than affecting state performance through changes to static design variables.
- Perhaps most importantly, the inclusion of both static design variables and component failure rates in the design analysis allows a region of system availability to be reached that is unobtainable via the independent variation of either one.

The combined multistate approach demonstrated an improvement in system availability of 11%, at a 3% lower cost, when compared to the baseline UAV designed for nominal performance. Variation of component failure rates or static design variables alone showed an improvement of only 6.5%. Furthermore, when considering multiple objectives of system availability, expected performance, nominal performance, and cost, the combined approach was still able to achieve an 11% improvement in availability, with only a 4.5% decrease in nominal performance, albeit at a small 6% increase in aircraft flyaway cost.

Chapter 6. This chapter complements Chapter 5 by demonstrating application of multistate analysis and design to a lower level aerospace subsystem. The case study is the lubrication system for a high bypass ratio geared turbofan (GTF) engine in the 20,000- to 30,000-lbf thrust class. Key findings demonstrate that:

- Even in the simpler design space characterized by the lubrication subsystem,

sensitivity of expected performance to changes in static design variables varies significantly between the nominal case and two multistate scenarios of differing time duration. In one case, the sign of the sensitivity even reverses trend. The impact of this is that, designing for best performance in the nominal scenario, while affecting availability only through component failure rates, will likely result in an inferior multistate design.

- The surrogate function for availability proves effective within a gradient-based algorithm for generation of Pareto fronts.
- Variation of static design variables alone led to improvement of subsystem availability by 22% over a time duration of 500-hrs (Fig. 6-11). When considering oil system cooling size as a representation of cost, and adjusting accordingly, the best Pareto solution still resulted in an improvement of 10%.

This case study is successful in demonstrating how specific changes to the lubrication system's design improve the robustness of its performance across several modes of failure. Additionally, the methodology is demonstrated such that it may be extended to a more detailed multistate analysis given higher fidelity tools and models available to engine industry experts.

Chapter 7. The final chapter summarizes key results of the thesis. It draws together major findings and conclusions arising from the three central case studies, and uses these to develop some general principles for early-phase multistate analysis and design. Finally, the chapter recommends areas of research for further improvement in multistate design, outlining a performance space mapping approach for reducing the high computational burden of the multistate problem.

Chapter 2

Understanding Multistate Design

Chapter 2 presents the basic concepts and existing research in multistate design, and lays the foundation for modeling multistate systems. The first section reviews literature in the three main areas of current multistate design research. Next, multistate design is defined within the scope of the thesis, followed by the development of multistate nomenclature and terminology used throughout the remainder of the dissertation. The remaining sections deal with the modeling of state transitions, introducing Markov chains, and several issues of multistate performance modeling.

2.1 Review of Literature

Research into the analysis and design of multistate systems has typically focused on 1) systems with a predictable state performance structure, 2) control design and optimization, and 3) improvements in component failure rates and redundancy. This section reviews the literature of multistate design in more detail as well as relevant research in multidisciplinary design optimization.

2.1.1 Multistate Coherent Systems

There are many systems where a certain predictable structure applies to the various levels of state performance. These are often comparatively simpler systems such as

those related to flow or data transmission, e.g. pumping stations or circuit boards. Due to the possibility of more structured analysis, this is the area where the concept of a multistate system was first developed in the 1970's [77, 16]. El-Neweihi et al. [47] defined more succinctly the concept of a *multistate coherent system* as one having a *coherent* structure, where performance is monotonically increasing with relation to state, and where all states are relevant. This type of structure primarily includes series, parallel, and k-out-of-n systems.[1] As an example, for a flow system consisting of two elements, a & b, connected in series, total system performance, G, is a direct function of the element performance rates, g^a and g^b, according to the system's structure through

$$G(g^a, g^b) = min\{g^a, g^b\} \tag{2.1}$$

or, if connected in parallel,

$$G(g^a, g^b) = g^a + g^b \tag{2.2}$$

The performance predictability inherent in these types of systems eventually led to methods based on a universal generating function (UGF or z-transform function) to rapidly determine the system's expected performance and availability in systems with hundreds or thousands of states [110]. A simple UGF, e.g. for an element i with total failure in the parallel system above ($m = 2$ states), takes the polynomial form

$$U^i(t,z) = \sum_{k=1}^{m} p_k^i(t) z^{g_k^i} = (1 - p^i_{operating}(t))z^0 + p^i_{operating}(t) z^{g^i}; \qquad (i = a, b) \tag{2.3}$$

where t is time, p_k^i is the probability of being in state k with performance g_k^i, and z is the exponent base. z transforms with the operator δ_G such that $\delta_G(p_k^i z^{g_k^i}) = p_k^i g_k^i$ [67]. The parallel system UGF, with number of elements $n = 2$, is determined through the product of polynomials (time dependence and $_{operating}$ dropped for conciseness),

$$U_{sys}(z) = \prod_{i=1}^{n} U^i(z) = (1-p^a)(1-p^b)z^0 + p^a(1-p^b)z^{g^a} + p^b(1-p^a)z^{g^b} + p^a p^b z^{g^a+g^b} \tag{2.4}$$

[1] k-out-of-n systems are those requiring at least k of n components to be working (not working) in order to be considered functional (failed). Series and parallel systems are a special class of these.

where the coefficients of each term are multiplied, and exponents are summed. After simplifying the polynomial, the expected multistate system performance E_G is given by

$$E_G = \delta_G(U_{sys}(z)) = \delta_G(p^a z^{g^a} + p^b z^{g^b}) = p^a g^a + p^b g^b \tag{2.5}$$

The above example demonstrates the important fact that in multistate coherent systems, *system* expected performance may be expressed as a direct structured function of individual *element* performance rates and failure probabilities.[2] In more complex vehicle systems, however, this is rarely the case, due to strong interdependence between element performances, which often requires a fully coupled system analysis in order to determine performance (both at the system and element level).

First introduced in the 1980's, the u-function method was applied to real power system assessment and optimization in the 1990's in [70]. It was mostly in this area where further research in optimization methods occurred, including applications using heuristic approaches such as genetic algorithms [104] and ant colony optimization [73]. Except for extremely simplified cases such as that found in [69], application to aerospace systems with much more complex performance behavior has been limited.

2.1.2 Control Design and Optimization

A large amount of multistate system modeling and design research belongs to the field of control design and control optimization (also referred to as *dynamic* optimization). The focus on this front is determining the system's state once in operation and effectively controlling it to maximize mission performance. In the case of aircraft, this may include the detection of failure or damage to flight control effectors and using the remaining functional effectors to create compensating forces and moments [100]. Specific cases have developed and tested emergency control laws for partially or completely failed aircraft systems, motivated by the many real-world instances where

[2] Although the example shown was specific to a parallel system, the UGF method is applicable to other multistate coherent systems, where the operator, δ, takes a more complex role in defining the rules by which the elements' probability distributions of performance (PDF's) are transformed to the system PDF.

such control laws may have been helpful [26, 43]. Burcham et al. [27] documents the extensive development and evaluation of an emergency flight control system for an F-15 using only differential thrust. Results from the 36-flight evaluation showed that such a system can be used to successfully land an aircraft that has suffered from a major flight control system failure. A similar endeavor in Monaco et al. [111] details the successful retrofitting of an F/A-18 with a model-based adaptive control system to respond to states brought about by flight control failure, damage, or adverse environmental conditions.

Oriented more towards space systems, this category also includes the State Analysis methodology developed under NASA's Mission Data System (MDS) Framework [66, 60]. The goal of State Analysis is to "improve the current state-of-the-practice by producing requirements on system and software design in the form of explicit models of system behavior, and by defining a state-based architecture for the control system" [58]. Figure 2-1 is a diagram taken from Dvorak et al. [46] showing how the methodology attempts a unified approach to system analysis, control system software design, and system operation.

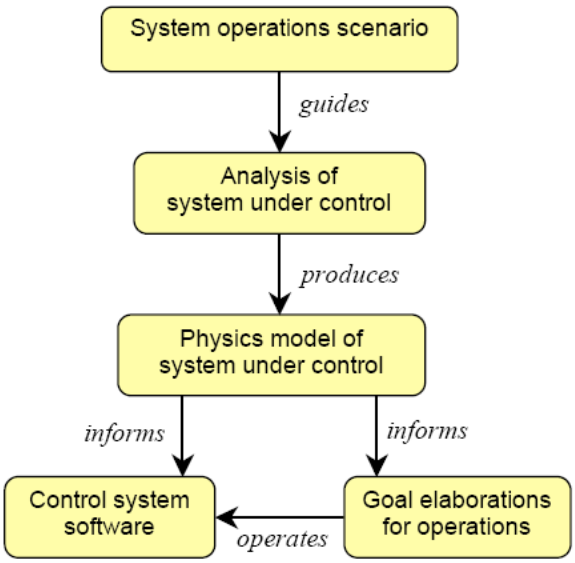

Figure 2-1: State Analysis methodology

Work with the MDS framework and State Analysis has also been successfully

applied in conjunction with advances in the area of hybrid system control optimization [24]. Hybrid systems are those which exhibit both continuous state and discrete state dynamics, a category into which most aerospace systems fall. Some examples of work in this area include control optimization for robust execution in the face of uncertainty [21], extension of the branch and bound method in solving hybrid discrete/linear optimization problems [68], and an investigation into the complexity of hybrid system optimization when transformed into a mixed-integer linear programming problem [107]. An excellent review and introduction to hybrid systems control is given in Labinaz [65]. Research in this area is substantial and highly innovative, dealing predominantly with control, automation, and dynamic optimization rather than the parametric (static) optimization of the system's up-front physical design.

2.1.3 Design for Reliability

This third front turns focus to the system's reliability through the failure rate of its components and sub-elements. A great deal of successful work has used integrated system modeling with Markov models to determine the system reliability (and system availability) of large, complex systems performing life-critical applications [9, 11]. Markov analysis ensures that highly improbable states and the events leading up to those states are accurately measured and tracked. A generic Markov state transition diagram is depicted in Figure 2-2, shown here for multiple states of failure without repair. The diagram is read from left to right, starting from the nominal state to states with increasingly serious failures.

In this formulation, the probability P_K that the system finds itself in any particular state of performance G_K (at time t) can be determined by solving a system of differential equations derived from the transition probabilities Pr. These transition probabilities, in the case of failures, are typically derived from known values of component or element *mean-time-between-failure (MTBF)*. The simplest formulation for the failure rate results in $Pr_{\ldots-K} = \lambda_i$, where λ_i is the inverse of the MTBF for the i^{th} component. Coupled with the integrated system model, the methodology enables determination of how overall system availability and performance change in response

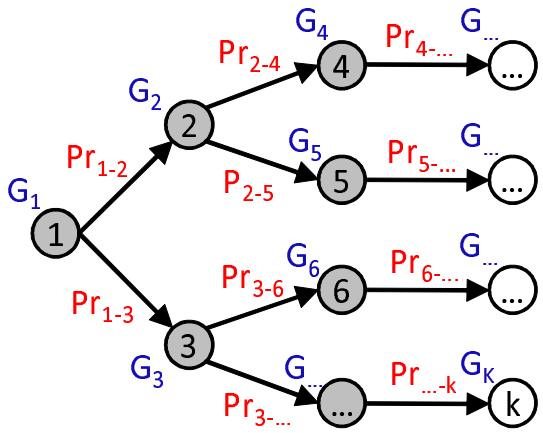

Figure 2-2: Markov state transition diagram

to variation of component failure rates and time.

The motivation for this thesis originally developed in response to the sponsor's need for expanding this type of reliability analysis beyond that involving just component failure rates. Recent work in Dominguez-Garcia [39, 40] has moved in this direction by merging system behavioral analysis with the integrated Markov model generation described in [10], allowing evaluation of performance for multiple system events (e.g. multiple failures and/or sequences of failures). By mapping the effect of system faults into the appropriate performance space, the research acknowledges the link between a system's core design variables and expected performance in the face of degradation, but stops short of manipulating them in a comprehensive manner such that robustness is improved.

Finally, there are many mature techniques to represent multistate systems for the evaluation of reliability. These include fault trees, block diagrams, dynamic fault trees [45], as well Markov models, some of which have been extended to relatively complex phased-mission analyses [96]. Literature is extensive on the topic, but a good overview can be found in [56, 87]. Most of these techniques require the analyst to specify which states are classified as 'failed', often using qualitative descriptions of the system's functionality. Some are more easily adapted to quantitative analysis (such as Markov models) than others, allowing the integration of analytical or simulation-

based performance into the overall system reliability model.

2.1.4 Relevant Methods in Multidisciplinary Design Optimization

Multidisciplinary Design Optimization (MDO) encompasses a body of algorithms, formulations, and techniques that facilitates the efficient design of engineering systems. These systems are influenced by different physical interacting phenomena, which are aligned with different engineering disciplines. Decomposition into disciplines or subelements is often needed. Many of these tools are appropriate for the solution of the multistate problem, as well. Although its roots lie in structural optimization, the past two decades have seen MDO's increasing use across numerous engineering fields. Several sources provide reviews of the topic, some of the more recent are Tedford and Martins [105], Alexandrov [4], and Agte et al. [3]. More dated, but very comprehensive is Sobieszczanski-Sobieski and Haftka [98].

Formal MDO notation generally follows that of the Nonlinear Programming (NLP) format, where the optimization problem is stated as Eqn. 2.6:

$$\begin{aligned} \textit{given} \quad & \mathbf{c} = [c_1, ..., c_{n_c}] \\ \textit{minimize} \quad & J = f(\mathbf{x}, \mathbf{c}) \\ & \mathbf{x} = [x_1, ..., x_{n_x}] \\ \textit{s.t.} \quad & \mathbf{h}(\mathbf{x}, \mathbf{c}) = 0 \\ & \mathbf{g}(\mathbf{x}, \mathbf{c}) \leq 0 \\ & x_{i,LB} \leq x_i \leq x_{i,UB}, \qquad i = 1, 2, ..., n_x \end{aligned} \tag{2.6}$$

where $\mathbf{c}$ is a vector of fixed parameters that influence the behavior of the system (material properties, operating conditions, etc.), f is the function to be minimized, $\mathbf{x}$ is a non-dimensional vector of static design variables with lower and upper bounds (may be either continuous or discrete), and $\mathbf{h}$ and $\mathbf{g}$ are equality and inequality constraints, respectively. J can be also be a vector of multiple objectives.

The formulation in Eqn. 2.6 proves very effective in solving problems of multistate performance. Most notable is its usefulness in refining the constrained design for system availability and expected performance, as demonstrated in Eqn. 5.5 of Chapter 5, and in forming the dual objective Pareto fronts of Section 6.7.2 in Chapter 6.

In addition to the NLP single optimization loop, shown in Figure 2-3 for reference, the MDO problem may also be organized into a decomposed structure such as that shown in Figure 2-4.

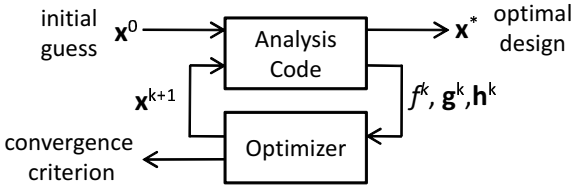

Figure 2-3: NLP - single optimization loop [3]

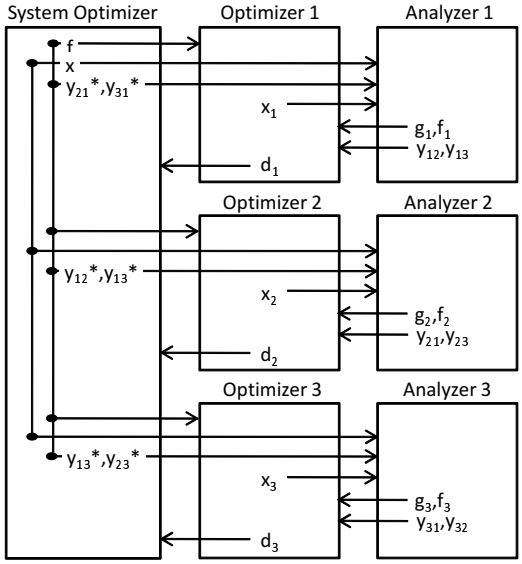

Figure 2-4: MDO problem decomposed into two levels - NAND @ disc. level, SAND @ sys. level [12]

Balling and Sobieski [12] describe the fundamental MDO approaches as follows:

> The fundamental approaches to MDO formulation vary in two aspects. First is the distinction between single-level optimization and multilevel optimization. In multilevel optimization approaches, the disciplinary design variables are determined by disciplinary optimizers and the system design variables are determined by the system optimizer. In single-level optimization approaches, both disciplinary and system design variables are determined by the system optimizer. Second is the choice between simultaneous analysis and design (SAND) and nested analysis and design

(NAND). This distinction can be made at both the system and the discipline levels. At the discipline level, SAND implies that the disciplinary design and state variables are determined simultaneously by the optimizer, whereas NAND implies that the optimizer determines only the disciplinary design variables and requires determination of the state variables at each iteration.

There are several decomposition methods derived from the above elements in conjunction with data organization structures such as the design dependence matrix (a.k.a. N-square diagram, N^2, or design structure matrix, DSM, described in Stewart [102]). Other tools that have seen very successful use in MDO include many Design of Experiment (DOE) and sensitivity analysis processes for effective exploration of the design space. This thesis uses the DOE methods of Latin-hypercube spacing [62] and orthogonal arrays [54] for efficiently sampling the design space for maximum coverage and determining the effects of design variables on performance output. Both of these methods are described further in Chapters 5 and 6, respectively.

Sensitivity analysis may be used at different system levels and stages of the design process to provide invaluable information to the designer concerning any number of outputs. This may include: System Sensitivity Analysis (SSA) [97], Subsystem Sensitivity Analysis (SSSA) [52], sensitivity analysis of optimum w.r.t parameters, or post-optimum sensitivity analysis [17]. The above make possible the thorough mapping of gradient information from the system level all the way down to the component level. Typically, this gradient information is only calculated for the effects of the system's static design variables. For multistate analysis and design, the above sensitivity analyses are extended to include the integrated effects of component failures rates, as well as the static design variables.

Finally, in addition to gradient-based methods, many heuristic algorithms have become very powerful when used in the context of multidisciplinary design optimization. These include genetic algorithms [72], simulated annealing [93], and particle swarm optimization [15], to name a few. A large amount of work has combined both gradient and heuristic methods to improve very complex designs [50, 6] in a pro-

cess typically referred to as hybrid optimization (not to be confused with the hybrid systems discussed in Section 2.1.2).

Due to its widening use as a means of analysis, rather than just optimization, many refer to MDO under the broader term Multidisciplinary Design Analysis and Optimization (MDAO). A MDAO framework including many of the processes and methods described above is shown in Fig. 2-5.

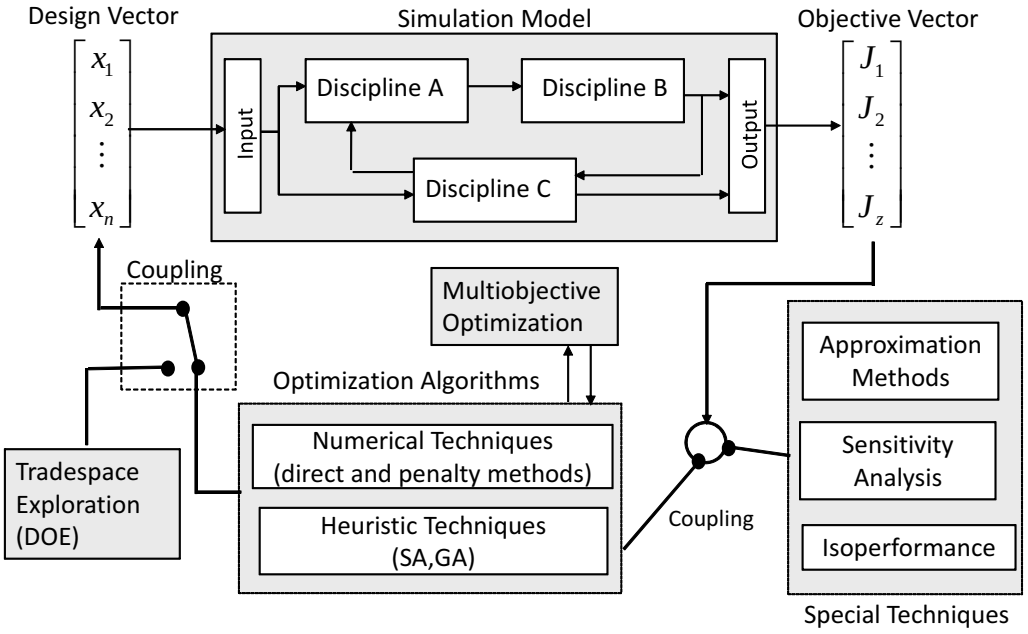

Figure 2-5: Multidisciplinary Design Analysis and Optimization framework [34]

This general framework serves as the foundation for the multistate optimizations performed throughout the thesis, and is extended to include a Markov state analysis loop outside of the simulation model. This is best demonstrated in Fig. 6-5, of Chapter 6.

2.2 Definitions and Context

There are many technical connotations associated with the term *multistate* in engineering science. The following section defines its meaning in association with aerospace design, and in the context of this research. As a starting point, Figure 2-6 is

proposed as a novel view on system state change hierarchy, organized according to the distinct means by which the state of a particular aerospace system may potentially change or be changed. Note that continuous or discrete state changes are not ruled out at any particular level, although continuous states typically dominate at the lower levels while discrete states dominate the higher. This is due mainly to the fact that the upper two levels require the ceasing of operations in order to change state, while the lowest levels allow the possibility of online state change via continuous variation of controls.

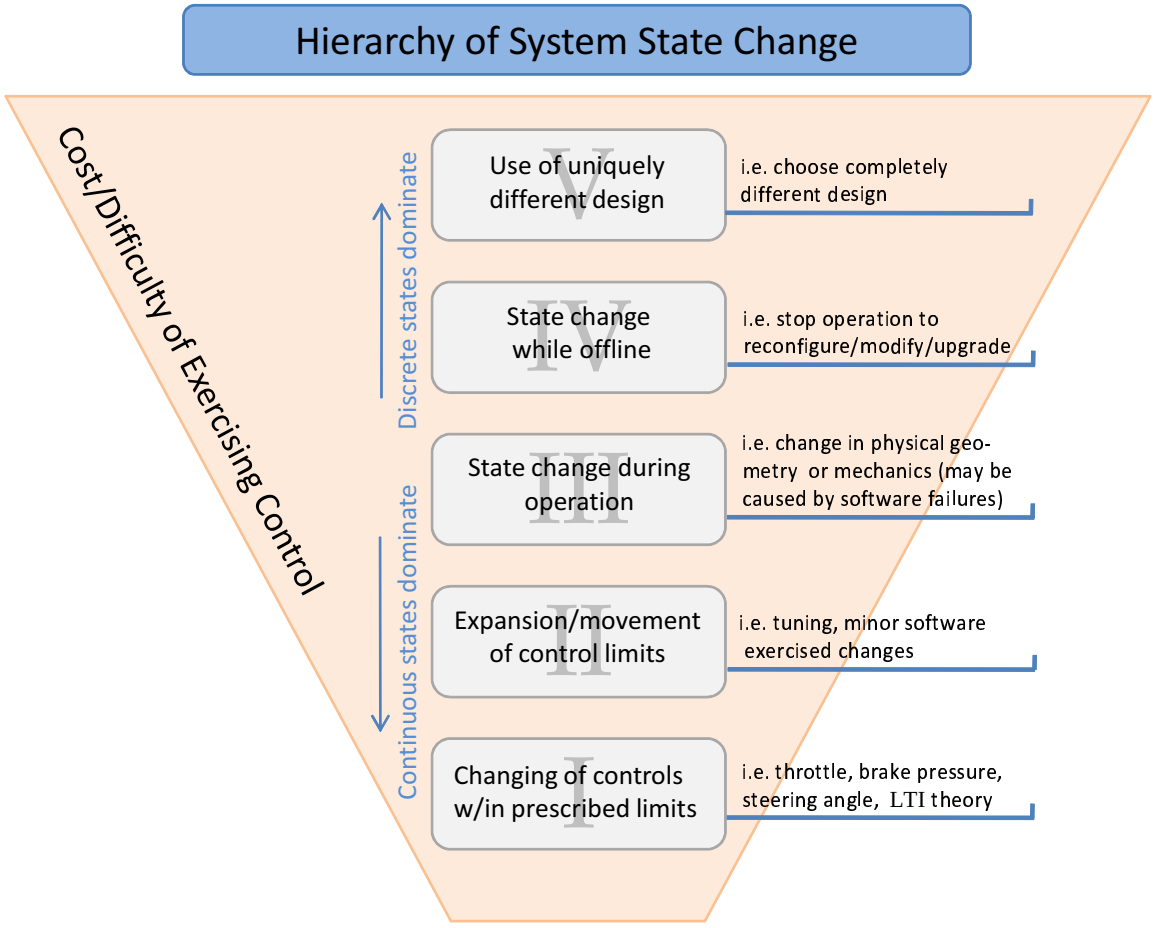

Figure 2-6: Hierarchy of system state change

At the most general level, shown as *Level I*, any system to which adjustments may be made in order to modify performance could be characterized as having multiple states. A pilot at the departure end of a runway changes the state of the aircraft by

using the throttle to increase fuel flow rate in order to take off. The flight control system then constricts movement limits on control surfaces as the aircraft accelerates (*Level II*). At *Level III*, the aircraft's state further changes when the pilot retracts the flaps upon reaching a safe climb altitude. State transitions at *Level IV* and *Level V* occur when the system must be taken out of operation in order to make configuration changes or to meet requirements with an entirely different design.

Level III is the region where hardware or software failures may lead to state transitions and the area where this research focuses. More specifically, these states have distinct performance levels, brought about by discrete changes in the system occurring at stochastically predictable points in continuous time. They occur while the system is operating. The fact that they are stochastically predictable allows their inclusion in the early-stage design loop, given that one can accurately model their performance and efficiently handle the extra computational burden.

With the above in mind, three succinct definitions arise, defined here within the specific context of this thesis:

- **state**: a discrete condition of the system, brought about by a discrete change in the performance rate (e.g. operating $\Rightarrow$ failed) of one or more elements that compose that system.

- **multistate system**: a system subject to the above defined states, where each state is a member of the set composed of all possible permutations of its elements' performance rates.

- **robust system**: a system that consistently achieves satisfactory performance across a broad range of operating conditions for a predicted set of system states, including partially degraded states.

The above definitions of state fall more in line with the traditional terminology used in reliability analysis [22, 69], than with that used in controls theory, where these might often be referred to as operating *modes*.

2.3 Multistate Modeling

Now that a performance-centric definition of *multistate* has been provided, this section defines a terminology and nomenclature for the modeling of multistate systems, describes a process for determining state probabilities, and presents two indices of multistate performance. This sets the framework for the analysis performed in Chapter 3, maintaining terminology, where possible, from multistate coherent systems [69] as reviewed in Section 2.1.1, and from that of MDAO, reviewed in Section 2.1.4. It begins by describing the probability distribution of performance for the elements of a system in Eqns. 2.7 through 2.10, and the resulting probability distribution of performance for the system in Eqns. 2.11 through 2.15. At the system level, the performance probability distribution becomes a function of the system's static design variables and control laws, as well as its element transition rates as defined in Section 2.3.2. The *inclusion of the functional dependency of each of these variables on the system's multistate performance response*, as well as *the integration of Markov analysis directly into the early-stage design loop for complex systems* comprise a novel approach to design that is first tested on the case study in Chapter 3, and then more formally developed and applied in Chapters 4, 5, and 6.

2.3.1 Probability Distributions of Performance

In general, any system is composed of n elements, each element i susceptible to m states, and each state characterized by a performance g_k^i, $k \in \{1, 2, ..., m\}$. An element's state performance set is then defined as:

$$\breve{\mathbf{g}}^{\mathbf{i}} = \{g_1^i, g_2^i, ..., g_m^i\} \tag{2.7}$$

Element state performance, g_k^i, may be a continuous or discrete function of the element's physical design. If it is only important to the system that the element is functioning or non-functioning, Eqn. 2.7 may be simplified to:

$$\breve{\mathbf{g}}^{\mathbf{i}} = \{g_{OP}^i, g_F^i\} \tag{2.8}$$

where OP indicates the *operational* state, F indicates *failed* state, and $m = 2$. This simplification by no means implies that the system composed of elements i has only two states or two levels of performance.

In the multistate system, the performance $g^i(t)$ of element i at any point in time, $t \geq 0$, is a value randomly taken from $\breve{\mathbf{g}}^{\mathbf{i}} : g^i(t) \in \breve{\mathbf{g}}^{\mathbf{i}}$. Thus, across a system's mission time interval [0,T], an element's, and consequently, the system's performance may be defined as a stochastic process. Often there exist means of stochastically determining when and through what mechanism an element will occupy state k. Methods for doing this will be discussed in the next section, but for now it is sufficient to say that the probabilities associated with the state an element occupies at time t may be represented as the set:

$$\breve{\mathbf{p}}^{\mathbf{i}} = \{p_1^i(t), p_2^i(t), ..., p_m^i(t)\}, \quad \text{where} \quad p_k^i = Pr\{g^i(t) = g_k^i\} \tag{2.9}$$

This corresponds directly to the element's state performances in Eqns. 2.7 or 2.8. The state probability and performance pairs, $\{[p_1^i(t), g_1^i], [p_2^i(t), g_2^i], ..., [p_m^i(t), g_m^i]\}$ comprise the entire probability distribution of performance for the element i at time, t. Note that the element states arise from the entire set of mutually exclusive transitions that can occur, therefore,

$$\sum_{k=1}^{m} p_k^i(t) = 1 \quad \text{for} \quad 0 \leq t \leq T \tag{2.10}$$

Up to this point, little has been said about the system's performance. In the case of the multistate coherent systems described in Section 2.1.1, the determination of performance for a system composed of n elements i follows directly from the individual state performance of its elements. In the case of much more complex systems, the system performance is a more complicated function of state, system static design variables, $\mathbf{x}$, control laws, $\mathbf{r}$, and operational parameters, $\mathbf{c}$. Note that $\mathbf{x}$ and $\mathbf{c}$ were previously defined for Eqn. 2.6 of Section 2.1.4, and $\mathbf{r}$ is a general variable that represents targeted variation to the system's control laws, e.g. gains.

The determination of system state (as opposed to performance), however, is made directly from the state of the elements. Consider that the system, composed of n elements i, has M states, each state with performance $G_K^s(\mathbf{x}, \mathbf{r}, \mathbf{c})$, $K \in \{1, 2, ..., M\}$, such the set of system state performances may be represented as:

$$\breve{\mathbf{G}}^{\mathbf{s}} = \{G_1^s(\mathbf{x}, \mathbf{r}, \mathbf{c}), G_2^s(\mathbf{x}, \mathbf{r}, \mathbf{c}), ..., G_M^s(\mathbf{x}, \mathbf{r}, \mathbf{c})\} \tag{2.11}$$

The system performance, $G^s(t)$, is a random value drawn from the family of functions $\breve{\mathbf{G}}^{\mathbf{s}} : G^s(t) \in \breve{\mathbf{G}}^{\mathbf{s}}$

The system states K are determined by the possible permutations of the elemental states k. The number of system states, M, depends on the rules that govern those permutations. For instance, the total number of system states will be much greater if the emerging performance levels, G_K^s, are dependent on the order of element state transition in addition to just their states (i.e. system performance is different when element i transitions before $i+1$ vs. $i+1$ before i). When order is not important and the element performance set is limited to the failure case of Eqn. 2.8, the size of M is equal to 2^n (n is the number of elements). If the emergent performance *is* order dependent, the total number of states is,

$$1 + \sum_{j=1}^{n} \frac{n!}{(n-j)!} \tag{2.12}$$

In either case, one can see that the total number of system states grows very rapidly, even when the number of element states, m is limited to two.

As with the elements, there exists a corresponding set of system state probabilities,

$$\breve{\mathbf{P}}^{\mathbf{s}} = \{P_1^s(t), P_2^s(t), ..., P_M^s(t)\}, \quad \text{where} \quad P_K^s = Pr\{G^s(t) = G_K^s\} \tag{2.13}$$

such that

$$\sum_{K=1}^{M} P_K^s(t) = 1 \quad \text{for} \quad 0 \le t \le T \tag{2.14}$$

The probability-performance pairs

$$\{[P_1^s(t), G_1^s(\mathbf{x}, \mathbf{r}, \mathbf{c})], [P_2^s(t), G_2^s(\mathbf{x}, \mathbf{r}, \mathbf{c})], ..., [P_M^s(t), G_M^s(\mathbf{x}, \mathbf{r}, \mathbf{c})]\} \tag{2.15}$$

then make up the probability distribution of the state emergent performance for the system at any time t.

The above framework handily extends itself to the tiered lumping of elements and systems across multiple layers of system decomposition. Figure 2-7 depicts this graphically, where the top level system, L, is composed of the elements at $L-1$, each of which is individually its own system composed of elements at $L-2$, and so on. The performance and probability distributions for each of these tiered system/elements pairings is characterized by the relationships that system performance sets, $\breve{\mathbf{G}}^{\mathbf{s}}$, are functions of the element performance sets, $\breve{\mathbf{g}}^{\mathbf{i}}$, and system probability sets, $\breve{\mathbf{P}}^{\mathbf{s}}$, are functions of the element probability sets, $\breve{\mathbf{p}}^{\mathbf{i}}$. These may potentially be used to form a dependence chain spanning from the lowest level of base decomposition to the highest level, L.

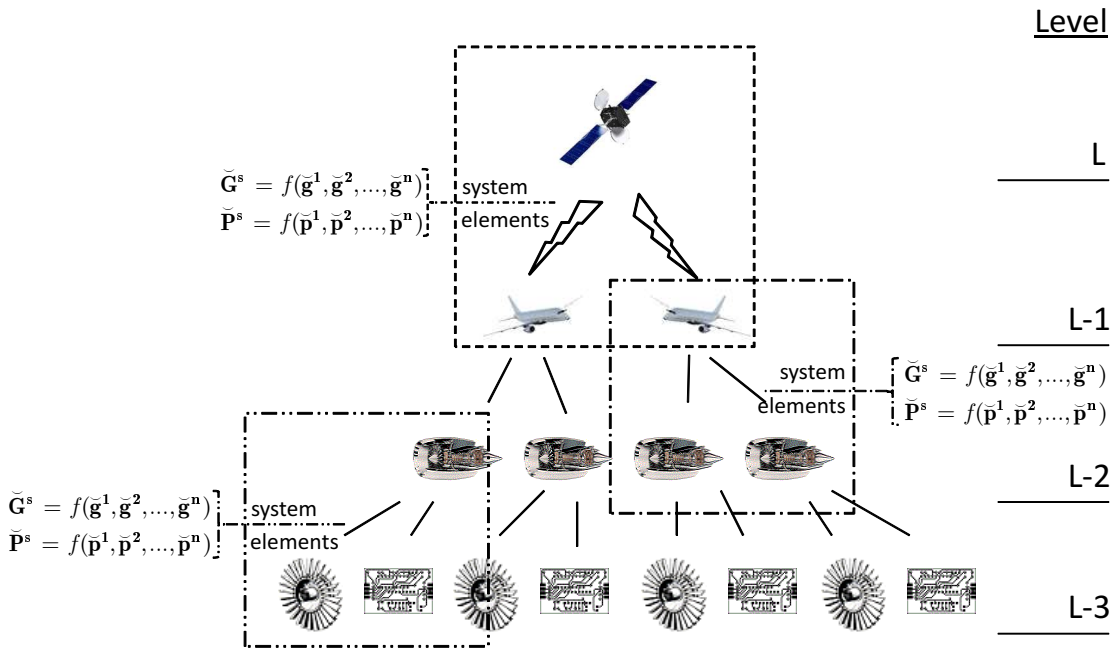

Figure 2-7: Tiered multistate systems

While conceivable that future improvements in methods and computational ability will allow the full analysis of multiple system tiers for multiple states, for now this thesis limits itself to the simultaneous analysis of one system involving potential failure of one level of subelements. This does not imply that the analysis neglects the effects of failures at the lowest levels of decomposition. The failure of a component at level $L-1$ may indeed be caused by the failure of a component at level $L-2$ or $L-3$. As long as the element transition rate (typically 1/MTBF in the case of failures) corresponds to the proper level of decomposition, how the failure occurs is irrelevant to the analysis.

2.3.2 Markov Analysis

The preceding section established that the performance of any system may be modeled as a stochastic process, characterized by a set of state performance ($\breve{\mathbf{G}}^{\mathbf{s}}$) and probability ($\breve{\mathbf{P}}^{\mathbf{s}}$) pairings that describes the system's performance probability distribution at any time $t \geq 0$ [69]. The following section describes a process by which one may efficiently determine the values in $\breve{\mathbf{P}}^{\mathbf{s}}$, using information about the rates of state transition of its elements.

In general, a stochastic process is a family of random variables indexed by some parameter, such as time or space (e.g. $G^s = \{G^s(t) : t \geq 0\}$). The values assumed by the process vary according to the assignment of these random variables drawn from a larger set of all possible outcomes [20] (e.g. $G^s(t) \in \breve{\mathbf{G}}^{\mathbf{s}}$). The set of all possible outcomes comprises the state-space, and, in the case of multistate system analysis, the index is typically time, t. Both the state-space and time may be classified as continuous or discrete, giving rise to four categories of stochastic processes. The category of discrete-state and continuous-time occurs very frequently in the analysis of multistate failures, given that one can probabilistically predict the transition rates of system elements, in the continuous-time spectrum, based on historical data regarding their mean-time-between-failure or mean-time-to-repair. The process with a discrete-state space is typically called a chain.

Extending nomenclature one step further, under the simplification of Eqn. 2.8,

the transition probabilities between elemental states k may be defined as

$$\lambda_i(t, \Delta t) = Pr\{g^i_{t+\Delta t} = g^i_F | g^i_t = g^i_{OP}\} \tag{2.16}$$

which is the probability that the element is in a state of *failure* at time, $t + \Delta t$, given that it was in a state of *operating* at time, t, and

$$\mu_i(t, \Delta t) = Pr\{g^i_{t+\Delta t} = g^i_{OP} | g^i_t = g^i_F\} \tag{2.17}$$

which is the probability that the element is in a state of *operating* at time, $t + \Delta t$, given that it was in a state of *failure* at time, t. The above transition rates form the sets $\boldsymbol{\lambda^s} = \{\lambda_1, \lambda_2, ..., \lambda_n\}$ and $\boldsymbol{\mu^s} = \{\mu_1, \mu_2, ..., \mu_n\}$. If the system states that occur at time $t + \Delta t$ as a result of these transitions only depend upon the system state at time t, the process is said to be *Markovian*, representable by the well developed theory first introduced by A. Markov in 1907 [55].

Furthermore, when the transition probabilities do not depend on t, but only Δt, the stochastic process is said to be in a *steady state* and the Markov process is *homogeneous*. The respective probabilities λ_i and μ_i are then equal to MTBF^{-1} and MTTR^{-1} (mean-time-to-repair), which typically have units [1/hr] and are referred to as failure rates and repair rates. Figure 2-8 shows a generic representation of the resulting discrete-state Markov chain, for a three element system without repair (for an example with repair, see Fig. 2-10). Appropriate nomenclature from the previous section has been included and the state definitions are given in Table 2.1. In this formulation, P^s_K may be interpreted as the probability that the system finds itself in any particular state of performance G^s_K at time t. These probabilities may be determined through Markov analysis as described later in this section via Eqns. 2.18 through 2.24, knowing the transition probabilities λ_i or μ_i.

There are some important characteristics of the formulation in Fig. 2-8 that deserve note, and help in understanding the general process of constructing Markov chains (for failure analysis). To begin, the structure of the chain is first determined by the state definitions, and then by the transition paths. For instance, State 8 is

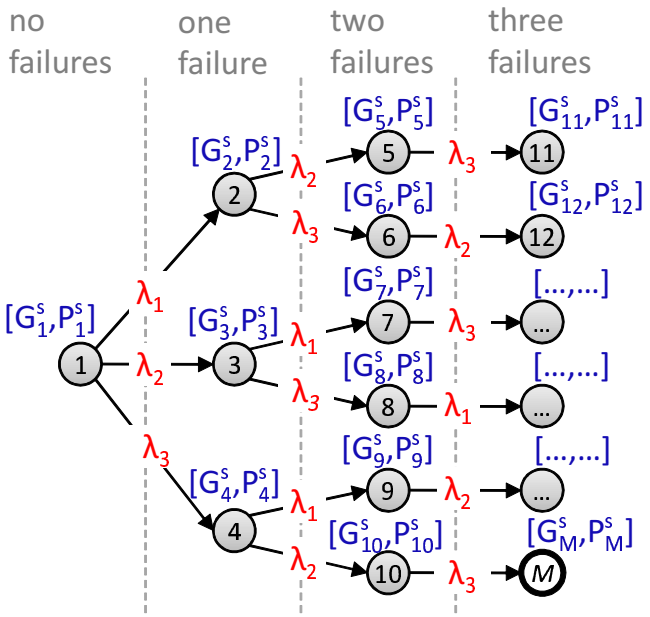

Figure 2-8: Markov chain formulation for a generic three-element system

Table 2.1: State definitions for Markov chain in Fig. 2-8

State	Element 1	Element 2	Element 3
State 1	OP*	OP	OP
State 2	F*	OP	OP
State 3	OP	F	OP
State 4	OP	OP	F
State 5	F	F	OP
State 6	F	OP	F
State 7	F	F	OP
State 8	OP	F	F
State 9	F	OP	F
State 10	OP	F	F
State 11	F	F	F
State 12	F	F	F
...	...	...	...

* OP = Operating, F = Failed

defined by the fact that Elements 2 and 3 are failed, therefore it is located at the *two failures* level. In the case of the above depiction, the fact that Element 2 failed before Element 3 is important, therefore the path to State 8 is State 1→State 3→State 8. If symmetry is assumed, that is, state performance does not depend on the order in which the elements have failed, performance in State 8 is the same as in State 10 ($G^s_{10} = G^s_8$), and the Markov chain may be recombined as that in Fig. 2-9. In this case, State 7 takes the place of States 8 and 10 in Fig. 2-8, and is arrived at via paths State 1→State 3→State 7 OR State 1→State 4→State 7. The probability of being in a state with both Elements 2 and 3 failed, regardless of path, is exactly the same for both Fig. 2-8 and Fig. 2-9, with P^s_7 in Fig. 2-9 equal to the sum of P^s_8 and P^s_{10} in Fig. 2-8. It is only the state performances that necessitate the generalization of Fig. 2-8. The following simple example problem demonstrates the process for solving a Markov chain for all P^s_K. Although the example problem is for a simpler chain than those shown in Figs. 2-8 or 2-9, one easily observes that the advantage of the Fig. 2-9 formulation is a smaller set of equations in the system of ODE's in Eqn. 2.23.

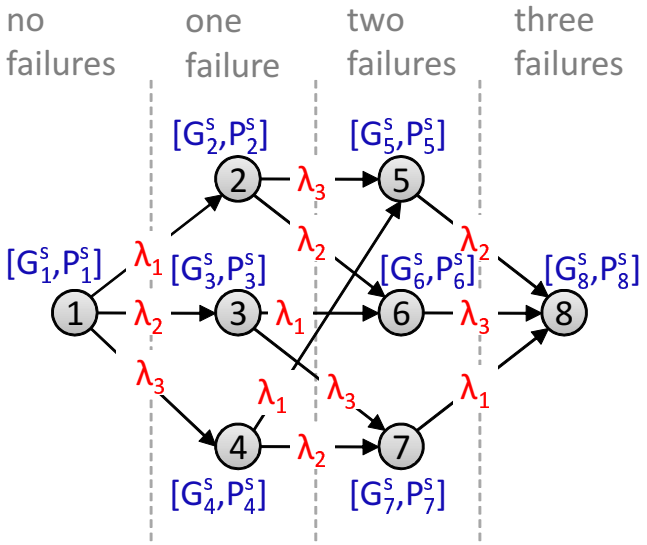

Figure 2-9: Markov chain formulation for a symmetric three-element system (state performance is order independent)

Consider the possible failures of two engines, depicted by the Markov formulation in Fig. 2-10. For generality, cyclic transitions are allowed via repair rates, modeling

perhaps a future long-duration air vehicle with on-board diagnostics and possible in-flight repair. Although both engines may have the same chance of failing, the performance of the vehicle may be different depending on whether the right or left engine is operating, thus there are four distinct states of operation.

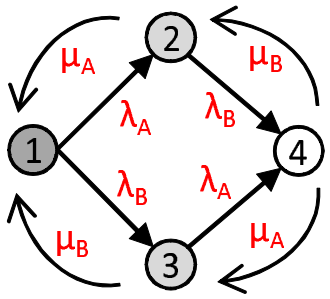

Figure 2-10: Markov diagram for two-engine failure scenario with repair

State 1 has both engines operating, while in State 2 only the starboard engine B is functional and in State 3 only the port engine A is functional. State 4 is the fully failed state in which both engines are non-functioning. The λ_i values are the failure rates of A and B while the repair rates feed transition in the upstream direction. Note that direct transition from State 1 to State 4 could occur with the exact simultaneous failure of both engines, but this would in nearly all circumstances be caused by the failure of a third element somewhere in the system, and is not considered here.[3]

Beginning with State 1, for a time period $[t, t+\delta t)$, the probability that the aircraft *leaves* State 1 is given by

$$Pr_{1\rightarrow} = \lambda_A \delta t + \lambda_B \delta t = (\lambda_A + \lambda_B)\delta t \tag{2.18}$$

Subsequently, it follows that the probability of *being* in State 1 at time $t + \delta t$ is determined from

$$P_1^s(t+\delta t) = P_1^s(t)(1-(\lambda_A+\lambda_B)\delta t) + P_2^s(t)\mu_A \delta t + P_3^s(t)\mu_B \delta t \tag{2.19}$$

[3]Another possibility is that both engines happen to fail through independent causes at the same instant. However, this probability tends to zero at the limit, and all paths to State 4 must pass through State 2 or State 3 for some, possibly infinitesimally small, period of time.

which can be stated as, "the probability that the system is in State 1 at $t + \delta t$ is equal to summation of probabilities composed of: 1) the probability that it has not left State 1, 2) the probability that it has arrived at State 1 from State 2, and 3) the probability that it has arrived at State 1 from State 3." The same may be done for States 2, 3, and 4:

$$P_2^s(t+\delta t) = P_2^s(t)(1-(\mu_A+\lambda_B)\delta t) + P_1^s(t)\lambda_A\delta t + P_4^s(t)\mu_B\delta t \tag{2.20}$$

$$P_3^s(t+\delta t) = P_3^s(t)(1-(\lambda_A+\mu_B)\delta t) + P_1^s(t)\lambda_B\delta t + P_4^s(t)\mu_A\delta t \tag{2.21}$$

$$P_4^s(t+\delta t) = P_4^s(t)(1-(\mu_A+\mu_B)\delta t) + P_1 2^s(t)\lambda_B\delta t + P_3^s(t)\lambda_A\delta t \tag{2.22}$$

After differentiating at the limit as δt approaches zero, the above provides the system of first order linear differential equations

$$\frac{d\breve{\mathbf{P}}^{\mathbf{s}}(t)}{dt} = A\breve{\mathbf{P}}^{\mathbf{s}}(t) \tag{2.23}$$

where A is the matrix shown in Eq. 2.24.

$$A = \begin{bmatrix} -(\lambda_A+\lambda_B) & \mu_A & \mu_B & 0 \\ \lambda_A & -(\mu_A+\lambda_B) & 0 & \mu_B \\ \lambda_B & 0 & -(\mu_B+\lambda_A) & \mu_A \\ 0 & \lambda_B & \lambda_A & -(\mu_B+\mu_A) \end{bmatrix} \tag{2.24}$$

Whereas twenty years ago the solution to Eq. 2.23 required careful formulation regarding computational efficiency, today many commercial solvers exist capable of rapidly executing it for hundreds or even thousands of states.

Markov analysis provides an efficient means of stochastically modeling state transition events that might occur in a large, complex system, without having to perform a full Monte Carlo analysis of the performance space. It does this by constructing the system level state probabilities on the basis of the individual element state probabilities. This is attractive because it allows the explicit enumeration of every unique combination and sequence of possible events regardless of probability. A Monte Carlo

analysis, on the other hand, may not find highly improbable event sequences (such as two simultaneous low-probability failures) without a very large number of simulations. This advantage of the Markov process may sometimes come at the expense of a large state-space in the Markov model, which may be controlled by truncating the number of independent events (levels of failure) or by aggregating states.

In practice, combining the Markov model construction of more complex architectures with an integrated system model allows the user to enumerate the dependency structure of the individual components. This capability ensures that dependent failures or cascading effects are adequately represented in the performance index estimates, which are not typically captured through other estimation techniques.

2.3.3 Indices of Multistate Performance

If the performance levels $G_K^s(\mathbf{x}, \mathbf{r}, \mathbf{c})$ can be determined, and $P_K^s(\boldsymbol{\lambda}^s, \boldsymbol{\mu}^s)$ calculated from Eqn. 2.23, the system's expected availability, E_A, and expected performance, E_G, arise as indices of multistate performance. These indices, or some form of them, are integral to the multistate analysis and design methodology developed Chapter 4, in that they compose the objective functions used to measure the effects of changes to static design variables, $\mathbf{x}$, and element transition rates, λ_i and μ_i, on overall multistate performance output. They should be considered in contrast to the system's nominal performance, defined as the system's design performance level in the fully operational state.[4]

First, consider that over a mission time interval [0,T], some performance threshold requirement, W, exists that divides the set of system state performances into two categories of *acceptable* and *unacceptable*. The summation of probabilities from the set, $\breve{\mathbf{P}}^{\mathbf{s}}$, corresponding to the *acceptable* category, is a measure of the system's expected availability at any time t. For the cases modeled in the remainder of this thesis, the mission interval itself is the time of interest, therefore $t = T$ and the dependency on

[4]Note that this definition does not preclude the system from obtaining a level of nominal performance in a state other than fully operational. As the methodology stresses performance in the face of degradation, it is only appropriate that it should be possible to maintain a nominal performance rate in an other than fully operational state.

time is accounted for implicitly through the probabilities resulting from Eqn. 2.23.

The resulting equation for availability is [67]:

$$E_A = \sum_{z=1}^{Z} Q(W_z)\frac{T_z}{T} \quad \text{where} \quad Q(W_z) = \sum_{G_K^s \geq W_z} P_K^s \tag{2.25}$$

Here, T represents the mission interval time, potentially divided into Z intervals of T_z where each interval may have its own acceptable minimum performance level, W_z. For cases of constant W, the availability is simply the summation of state probabilities corresponding to states with performance greater than or equal to W, as shown in the equation on the right.

Eqn. 2.26 gives the analogous formulation for expected performance,

$$E_G = \sum_{K=1}^{M} P_K^s G_K^s \tag{2.26}$$

which is the summation of each of the state performances, weighted by the probability that they occur.

2.4 Chapter Summary

The objective of this chapter was to provide an overarching understanding of multistate design in the context of complex systems. It began with a detailed review of literature in multistate design, and placed the thesis work in its proper scope within an expanded hierarchy of system state change. Next, certain elements of the reviewed research were used to extend the multistate nomenclature and framework from relatively simple systems to one suitable for analysis of more complex aerospace systems. Markov analysis was then shown to be an effective method for calculating the state probabilities required to complete the above analysis. It enables assessment of individual state probabilities, performances, and interstate transitions individually, separately, and concurrently, allowing for computation of the system level probabilities through Eqn. 2.23, covering all combinations of possibilities. These would otherwise

require a very large and expensive Monte Carlo analysis to query the performance space for the full scope of failure permutations. Finally, two measures of multistate performance were introduced, *system availability* and *expected performance*, which, although rather basic in form, are very complex functions of many inputs, including design variables, failure and repair rates, mission duration, and operational parameters.

Chapter 3

Case Study - I: Twin-Engine Aircraft

The objective of this chapter is to quantify the effect of changes to a known aircraft's *static* design variables on its performance output for differing aircraft states. This is accomplished through design sensitivity analysis by evaluating the expected performance and availability of the system across various time periods and subject to changes in component or element mean-time-between-failures. The goal is to establish that such sensitivities exist and can be useful for more detailed performance evaluation and tradespace exploration with robust, long-endurance system concepts.

The above is accomplished by applying the basic framework laid out in Chapter 2, extended to more complex aerospace systems, and enabled by the development of a multi-modal performance model, which is validated through extensive flight test data collected at Edwards AFB Flight Test Center. It includes elements for determining responses in aircraft expected performance and availability to changes in 1) static design variables and 2) component failure rates, accounting for 3) control design variables (gains) where appropriate, which are the three driving input categories affecting the aircraft's performance robustness. The approach is made novel through its *inclusion of the functional dependency of each of these variables on the system's multistate performance response*, and *the integration of Markov analysis directly into the early-stage design loop* (a more formal development is given in Chapter 4). Markov chain

analysis within the design loop stochastically models the state transitions based on failure rates, and gain optimization through simulation ensures controllability at each design point. Results showed unsafe performance in 15% of the aircraft's geometry-state responses under investigation. While many occurred in the fully failed state and were expected, five occurred in partially degraded states where the majority of geometries were able to meet performance requirements. Furthermore, this behavior clearly exhibited itself in the resulting design sensitivities, confirming that such an approach allows designers to identify elements that might drive system loss through analysis of performance changes across system states and their respective response to changes in design variables.

The chapter begins with a description of the twin-engine aircraft design model and the flight test data used for its validation. The second section outlines the specific approach as applied to the case study, and the final sections present results of the multistate analysis, including sensitivities of performance metrics to design variables. More detail on the multi-modal simulation-based design model is provided in Appendix A and an analysis of *reachability* for the worst performing states is given in Appendix B.

3.1 Aircraft Integrated System Model

This section describes development of the multistate design model and techniques used in evaluating multistate performance. These are the tools necessary for populating the system state performance set, $\breve{\mathbf{G}}^{\mathbf{s}}$, to be used along with the probability set, $\breve{\mathbf{P}}^{\mathbf{s}}$, in forming the system's probability distribution of performance.

The design problem for the case under study is divided into an *aspect* oriented hierarchy with subdisciplines of *mass and inertias*, *aerodynamic forces and moments*, *propulsion*, and *performance*. Fig. 3-1 shows a simplified depiction of the design structure matrix (DSM) depicting model information flow. All geometry is entered as basic aircraft design variables such as aspect ratio, taper ratio, wing sweep, fuselage height and width, engine location, etc., which are used to calculate mass and inertias

for the aircraft's various components. These geometric parameters are also passed to a preprocessor for input to a vortex lattice code as geometric coordinates for discretized lifting surface panels. A few of the geometric parameters are handled directly by a flight simulator executable in the *performance* module, such as the location of the fuel tanks, included so that the inertial effects of fuel burn may be directly accounted for during run-time.

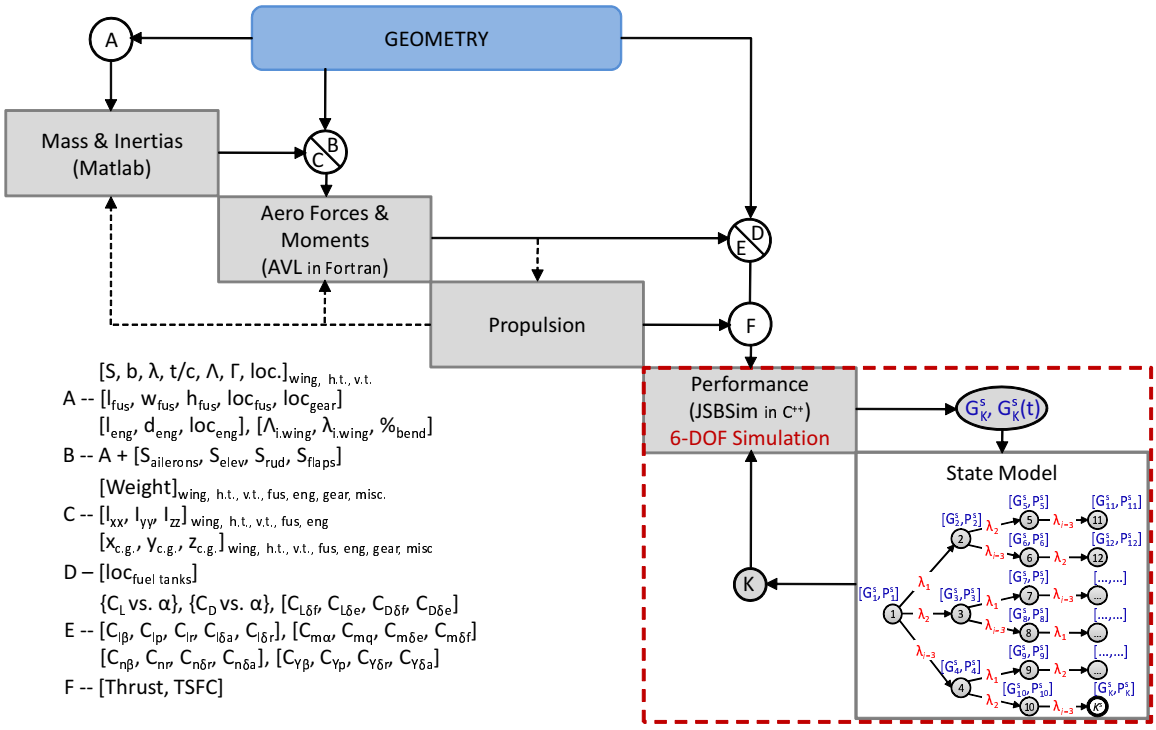

Figure 3-1: Multistate aircraft design model data flow

The *mass and inertias* discipline computes various component weights using empirically based equations from Brandt et al. [25] and Roskam [92]. Inertias are then calculated for each of these components by discretizing them into smaller divisions, computing the divisional centers of gravity, and summing the discretized inertias to get I_{xx}, I_{yy}, I_{zz}, and I_{xz} for the wing, tail, fuselage, etc. The remaining products of inertia, I_{xy} and I_{yz}, are not considered, due to the aircraft's symmetry of mass and geometry about these axes. Each component value is passed to the *aerodynamic forces and moments* module, where total vehicle inertias are computed through the parallel axis theorem and used to help determine the aircraft's response characteristics. All

of the code in the *mass and inertias* discipline is written in MATLAB®.

A vortex lattice solver is used in the *aerodynamic forces and moments* discipline. This is the publicly available GNU licensed Athena Vortex Lattice (AVL), which employs an extended vortex lattice model for lifting surfaces and a slender body model for fuselages and nacelles [8]. Athena Vortex Lattice is written in Fortran and takes as input the aircraft geometry coordinates (which in this case have been processed from the aircraft geometric design variables) and specified mass properties. Output data are all of the aircraft control derivatives passed to the *performance* module shown in Fig. 3-1. This is also where the aircraft's drag polar is calculated, providing both C_L and C_D as a function of angle-of-attack. Lift and drag characteristics for various flap configurations (leading or trailing edge) may be computed as a function of angle-of-attack as well. These are determined for any aircraft geometry coming out of the aerodynamics module and then used in the *performance* simulation to model various in-flight configuration changes. Thrust and specific fuel consumption are calculated in the *propulsion* discipline, which is a look-up table for each of these values based on flight speed and altitude.

The heart of the design model is an open-source 6-DoF flight simulator called JSBSim [18], modified to run in batch mode as an S-Function in MATLAB's Simulink.® The development of JSBSim began over a decade ago with Berndt [18], and over the years has grown into a major project involving dozens of engineers. It is very powerful as a means of evaluating aircraft flight dynamics and includes the means for fully configuring the flight control system, propulsion, aerodynamics, and landing gear of any general aircraft. This is typically done through a front-end *.xml* input file, where the aircraft's characteristic parameters are read in once at the onset of the simulation and then control inputs are treated as dynamic properties updated several times per second during run-time. Mills [76] began work on the basic implementation of the S-Function over three years ago and work for this thesis continued its development further, including modifications to the flight simulation engine itself. The resulting updates to the code (C^{++}) enable the effects of nearly all aircraft design variables to be treated as dynamic properties in the same way as control inputs, such that

they can be varied as a functions of time during the execution of the flight model in Simulink. This makes possible the rapid evaluation of a wide range of aircraft performance parameters for a nearly limitless number of aircraft configurations, including simulation of failure states, e.g. loss of actuators and engine failures. See Appendix A for more detail about the simulation model.

3.1.1 Performance Validation

To demonstrate the multistate design problem, the analysis begins with the baseline configuration of a Beechcraft Super King Air Model 200, as shown in Figs. 3-2 and 3-3. This aircraft was chosen because its behavior is well understood and there are ample geometry data which are publicly available [37, 53]. Additionally, the author of this thesis has numerous flight hours testing the C-12C, which is the Air Force modified version of the Super King Air to which this particular computational model was calibrated. The aircraft is powered by two Pratt and Whitney PT6A-41 turboprop engines, each rated at 850 horsepower (sea level), and is equipped with a rudder boosted yaw damper system.

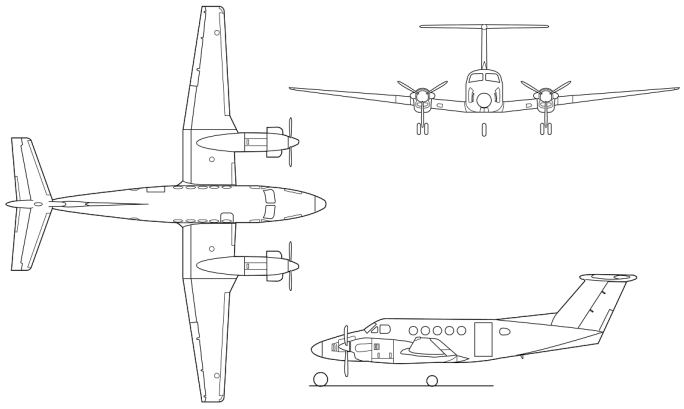

Figure 3-2: Super King Air Model 200 3-view (public domain)

Care was taken to ensure that results from the vortex lattice analysis and from flight simulation were representative of the real-world aircraft. Thus, comparisons were made to flight test validated data taken from an in-flight performance evaluation of the Beech C-12C performed at Edwards AFB, CA, in 2001 [106], and raw flight

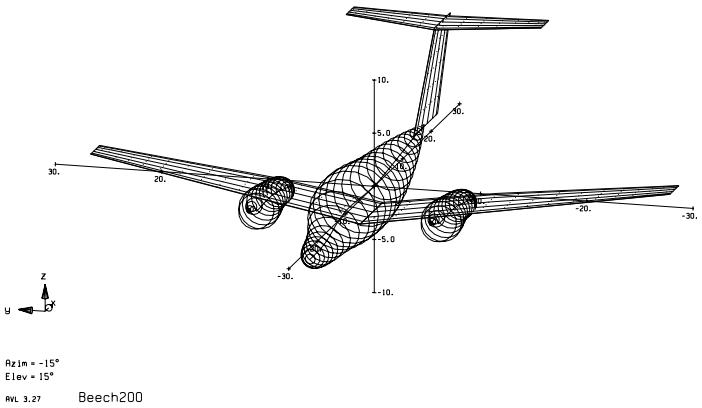

Figure 3-3: AVL representation of the Super King Air Model 200

test data from an extensive program to estimate the C-12C aerodynamic stability and control derivatives at Edwards AFB in March of 2010 [31]. The data from 2001 were used for the aerodynamic calibration, and the results in Fig. 3-4 show satisfactory comparison between the computed and flight test validated drag polars.

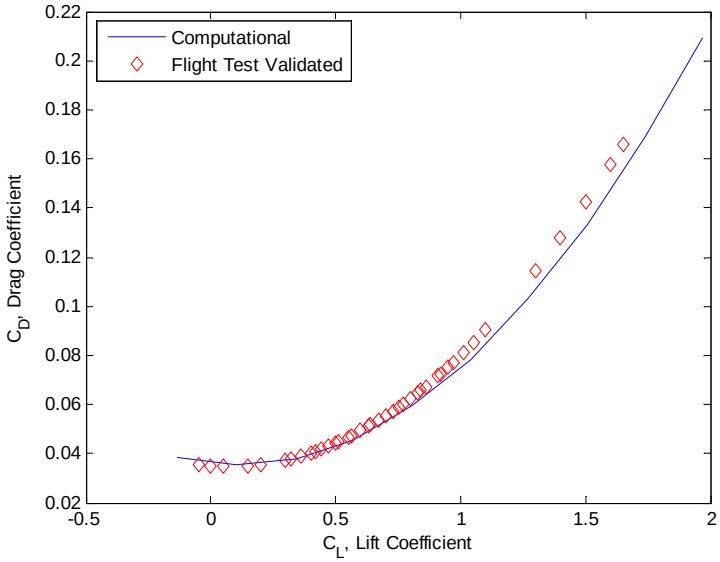

Figure 3-4: Drag polar comparison of computational data to data validated by flight test (flown October 2001)

Data from the more recent testing in 2010 were used to validate the stability and control characteristics of the integrated model. In general, the existing pre-calibrated

model arising from the analyses depicted in Fig. 3-1 was quite accurate and only small adjustments (less than 5% from baseline) were made to the mass estimation routines and control surface geometries in order to reach the demonstrated results for angle-of-attack and sideslip shown in Fig. 3-5 and 3-6.

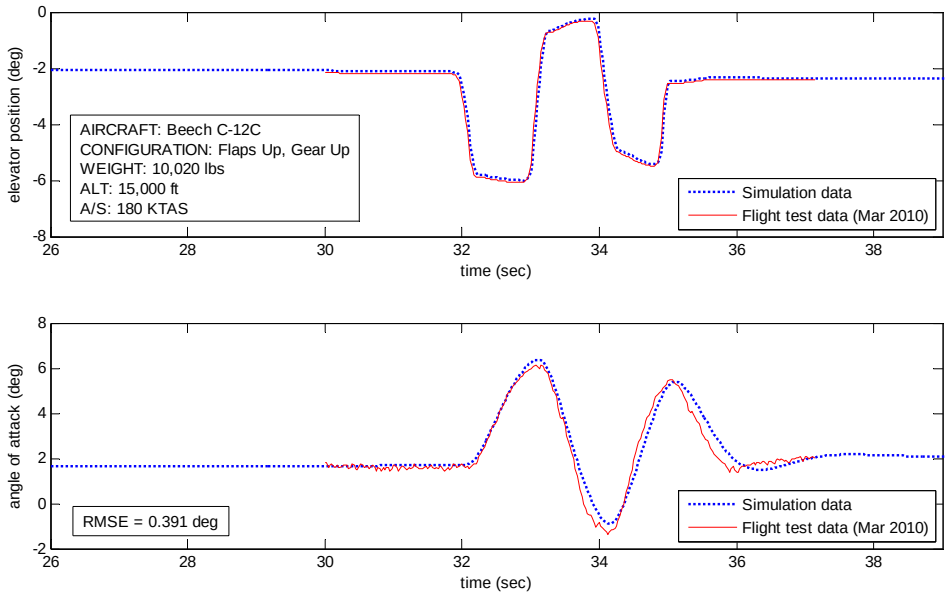

Figure 3-5: Comparison of angle-of-attack response

The data depicted in Fig. 3-5 show excellent matching between the computed and flight test angle-of-attack response to an elevator doublet, with a root-mean-square error (RMSE) of less than 0.4 degrees. In the yaw-axis, shown in Fig. 3-6, results are satisfactory in that both response frequencies are the same, although the computed model shows more damping than the actual aircraft response, resulting in a higher RMSE of 1.81 degrees. This does not significantly affect the impact of this study's results for two reasons. First, a more comprehensive estimate of the aircraft's yaw-roll interaction is $|C_{n\beta}/C_{l\beta}|$. As described in the results section of this chapter, the aircraft model predicts a $|C_{n\beta}/C_{l\beta}|$ of 0.38, while that derived from the flight test is 0.35 and comes from data across several flights. Both $|C_{n\beta}/C_{l\beta}|$ values are in close agreement and border the region typically indicative of poorly damped Dutch roll. Secondly, although the flight-test response implies a less damped Dutch roll mode

than the simulation, the simulation is nonetheless very successful in capturing the performance degradation due to the King Air's Dutch roll mode, as will be shown in Section 3.3.

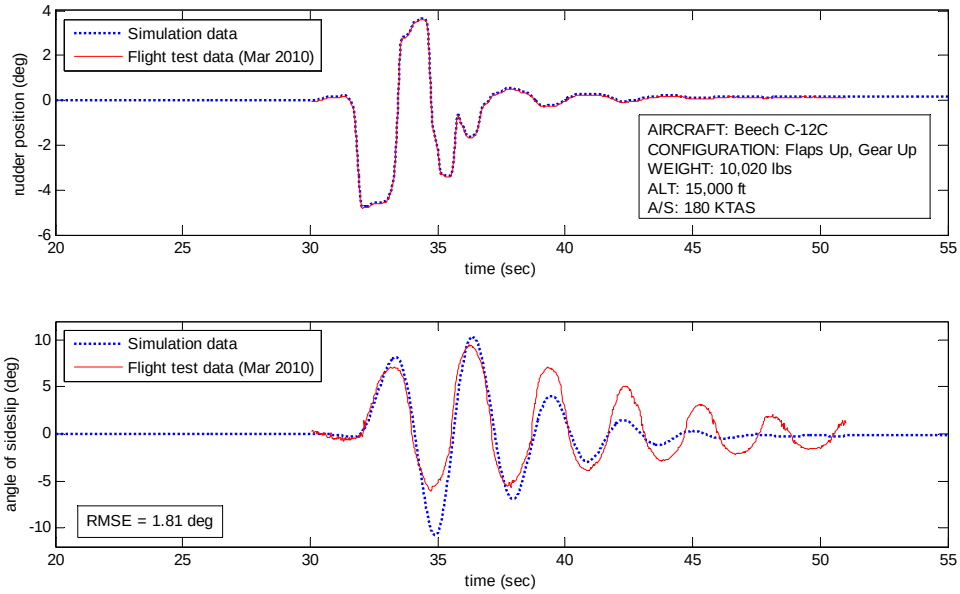

Figure 3-6: Comparison of angle-of-sideslip response

3.2 Case Approach

The preceding section described development of the design model and techniques used in evaluating multistate performance. This is necessary for populating the system state performance set, $\breve{\mathbf{G}}^{\mathbf{s}}$. Chapter 2 described the Markov process used in determining the elements of the system probability set, $\breve{\mathbf{P}}^{\mathbf{s}}$. The following section describes the case-specific choice of performance objective for use as $G^s(t)$, and the multistate problem set-up, including selection of failure modes and a control technique used in their modeling.

3.2.1 Design Sensitivity of System Availability and Expected Performance

While each of the multistate performance metrics (Eqns. 2.25 and 2.26 in Chapter 2) is useful in its own right, they are even more effective when combined with system sensitivity analysis. Namely, it is desirable to know how these quantities change as system variables are modified. This approach has been used in the past for system reliability analysis [9, 23], using only the component failure rates. In these cases, the absolute system reliability was of less concern than identifying those elements that drove the system loss probability. These elements were discovered through sensitivity analysis, calculating reliability across i number of cases, where each case modified the failure rate of the i^{th} component. The components that drove system loss were those that exhibited the largest sensitivity, or change in reliability given a change in λ_i.

Assuming a single, fixed time period (e.g. $T_z = T$ in Eqn. 2.25), an analogous sensitivity for E_A appears as

$$\frac{dE_A(\boldsymbol{\lambda^s}, \boldsymbol{\mu^s})}{d\boldsymbol{\lambda^s}} = \sum_{G_K^s \geq W} \frac{dP_K^s(\boldsymbol{\lambda^s}, \boldsymbol{\mu^s})}{d\boldsymbol{\lambda^s}} \tag{3.1}$$

which can, of course, also be shown for the repair rates, $\boldsymbol{\mu^s}$. The sensitivity in this case was not necessarily used for direct optimization - it is elementary to know that reducing a component failure rate will, generally, increase reliability. Rather, it was used to point the system designers to the portion of the system architecture that had the greatest effect on reliability. The remedy lied with finding a higher-reliability component, introducing redundancy, or changing mission parameters.

For the case under study here, system sensitivity analysis is extended to include a broader variable set. In this way, it is possible not only to observe sensitivity of availability and expected performance to component failure rates, but also to traditional aircraft design variables, $\mathbf{x}$ (wing span, wing area, engine placement, etc.), or even operational parameters, $\mathbf{c}$ (cruise altitude, cruise speed, etc.). Following the same assumption on time as Eqn. 3.1, this time using expected performance as the

example, this takes the form

$$\frac{dE_G(\boldsymbol{\lambda^s}, \boldsymbol{\mu^s}, \mathbf{x}, \mathbf{r}, \mathbf{c})}{d\mathbf{x}} = \sum_{K=1}^{M} P_K^s(\boldsymbol{\lambda^s}, \boldsymbol{\mu^s}) \frac{dG_K^s(\mathbf{x}, \mathbf{r}, \mathbf{c})}{d\mathbf{x}} \tag{3.2}$$

for sensitivity to design variables, $\mathbf{x}$.

Note that by way of the inequality in the summation of Eqn. 3.1, expected availability becomes a function of $\mathbf{x}$, $\mathbf{r}$, and $\mathbf{c}$ as well, although not necessarily a continuous one. This piecewise constancy does not preclude the local calculation of design sensitivities, but it does pose a problem for gradient-based optimization algorithms. More will be discussed on this in Chapter 4.

The individual Markov state probabilities P_K^s in Eqn. 3.2 act as "weights" to a weighted performance equation. Hence, for short missions, where there is little chance for the system to enter any but the nominal state, expected performance sensitivity will look much like a standard design sensitivity analysis. However, as system lifetime or mission duration increases, the probabilities of the off-nominal Markov states increase and sensitivities may change dramatically. Consider, for example, the DARPA proposal for an ultra long-endurance UAV with an on-station time of five years [32]. In this case, expected performance sensitivity is a promising metric for identifying those system parameters that have the greatest effect on both nominal and off-nominal system performance, and this analysis may be critical for mission success.

3.2.2 Aircraft Performance Metrics

The performance function of interest is chosen as *expected* specific excess power, P_s,[1] in a climbing turn, which must be evaluated for the nominal condition and each of the failure states in order to compute Eqns. 3.1 and 3.2. P_s is computed from the flight simulation code using the outputs dh/dt, dV/dt, and V in the equation $P_s = dh/dt + (V/g)(dV/dt)$. The expected performance and availability equations

[1]Note that P with a subscript s refers to specific excess power, not to be confused with P^s, which refers to the state probabilities. These are both broadly adopted notations in their respective fields, thus were preserved here despite a slight risk of confusion.

resulting from this formulation are given in Eqns. 3.3 and 3.4.

$$E_G(P_s(\mathbf{x}), \boldsymbol{\lambda^s}) = \sum_{K=1}^{M} P_K^s(\boldsymbol{\lambda^s}) P_s(\mathbf{x})_K = \sum_{K=1}^{M} P_K^s(\boldsymbol{\lambda^s})[\dot{h}(\mathbf{x}) + \frac{V(\mathbf{x})}{g}\dot{V}(\mathbf{x})]_{avg,K} \tag{3.3}$$

$$E_A(P_s(\mathbf{x}), \boldsymbol{\lambda^s}) = \sum_{[\dot{h}(\mathbf{x})+\frac{V(\mathbf{x})}{g}\dot{V}(\mathbf{x})]_{avg,K} \geq W} P_K^s(\boldsymbol{\lambda^s}) \tag{3.4}$$

Here, h is altitude, V is velocity, g is the gravity constant, and the *avg* subscript indicates the values are averaged over the last ten seconds of the simulation, allowing the aircraft a chance to stabilize before the performance metric is computed. W is defined as 200 ft/min for a minimum safe rate of climb (allowing calculation of Eqn. 3.4), and bank angle must be maintained within $\pm 5°$ to be in the safe region for calculation of $E_A(\phi(\mathbf{x}), \boldsymbol{\lambda^s})$. Total availability then becomes

$$E_A(P_s(\mathbf{x}) \cap \phi(\mathbf{x}), \boldsymbol{\lambda^s}) = \sum_{P_s(\mathbf{x}) \geq 200 \text{ fpm } \& \ \phi_{dev}(\mathbf{x}) \leq \pm 5°} P_K^s(\boldsymbol{\lambda^s}) \tag{3.5}$$

Each simulation was run for a period of sixty seconds (accelerated in batch mode), beginning from a full-throttle, constant velocity climbing turn at 30° of positive bank (to the right). Initial conditions were set at an altitude of 5000 ft and a velocity of 140 knots, which is close to the best speed for a cruise climb in the Beech 200. Engine failure was modeled by cutting the throttle to zero after ten seconds and control failures disallowed the use of the particular control surface throughout the simulation, assuming that it was stuck in the neutral position. In the case of engine failure, the model accounts for additional drag effects of the windmilling engine.

Rather than perform the full re-optimization of an existing aircraft, at this stage the interest was in identifying those elements that might drive system loss probability through sensitivity analysis. Therefore, a subset of aircraft geometry variables were selected and their values perturbed by $\pm 10\%$, with the exception of wing sweep, which was varied from 0 to 15 deg. These variables and their values are given in Table 3.1. Baseline values correspond to those of the aircraft in Fig. 3-2. Note that the values for the deflecting control surfaces are displayed to the reader as percentages of wing,

horizontal tail, or vertical tail chord, for ease of interpretation, although these are not the actual design variables (see footnote on Table 3.1).

Table 3.1: Aircraft geometry perturbations

Design Variable:	**Low Value**	**Baseline**	**High Value**
Wing Area	272.7 ft^2	303 ft^2	333.3 ft^2
Wing Span	49.05 ft	54 ft	59.95 ft
Horizontal Tail Area	65.7 ft^2	73 ft^2	80.3 ft^2
Horizontal Tail Span	16.51 ft	18.3 ft	20.17 ft
Vertical Tail Area	105.12 ft^2	116.8 ft^2	128.48 ft^2
Vertical Tail Height	7.5 ft	8.33 ft	9.16 ft
Spanwise Engine Location	7.72 ft	8.58 ft	9.44 ft
Aileron Chord*	15.3%	23%	30.7%
Elevator Chord*	23%	30%	37.0%
Rudder Chord*	17.5%	25%	32.5%
Wing Sweep	0 deg	4 deg	15 deg

* The design variables to which the ±10% perturbations were applied are the distances between the leading edge of the lifting surface and the leading edge of the deflecting control surface. This dimension facilitates input to the vortex lattice code, but is meaningless to the reader without the chord length.

3.2.3 State and Geometry-specific Gain Optimization

Proportional-integral-derivative (PID) controllers with a lead-lag compensator were used to maintain airspeed (elevator channel), bank (channel dependent on failure state), and yaw (rudder or throttle channel according to state), according to the block diagram in Fig. 3-7.

In order to ensure the aircraft maintained the best possible control while achieving the bank and climb requirements, gains **r** for each of these controllers were tuned by first using the Ziegler-Nichols (Z-N) method [113] to determine a feasible starting point.[2] This was then fine-tuned with an *interior-point* constrained optimization algorithm according to the optimization formulation given in Eqn. 3.6, shown for the

[2]The Ziegler-Nichols method is an popular empirical method for determining gains within a PID controller. By setting the integral (I) and derivative (D) gains to zero, an ultimate gain, K_u, is found by increasing the proportional (P) gain from zero until the output begins to oscillate at constant amplitude. The ultimate gain and oscillation period are then used to determine the P, I, and D gains.

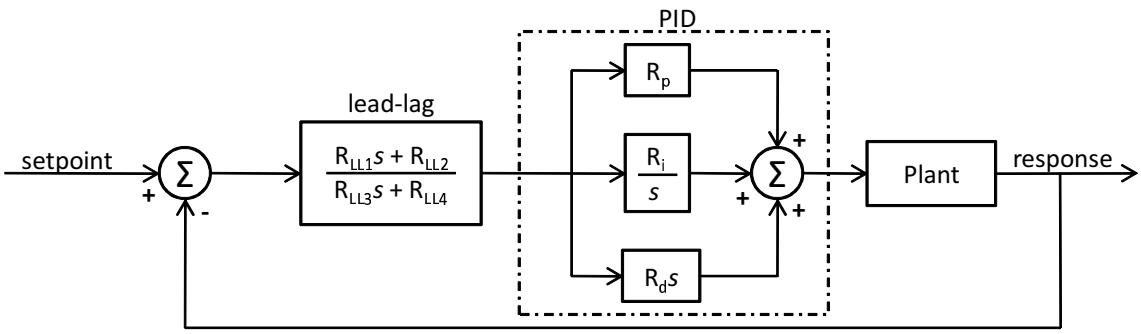

Figure 3-7: Controller block diagram

bank angle task.

$$\begin{aligned} &given \;\; \text{state } K, \;\; \text{geometry } \mathbf{x}, \;\; \text{parameters } \mathbf{c} \\ &minimize \;\; J(\mathbf{r}) = \frac{\sum(\phi(\mathbf{r}) - \phi_{setpoint})^2}{t/\Delta t} \\ &\qquad \mathbf{r} = [R_p, R_i, R_d, R_{LL1}, R_{LL2}, R_{LL3}, R_{LL4}] \\ &s.t. \;\; r_{i,LB} \leq r_i \leq r_{i,UB}, \qquad i = 1, 2, ..., n_r \end{aligned} \tag{3.6}$$

The lead-lag compensator was used when necessary, constructed as

$$\frac{R_{LL1}s + R_{LL2}}{R_{LL3}s + R_{LL4}} \tag{3.7}$$

such that when the coefficients are $[R_{LL1} = 0, R_{LL3} = 1, R_{LL2} = R_{LL4}]$, it becomes strictly a lag compensator and when all coefficients are zero, the compensator is not in use.

The above tuning and optimization procedure proved very effective in controlling the aircraft to the maximum extent possible for each unique state and geometry pairing. Often the Ziegler-Nichols results were more than sufficient to control a wide range of states, K, and geometries, $\mathbf{x}$, to within negligible deviations. This was especially true in the longitudinal axis for the control of airspeed. For the cases where more refinement was required in the roll axis, the optimization in Eqn. 3.6 was performed from ten random starting points within the bounds on $\mathbf{r}$ determined from

the Z-N results, in order to better search the non-linear design space. If bounds were reached, they were readjusted and the process reinitialized. The worst performing cases at the end of the procedure were then analyzed according to their *reachability* characteristics as reported in Appendix B.

The optimization approach given in Eqns. 3.6 and 3.7 would not be necessary in a single state performance analysis. A single state analysis would require only 23 performance simulations to obtain design sensitivities for each of the static design variables, as opposed to the 184 (23 x 8) required for the full multistate analysis. The majority (if not all) of these 23 simulations could be controlled by the same set of controller gains, given the small changes in the system geometry. In the multi-state case, however, it is extremely time consuming to manually set the gains for each geometry-state pairing. By allowing each of the gains, as well as the lead-lag coefficients, to be independent variables in Eqn. 3.6, the optimization can take place automatically within the design loop, and its results verified at the end of the design analysis. Such an automated process will be applicable to any system controllable through PID controllers. In the case of conceptual design, this will likely be sufficient for many types of systems. Where more complex controllers are necessary, more complex methods will also be required. Fortunately, there is a wide body of research within controls theory that focuses on such problems (which are beyond the scope of the research presented here).

3.2.4 State Definition

The previous subsections described the calculation of design sensitivities for the aircraft's multistate performance and a means of controlling the system in each of the states. The determination of which states to include in the analysis is also extremely important. While the next chapter describes some formal methods to assist in this determination, in this preliminary examination, failures were limited to those most directly affecting performance and dynamics, specifically failure of the rudder, ailerons, and/or a single engine. These correspond to the failure rates λ_R, λ_A, and λ_E, respectively. Typical values of failure rates were used to illustrate effectiveness of the

technique at identifying potential issues with the design's multistate performance, even given low frequency of failure. Flight control system failure rates were conservative estimates often used by experts of 1/500000 hrs. Guidance for these values can be derived from National Transportation and Safety Board (NTSB) data, such as its Annual Review of Accident Data. For example, 2006 data show that Part 135 airplane operations had one accident attributable to flight control system failure over 2.5 million hours of operation [81]. Since the Super King Air is generally a Part 135 on-demand or scheduled charter aircraft, and not all flight control system failures result in what the NTSB considers an accident, a 500,000 hour MTBF for the aileron and rudder control system is a reasonable estimate. Failure rates can vary widely across aircraft depending on the type of system and/or if software-in-the-loop is used (for some examples of very poor rates, e.g. 1/5000 hrs in UAVs, see [84]). However, for purposes of design the direction of performance improvement is much more important than the absolute magnitude of system availability or expected performance resulting from a specific combination of failure rates. For the engine, failure rates were set at $8\text{x}10^{-6}$ failures per hour, which was then doubled since only the possibility of losing one engine was considered. Engine failure rates for the Pratt & Whitney PT-6 come from [36].

If sequence dependence is ignored, the failure of the above elements results in only eight system configurations to consider, as depicted in the aggregated Markov model shown in Fig. 3-8. This model appears somewhat different than that shown in Fig. 2-8 because several of the downstream states can now be reached from multiple upstream states due to the aggregation. The ODE solution of the model in order to determine each state probability P_K^s, however, is performed in the same manner. The states in the aggregated Markov model are shown in Table 3.2.

Two time periods were used for the analysis of the Markov model and calculation of state probabilities, P_K^s. The first was a typical mission duration of 8 hours and the second was a 20,000-hour time period providing an indication of problem areas that might manifest themselves over the system lifetime. Results for both time periods are provided in Section 3.3.

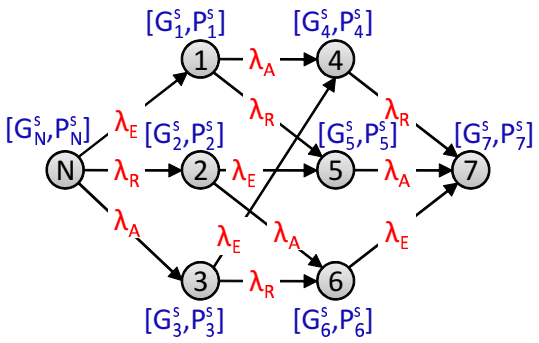

Figure 3-8: Twin-engine case study Markov formulation

Table 3.2: Aircraft states

State	Rudder	Aileron	Left Engine	Turn Control
Nominal (N)	OP*	OP	OP	ailerons/rudder
State 1	OP	OP	F*	ailerons/rudder
State 2	F	OP	OP	ailerons
State 3	OP	F	OP	rudder
State 4	OP	F	F	rudder
State 5	F	OP	F	ailerons
State 6	F	F	OP	differential thrust
State 7	F	F	F	n/a

* OP = Operating, F = Failed neutral (actuators); Failed off (engine)

To summarize Section 3.2, it was shown how system sensitivity analysis can be extended beyond the functional dependencies on state transition rates given in Eqn. 3.1 to include the effects of static design variables in Eqn. 3.2. This extension is applicable to any complex system composed of functional subcomponents or elements, and in which general performance is dependant upon its static design. Next, specific excess power in a turning climb was chosen as a case-specific performance objective for use as $G^s(t)$, and its functional dependencies in expected form shown in Eqns. 3.3 - 3.5. Finally, the multistate problem set-up was described, including selection of failure modes and a control technique used in their modeling. In general, the control technique is applicable to any system controllable through the use of a PID controller, which should be sufficient for the conceptual design of many types of systems.

3.3 Data Analysis

This section presents results of the multistate analysis, including the multistate design sensitivities with respect to the static design variables. Each geometry in Table 3.1 was run for each Markov state, including one baseline geometry plus 11 low values and 11 high values for a total of 23 geometries. This resulted in 184 simulation runs when applied to the eight Markov states. Total computational time, not including gain optimization, was under two minutes on a desktop with an Intel Quad i7 2.8GHz CPU and 9.0GB of RAM. This time included the benefits of splitting the computations across eight processing threads, such that the respective Markov states were computed in parallel.

3.3.1 Multistate Aircraft Performance

To best show the effects of each geometry on the performance metric, the scatter-plots in Fig. 3-9 were constructed, plotting bank angle vs. specific excess power for each state. Each plot contains 23 geometries, with the baseline geometry marked by dashed lines. Note that several geometries may overlap, thus not all 23 instances are discernible on each plot. The *safe region* is defined in each plot by a rectangle bounded by the W limits of $\geq$ 200 ft/min for P_s and within $\pm 5^\circ$ of the commanded bank angle of 30° as defined previously in Section 3.2. Geometries within the safe region are considered operational for the particular failure sequence, whereas those outside of this region will not allow safe completion of the mission. This information is used when classifying the performance of a particular Markov state for the calculation of the expected availability as per Eqn. 3.5.

Of the 184 simulation cases (23 geometries x 8 states), 28 did not achieve safe performance as established by the W criterion on climb rate and bank angle. Twenty-three of these resulted in total loss of aircraft and came from State 7, which was to be expected since there was no way to control the aircraft without use of rudder, aileron, or differential thrust. Four unsatisfactory cases came from the analysis of State 4, where the left engine and ailerons were failed, requiring bank angle and turn to be

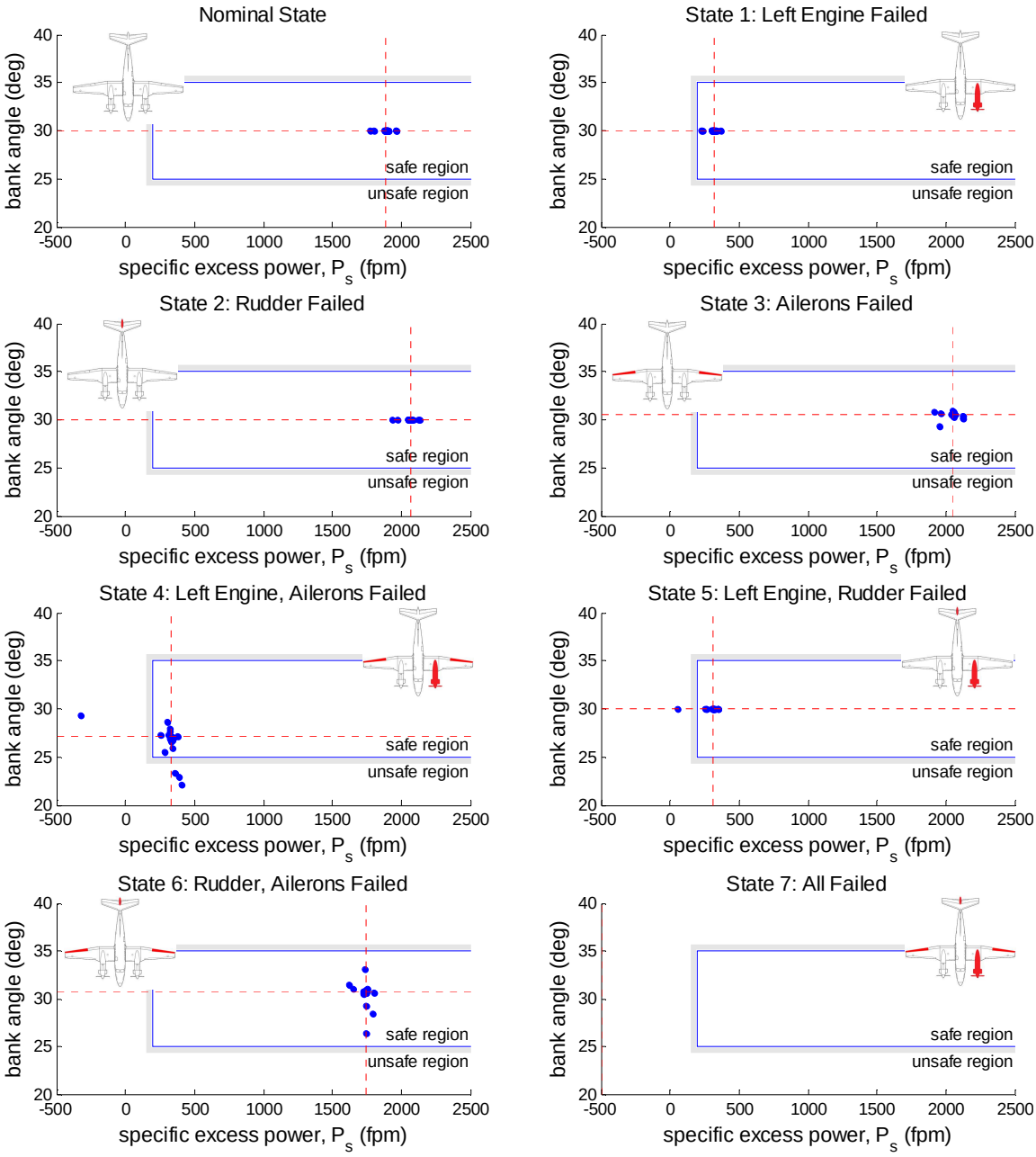

Figure 3-9: Effect of geometry perturbation on P_s vs. bank angle for each Markov state (states correspond to those in Fig. 3-8), *inset aircraft diagrams show failed components

controlled with only the rudder in the face of asymmetric thrust. The remaining case came from State 5, with the left engine and rudder failed and bank angle controlled with ailerons.

The most critical failing geometries of State 4 were those with the vertical tail height decreased by 10% and the spanwise engine location at the greatest distance from the fuselage. The short tail height was also the failing geometry of State 5. Experimentation with the control scenarios for this state, as well as numerous hours of flight testing actual Beech 200 aircraft, motivated suspicion that an unsatisfactory Dutch roll mode might be to blame. Indeed, inspection of the control derivatives showed that these two geometries had the lowest values for $|C_{n\beta}/C_{l\beta}|$ of all 23 cases. A general rule in aircraft design is that $|C_{n\beta}/C_{l\beta}|$, which is a measure of the aircraft's directional stability in relation to its lateral stability, should be greater than 0.33 for satisfactory Dutch roll [25]. For the case with the reduced tail height, this value was 0.19 and for the outboard engine placement it was 0.31.

There are a few items to note concerning this finding. First, the design model predicted a $|C_{n\beta}/C_{l\beta}|$ of 0.38 for the baseline aircraft and data collected from the flight testing in March 2010 [31] indicated a value somewhat less than this but within the margin of error. Both of these values are very close to the 0.33 threshold and become more critical at higher angles of attack, as less of the tail is in undisturbed flow. This is a known characteristic of the Beech 200 and one of the reasons why the aircraft is equipped with a yaw damper (the yaw damper is only certified for nominal operation and is shut off in failure conditions, per flight manual emergency procedures). Second, in five of the eight states, these poor Dutch roll characteristics did not result in a loss of the aircraft. However, in the adverse circumstances presented by State 4, the rudder was unable to dampen the Dutch roll mode while also being required to control bank angle in a turning climb. While it may be argued that this particular outcome is specific to the scenario and optimum control laws presented here, it does demonstrate the emergence of critically negative behavior in off-nominal conditions that can be affected by relatively small changes in geometric design variables. Specifically, a slightly more effective vertical tail would have been helpful in supporting

both simultaneous functions; controlling the Dutch roll mode, and maintaining bank angle.

Finally, regarding engine placement, in some cases intuition might be correct in suggesting further outboard engine location is desirable for better turn control through differential thrust. However, results show that the effect of this placement on inertial and mass properties should not be overlooked, especially when certain stability characteristics lie on the margin as in the case of State 4.

3.3.2 Design Sensitivities

The determination of which parameters have the greatest effect on overall system performance and availability is very important. As mentioned earlier, the expected performance in Eqn. 3.2 tends to treat the Markov state probabilities as "weights." Thus, given sufficiently low failure rates, a short Markov time period will have expected performance values nearly identical to the nominal state. As overall system lifetime increases, or mission duration in the case of long-endurance vehicles, the expected system performance will change as off-nominal probabilities increase. To illustrate this, consider an 8-hour mission and a 20,000-hour system lifetime, both typical for this type of aircraft. If no repairs are made, the Markov state probabilities will be as those depicted in Table 3.3, given the failure rates mentioned earlier. Even if repairs are considered, these values provide some indication of the amount of resources that must be allocated towards maintenance. The third column in Table 3.3 is not necessarily applicable to this aircraft, but is included to emphasize the impact of this analysis on systems expected to operate for long periods of time in austere environments, for instance an ultra long-endurance unmanned vehicle with a continuous mission duration of months or years.

Given these probabilities, it is possible to determine the expected system performance and availability. More importantly, one may solve the expected performance sensitivity for the 8-hour sortie, 20,000-hour system lifetime, or 5-year case, or likewise observe changes in expected availability. The design variable sensitivities are perturbations from the baseline geometry, figured from a central difference on the

Table 3.3: Steady-state Markov probabilities

Markov State	8-Hour Sortie	20,000-Hour System Lifetime	5-Year Sortie
Nominal	99.9%	67.0%	41.6%
State 1	0.01%	25.3%	42.3%
State 2	$< 0.001\%$	2.7%	3.8%
State 3	$< 0.001\%$	2.7%	3.8%
State 4	$< 0.001\%$	1.0%	3.9%
State 5	$< 0.001\%$	1.0%	3.9%
State 6	$< 0.001\%$	0.1%	0.35%
State 7	$< 0.001\%$	0.04%	0.35%

high and low variations in Table 3.1, according to Eqn. 3.8.

$$\frac{\Delta E_{A,G}(\mathbf{x}, \boldsymbol{\lambda^s})}{\Delta \mathbf{x}} = \frac{E_{A,G}(\mathbf{x} + \Delta \mathbf{x}, \boldsymbol{\lambda^s}) - E_{A,G}(\mathbf{x} - \Delta \mathbf{x}, \boldsymbol{\lambda^s})}{2\Delta \mathbf{x}} \tag{3.8}$$

Similar calculations were made for perturbations to the individual component failure rates (aileron, rudder, and engine), also varied by 10%. Values were normalized by the baseline aircraft geometry, failure rates, and 'expected' values. The sensitivities for the 8- and 20,000-hour expected P_s are shown in Fig. 3-10.

The 8-hour sortie represents a nominal aircraft sensitivity analysis for specific excess power, as might traditionally be performed in aircraft design. Here, wing span b is the most sensitive component. This is due to the significant increase in wing mass with the increase in aspect ratio, which outweighs the reduction in induced drag that occurs with a larger span. Wing area S is the next highest contributor, again due mostly to changes in the mass of the lifting surface. The sign of this sensitivity is opposite to that with wing span, as would be predicted by the location of S in the denominator of the equation for aspect ratio, $\mathcal{AR} = b^2/S$.

Results change for the 20,000-hour system lifetime sensitivity. Wing span and area remain two of the three most influential variables; this is to be expected given that the nominal state still has a 67% probability and thus retains a significant influence. However, previously insensitive variables are now more prominent. These are engine failure rate, vertical tail height, and vertical tail area. The first, engine failure rate, comes as little surprise given the relatively high probability of an engine failure, which

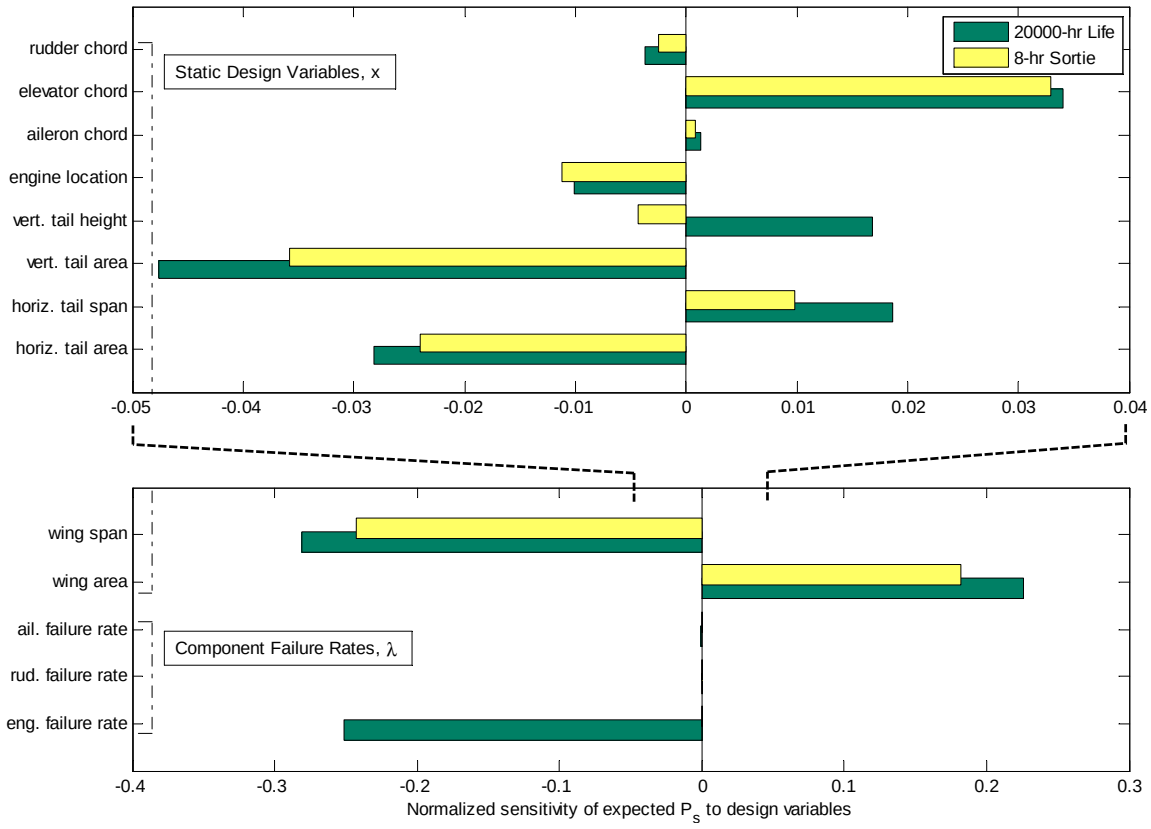

Figure 3-10: Comparison of design sensitivities: $\mathbf{P_s}$, sensitivity $= \Delta E_G(P_s)/\Delta x * (x_0/E_{G,0}(P_s))$, *top chart zoomed in for detail

is 27.3% per summation of Markov States 1, 4, 5, and 7 in Table 3.3. Hence, reducing engine failure rate would, naturally, have a beneficial effect on the expected specific excess power. The vertical tail height is less obvious. In this case, the derivative actually changes sign, in addition to magnitude, between the more nominal scenario and the extended time duration scenario that gives more weight to the off-nominal states. This arises from the unsatisfactory performance shown in States 4 and 5, as well as from having nearly the worst performance in State 3. The fact that this geometry performs quite well in the remainder of the states illustrates the importance of observing the design space from a multistate perspective, especially when long time durations are considered.

Fig. 3-11 shows the same type of sensitivity results, but for expected bank angle deviation instead of specific excess power. Again, vertical tail height is an extremely

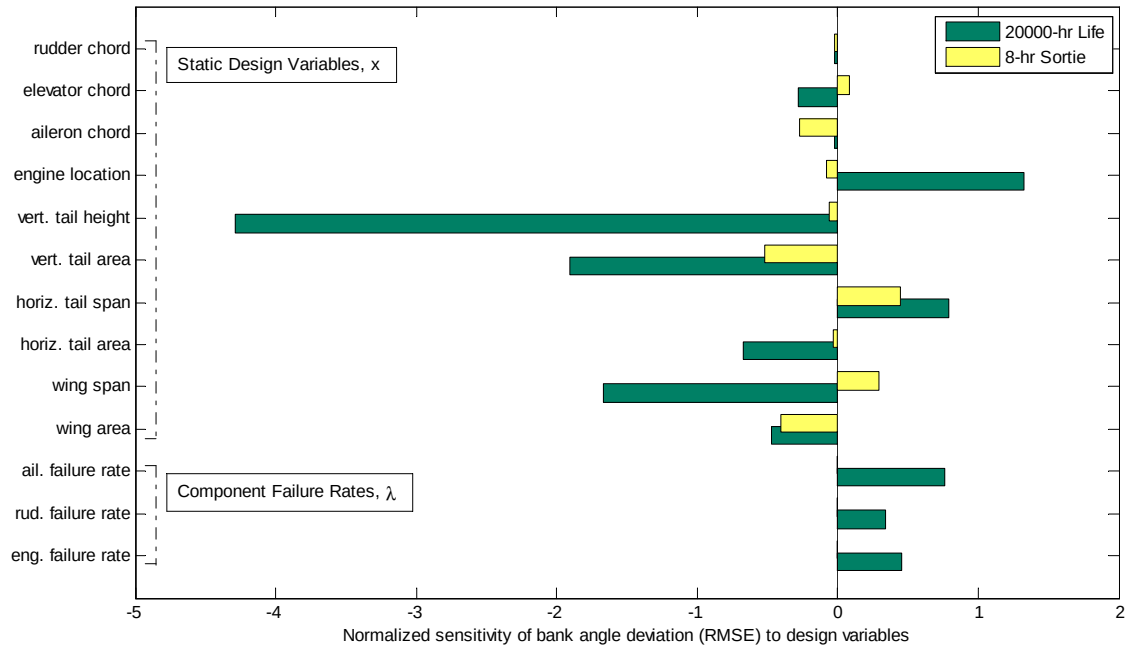

Figure 3-11: Comparison of design sensitivities: ϕ_{dev}, sensitivity $= \Delta E_G(\phi_{dev})/\Delta x * (x_0/E_{G,0}(\phi_{dev}))$

important factor in the 20,000-hour scenario, while relatively benign in the 8-hour sortie. In addition, several sensitivities such as wing span, engine location, and elevator chord change in both sign and magnitude. Note that sensitivity to engine failure rate is much less significant in comparison to the other failure rates than in Fig. 3-10. This is due to the fact that a significant portion of bank angle deviation occurs in States 3 and 6, in which the engine has not failed.

Finally, the data in Fig. 3-12 demonstrate how changes in design variables and component failure rates affect the system availability. The driving factors are those pointed out previously in the analysis of the scatterplots in Fig. 3-9. Although the engine has the highest component failure rate, its effect on expected availability is less than the other two components since the failure rate sensitivities were performed from the baseline geometry, which only has unsatisfactory performance in State 7. The distribution of probabilities across Markov states for this geometry is such that changes to aileron and rudder failure rates actually increase the weighting of State 7 more than do changes to the engine failure rate. Only the 20,000-hr and 5-yr results

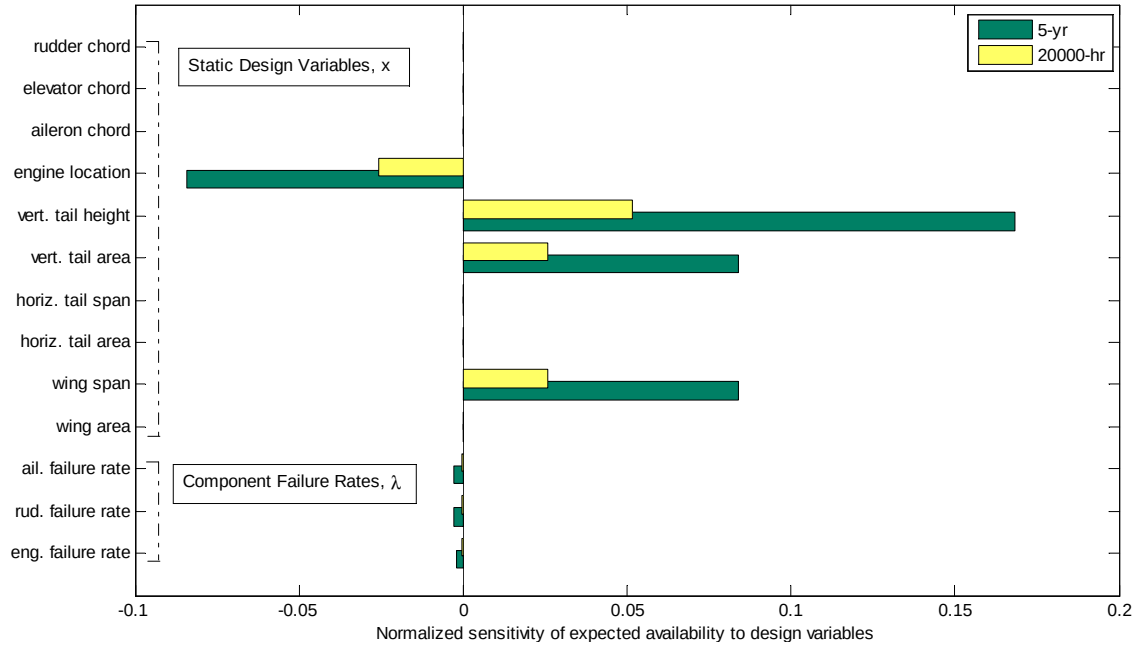

Figure 3-12: Comparison of design sensitivities: E_A, sensitivity $= \Delta E_A(P_s, \phi)/\Delta x * (x_0/E_{A,0}(P_s, \phi))$

are shown, as those for the 8-hr duration are insignificant in magnitude.

The sensitivity results in Fig. 3-12 are compelling, in that they show that improvements to the system's availability are much more effectively gained through changes in static design variables than through changes in component failure rate. This is important, from the perspective of reliability analysis, because improvements in reliability are nearly always sought after in the space of $\boldsymbol{\lambda^s}$ rather than affecting through changes to static design variables, $\mathbf{x}$.

3.4 Case Summary

As mentioned, the objective of this chapter was to quantify the effect of changes to a known aircraft's *static* design variables on its performance output for differing aircraft states. This was successfully accomplished through design sensitivity analysis by evaluating the expected performance and availability of the system across various time periods and subject to changes in static design variables and component failure rates.

Such analysis differs from traditional early-stage design methods, which concentrate on the system in its nominal state of operation, only infrequently considering failure states through piecemeal application of constraints. Results from this chapter suggest a weakness in the traditional methodology, showing how small changes in static design variables may improve performance in the nominal condition, while hurting performance in off-nominal conditions, resulting in decreased expected performance or availability across system lifetime or long mission durations. The analysis in this chapter also differs from reliability analysis, which focuses solely on component failure rates and the benefits of redundancy but does not consider how well or poorly the system performs with partial failures. Again, results suggest a weakness with this approach, showing that in many cases, improvements to the system's availability or expected performance are more effectively gained through changes in static design variables than through changes in component failure rate.

Specifically, results from the Super King Air analysis showed that of 184 geometry cases, 28 did not achieve satisfactory performance. Many occurred in the fully failed state and were expected, but several occurred in partially degraded states in which the majority of geometry cases were able to meet performance requirements. More importantly, this behavior clearly exhibited itself in the resulting design sensitivities, confirming that such an approach will allow designers to identify those elements that might drive system loss probability through an analysis of performance changes across system states and their respective response to changes in design variables. The results provide promising evidence as to the utility of expected performance and system availability analysis applied to a complex aircraft system, and its ability to provide design engineers with data to generate more robust solutions early in the design process.

As a final note on the Super King Air application study, development of the model and stochastic analysis techniques required to obtain the above results highlighted two areas for specific attention regarding multistate design. The first is that, even though the direct effects of multistate analysis are best realized in longer time duration systems, the benefits of the analysis should be probabilistically observable

over operational lifetimes of shorter duration systems as well. The second item is that the piecewise constant function of system availability will pose great difficulty for gradient-based optimization algorithms. Chapter 4 addresses both of these issues, within the context of a formalized multistate analysis and design methodology.

Chapter 4

Methodology and Tools for Multistate Analysis and Design

This chapter proceeds in developing a generalized methodology for multistate analysis and design, based upon its effectiveness as demonstrated in Chapter 3. The chapter encompasses three main sections. The first section lays out a methodology for multistate analysis and design as may be applied to early-stage development of complex aerospace systems. The second section focuses in on one aspect of that methodology and develops a multilayer Markov analysis technique enabling translation of single sortie component and vehicle level availability into metrics for a multiple sortie mission campaign. Finally, the third section discusses multistate optimization, specifically, the case of system availability, essentially a piecewise constant function in which improvement corresponds directly to increasing performance in off-nominal states above a certain threshold.

4.1 Multistate Analysis and Design

Consideration of the multistate problem is proposed at the earliest stages of the design process in Fig. 4-1, beginning with *requirements* and *concept development*. Next is an analysis of *failure modes*, an exercise typically taking place much later in the design cycle. It is moved forward here in order to provide a vector of transition rates

used later in the early phase integrated Markov analysis. The third step classifies the system according to the performance metric of interest and the nature of its mission, followed by *computational analysis*, where analysis of a point design, design of experiments, or optimization may be exercised. Finally, *analysis and visualization of results* are performed as the last step, before deciding whether to iterate again upon an updated architecture or transition rate vector.

4.1.1 Step 1: Requirements Definition and Concept of Operations

Defining requirements and a concept of operations should occur near the beginning of any design process and there are many sources describing activity here [38, 82]. To summarize from the NASA Systems Engineering Handbook [78], it should "transform stakeholder expectations into a definition of the problem" and should output clear measures of performance against which the design may be validated.

The step is included here for completeness and to underscore the fact that additional considerations must be made for systems designed under the multistate paradigm. These include, for example:

- Establishment of criteria for the acceptable performance threshold, W.
- Setting of realistic requirements for system availability and/or expected performance.
- Determination of how the system will be operated in off-nominal states.
- Establishment of a range of acceptable operational parameters, $\mathbf{c}$.

The importance of the above may vary from system to system, depending on its nature. Regarding the establishment of criteria for W, it is not sufficient to merely define unacceptable performance as that resulting in loss of the system. Many criteria exist whereby the operator would choose to abort the mission even though the system was still capable of safely operating. This may be directly related to the value of G_K^s itself or to the resulting operational conditions arising from that value.

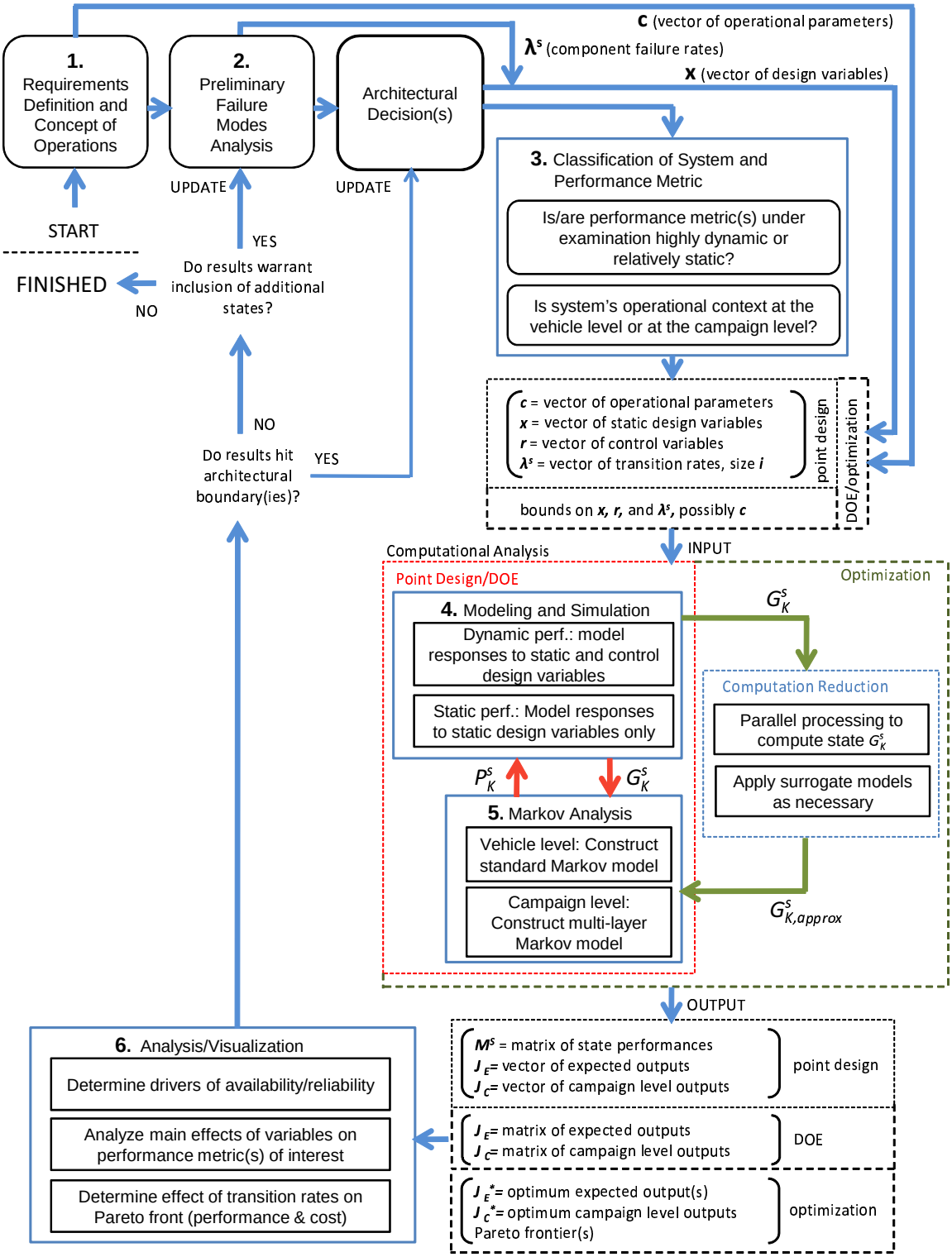

Figure 4-1: Multistate Analysis and Design Process

For example, a failure within a UAV system may result in a loss of endurance, but minimizing this loss may require increasing or decreasing the cruise altitude by several thousand feet. Consequently, it will be important to determine the range of flexibility in mission parameters, typically in the form of operational parameters, **c**, as part of the requirements definition.

4.1.2 Step 2: Preliminary Analysis of Failure Modes

The most common form of failure mode analysis is formally referred to as Failure Mode and Effect Analysis (FMEA), the purpose of which is to "study the results or effects of item failure on system operation and to classify each potential failure according to its severity" [35]. It is widely used throughout industry and the originating military standard (MIL-STD-1629A) is a 54-page document describing a process which may be succinctly summarized as:

1. Describe the system elements.
2. Determine their function(s).
3. Identify their failure mode(s).
4. Identify the potential cause(s) and effect(s) of the failure.
5. Describe proper corrective action.
6. Classify the failure(s) according to severity.

The FMEA is typically performed after the static design is set. This allows more detailed analysis of failure effects, but generally limits corrective action to improving element failure rates or restricting the operational envelope. There are some failures to which this later stage analysis is best suited. However, effects of many failures can be accurately predicted much earlier in the design cycle. Integrating a preliminary FMEA into the early-phase design loop as in Fig. 4-1 has the purpose of 1) identifying these types of failures, 2) determining their estimated rate of occurrence, and 3) rank ordering them according to their occurrence rate and effect on performance.

Much of the analysis at this early stage will be based on the designer's experience and any historical data that may be available, especially concerning the rates of

failure. The most important output of this step is the vector of transition rates, $\lambda^{\mathbf{s}}$, that will eventually be used as input to the computational analysis. As was discussed in Chapter 2, the probabilities, P_K^s, resulting from the Markov analysis, act as weights in the multistate performance indices. Thus, the more highly probable and highly consequential failures that are represented in the transition rate vector, the better. Depending on results of the initial performance and Markov analysis, the failure modes analysis may be iteratively updated to include more or less states, or to reorder the failure mode ranking.

4.1.3 Step 3: System and Performance Classification

The classification of the system and its performance metric is necessary in determining the type of analysis to be performed as part of Step 4 and Step 5. Whether that analysis is *dynamic* or *static* depends upon the level of fidelity sought and the kinematic nature of the metric. With metrics such as range or endurance, the effects of shorter time duration kinematics are generally negligible compared to the cumulative effects of motive resistance (drag), propulsive forces, and energy consumption. Thus, a *static* analysis is possible through physics-based analytic equations that assume the system is dynamically controllable. Such analyses are common at the conceptual design level and will be relatively accurate, assuming one can integrate the effects of failure states into the analysis. On the other hand, if higher fidelity is sought in a shorter time duration maneuver, such as that of the turning climb in Chapter 3, the analysis is *dynamic* and the effects of controllability may be accounted for through simulation. The primary difference between the two is that one directly includes the effects of control variables, $\mathbf{r}$, in the analysis and the other assumes the best case scenario of a fully controllable system. This involves a trade-off between fidelity of analysis and computational time.

The second categorization under this step has to do with the system's operational context and will determine the depth of Markov analysis performed in Step 5. If the system will only be considered in the context of its own singular operation (*vehicle level*), the Markov analysis as described in Section 2.3.2 of Chapter 3 is applicable

and sufficient. If the system is to be operated as part of a larger campaign involving multiple sorties and multiple vehicles, the Markov analysis technique developed in Section 4.2.1 will be applicable.

4.1.4 Step 4: Modeling and Simulation

Under the modeling and simulation step lies responsibility for populating the state performance set, $\breve{\mathbf{G}}^{\mathbf{s}}$. The analysis takes as input the number of elements, n, vector of parameters, $\mathbf{c}$, static design variables, $\mathbf{x}$, performance threshold(s), $\mathbf{W}$, and if the response of a dynamic performance metric is sought, the vector of control variables, $\mathbf{r}$. Output is a truncated set of state performances, $\breve{\mathbf{G}}^{\mathbf{s,t}}$, defined as,

$$\breve{\mathbf{G}}^{\mathbf{s,t}} = \breve{\mathbf{G}}^{\mathbf{s}}|_{G_K^s \geq W} \cup \breve{\mathbf{G}}^{\mathbf{s}}|^{+}_{G_K^s \leq W} \Rightarrow \breve{\mathbf{G}}^{\mathbf{s,t}} \subseteq \breve{\mathbf{G}}^{\mathbf{s}} \tag{4.1}$$

Here, $\breve{\mathbf{G}}^{\mathbf{s}}|_{G_K^s \geq W}$ includes all G_K^s belonging to the subset of *acceptable* states, as determined by the performance threshold, W, and $\breve{\mathbf{G}}^{\mathbf{s}}|^{+}_{G_K^s \leq W}$ includes those G_K^s in the *unacceptable* subset that have not evolved from a previously *unacceptable* state.[1] This is a computation saving measure, ensuring that states in a known condition of *failed* are not unnecessarily evaluated for performance. The process follows the pseudo-code in Table 4.1 and assumes that, once the system enters an *unacceptable* state, any additional failures will not cause it to again enter the *acceptable* region. If this assumption does not hold, or the performance values of the lower tier *unacceptable* states are for some reason important, one can perform analysis for the entire set $\breve{\mathbf{G}}^{\mathbf{s}}$.

It is important to note that the state performances, G_K^s, at any particular failure level (FL) are not explicitly coupled to each other. Returning to the Markov diagrams in Figs. 2-8 and 2-9, of Chapter 2, given here again as Figs. 4-2 and 4-3 for reference, observe that states at a common FL may be calculated in parallel during the execution of the algorithm in Table 4.1, given the proper computational architecture.

[1] If the Markov chain has been simplified due to failure symmetry, such as that shown Fig. 2-9 or Fig. 4-3 on the next page, the members excluded from $\breve{\mathbf{G}}^{\mathbf{s,t}}$ are those in which all of the arrival paths come from states that have already been classified as *unacceptable*.

Table 4.1: Pseudo-code for processing of states through Markov chain

Activity	**Description**
Input:	number of elements, n; vector of parameters, $\mathbf{c}$; vector of design variables, $\mathbf{x}$; vector of control variables, $\mathbf{r}$; performance threshold, W
Process:	-Set desired number of failure levels, FL (max is equal to n) -Find nominal performance, $G_1^s(\mathbf{x}, \mathbf{r}, \mathbf{c})$, for failure level 0 -For 1 to the number of desired failure levels –Calculate each state performance, $G_K^s(\mathbf{x}, \mathbf{r}, \mathbf{c})$, for which the performance in any of the preceding arrival states (at failure level - 1) was $\geq W$ –Store performance, $G_K^s(\mathbf{x}, \mathbf{r}, \mathbf{c})$, in $\breve{\mathbf{G}}^{\mathbf{s,t}}$
Output:	truncated state performance set, $\breve{\mathbf{G}}^{\mathbf{s,t}}$

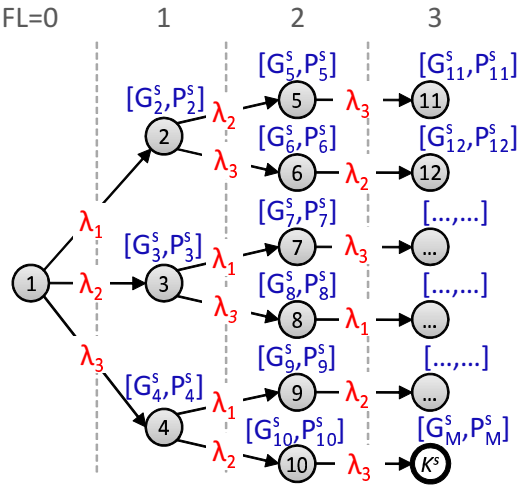

Figure 4-2: Markov chain formulation for a generic three-element system

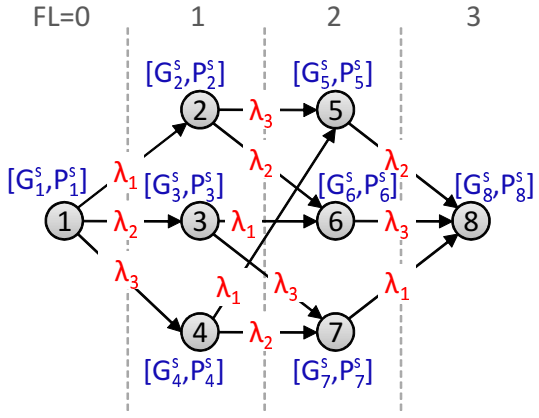

Figure 4-3: Markov chain formulation for a symmetric three-element system (state performance is order independent)

Additionally, if massively parallel processing is available, the time saved by avoiding analysis of states in a known condition of *failed* may be less than the increase in time required to analyze the FL's in series (as is done through the process in Table 4.1). Under this circumstance, it is advantageous to concurrently calculate the entire set, $\breve{\mathbf{G}}^{\mathbf{s}}$, and categorize the state performances *a posteriori*. This will often be the case for smaller numbers of states and if the symmetry simplification has been made, depending on the available number of processors.

4.1.5 Step 5: Markov Analysis

Input to Step 5 are the truncated state performance set, $\breve{\mathbf{G}}^{\mathbf{s,t}}$, and the transition rates, $\boldsymbol{\lambda}^{\boldsymbol{s}}$ and $\boldsymbol{\mu}^{\boldsymbol{s}}$. It returns as output the set of state probabilities, $\breve{\mathbf{P}}^{\mathbf{s}}$, calculated through Markov analysis as described in Chapter 2, and the multistate performance indices given in Eqns. 2.25 and 2.26. If a campaign type analysis is desired, this may be performed according to the process described in Section 4.2.1.

4.1.6 Step 6: Analysis and Visualization of Results

Steps 4 and 5, above, may be performed on a single design point, as part of a Design-of-Experiments (DOE) analysis, or within an optimization routine. In each case, they have the potential to generate very large amounts of data. The number of system evaluations will be on the order of M x d, where M is the number of system states and d is the number of design point evaluations. Because of this, efficient analysis of data becomes very important and results from each system and state evaluation should be stored, when possible. Although the indices of expected performance and availability provide an aggregated measure of performance, observing individual state performances often helps deduce the design cause of a particular state behavior. This provides intuition into the design problem and insight regarding updates to future design cycles.

Visualizing results is best done through one of three means, depending on the type of design analysis performed. Examples of each of these are given in the case studies

throughout the thesis. The first is a graphical representation of design sensitivities, as already demonstrated in Chapter 3. These sensitivities are typically normalized local gradients that reflect how the performance metric of interest changes w.r.t. changes in each of the design variables (or component failure rates and parameters, if desired). This visualization is best suited to the analysis of a particular point within the design space, i.e., for the improvement of an existing design or more detailed refinement after a general solution has been found. It provides valuable information to the designer regarding how to best improve the design.

A second means of observation requires systematically sampling the design space through one or more DOE methods. There are several statistical techniques available for this, including orthogonal arrays [54], Latin-hypercube spacing [62], or full-factorial design, to name a few. Each has advantages and disadvantages, but the general intent is to maximize coverage across design space boundaries and characterize the global behavior of output with respect to input(s). Orthogonal arrays are especially suited for determining the main effects of design variables on system output, but generally require the evaluation of more design points than Latin-hypercube spacing, for the same degree of coverage across the design space. Latin-hypercube spacing, on the other hand, has the advantage that it provides a balance between spreading the design points out to the maximum distance possible while maintaining relatively uniform spacing between them.

Finally, when performing multistate design analysis as part of an optimization routine, there are several measures of performance that should be considered in determining an "optimum" solution. These include the system availability, E_A, the expected performance, E_G, nominal performance, $G^s_{1(N)}$, and cost, if available. Comparing these outputs is accomplished by the pairwise plotting of their respective Pareto fronts,[2] which are composed of the design points that cannot be improved without decrementing performance in at least one of the outputs (the *non-dominated* points) [85]. There are a number of algorithms available for the optimization-based

[2]It is possible to compare multiple objective outputs in the form of a multidimensional Pareto front, but with higher dimensions the visual analysis is much more difficult.

determination of Pareto fronts, including the Adaptive Weighted Sum approach [61] and the Normal Boundary Intersect (NBI) method [33], which is particularly suitable for parallel computation. Special consideration must be given to the optimization of E_A, as described in Section 4.2.2.

4.2 Supporting Methods

The above section detailed the steps of multistate analysis and design, as shown in framework of Fig. 4-1. The following two sections serve dual purposes in support of this. They provide more detailed descriptions of subprocesses under the *Markov Analysis* and *Optimization* blocks within the computational analysis methods of Fig. 4-1. They also address the two specific focus areas highlighted at the end of Chapter 3. Correspondingly, the sample problem described in Section 4.2.1 below provides an in-depth example of the Markov analysis process in general, in addition to demonstrating the multilayer extension to campaign analysis.

4.2.1 Multilayer Extension of Markov Analysis

The multilayer campaign analysis method proposed here is intended as a means of translating vehicle level metrics into measures of multistate campaign performance. This demonstrates how the multistate design of shorter duration vehicles can directly affect longer term operational measures such as mission availability, attrition, and sortie aborts. The technique is possible through Markov chain formulations when the campaign level metric of interest has direct roots in the performance output of the vehicle level system. This is often the case, as in unmanned surveillance missions requiring omnipresence over the mission area, or reconnaissance scan missions that must cover a certain distance per time period. First, a short description of related methods is provided, followed by an overview of the process, as shown in Fig. 4-4, and a detailed numerical example.

There are few references to such hierarchical modeling of discrete-state continuous-time Markov chains in literature. One area is that of *cyclic dynamics* in the field of

physics, where reference is made to multilayer Markov chains for use in modeling polymers in shear flow [44]. Here, the layers span across different dimensions of space (x-direction and y-direction), rather than time, and states are not aggregated, as in the procedure described below. Another area is that dealing with redundancy modeling in reliability analysis, where a hierarchical Markov model is described in the context of combining the techniques of redundancy modeling, at the lower level, with the upper level system-based Markov models [59]. Application of both of the above mentioned methods to the problem of extending vehicle level performance metrics to a extended time campaign analysis is limited, at best.

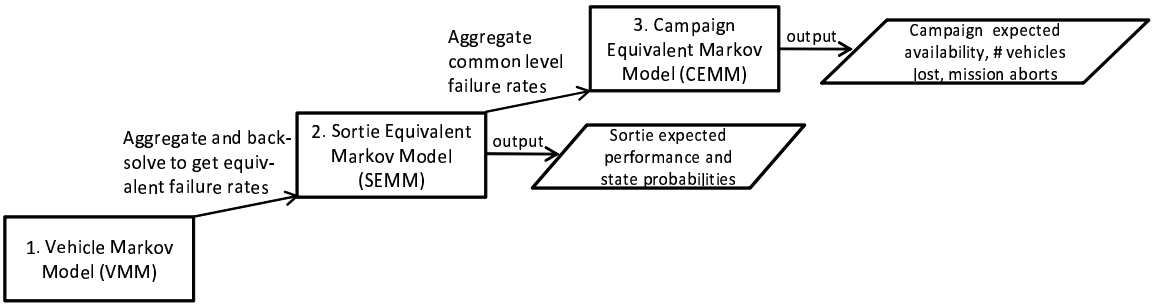

Figure 4-4: Multi-layer Markov analysis procedure

The first step in the procedure introduced here, shown in Fig. 4-4, to create a vehicle level Markov model (VMM) fully representing the functional behavior of the vehicle system in the campaign appropriate failure states. Given component failure rates, $\boldsymbol{\lambda}^{VMM}$, the state probabilities, $\check{\mathbf{P}}^{\mathbf{VMM}}$, are determined using the methods described in Section 2.3.2 of Chapter 2.[3]

Once the vehicle state probabilities and performances are determined, the next step is to form the Sortie Equivalent Markov Model (SEMM). This is accomplished by aggregating the vehicle state probabilities into probability bins, the divisions of which are determined by performance criteria on the vehicle or mission's objective of interest. For instance, typical performance categories at the sortie level are *nominal (N)*, *degraded (D)*, *abort (A)*, and *loss (L)*. The correct binning of probabilities into

[3]In this first step, $\check{\mathbf{P}}^{\mathbf{VMM}}$ and $\boldsymbol{\lambda}^{VMM}$ correspond to the sets $\check{\mathbf{P}}^{\mathbf{S}}$ and $\boldsymbol{\lambda}^{S}$, defined in previous sections.

the SEMM results in $\breve{\mathbf{P}}^{\mathbf{SEMM}}$, making it possible to back-solve the Markov chain for equivalent transition rates, $\boldsymbol{\lambda}^{\boldsymbol{SEMM}}$, between the binned sortie states.

The above is accomplished by forming the SEMM such that each state is entered through a unique chain of transitions. This ensures there are no more than $K^{SEMM}-1$ unknown equivalent transition rates, where K^{SEMM} is the number of SEMM states. It follows that a unique solution for $\boldsymbol{\lambda}^{\boldsymbol{SEMM}}$ exists, taken from the system of ODEs describing the SEMM Markov chain. This solution is most easily determined through the least squares minimization problem in Eqn. 4.2,

$$min_{\boldsymbol{\lambda}^{\boldsymbol{SEMM}}} \sum_{K=1}^{M^{SEMM}} \|P(\boldsymbol{\lambda}^{\boldsymbol{SEMM}})_K - P_K^{SEMM}\|^2 \tag{4.2}$$

where $\breve{\mathbf{P}}(\boldsymbol{\lambda}^{\boldsymbol{SEMM}})$ is the solution to Eqn. 2.23 in Chapter 2.

The final step involves relating the sortie level transition rates, $\boldsymbol{\lambda}^{\boldsymbol{SEMM}}$, to the transition rates for the Campaign Equivalent Markov Model (CEMM), which include both $\boldsymbol{\lambda}^{\boldsymbol{CEMM}}$ and $\boldsymbol{\mu}^{\boldsymbol{CEMM}}$. In most cases, the members of $\boldsymbol{\lambda}^{\boldsymbol{CEMM}}$ may be determined by summing members of $\boldsymbol{\lambda}^{\boldsymbol{SEMM}}$ that occur at common levels of failure and enter states of the same performance category. Otherwise, the unknown CEMM rates can be organized such that they are solvable through Eqn. 4.2 as before. The set $\boldsymbol{\mu}^{\boldsymbol{CEMM}}$ represents campaign equivalent repair rates by way of sortie regeneration and replacement. These repair rates are known values derived from average sortie duration, logistics of the particular mission scenario, and available campaign infrastructure. Finally, the probabilities, $\breve{\mathbf{P}}^{\mathbf{CEMM}}$, are found through the solution of Eqn. 2.23 for the CEMM.

The following step-by-step procedure is prescribed for the above:

1. Given $\boldsymbol{\lambda}^{\boldsymbol{VMM}}$, solve vehicle level Markov system to obtain $\breve{\mathbf{G}}^{\mathbf{VMM}}$, $\breve{\mathbf{P}}^{\mathbf{VMM}}$.
   a) Aggregate members of $\breve{\mathbf{P}}^{\mathbf{VMM}}$ into probability bins based on sortie level performance categories defined by $\mathbf{W} = [W_{min,N}\ W_{min,D}\ W_{min,A}]$. This provides $\breve{\mathbf{P}}^{\mathbf{SEMM}}$.
   b) Check that $\sum_{K=1}^{M^{SEMM}} P_K^{SEMM} = 1$.

2. Form Sortie Equivalent Markov Model (SEMM) with the unknown set, $\boldsymbol{\lambda}^{\boldsymbol{SEMM}}$, and $\breve{\mathbf{P}}^{\mathbf{SEMM}}$ from above.

   a) Check that each state, K, results from a unique chain of transitions.

   b) Solve SEMM by operating on Eqn. 2.23 with the least squares minimization in Eqn. 4.2 to obtain values for $\boldsymbol{\lambda}^{\boldsymbol{SEMM}}$.

3. Form Campaign Equivalent Markov Model (CEMM) with $\boldsymbol{\lambda}^{\boldsymbol{CEMM}}$, $\boldsymbol{\mu}^{\boldsymbol{CEMM}}$, and the unknown set, $\breve{\mathbf{P}}^{\mathbf{CEMM}}$, the divisions of which are based on campaign level performance categories defined by $\mathbf{W} = [W_{min,N}\ W_{min,D}]$.

   a) Determine $\boldsymbol{\lambda}^{\boldsymbol{CEMM}}$ by summing members of $\boldsymbol{\lambda}^{\boldsymbol{SEMM}}$ that occur at common levels of failure and enter states of the same SEMM performance category.

   b) Determine $\boldsymbol{\mu}^{\boldsymbol{CEMM}}$ from campaign level logistics.

   c) Solve CEMM through Eqn. 2.23 to obtain $\breve{\mathbf{P}}^{\mathbf{CEMM}}$.

The following example demonstrates the above process on a simple four component air vehicle reconnaissance system, and provides a more in-depth view of the Markov solution process. The system has an endurance of 40 hours and takes part in a 5-year multiple sortie campaign to map a land mass located 10 hours away from its home base. Its components, A, B, C, D, compose $\boldsymbol{\lambda}^{\boldsymbol{VMM}}$ and have failure rates of:

- $\lambda_A = 1/500$hrs
- $\lambda_B = 1/500$hrs
- $\lambda_C = 1/200$hrs
- $\lambda_D = 1/300$hrs

The vehicle's operational velocity is 240 nm/hr and the failure of each respective component decrements the velocity according to the schedule given in Table 4.2. Table 4.3 provides the values for cases where certain order and set dependent failures decrement the velocity. For instance, if the state is defined by only two failures, arrived at by the failure of Element A followed by failure of Element D (A→D), the

velocity is 210 nm/hr. In all other cases, the decrements come from Table 4.2 and are simply summed with those of the other failures.[4]

Table 4.2: General performance decrements

Failure of component:	A	B	C	D
Velocity decrement:	-40 nm/hr	-20 nm/hr	-20 nm/hr	-60 nm/hr

Table 4.3: Set specific performance decrements

Failure of component:	**Velocity decrement:**
only A:	-30 nm/hr
A→B, B→A:	-120 nm/hr
only A→D:	-30 nm/hr
only B→A:	-60 nm/hr
C→D, D→C:	-120 nm/hr
only D→B:	-40 nm/hr

The vehicle's performance can fall into one of four categories. The first is the nominal case, which occurs as long as the vehicle can travel at 220 knots or higher. If the achievable velocity is higher than 180 knots but less than 220, the mission can continue but at a degraded state. When the velocity falls below 180 knots, the sortie must be aborted and the vehicle returns to base. If it falls further below 140 knots, the vehicle crashes. The failure rates and above categorization give rise to the Vehicle Markov Model (VMM) in Fig. 4-5, shown for the general, non-symmetric case. The performance criteria may be summarized as:

- Nominal: $V_{cr} \geq (W_{min,N} = 220)$, green
- Degraded: $(W_{min,D} = 180) \leq V_{cr} < (W_{min,N} = 220)$, blue
- Abort: $(W_{min,A} = 140) \leq V_{cr} < (W_{min,D} = 180)$, yellow
- Loss: $V_{cr} < (W_{min,A} = 140)$, red

The values next to the states in Fig. 4-5 are the state probabilities found by solving the system of ODEs in Eqn. 2.23 with the component failure rates, $\boldsymbol{\lambda}^{\boldsymbol{VMM}}$,

[4]Thus, State 8 (A→D) in Fig. 4-5 is classified as *degraded* with $V_{cr} = 210$ nm/hr, while State 15 (D→A) is classified as *abort* with $V_{cr} = 140$ nm/hr.

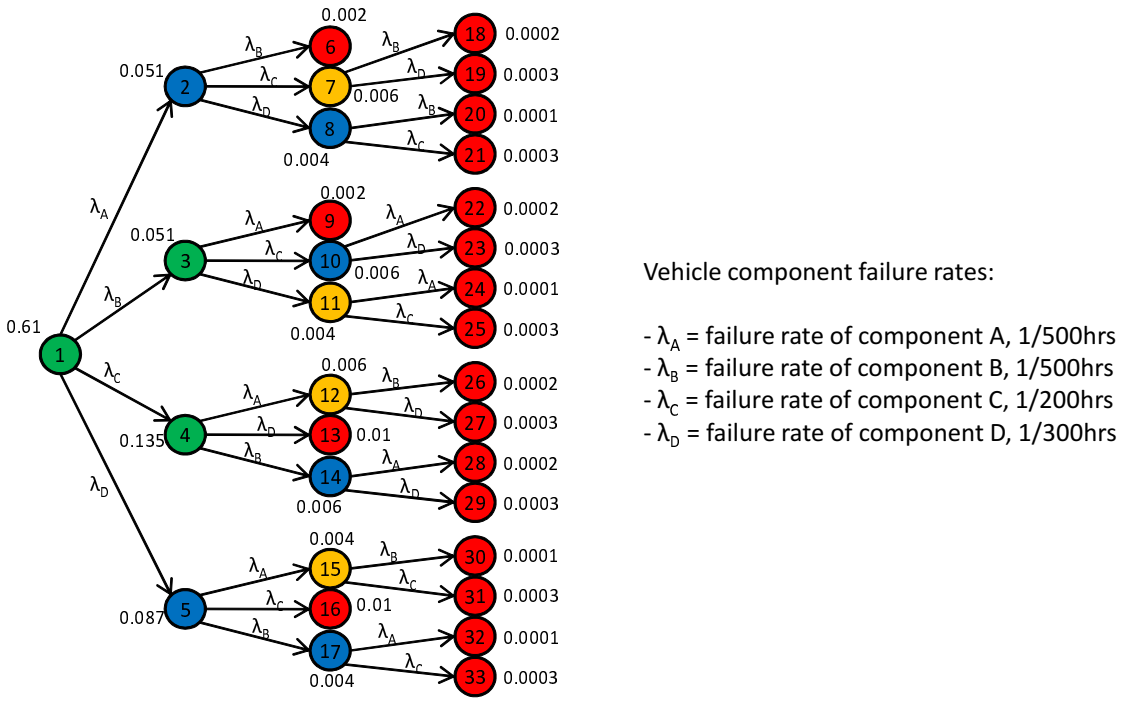

Figure 4-5: Vehicle Markov Model (VMM)

and the vehicle's design endurance time as inputs. They represent the probability that the system will find itself in that particular state at the end of the operational period defined by the vehicle's endurance. Having solved the VMM for both the performance, $\breve{\mathbf{G}}^{\mathbf{VMM}}$, and probabilities, $\breve{\mathbf{P}}^{\mathbf{VMM}}$, it is now possible to form the sortie equivalent model by aggregating the VMM probabilities such that one may solve for SEMM equivalent transition rates, $\boldsymbol{\lambda}^{\boldsymbol{SEMM}}$, through Eqn. 4.2. The criteria on vehicle performance were established above as applied to the sortie model, therefore the remaining task is to organize the transition paths such that the rates may be uniquely defined by the SEMM state probabilities. The nominal and degraded states are fairly straightforward in this example, given by,

$$P_N^{SEMM} = P_1^{VMM} + P_3^{VMM} + P_4^{VMM} \tag{4.3}$$

$$P_D^{SEMM} = P_2^{VMM} + P_5^{VMM} + P_8^{VMM} + P_{10}^{VMM} + P_{14}^{VMM} + P_{17}^{VMM} \tag{4.4}$$

where P_N^{SEMM} and P_D^{SEMM} refer to the nominal and degraded states in Fig. 4-6.

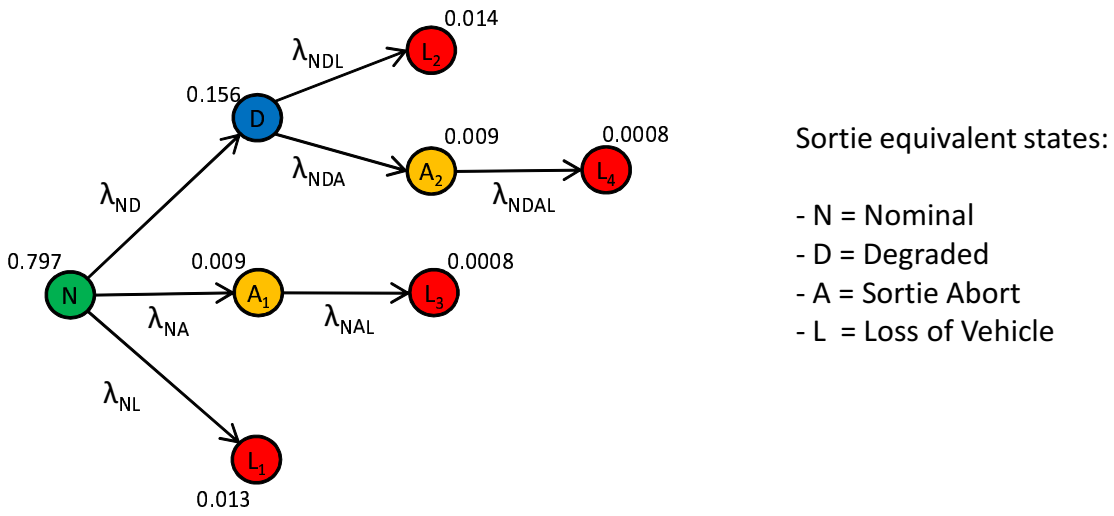

Figure 4-6: Sortie Equivalent Markov Model (SEMM)

The abort and loss states are a little more complicated due to the various paths possible, but may be determined in a similar manner. For example, state $K = A_2$ in the SEMM (Fig. 4-6) is the *abort* state defined by the receiving path $N \rightarrow D \rightarrow$, and its probability calculated as,

$$P_{A_2}^{SEMM} = P_7^{VMM} + P_{15}^{VMM} \tag{4.5}$$

State L_3 is the *loss* state defined by the receiving path $N \rightarrow A \rightarrow$ (found as green$\rightarrow$yellow$\rightarrow$ in the VMM), and calculated as,

$$P_{L_3}^{SEMM} = P_{24}^{VMM} + P_{25}^{VMM} + P_{26}^{VMM} + P_{27}^{VMM} \tag{4.6}$$

The complete SEMM is shown in Fig. 4-6, with the summed probabilities shown next to the states.[5] Sorting and summing of the probabilities, such as that done in the above four equations, is very complex when done algorithmically for an unknown number of states with varying performance distributions. The algorithm developed for this has been included in Appendix C.

Given the state probabilities in the SEMM, the equivalent transition rates are

[5]Displayed probabilities may be slightly off due to rounding.

found by solving Eqn. 4.2, where P_K^{SEMM} are the values from Fig. 4-6. This results in the equivalent transition rates given in Table 4.4

Table 4.4: SEMM equivalent transition rates

$\boldsymbol{\lambda^{SEMM}}$	**Value [1/hr]**
λ_{ND}	1/194.2
λ_{NA}	1/3454
λ_{NL}	1/2763
λ_{NDL}	1/237.3
λ_{NDA}	1/335.0
λ_{NAL}	1/239.8
λ_{NDAL}	1/158.4

The SEMM equivalent transition rates may now be used to determine $\boldsymbol{\lambda^{CEMM}}$ through the summations next to the campaign model in Fig. 4-7. To understand these, note that the campaign itself is now viewed as the system, with its own performance output that depends on the operational status of its constituent elements. In this example, the real-time campaign performance metric of interest is the rate at which mapping data is collected over the land mass in nautical miles per hour. Since only a single vehicle is required to operate over the land mass at a time, this rate is the velocity of the operating vehicle, which might be in a nominal or degraded state. From the campaign standpoint, when the vehicle aborts or crashes, no data is being collected and therefore the campaign is in a failed state until another aircraft arrives.

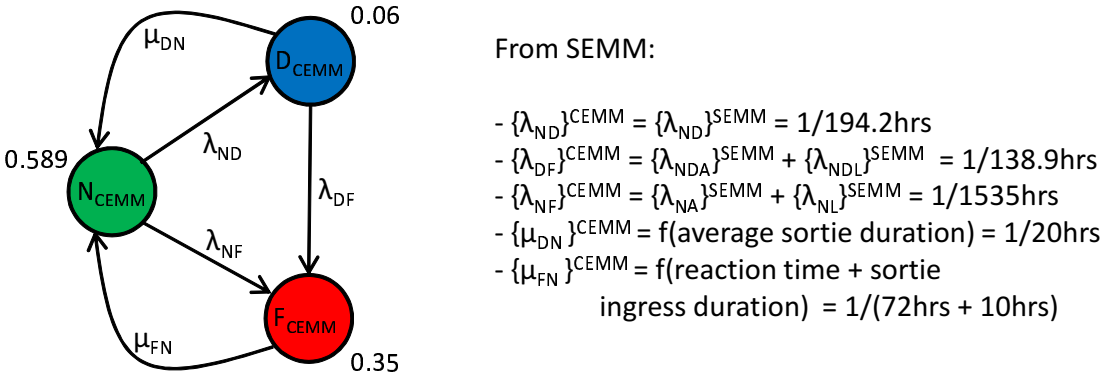

Figure 4-7: Campaign Equivalent Markov Model (CEMM)

The repair rates, $\boldsymbol{\mu}^{\boldsymbol{CEMM}}$, are functions of sortie duration, travel time to and from the land mass, and the reaction time required for the operators of the system to respond. A safe estimate of the repair rate from the degraded to the nominal state in this example, μ_{DN}, is the inverse of 1/2 the average sortie duration, since it is assumed that any failure is just as likely to occur at the beginning of the mission as near the end,[6] and the vehicle continues operation unless it has reached the abort state. If the vehicle aborts or crashes, one can assume that the operators would take some time to determine the cause of the abort or crash before sending a replacement vehicle, so as not to repeat it. Therefore, the repair rate, μ_{FN}, is merely the inverse of this reaction time plus the sortie ingress duration.

With the transition rates determined, the members of $\check{\mathbf{P}}^{\mathbf{CEMM}}$ are found in the traditional manner through Eqn. 2.23, for the campaign time of 5-years. These are given as the numbers next to the states in Fig. 4-7. The expected performance in each of the CEMM states can be derived from the VMM in order to obtain performance outputs for the overall campaign. The expected nominal performance, $\bar{G}_N^{CEMM}$, is calculated through Eqn. 4.7,

$$\bar{G}_N^{CEMM} = \sum_{G_K^{VMM} \geq 220} G_K^{VMM} \frac{P_K^{VMM}}{\sum_{G_K^{VMM} \geq 220} P_K^{VMM}} \tag{4.7}$$

summing only the nominal states in the VMM. A similar procedure is used to find $\bar{G}_D^{CEMM}$ and $\bar{G}_F^{CEMM}$, remembering to account for the fact that both *abort* and *loss* states fall into the *failed* category in the CEMM, and that if the campaign performance metric of interest requires the vehicle to be operating over the land mass, the *failed* performance is by definition zero. The results from this example are: $\bar{G}_N^{CEMM}$=235 NM/hr, $\bar{G}_D^{CEMM}$=206 NM/hr, and $\bar{G}_F^{CEMM}$=0 NM/hr. Eqn. 4.8 is used to determine

[6] This assumption stems from those made in defining a Markov process, namely that the transition rate distribution is not time dependent. In the case where this does not apply, it is still possible to solve for the state probabilities through what is known as a *semi-Markov* process [69], where Eqn. 2.23 is composed of linear integral equations rather than ODEs.

the total campaign expected performance, E_G^{CEMM},

$$E_G^{CEMM} = \sum_{K=1}^{M^{CEMM}} \bar{G}_K^{CEMM} P_K^{CEMM} = 151\text{nm/hr} \tag{4.8}$$

and campaign expected availability is $E_A^{CEMM} = P_N^{CEMM} + P_D^{CEMM} = 65\%$. The above solutions allow derivation of several additional measures of performance, the mechanics of which may depend on specific campaign logistics. The total expected science distance covered over the 5-year campaign is 6.4 million mapping miles. This is determined by multiplying the expected campaign mapping rate by the 5-year time period, and accounting for science mile loss due to additional ingress/egress required for sortie aborts and losses. These are the only times in which there is not a vehicle over the continent. The probabilities of an abort or loss state from the SEMM is 1.8% and 2.9%, respectively, which can be used to estimate the total number of vehicles lost over the campaign. In this case, with an average sortie duration at a little less than 40 hours, of which half is spent over the land mass, 1378 sorties will be used to cover the 6.4 million miles. One can expect 25 sortie aborts and 40 vehicles to be lost. When integrated with an accurate vehicle model, the above methodology accurately represents campaign performance output and attrition as a function of component failure rates, vehicle static design variables, endurance, speed, and campaign architecture.

4.2.2 Optimization of System Availability

The final topic of this chapter moves from the *Point Design/DOE* block of computational analysis in Fig. 4-1 to that of *Optimization*. While the main focus of the research is design analysis, rather than optimization, in some cases a numerically optimal solution for system availability may be desired. This is necessary for determining a Pareto front through one of the optimization-based methods given in Section 4.1.6, or if the designer is solely interested in the absolute maximum attainable value of E_A.

A formal optimization statement for maximizing E_A (for $T_z = T$) is given in

Eqn. 4.9.

$$\begin{aligned} \textit{given} \quad & \text{parameters, } \mathbf{c} \\ & \text{transition rates, } \boldsymbol{\lambda^s} \\ \textit{minimize} \quad & -E_A(\mathbf{x},\mathbf{c}) = \sum_{G_K^s(\mathbf{x},\mathbf{c}) \geq W} -P_K^s(\boldsymbol{\lambda^s}) \\ s.t. \quad & \mathbf{h}(\mathbf{x},\mathbf{c}) = 0 \\ & \mathbf{g}(\mathbf{x},\mathbf{c}) \leq 0 \\ & x_{i,LB} \leq x_i \leq x_{i,UB} \quad i = 1,2,...,n_x \end{aligned} \tag{4.9}$$

where the inequality in the summation indicates that only those state probabilities corresponding to states with performance greater than or equal to W are summed.

This results in E_A being a piecewise constant function. To show this visually, the Gaussian function in Eqn. 4.10 was constructed and modified to model the performance of a multistate system with six failure modes (see Appendix D for more details on how this was accomplished).

$$\begin{aligned} G_K^s(\mathbf{x}) =& (1 - 0.4u_K^1(\mathbf{x}))^2 e^{-(0.4u_K^1(\mathbf{x}))^2 - (u_K^2(\mathbf{x})+1)^2} \\ & ... - 10(4u_K^1(\mathbf{x}) - 0.5u_K^2(\mathbf{x})^4) e^{-(0.4u_K^1(\mathbf{x}))^2 - u_K^2(\mathbf{x})^2} \\ & ... - e^{-(4u_K^1(\mathbf{x})-2)^2 - u_K^2(\mathbf{x})} - 0.3(0.8u_K^1(\mathbf{x}) + u_K^2(\mathbf{x})) \end{aligned} \tag{4.10}$$

where $\mathbf{x} = [x_1\ x_2]$. Figure 4-8 graphically shows the output space of this function for expected availability characterized by $G_K^s \geq 3.0$, evaluated for all sixty-four states.

Gradient-based optimization algorithms will have extreme difficulty forming search paths through the performance space in Fig. 4-8 and will exhibit very poor convergence, if they converge at all. There are heuristic methods capable of searching such non-smooth functions, but they are generally less efficient than the gradient methods, and do not provide the same valuable sensitivity information to the designer.

Fortunately, there are certain characteristics of the availability function that enable one to adapt the problem for a gradient-based solution. First, improvement of availability directly requires increasing performance in the off-nominal states to a

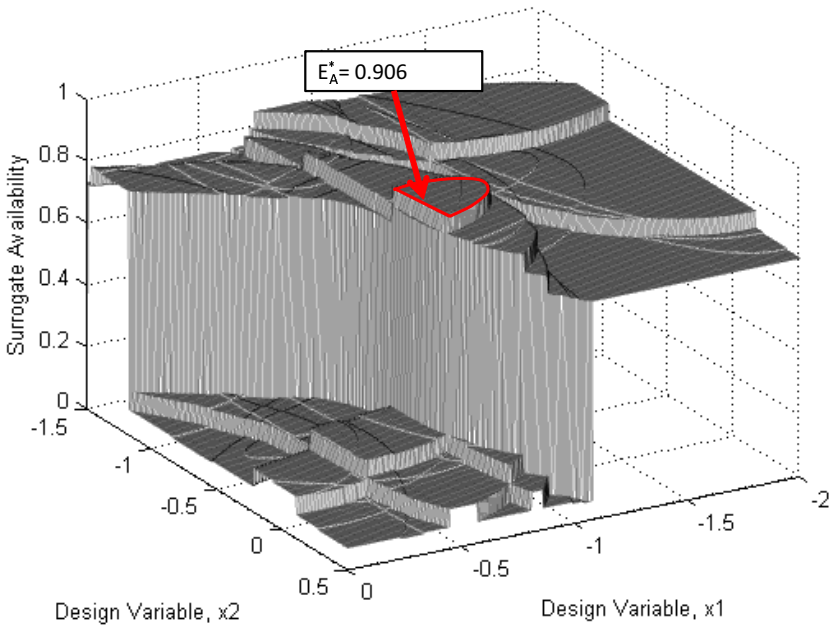

Figure 4-8: Plot of E_A for Gaussian test function

value above the threshold given by $G_K^s(\mathbf{x}, \mathbf{c}) \geq W$. This means that, at any point other than a local optimum, reducing the performance deficiency between the current design point and the next jump in E_A requires that the performance in at least one of these off-nominal states must increase. Secondly, the information required to decide which off-nominal state will provide the greatest jump in E_A is available in the form of the state probabilities, $\breve{\mathbf{P}}^{\mathbf{s}}$. Finally, improvements in state performance past that required to meet the performance threshold result in no further improvement in availability. A continuously smooth function that captures the above characteristics should enable a gradient-based algorithm to converge to an optimum (at least locally).

For this, one may define $\breve{\mathbf{D}}^{\mathbf{s}}$ as the set of state performance deficiencies, composed of D_K^s, given in Eqn. 4.11.

$$D_K^s = W - G_K^s \tag{4.11}$$

Next, an inverse exponential function is proposed in Eqn. 4.12, weighted by P_K^s, and

modified such that improvements in G_K^s beyond W are non-influential.

$$\tilde{S}_{E_A} = \sum_{K=1}^{M} P_K^s B \quad \text{where } B = \frac{b}{b^{(max[1+D_K^s,1])}} \tag{4.12}$$

The term B has the effect of modeling transitions between levels of availability, and the exponent base, b, determines the degree of smoothing between those transitions. Figure 4-9 shows B for several different exponent bases.

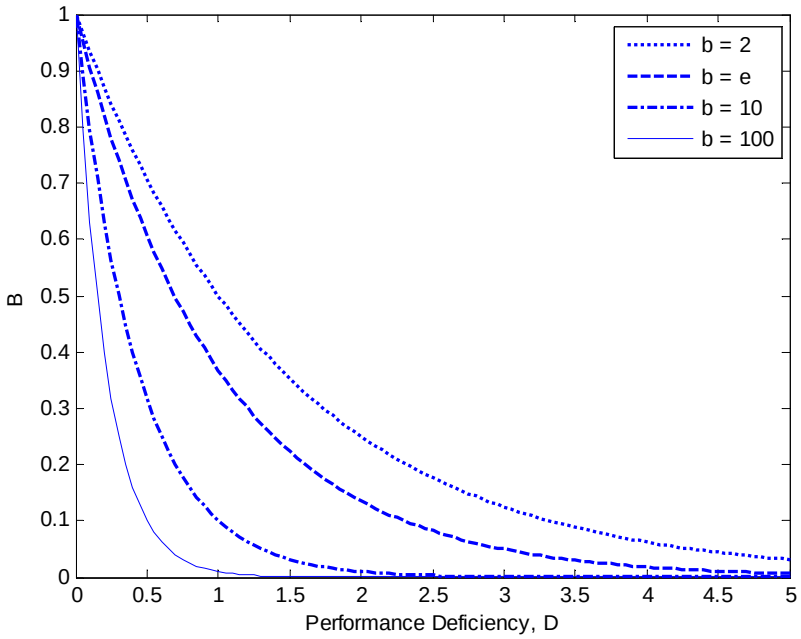

Figure 4-9: Plot of B for several different exponent bases, b

Equation 4.12 may be thought of as a surrogate representation of E_A.[7] It is a function of the same variables and maintains the same three characteristics described

[7]Although arrived at through different processes, Eqn. 4.12 is in some ways similar to the Kreisselmeier-Steinhauser (KS) function, which uses a logarithmic (base e) summation to aggregate constraints into a single objective for gradient-based optimization [63]. Both use a type of 'shaping' or 'draw-down' factor (such as b), with the distinct difference that Eqn. 4.12 approaches the exact surface of E_A as b goes to infinity, while the KS function approaches only the value of a maximum constraint as its 'draw-down' factor approaches infinity. Thus, the surrogate E_A accurately models each of the individual aggregated elements, while the KS function only models one (the max constraint) at any given point in the design space. Logarithmic functions for the surrogate E_A were also tested but a solution could not be found that was both bounded by the interval [0,1] and distributive such that P_K^s could be used as a multiplier.

above. It smooths the availability function, depending on b, and may be used within a gradient-based optimization routine. The degree of smoothness is left up to the designer, but general good practice is to run one optimization across the entire design space with a relatively low value of b. This corresponds to gently sloping transitions between E_A levels and should result in a solution near the region of highest E_A. This is due to the fact that the surrogate E_A function effectively models the general *shape* of the actual E_A even when its approximated value at any give point is not highly accurate (note the comparison of surfaces between Figs. 4-10 and 4-11). Once this solution is found, b may be increased and a second optimization run for more accurate results.

Figures 4-10 and 4-11 show plots of $\tilde{S}_{E_A}$ for the Gaussian problem, with two different values of b. Even though the plots are smoothed and might not fully match the real E_A function values, the region of optimal design in Fig. 4-8 encompasses the optimal design points above, and their optimal values are within 0.3%. Additionally, the Gaussian functions in this example are extremely non-linear (purposefully), and many functions would require much less smoothing.

Figure 4-12 shows a plot of the Pareto front for $\tilde{S}_{E_A}$ vs. E_G, with the exact solution for E_A shown on the rightmost y-axis. The front was successfully calculated using the Normal Boundary Intersect (NBI) method, with $b = 100$.

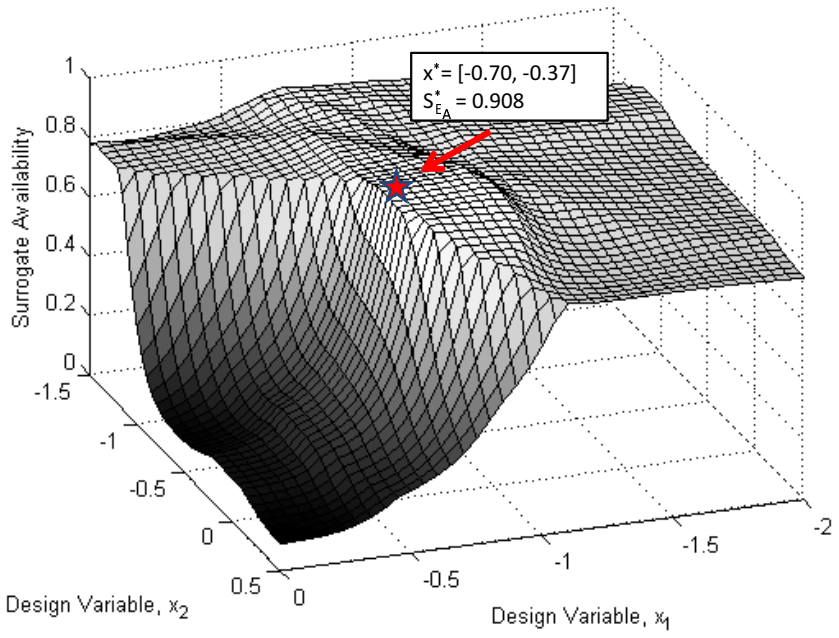

Figure 4-10: Output space of surrogate availability function, $\tilde{S}_{E_A}$, $b = 100$

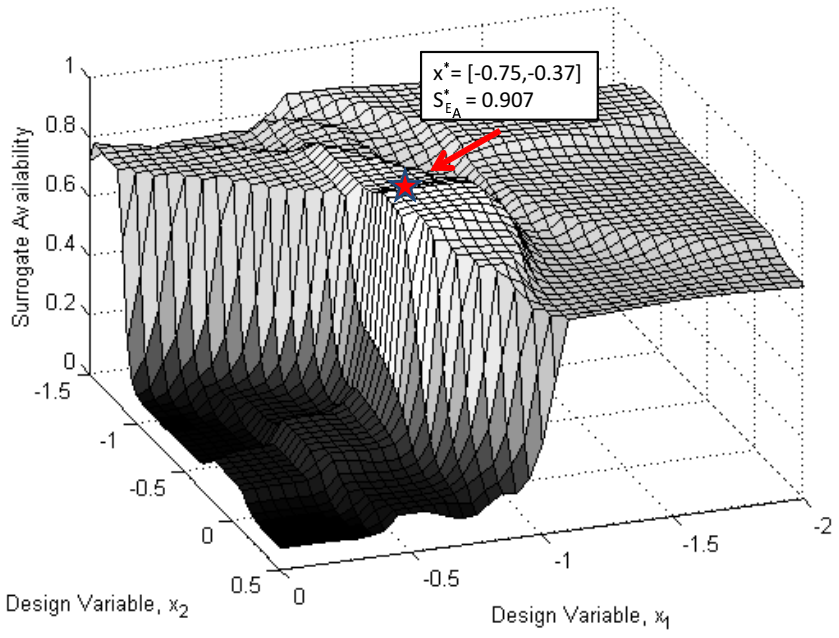

Figure 4-11: Output space of surrogate availability function, $\tilde{S}_{E_A}$, $b = 1000$

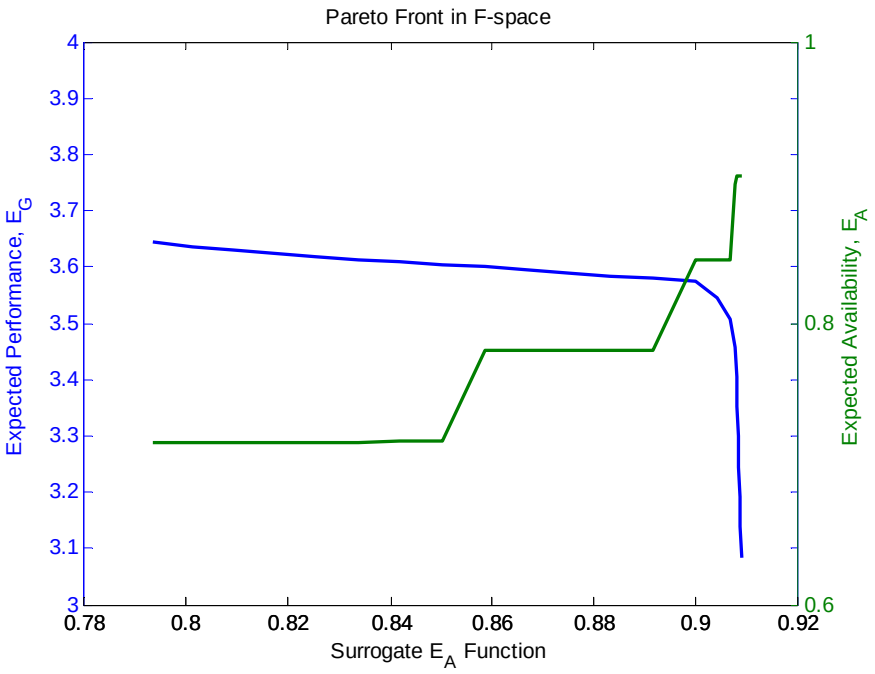

Figure 4-12: Pareto front of $\tilde{S}_{E_A}$ vs. E_G, showing exact E_A

4.3 Chapter Summary

This chapter encompassed several methodological contributions of the thesis, setting the framework for analysis of the case studies in Chapters 5 and 6. A generalized methodology for early-phase multistate analysis and design was laid out, moving preliminary analysis of failure modes to the front of the design cycle and integrating Markov state analysis into the computational design loop. Several means for visualizing the multistate design space were outlined, with specific examples of each occurring in case studies throughout the thesis. Where areas from the Super King Air study suggested further attention, supporting methods were developed and placed within the proper context of the above framework.

Specific contributions of this chapter include:

- A generalized methodology for multistate analysis and design, shown in Fig. 4-1. This is an integrated multistate design approach, with novel attributes in that

it:

  - formulates responses in system expected performance and availability as functions of static design variables and component failure rates, accounting for control design variables where appropriate
  - integrates Markov state analysis into the early-phase computational design loop for complex systems, and
  - moves preliminary analysis of failure modes and effects to the front of the design cycle.

- A multilayer extension of Markov analysis, for translating single sortie component and vehicle level availability to multiple sortie mission campaign robustness. This demonstrates how the multistate design of shorter duration vehicles can directly affect longer term operational measures such as mission availability, attrition, and sortie aborts.

- The development and demonstration of a "surrogate" function for system availability. The function is adjustable for differing degrees of smoothness and allows the otherwise discrete metric to be optimized via gradient-based optimization algorithms (Fig 4-12).

Chapter 5

Case Study - II: Long Endurance Unmanned Aerial Vehicle

This chapter applies the methodologies formalized in Chapter 4 to the design and analysis of a long endurance unmanned aerial vehicle. Case requirements come from a representative UAV ice surveillance mission over Antarctica, under consideration at NASA as a complement to the current IceBridge campaign, an operation currently executed through a series of missions flown by a Douglas DC-8 and a Lockheed P-3 Orion. The analysis is performed for two scenarios. *Scenario I* is the case of a mission lasting three months time aloft, which demonstrates the effectiveness of the approach to an ultra long duration vehicle. In this scenario, an initial design point is chosen from a study of long endurance UAV technologies recently performed at NASA. This aircraft is optimized for nominal performance and compared to design spaces for the same aircraft designed for multistate performance through: a) variation of only its up-front static static design variables, b) variation of only its component failure rates, and c) combined multistate approach varying both. *Scenario II* is the case of a one-to-two day duration vehicle, involved in a 5-year multi-sortie campaign requiring omnipresence over the continent. This demonstrates application of the approach to shorter duration systems involved in ultra long duration campaigns where coverage is provided by multiple vehicles. In this scenario, the design space is systematically sampled via a Design of Experiments technique, allowing examination of the main

effects of design variables on campaign level performance metrics.

Results clearly showed three distinct design spaces for the ultra long endurance aircraft designed through a), b), and c) above. The combined multistate approach demonstrated improvement in system availability of 11%, at a 3% lower cost, when compared to the baseline aircraft designed for nominal performance. Variation of component failure rates or static design variables alone showed improvement of only 6.5%. Furthermore, when considering multiple objectives of system availability, expected performance, nominal performance, and cost, the combined approach was still able to achieve an 11% improvement in availability, with only a 4.5% decrease in nominal performance, albeit at a small 6% increase in aircraft flyaway cost. Finally, results from the multi-sortie campaign analysis demonstrated that lower level static design variables have a clear and measurable effect on campaign level performance, such as availability, number of failed sorties, and vehicles lost. The effects of these variables do not necessarily align with the effects they have on nominal performance.

The next several sections follow the steps laid out in the multistate analysis and design process shown in Fig. 4-1, of Chapter 4.

5.1 Step 1 - Requirements Definition and Concept of Operations

Requirements for this case study are derived from a representative UAV mission to collect mapping data over the ice sheets of Antarctica. This mission began several years ago with the launch of NASA's Ice, Cloud, and Land Elevation Satellite (ICESat) in 2003. Data collected by the satellite are providing a long duration time-history of ice sheet mass balance, as well as important information concerning clouds and aerosol height in the observation area. In 2009, ICESat stopped collecting data when the last of three lasers on the satellite's Geoscience Laser Altimeter System (GLAS) ceased emitting light [80]. After several attempts to restart the lasers, the satellite was decommissioned in August of 2010. The launch of a replacement system is not

planned until 2015.

NASA is currently attempting to cover this 6-year gap through a series of flights using a Douglas DC-8 and a Lockheed P-3 Orion [79]. While this solution is capable of minimally covering the transitional period until 2015, data coverage is sporadic and requires the use of expensive resources and aircrews. This has motivated NASA into considering other methods, such as long endurance UAVs, to provide much better data coverage for future gaps and perhaps eventually replace satellite operations altogether.

The analysis in this chapter begins from results of a preliminary study at NASA, which suggests that a favorable base of operations for a long-endurance UAV campaign to Antarctica is from the Falkland Islands off the southern tip of South America [103]. The original intent of the campaign was to match the data point density of that obtained by ICESat. However, an alternative ground track based on a grid pattern was found to be sufficient in that it met the continental edge point density of the satellite while being much more efficient from the standpoint of an aircraft. Based on this ground track and the required edge point density, approximately 100,000 total nautical miles (nm) over-continent are required to complete one survey of the land mass. The average distance to the area of operations from the chosen base location is 2100 nm. A simplified diagram of the survey area, including the base of operations is shown in Fig. 5-1.

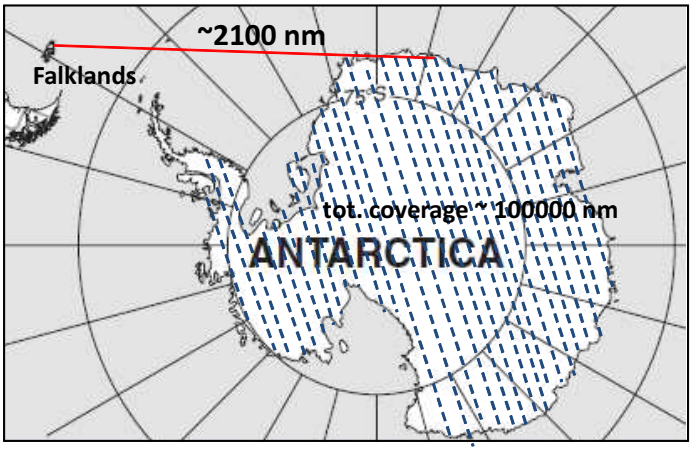

Figure 5-1: Antarctica survey area and pattern

Operational requirements for the air vehicle are partially driven by the environmental conditions necessary for mapping the ice sheets and partially by the vehicle's concept of operations. Wind data averages over Antarctica indicate that minimum winds aloft velocity occurs between altitudes of 45k to 55k ft, and a much smaller altitude band at 60k ft ($\pm$ 500 ft). Although the 60k ft band is more desirable from an efficiency standpoint, the wind speed rises rapidly outside of this 1000 ft band. Even with the uncertainties involved in nominal operations, such small tolerances are undesirable, and exceedingly more so when considering operation in off-nominal states. Therefore, the target altitude in nominal operations is set at 50k ft.

In the first concept of operations, referred to throughout the remainder of the chapter as *Scenario I*, the ice surveillance mission is performed by a single ultra long endurance vehicle over the three months of Antarctic summer. This represents a mission carried out with what NASA considers the nearest-horizon technology for ultra long endurance aircraft, namely a liquid-hydrogen proton exchange membrane (LH_2-PEM) fuel cell, here augmented with solar-regeneration to extend endurance during the sun-intense summer. More on this may be found in an extensive study published by NASA in [83].

The second concept of operations (*Scenario II*) represents a multiple sortie campaign to continuously map the ice sheets over a time period of 5-years. The aircraft involved have endurance on the order of 40+ hours, which is at the high end of current in-production UAVs utilizing internal combustion engines [2]. This scenario maintains omnipresence over the continent, such that as Aircraft 1, shown in Fig. 5-2, comes to the end of its surveillance period, Aircraft 2 arrives over the operations area. On average, the ingress/egress distance is about 2100 nm, allowing fully functional air vehicles to remain over continent for approximately 20 hrs.

Table 5.1 presents a summary of the requirements for both *Scenarios I* and *II*. Some of the performance minimums are relaxed for the *Scenario I* aircraft, due to the more demanding endurance requirement. However, there still exist certain hard limits that stem from the environment. For example, the 95 kt minimum airspeed is to allow the aircraft enough maneuvering airspeed to overcome expected winds aloft

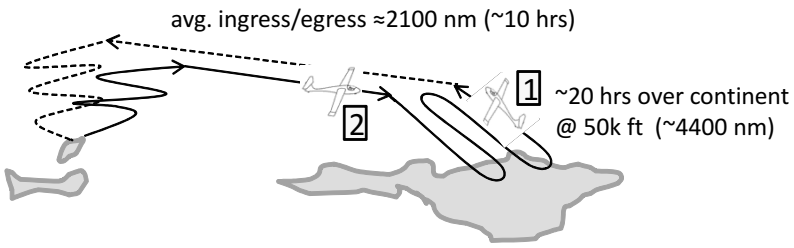

Figure 5-2: Multi-sortie campaign routing for the long endurance UAV

in the specified altitude band. For further explanation of the differences in velocity requirements, see the footnote in Section 5.5.2.

Scenario II requires at least five vehicles in order to provide enough downtime for maintenance. This means that two are in the air and three on the ground at any given time, with each aircraft having ~60 hours on the ground between flights. Results from the campaign analysis provide more detail on the actual number of aircraft needed, as a result of attrition and mission aborts.

Table 5.1: Requirements summary for the long endurance UAV

Requirement:	**Scenario I: Single Sortie Mission**	**Scenario II: Multiple Sortie Campaign**
Nominal Endurance	$\geq$ 90 days	$\geq$ 40 hrs
Nominal Cruise Altitude	50k ft	50k ft
Min. Cruise Altitude*	$\geq$ 35k ft	$\geq$ 35k ft
Min. Cruise Airspeed	$\geq$ 95 kts @ $h_{cr,min}$	$\geq$ 175 kts @ $h_{cr,min}$
Min. Rate of Climb	$\geq$ 30 fpm @ $h_{cr,min}$	$\geq$ 50 fpm @ $h_{cr,min}$
Payload	200 lbs	200 lbs
Number of Vehicles	1	$\geq$ 5

* Requirements that don't specify *nominal* are applicable to all states.

5.2 Step 2 - Preliminary Analysis of Failure Modes

The preliminary failure modes analysis begins from an extensive Department of Defense (DoD) study covering worldwide UAV operations from 1986 to 2003 [84]. The study encompasses data from over 200,000 hours of flight on aircraft built by competing manufacturers, operated by militaries of several different countries (primarily the

U.S. and Israel), and covering a wide variety of mission profiles, both autonomous and remotely piloted. Additionally, it makes comparisons between traditional manned and unmanned aircraft, and between U.S. and foreign aircraft. Two notable conclusions arise from these comparisons. First, "U.S. and foreign UAVs (Israeli) share virtually identical percentages of failure modes," as shown in Figs. 5-3 and 5-4.

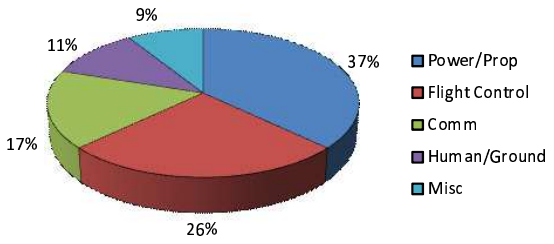

Figure 5-3: Average sources of system failures for U.S. military UAV fleet (based on 100,000 hrs) [84]

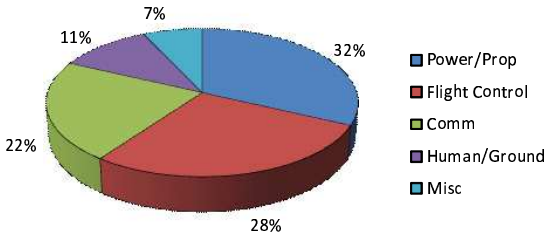

Figure 5-4: Average sources of system failures for Israeli military UAV fleet (based on 100,000 hrs) [84]

Secondly, "the proportions of human error-induced mishaps are nearly reversed between UAVs and the aggregate of manned aircraft, i.e., human error is the primary cause of roughly 85% of manned mishaps, but only 17% of unmanned ones." Thus, the above provides a good indication of where an early-phase multistate design analysis should concentrate, and suggests that the overwhelming majority of failure modes occur as a result of system failures rather than human error.

Concentrating on the propulsion and flight control systems, Table 5.2 gives the relevant information for a preliminary Failure Mode and Effect Analysis on a four-engine UAV. The components are listed in rank order from the most critical to least critical failure modes. The elevator failure is placed first due to the fact that its failure would be extremely difficult to trim with thrust and would leave little to no margin for maneuvering. Loss of roll control through ailerons, on the other hand, would more easily be compensated for through use of the rudder. Similarly, the failure of the outboard engine is more critical than the inboard, due to the larger thrust moments generated.

Table 5.2: FMEA data summary*

Component	Function	Failure Mode	Effect	Failure Rate [1/hr]	Trim Mechanism
elevator	pitch control	failed neutral	loss in pitch ctrl	1/10000	thrust
engine 2	provide thrust	shutdown	loss in thrust	1/100000	rudder/aileron
engine 1	provide thrust	shutdown	loss in thrust	1/100000	rudder/aileron
aileron	roll control	failed neutral	loss in roll ctrl	1/10000	rudder
rudder	yaw control	failed neutral	loss in yaw ctrl	1/10000	aileron
engine cowl/ gear door/ access panel	prevents rise in drag	stuck/ blown open	increase in parasite drag	1/5000	rudder/aileron

* Listed in order of most critical component failures.

The failure rates are based on data taken from [84]. Although the report is somewhat dated, there are to date no better data available. The failure rates of flight controls (ailerons, elevators, rudder) taken from the report are on the order of 1/5000hrs. In Table 5.2, they have been improved to reflect advancement in the past eight years. These are still far below the values used in the Super King Air analysis of Chapter 2, but that was a near purely mechanical system with direct interface to the pilot. The flight control system of a UAV is significantly more complex, as is reflected in the data of [84]. Most industrial endeavors would have very accurate failure rate data at hand, and this would likely be classified as sensitive information. For purposes of an early-phase multistate analysis, finding the design drivers of availability and expected performance is the objective, thus the specific value of state transition rates is less important that their relative magnitude. In this sense, the data from the DoD report are considered more than sufficient.

Note that each of the FMEA steps given in Section 4.1.2, of Chapter 4, are addressed in the above table, with the exception of the failures' *causes*. While subtle, this fact highlights an important aspect of the methodology. Namely, it does not attempt to *prevent* failures from occurring, outside of perhaps increasing an MTBF.

Therefore, the determination of the failure's cause is not the focus, but rather *the mitigation of its effect*, given that it occurs and does so at a predictable rate.

5.3 Step 3 - System and Performance Classification

Step 3 of the methodology requires classifying the system according to its level of analysis, and determining whether the performance metric is *dynamic* or *static*. In this particular case study, results will be given for both levels of analysis, the UAV system modeled at the single *vehicle* level (*Scenario I*), and at the multiple sortie *campaign* level (*Scenario II*). This demonstrates the differences between the two, and shows how the procedures from the lower level may be integrated into those of the higher.

The performance metric of interest is, naturally, endurance. While possible to run an entire flight mission using the same simulation routines and methods as in the case study of Chapter 3, the endurance is less affected by *dynamic* influences over the long flight duration and is readily modeled through the *static*, physics-based analytic equations in the next section. For this reason, the control variables, $\mathbf{r}$, are not used in the following analyses. The analytic equations assume the system is controllable, as is often done in conceptual level design. This process allows a more rapid evaluation of system states and thus facilitates the timely analysis of larger design spaces.

5.4 Step 4 - Modeling and Simulation

This step is divided into two subsections. The first subsection describes the analytical methods used in calculating elements of the multistate performance set, $\breve{\mathbf{G}}^{\mathbf{s}}$, for the long endurance UAV. The second presents the cost model used in determining aircraft flyaway cost, a useful metric in comparing the relative expense of changes in component failure rates to changes in static design variables. Step 4 is the same for both *Scenario I* and *Scenario II*.

5.4.1 Multistate Performance Model

The aircraft model disciplines follow closely those of the Super King Air in Chapter 2. The exception is that the UAV multistate performance model computes endurance through iterated analysis of analytic equations, rather than simulation. This follows the general design flow depicted in Fig. 5-5, and is described in greater detail below.

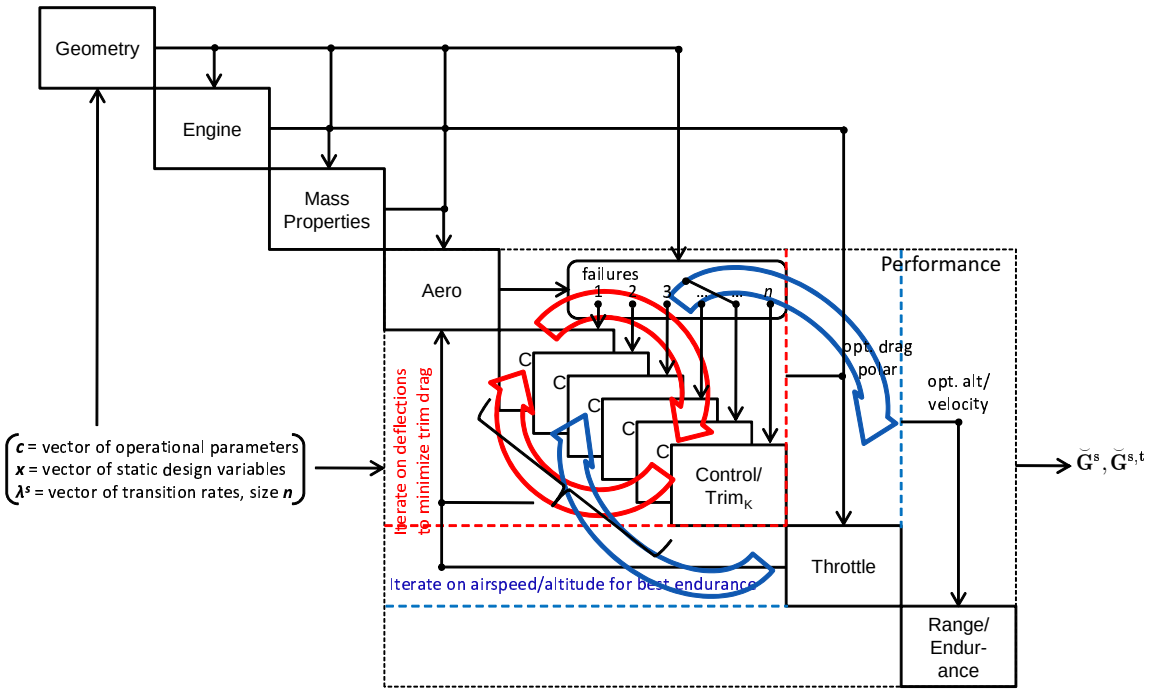

Figure 5-5: Design flow for ultra long endurance UAV

Endurance is calculated from Eqn. 5.1, which is the Breguet range equation [25] divided by the aircraft's cruise velocity.

$$G_K^s = Endurance_K = \frac{\eta_{prop}}{V_{cr,K}c}(\frac{C_L}{C_D})_K ln(\frac{W_1}{W_2}) \tag{5.1}$$

Here, η_{prop} is the propeller efficiency, c is power specific energy consumption, and $\frac{W_1}{W_2}$ is the ratio of the aircraft's weight at the beginning of the cruise segment over its weight at the end. The $V_{cr,K}$ and $(\frac{C_L}{C_D})_K$ terms are the aircraft's state specific cruise velocity and lift-to-drag ratio, respectively. Given the desired Mach number at cruise, the performance analysis iterates on altitude until induced drag is equal to

three times the parasite drag, or,

$$\frac{C_{L,K}^2}{\pi e \cancel{R}} = 3C_{D_o,K} \tag{5.2}$$

This is the level-flight condition for minimum power required in a propeller driven aircraft. In the case of an aircraft consuming combustible fuel, the analysis also accounts for decreasing weight, resulting in a cruise-climb to maintain the conditions of Eqn. 5.2.[1] Additionally, the analysis accounts for the case of a state with insufficient power at altitude, by reducing altitude and allowing Mach number to vary until min-power conditions are maintainable. The iterative processes are shown in Fig. 5-6.

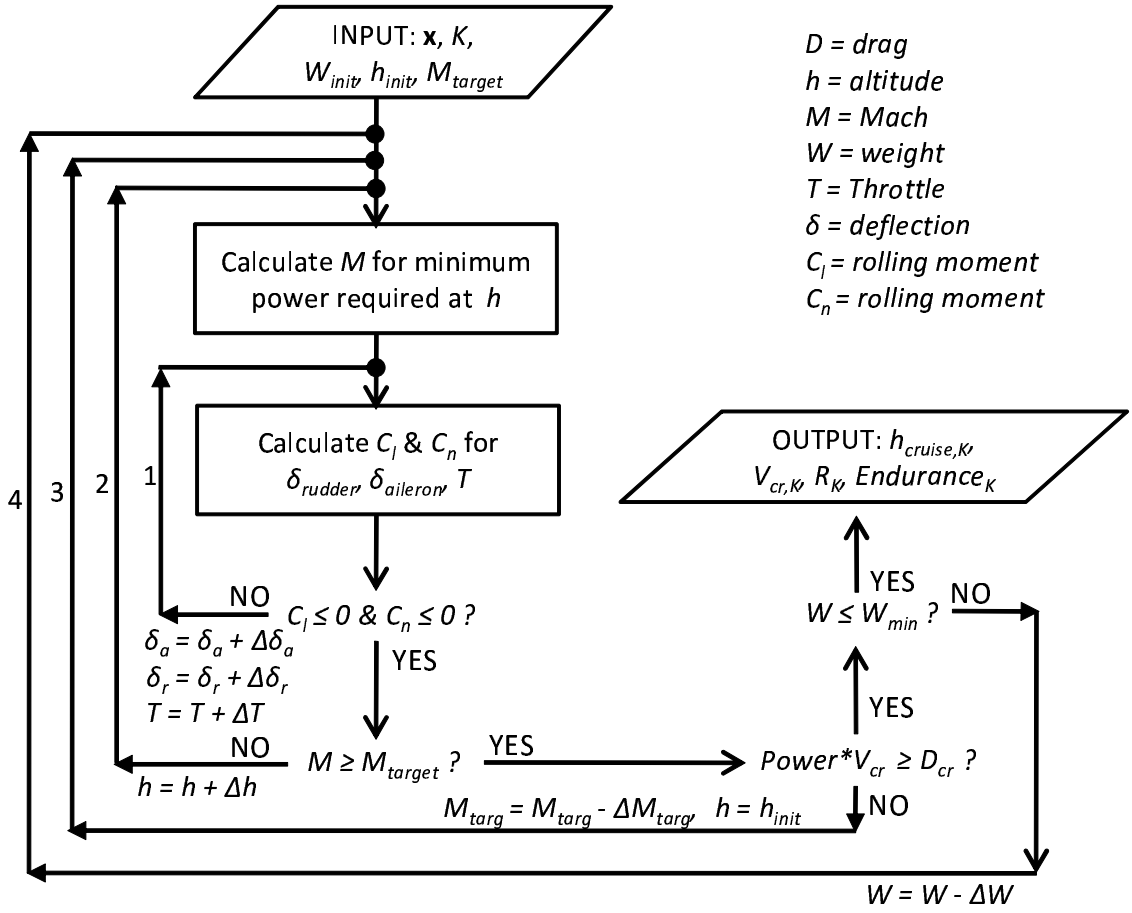

Figure 5-6: Iterative processes in UAV performance model

[1]In level, unaccelerated flight, the lift coefficient, C_L, varies directly with aircraft weight. Therefore, to maintain the optimum cruise velocity for minimum power required, an aircraft must climb as it burns off fuel.

The trim algorithms developed for the innermost loop (1) of Fig. 5-6 are fairly sophisticated and were derived from work under a 1998 NASA grant to calculate engine-out stability derivatives [51]. These methods were extended to include additional control surface failures, in support of this research, using analytic stability derivative equations developed from the 6-DOF equations of motion, as found in [90]. They are prerequisite to the outer loop processes (2,3,4) of Fig. 5-6 in that each state, K, must be trimmed for steady, level flight at each altitude and airspeed iteration. This is accomplished through the trim routine that takes as input the aircraft design vector, failure mode, and flight conditions, and returns the state specific control deflections required to drive the roll and yaw moments to zero. It also returns the corresponding state specific drag polar for that particular altitude and airspeed iteration, which is then used to calculate the state specific endurance, range, and other important performance outputs.[2] Appendix E provides more detail on the above methods, including sample output of the state performances.

5.4.2 Cost Model

The cost model is developed from three separate sources. The first of these is the RAND Corporation's Development and Procurement Cost of Aircraft model (DAPCA IV), as found in [86]. The DAPCA IV model uses cost estimating relationships based on historical data and aircraft physical properties to estimate various costs including engineering, tooling, manufacturing, and quality control, among others. In general, the DAPCA related cost data presented in Section 5.6 follows the functional dependency given in Eqn. 5.3:

$$\text{Cost} \uparrow \approx f(S \uparrow, \mathcal{R} \uparrow, \Lambda \uparrow, \lambda \uparrow, P_{max} \uparrow, N_{engines} \uparrow, W_{empty} \uparrow) \tag{5.3}$$

Several updates have been made to the above model over the years, including those to more accurately predict costs for unmanned aerial vehicles, using more recent UAV

[2] Although these iterative processes are quite involved, evaluation of 64 states for a single design point takes only about 30 seconds on a high-end computer, and is very robust. All of the design points attempted in this study converged without problem.

cost data found in [57] and [109]. Some results using these updates are published in [2].

The DAPCA IV model estimates cost for the basic air vehicle. The second two sources for the overall cost model involve estimating the dollar cost of changes to component failure rates. The Charles Stark Draper Laboratory, a sponsor of this research, recently led a study to relate similar subsystem components of differing complexity and MTBF to their respective costs [112]. While the focus of the study was on space systems, the MTBF vs. cost data involved a more general sampling of avionics and control hardware for aerospace systems. Without specifying the exact proprietary costs or mean-times-between-failure, the study findings are shown in the trend plots of Fig. 5-7.

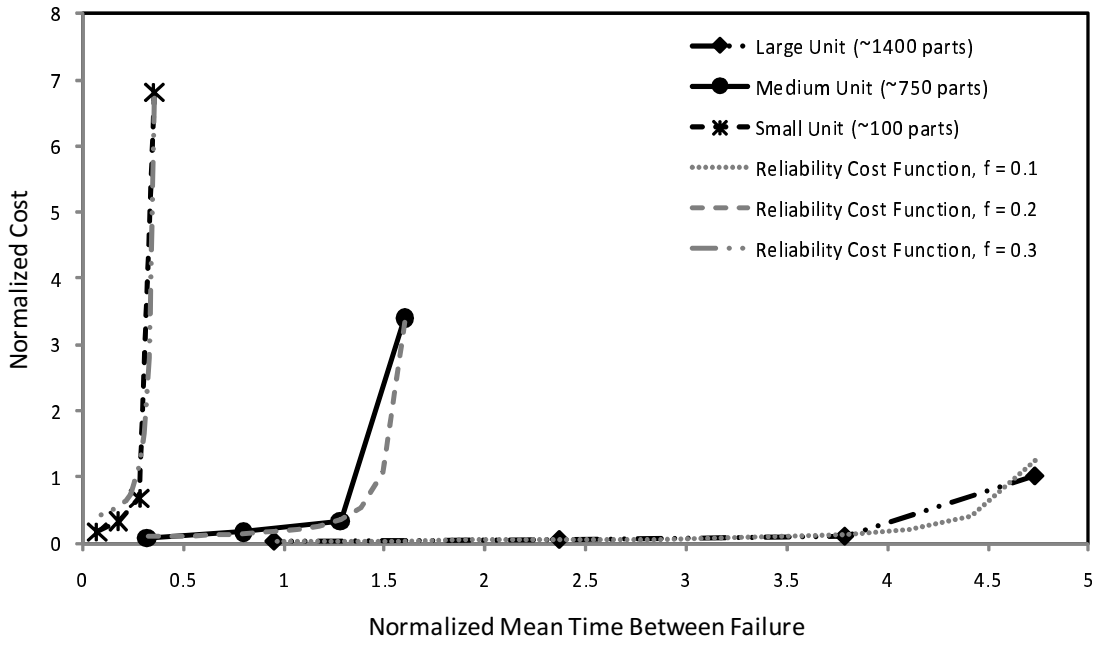

Figure 5-7: Comparison of reliability costs for various components, normalized by averaged cost and MTBF of Medium Unit

Figure 5-7 also depicts independent estimates from the third source [75] as the reliability cost functions next to the Draper data. This cost function estimates changes in component cost as a direct function of reliability, rather then MTBF, and is given

as Eqn. 5.4.

$$C(R) = Be^{(1-f)\frac{R-R_{min}}{R_{max}-R}} \tag{5.4}$$

Here, $C(R)$ is the cost function, f is a cost index of improving the component's reliability relative to other system components, R_{min} and R_{max} are the minimum and maximum reliabilities feasible for the current component state-of-the-art, and B is the baseline component cost. These f-adjusted functions are plotted alongside the Draper data of Fig. 5-7, with reliability, R, replaced by MTBF. They demonstrate the applicability of the cost function in estimating the current sample-derived data. The bow-shaped nature of the cost curves stems from the fact that, beyond a certain point, technological limits mean that improving a component's reliability (or MTBF) becomes asymptotically more expensive. As both data sets show, this trend increases with increasing component complexity.

Due to the agreement between the above trends and cost estimates, Eqn. 5.4 is used in estimating the cost variations of components with respect to MTBF in the analyses of Section 5.6. The baseline cost value is chosen as the initial subsystem cost output from the DAPCA IV model, with component MTBF's as shown in Table 5.2. This is then adjusted by Eqn. 5.4, according to the design-driven increase or decrease in MTBF. The engines are modeled as high complexity (large unit) components, the flight controls as moderate complexity (medium unit) components, and the access panel/cowling as a low complexity (small unit) component.

5.5 Step 5 - Markov Analysis

The previous step established the multistate modeling and simulation routines necessary for calculating the UAV's state performance set, $\breve{\mathbf{G}}^{\mathbf{s}}$, along with an estimate of the corresponding cost for achieving that performance set. The members of $\breve{\mathbf{G}}^{\mathbf{s}}$ are $G_K^s(\mathbf{x}, \mathbf{c})$. Step 5 now uses Markov analysis to calculate the probabilities, $P_K^s(\boldsymbol{\lambda}^{\boldsymbol{s}})$ belonging the UAV's state probability set, $\breve{\mathbf{P}}^{\mathbf{s}}$. In the case of the campaign in *Scenario II*, the probabilities are also dependent on the campaign "repair" rates, $\boldsymbol{\mu}^{\boldsymbol{CEMM}}$. Both scenarios are described in more detail below.

5.5.1 Scenario I: Single Sortie Mission

To this point, the Markov analysis technique for a single vehicle has been well developed in Section 2.3.2, of Chapter 2, and demonstrated in Section 3.2, of Chapter 3. The mechanics of the process remain the same here, but with a much larger number of states. Given a total of $n = 6$ elements, the size of $\breve{\mathbf{G}}^{\mathbf{s}}$ and $\breve{\mathbf{P}}^{\mathbf{s}}$ is $M = 2^n = 64$. Figure 5-8 is the Markov chain for States 1 through 22, truncated to the first two levels of failure for efficiency of space.

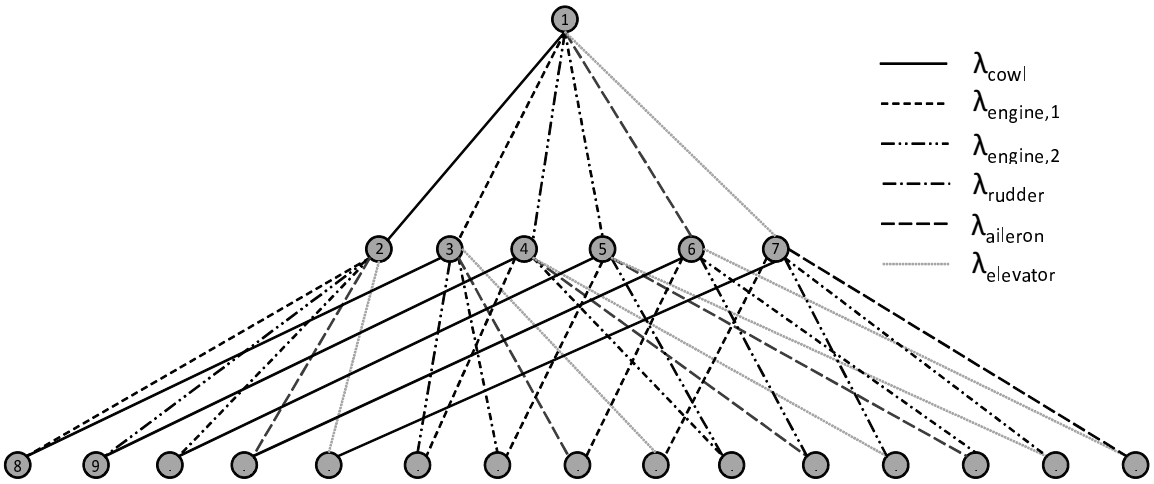

Figure 5-8: Markov chain for UAV (first two levels of failure)

The values of $\boldsymbol{\lambda}^{\boldsymbol{s}} = [\lambda_{cowl}, \lambda_{engine,1}, \lambda_{engine,2}, \lambda_{rudder}, \lambda_{aileron}, \lambda_{elevator}]$ are those in Table 5.2, and the model is evaluated over a time, T, equal to the aircraft's design endurance (∼three months). The states falling into the *acceptable* performance category are those with minimum cruise velocity greater than or equal to 95 knots, which is high enough above the maximum expected winds aloft to deliver sufficient ground speed in the target altitude band.

5.5.2 Scenario II: Multiple Sortie Campaign

The second scenario begins with the Markov model in Fig. 5-8, but for the UAV designed under the requirement of a 40-hour nominal flight duration. This model is termed the Vehicle Markov Model (VMM) in the multilayer analysis, and leads

development of the Sortie Equivalent Markov Model (SEMM) and the Campaign Equivalent Markov Model (CEMM) further downstream. The analysis procedure follows that of the example described in Section 4.2.1, but with many more states and design points.

As mentioned in Chapter 4, multiple sortie campaign analysis is possible when the campaign level metric of interest has direct roots in the performance output of the vehicle system. In the case of *Scenario II*, the campaign performance objective is the Science Mile Accumulation Rate (SMAR), which is determined by the cruise velocity of the individual air vehicles. From the campaign perspective, there are four categories of performance into which the vehicle output may fall, instead of just two. These are defined for *Scenario II* as:

- Nominal: $V_{cr} \geq (W_{min,N} = 215)$
- Degraded: $(W_{min,D} = 175) \leq V_{cr} < (W_{min,N} = 215)$
- Abort: $(W_{min,A} = 90) \leq V_{min}$ & $V_{cr} < (W_{min,D} = 175)$
- Loss: $V_{min} < (W_{min,A} = 90)$

The division point between *acceptable* and *unacceptable* states in *Scenario I* was determined by the cruise speed required to continue performing the mission at altitude. This corresponds to the division between the *degraded* and *abort* categories in *Scenario II*.[3] *Nominal* performance occurs when the aircraft is (near) fully functional and may include states in which a failure does not significantly affect performance. This corresponds to the highest rate of mapping coverage. *Degraded* includes states with less than nominal airspeed but higher than the stall speed at the bottom of the required altitude band. Finally, the vehicle is lost when its maximum velocity at sea level falls below its approximate stall velocity of 90 knots.

The fact that the VMM state performances, G_K^{VMM}, change with each variation in the design vector, $\mathbf{x}$, requires that the summing of probabilities, P_K^{SEMM}, into their respective SEMM performance bins (reference Eqns. 4.3 - 4.6, Chapter 4) be

[3]The velocity magnitudes are different (175 knots in *Scenario I* vs. 95 knots in *Scenario II*) due to the different sized aircraft. The 40-hour aircraft has a higher cruise speed and smaller wing area. It therefore has a significantly higher stall speed at the bottom of the required altitude band than the three month aircraft.

performed for each design point. To do so robustly, for a generalized number of states and performances, required the development of an involved sorting and summing algorithm, the code for which is provided in Appendix C. Numerical results for the SEMM and CEMM models are given in Section 5.6.2.

5.6 Step 6 - Analysis and Visualization of Results

The Super King Air case study in Chapter 3 demonstrated the use of sensitivity derivatives in determining relative effects of design variables and component failure rates on multistate performance metrics. The presentation of results in the following subsections takes a more global look at the design space, through the DOE and Pareto analysis techniques listed in Step 6 of Fig. 4-1. In the case of *Scenario I*, visualization occurs through a multi-objective analysis of Pareto non-dominated points, filtered from a design space generated via Latin-hypercube spacing. This demonstrates how the designer may visually choose preferable designs from the multi-objective design space, and further refine through gradient-based optimization of availability using the surrogate function introduced in Section 4.2.2, Chapter 4. In the case of *Scenario II*, a DOE analysis is performed by sampling the design space through an orthogonal array. Since the objective is to demonstrate the translation of vehicle level metrics to the campaign level, the *Scenario II* analysis stops short of determining an overall superior design, but examines instead the main effects of design variables on campaign availability and the number of sorties failed and vehicles lost.

Each of the UAV's in *Scenarios I* and *II* was first sized for nominal requirements, as a starting baseline for entry into the multistate analysis and design framework. In the case of *Scenario I*, this aircraft was taken from a representative example in the NASA UAV study of [83]. The *Scenario II* aircraft comes from a shorter duration UAV study in [2]. In both cases, the representative aircraft was then sized for scenario-specific nominal performance requirements using the conceptual-level aircraft design program described in [2]. This aircraft was used as the baseline.

Table 5.3 shows the resulting baseline aircraft design vectors, along with their

transition rates, $\boldsymbol{\lambda}^{\boldsymbol{s}}$. Upper and lower design bounds used in the following subsections appear as **ub** and **lb**. These are, in general, ±30% of the baseline values.

Table 5.3: Baseline UAV static design vector and transition rates

	Scenario I: Single Sortie Mission			**Scenario II: Multiple Sortie Campaign**		
Var	**lb**	**bsln**	**ub**	**lb**	**bsln**	**ub**
S [ft^2]	1873	2677	3480	351	501	652
b [ft]	182	260	338	79	112	146
b_{vt} [ft]	11.28	16.12	20.96	8.3	11.8	15.4
l_{eng} [%b]	10.5	15	19.5	10.5	15	19.5
Λ [deg]	0	1	30	0	1	30
P_{eng} [Hp]	77	110	143	110	160	210
S_{ht} [ft^2]	60	80	104	29.4	42	54.6
b_{ht} [ft]	15.8	22.5	29.2	10.85	15.5	20.15
λ_{cowl} [1/hr]	$1.4x10^{-4}$	$2x10^{-4}$	$2.6x10^{-4}$	$1.4x10^{-4}$	$2x10^{-4}$	$2.6x10^{-4}$
$\lambda_{engine,1}$ [1/hr]	$0.7x10^{-5}$	$1x10^{-5}$	$1.3x10^{-5}$	$0.7x10^{-5}$	$1x10^{-5}$	$1.3x10^{-5}$
$\lambda_{engine,2}$ [1/hr]	$0.7x10^{-5}$	$1x10^{-5}$	$1.3x10^{-5}$	$0.7x10^{-5}$	$1x10^{-5}$	$1.3x10^{-5}$
λ_{rudder} [1/hr]	$0.7x10^{-4}$	$1x10^{-4}$	$1.3x10^{-4}$	$0.7x10^{-4}$	$1x10^{-4}$	$1.3x10^{-4}$
$\lambda_{aileron}$ [1/hr]	$0.7x10^{-4}$	$1x10^{-4}$	$1.3x10^{-4}$	$0.7x10^{-4}$	$1x10^{-4}$	$1.3x10^{-4}$
$\lambda_{elevator}$ [1/hr]	$0.7x10^{-4}$	$1x10^{-4}$	$1.3x10^{-4}$	$0.7x10^{-4}$	$1x10^{-4}$	$1.3x10^{-4}$

5.6.1 Scenario I: Single Sortie Mission

Each of the plots within this subsection depicts a full sampling of the design space via Latin-hypercube spacing (3000 design points). Detailed descriptions of this type of sampling are abundant, one of which may be found in [62]. For purposes of visually representing a design space, its main advantage is that it provides a balance between spreading the design points out to maximum distance possible and maintaining relatively uniform spacing between them.

Each point in the following plots represents the multistate analysis of as many as 64 states, for one sampling of the vector [$\mathbf{x}$ $\boldsymbol{\lambda}^{\boldsymbol{s}}$]. The Pareto *non-dominated* points represent those design points that cannot be improved without decreasing performance in at least one of the two plotted performance objectives. These points were determined using a publicly available Pareto filtering algorithm [42]. A full analysis

of 3000 design points required approximately 12 hours, performed in parallel across 8 processing threads on an Intel Quad i7 2.8GHz CPU.

Figure 5-9 shows the design-driven performance space for nominal endurance versus the aircraft flyaway cost, which includes Non-Recurring Expense (NRE) estimates of manufacturing, tooling, engineering, and quality control from the models described in Section 5.4.2. This cost has been converted to current year dollars and normalized by that of the baseline NASA aircraft to protect proprietary data.

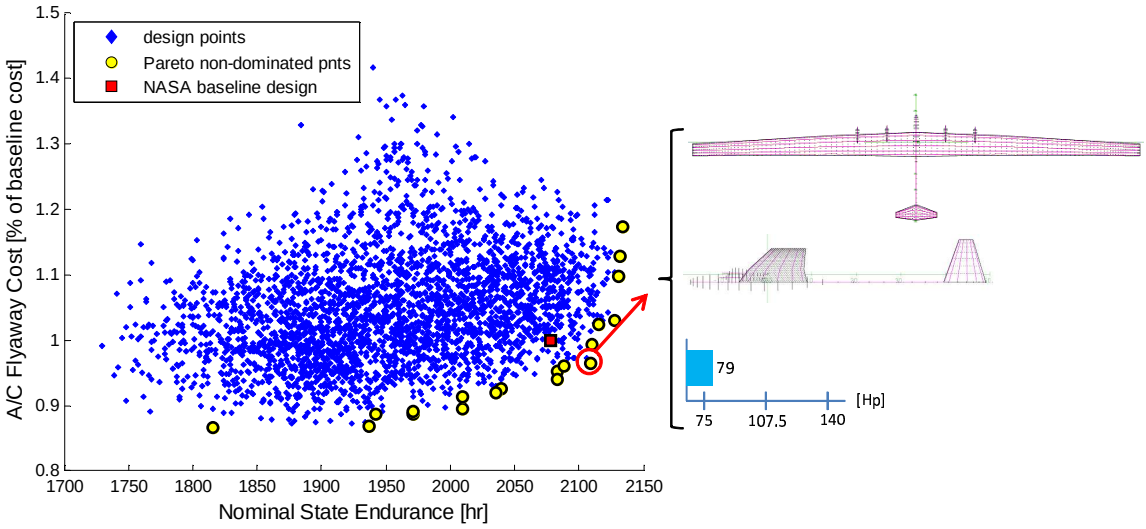

Figure 5-9: Design performance space for nominal endurance vs. A/C flyaway cost

The NASA baseline design point is displayed in Fig. 5-9, and is very close to that which a designer would likely pick as a 'best' balance between cost and nominal performance (less than 2% difference in either). This 'best' aircraft is shown to the right of the plot for visual reference, characterized by a high aspect ratio ($\mathcal{AR}$=25) and low wing sweep (Λ=4°), as one would expect for such a long duration, high altitude aircraft, designed for nominal performance.

The nominal-case performance space in Fig. 5-9 provides a reference point to which the next three plots may be compared. The first of these is a design space analysis for availability vs. flyaway cost, as shown in Fig. 5-10, where the NASA baseline static design remains fixed, and component failure rates are allowed to vary across the bounds defined in Table 5.3. Note that the increasing slope of the Pareto front

estimation represents the combined effects of the cost trends seen in Fig. 5-7. The aircraft geometry shown is that of the NASA baseline, with failure rates, $\boldsymbol{\lambda}^{s}$=[1/4297, 1/119588, 1/119588, 1/7819, 1/7829, 1/13013]/hr. In Fig. 5-10 only, aircraft geometry is the same for each of the 3000 design points (only failure rates are varied).

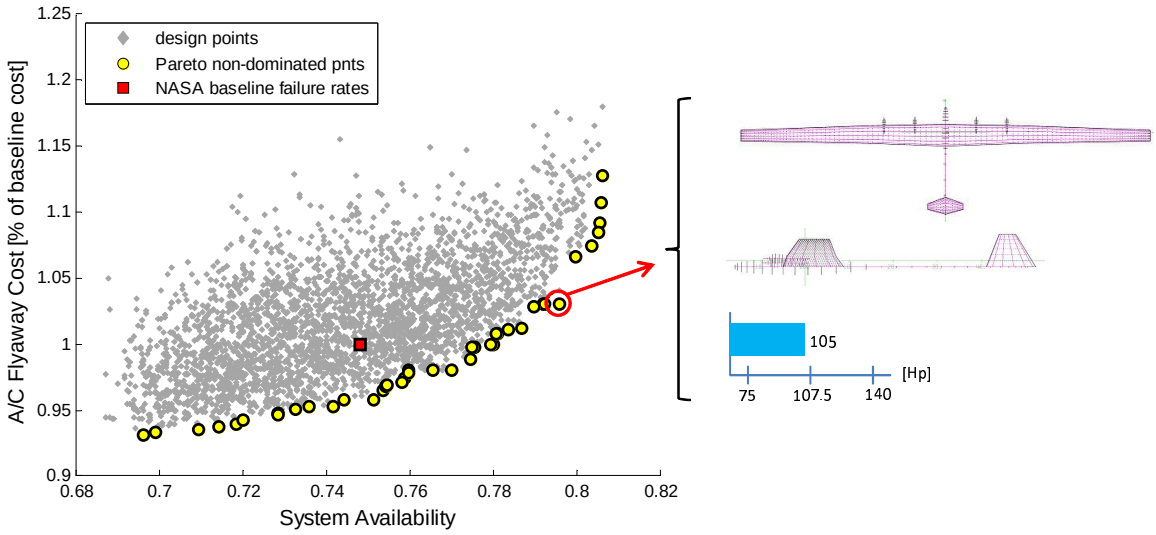

Figure 5-10: Design performance space for availability vs. cost - varying only $\boldsymbol{\lambda}^{s}$

Where the above figure shows results for the design space with a constant static design vector, $\mathbf{x}$, Fig. 5-11 displays results for constant baseline $\boldsymbol{\lambda}^{s}$, varying only static

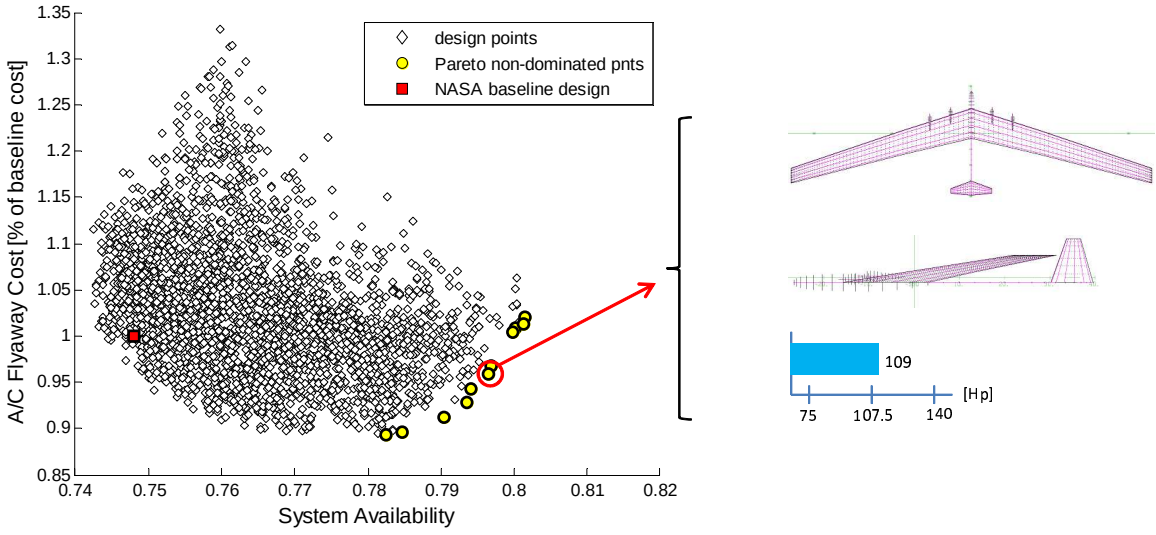

Figure 5-11: Design performance space for availability vs. cost - varying only $\mathbf{x}$

design variables. There are several very meaningful observations to make from this figure. First, the shape of the design performance space is distinctly different from that of Fig. 5-10. More on this will be discussed near the end of the section. Second, the baseline design lies at a point near opposite that of the non-dominated Pareto points for system availability. This indicates a probable trade-off between contesting values of availability and nominal design performance, an issue examined further in later figures. Finally, the aircraft's static design is decidedly different from that of the best designs in the previous two analyses. Most notable are the significantly increased wing sweep (Λ=18°) and larger tail (b_{vt}=19.3 ft). Both of these are characteristics that improve the aircraft's ability to resist failure-driven perturbations to yaw and roll. Higher wing sweep increases the lateral stability parameter, $C_{l\beta}$, decreasing the aileron deflection required to return to wings level. The larger tail increases directional stability, $C_{n\beta}$, lessening the rudder deflection required to return to zero degrees of sideslip. Neither of these characteristics help increase a subsonic aircraft's nominal-state endurance, as is demonstrated by the fact that this design has an endurance that is 11.7% below that of the baseline aircraft (see summary in Table 5.4).

Figure 5-12 shows the performance space in which both $\mathbf{x}$ and $\boldsymbol{\lambda}^{\boldsymbol{s}}$ are allowed to vary. The resulting aircraft has a lower wing sweep and tail height (Λ=12° and

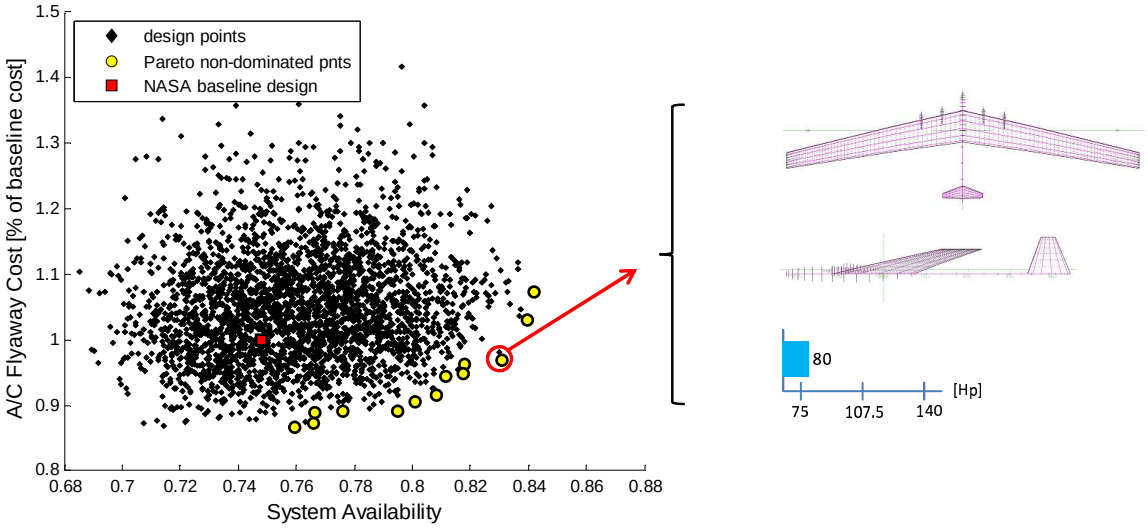

Figure 5-12: Design performance space for availability vs. cost - full multistate, $\boldsymbol{\lambda}^{\boldsymbol{s}}$ and $\mathbf{x}$

b_{vt}=17.7 ft), but a higher system availability. In this case, flyaway cost is about the same as in the previous analysis, showing that improved availability has been achieved, to some degree, by replacing extra wing sweep and tail size with more cost effective improvements in component failure rates.

To gain further insight into the effects of component failure rates versus static design variables, the performance spaces for each of the three previous analyses are overlaid upon one another in Fig. 5-13. This visually demonstrates two compelling results. First, the achievable improvement in availability via static design variables is nearly as large as that made via component failure rates. From the perspective of reliability analysis, this is significant due to the fact that improvements in reliability are nearly always sought after in the space of $\boldsymbol{\lambda^s}$ rather than affecting G_K^s through changes to static design variables, $\mathbf{x}$. Secondly, the inclusion of both $\mathbf{x}$ and $\boldsymbol{\lambda^s}$ in the design analysis allows a region of system availability to be reached that is unobtainable

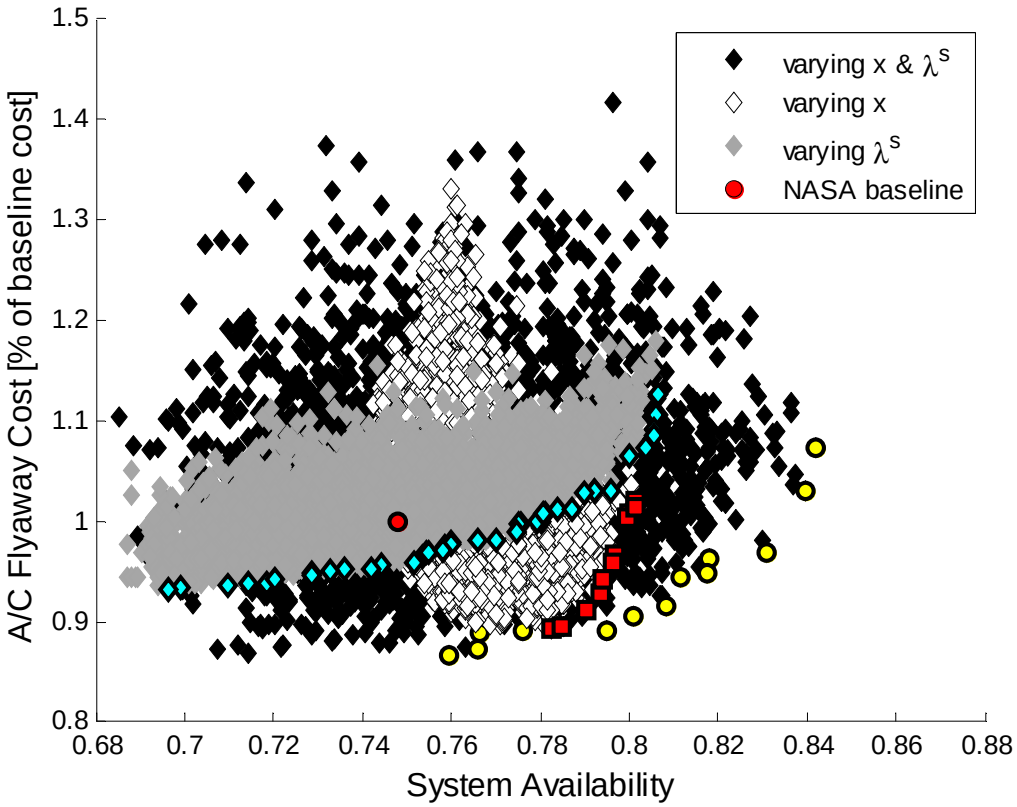

Figure 5-13: Design performance space overlays for availability vs. cost

via the independent variation of either one.

Table 5.4 presents a numerical summary of the above analyses. Some key observations are that the baseline improved design has the best nominal performance with an endurance of 2109 hours, while the combined multistate design has the best system availability with $E_A = 0.831$. As noted, however, this comes at the expense of an 11% decrease in nominal performance.

Table 5.4: Summary of designs for best cost and expected endurance

Design\Performance	Availability		Endur_{exp}		Endur_{nom}		A/C Cost
	[n/a]	% dev_{bsln}	[hr]	% dev_{bsln}	[hr]	% dev_{bslb}	% dev_{bsln}
NASA Baseline	0.748	0.00%	1510	0.00%	2078	0.00%	0.00%
Baseline Improved†	0.733	-2.00%	1576	4.37%	2109	1.5%	1.47%
$\boldsymbol{\lambda}^{\boldsymbol{s}}$ Variation*	0.796	6.40%	1589	5.21%	2078	0.00%	2.94%
$\mathbf{x}$ Variation‡	0.797	6.54%	1425	-5.63%	1835	-11.70%	-3.31%
Combined Multistate$^{\diamond}$	0.831	11.09%	1565	3.65%	1842	-11.32%	-2.94%

† Figure 5-9.
* Figure 5-10.
‡ Figure 5-11.
$^{\diamond}$ Figure 5-12.

This fact motivates the search for a further refined design, giving consideration to each of the performance objectives in Table 5.4; namely, nominal endurance, expected endurance, availability, and cost. In the true, probabilistic multistate sense, nominal performance should not necessary be given the same importance as the other three objectives, but in the real world it would likely be difficult to convince a customer they should invest millions of dollars in a system with seemingly poor performance in its intended operational state. Therefore, it is included in the following search.

Figure 5-14 displays a series of plots representing the performance spaces for 1) expected endurance, 2) cost, and 3) nominal endurance, against system availability. The non-dominated points from Plot 1, arising from the combined objectives of availability and expected endurance are mapped to the performance spaces of cost and nominal endurance in Plots 2 and 3, allowing the multi-objective analysis of four objectives through a two-dimensional representation.

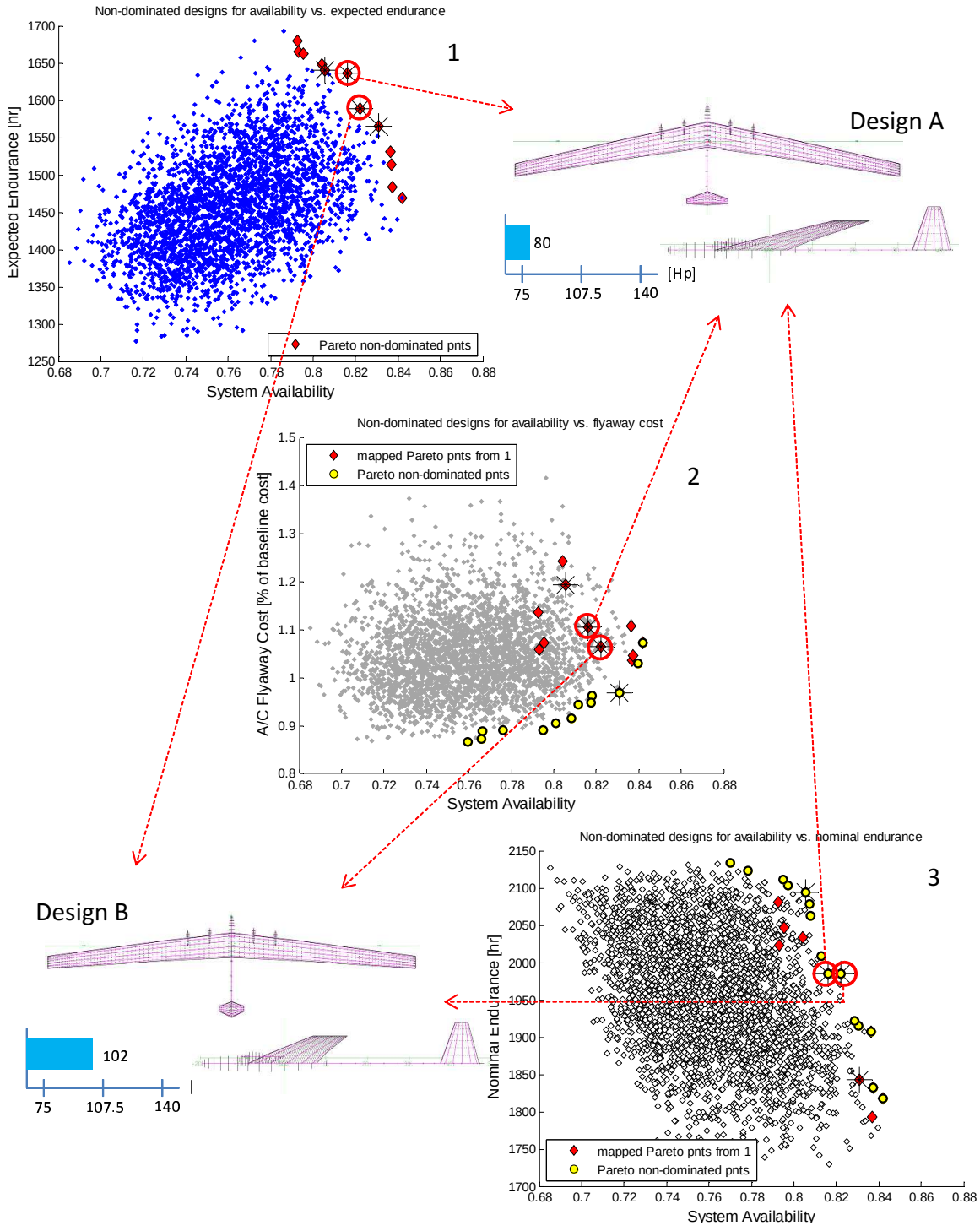

Figure 5-14: Design comparison via Pareto non-dominated points

Two designs are selected, based on their performance across all three output spaces. One favors higher expected performance over cost and system availability (Design A), and the other favors higher availability over expected performance (Design B). These designs are listed in Table 5.5 along with the NASA baseline.

Table 5.5: Refined designs from expanded multi-objective analysis

Design\Performance	Availability		Endur_{exp}		Endur_{nom}		A/C Cost
	[n/a]	% dev_{bsln}	[hr]	% dev_{bsln}	[hr]	% dev_{bslb}	% dev_{bsln}
NASA Baseline	0.748	0.00%	1510	0.00%	2078	0.00%	0.00%
Design A*	0.816	9.12%	1637	8.40%	1985	-4.47%	10.29%
Design B*	0.822	9.91%	1589	5.26%	1984	-4.49%	6.25%

* Figure 5-14.

Both Design A and Design B have slightly lower availability than the combined multistate design in Table 5.4, but with higher expected performance and significantly higher nominal performance. This comes at a relatively small increase in cost, especially in the case of Design B.

In a final step towards design refinement, the constrained optimization in Eqn. 5.5 improves the availability of Design B, with no loss in any of the other three objectives.

$$
\begin{aligned}
&\textit{given} && \text{parameters}, \mathbf{c} \\
&\textit{minimize} && -\tilde{S}_{E_A}(\mathbf{x}, \boldsymbol{\lambda}^{\boldsymbol{s}}, \mathbf{c}) = -\sum_{K=1}^{M} P_K^s(\boldsymbol{\lambda}^{\boldsymbol{s}}) \{ \frac{b}{b^{(max[1+(W-D_K^s,1])}} \}, \text{ where} \\
& && b = 10,\ D_K^s = W - G_K^s(\mathbf{x}, \mathbf{c}) \\
&s.t. && g_1(\mathbf{x}, \mathbf{c}) = \textit{Endur}_{nom} \geq 1984 \text{ nm} \\
& && g_2(\mathbf{x}, \boldsymbol{\lambda}^{\boldsymbol{s}}, \mathbf{c}) = \textit{Endur}_{exp} \geq 1589 \text{ nm} \\
& && g_3(\mathbf{x}, \boldsymbol{\lambda}^{\boldsymbol{s}}) = \textit{Cost} \leq 1.0625 \\
& && x_{i,LB} \leq x_i \leq x_{i,UB} \quad i = 1, 2, ..., 8 \\
& && \lambda_{i,LB}^s \leq \lambda_i^s \leq \lambda_{i,UB}^s \quad i = 1, 2, ..., 6
\end{aligned}
\tag{5.5}
$$

Using the surrogate equation for availability, $\tilde{S}_{E_A}$ (introduced in Section 4.2.2), proved

very effective in modeling the actual availability. Fig. 5-15 shows the iterative progression of the above gradient-based optimization, with the final design presented in Table 5.6.

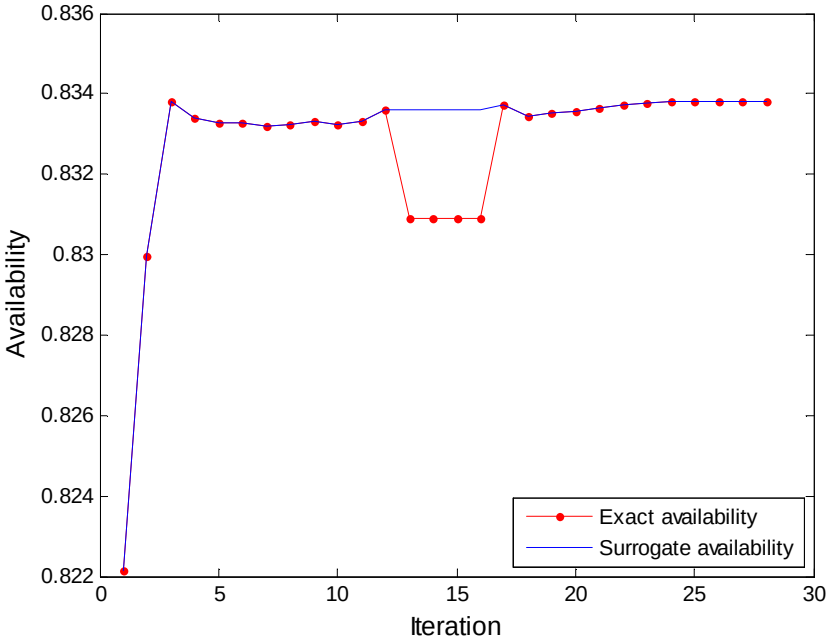

Figure 5-15: Plot of final optimization for *Scenario I*

Table 5.6: Final design resulting from gradient-based optimization of surrogate availability

Design\Performance	Availability		Endur_{exp}		Endur_{nom}		A/C Cost
	[n/a]	% dev_{bsln}	[hr]	% dev_{bsln}	[hr]	% dev_{bslb}	% dev_{bsln}
NASA Baseline	0.748	0.00%	1510	0.00%	2078	0.00%	0.00%
Design B	0.822	9.91%	1589	5.26%	1984	-4.49%	6.25%
Design C	0.834	11.5%	1610	6.62%	1984	-4.49%	6.25%

The final optimization (Design C) improves system availability by an additional 1.6%, accompanied by an additional 1.4% in expected endurance. These changes were achieved with less than 10% variation in any of the static design variables, most notably a 3.4% increase in aspect ratio, a 7.6% increase in vertical tail height, and a 9.3% reduction in maximum engine power (engine size). Within $\boldsymbol{\lambda}^{\boldsymbol{s}}$, the elevator

failure rate decreased by 14% while the others remained within 5% of initial values.

5.6.2 Scenario II: Multiple Sortie Campaign

In *Scenario I*, the multistate methodology was used to determine an overall superior vehicle design, based on the given multistate requirements. *Scenario II* now turns focus to examination of design variable effects on an overall multiple sortie campaign, consisting of shorter duration sorties. The majority of vehicle requirements for altitude, airspeed, and payload remain the same, with the exception of higher airspeed for sortie abort, now determined by the aircraft's stall speed, rather than the max speed required to overcome winds aloft. This results from the fact that the baseline shorter duration aircraft is designed for higher cruise speed in order to maximize Science Mile Accumulation Rate (SMAR) over the duration of the campaign. The formation and solution of the Vehicle Markov Model (VMM) is the same as that of the Markov chain in *Scenario I*, and analysis for the Sortie and Campaign Equivalent Markov Models (SEMM and CEMM) follows that described in Section 4.2.1, of Chapter 4, and Section 5.5.2, of this chapter.

Figure 5-16 shows results of the SEMM aggregation for the baseline aircraft given in Table 5.3. Values for P_K^{SEMM} are shown next to the SEMM states.

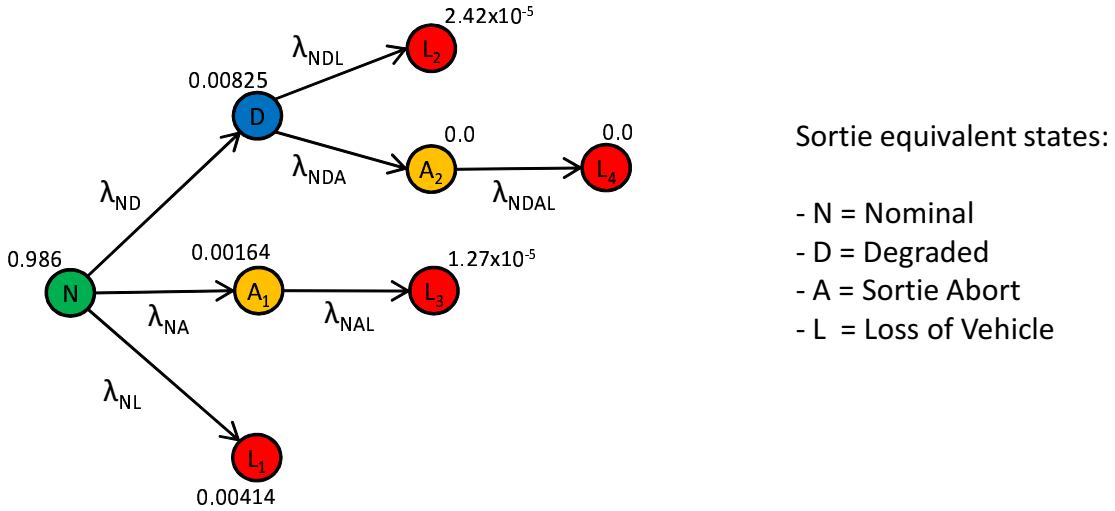

Figure 5-16: UAV Sortie Equivalent Markov Model (SEMM)

Note that, due to the much shorter sortie duration in *Scenario II*, the nominal state probability is higher than in *Scenario I*. Additionally, the distribution of state performances is such that the aircraft never enters an *abort* state from a *degraded* state (for this particular geometry, as shown by the probability value of 0.0 next to A_2). The sortie equivalent transition rates are determined from the least squares minimization in Eqn. 4.2, where λ_{NDA} and λ_{NDAL} are set to identically zero to facilitate the process. Table 5.7 lists the SEMM equivalent transition rates.

Table 5.7: UAV SEMM equivalent transition rates

$\boldsymbol{\lambda^{SEMM}}$	**Value [1/hr]**
λ_{ND}	1/4998
λ_{NA}	1/25024
λ_{NL}	1/9996
λ_{NDL}	1/7150
λ_{NDA}	0
λ_{NAL}	1/2675
λ_{NDAL}	0

The above rates are summed according to their failure levels, and used to form the CEMM shown in Fig. 5-17, along with the campaign repair rates. The probabilities, P_K^{CEMM}, resulting from the solution to this model are shown next to the CEMM states.

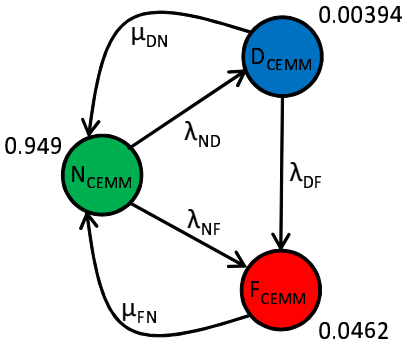

From SEMM:

- $\{\lambda_{ND}\}^{CEMM} = \{\lambda_{ND}\}^{SEMM} = 1/4998$hrs
- $\{\lambda_{DF}\}^{CEMM} = \{\lambda_{NDA}\}^{SEMM} + \{\lambda_{NDL}\}^{SEMM} = 1/7150$hrs
- $\{\lambda_{NF}\}^{CEMM} = \{\lambda_{NA}\}^{SEMM} + \{\lambda_{NL}\}^{SEMM} = 1/7142$hrs
- $\{\mu_{DN}\}^{CEMM}$ = f(average sortie duration) = $(1/(2Endur_{exp}))$hrs
- $\{\mu_{FN}\}^{CEMM}$ = f(reaction time + sortie ingress duration) = $1/(336+(2100*V_{cr}))$hrs

Figure 5-17: UAV Campaign Equivalent Markov Model (CEMM)

Although the VMM had a nominal state probability of 0.986, this translates to a campaign nominal state probability of only 0.949, when accounted for across the

entire 5-year campaign. Furthermore, the campaign performance is in a state of failure for a total of nearly three months, as indicated by the failure state probability in Fig. 5-17 (0.0462*43800[hr]=2023.6[hr]=84.3[days]). Overall campaign availability is $E_A^{CEMM} = P_N^{CEMM} + P_D^{CEMM} = 0.953$.

The total number of sorties, $N_{sorties}$, required for the campaign is 1915, calculated as described in Chapter 4, with an estimate of sorties failed and vehicles lost given in Eqns. 5.6 and 5.7:

$$F_{sorties} = (P_A^{SEMM} + P_L^{SEMM})N_{sorties} = 11 \tag{5.6}$$

$$L_{sorties} = (P_L^{SEMM})N_{sorties} = 8 \tag{5.7}$$

The above metrics, when considered along with accurate maintenance data, provide a measure of the minimum number of vehicles required in order to accomplish the 5-year campaign. Initially, Step 1 in Sections 5.1 assumed at least five vehicles would be required, allowing for a 60-hour downtime between a vehicle's consecutive flights. Given the information above, at least eight to eleven additional vehicles would be necessary in order to complete the campaign.

Equations 5.6 and 5.7 show results for only the baseline aircraft. In order observe how these metrics change with variations in the design vector, Figures 5-18 through 5-22 show the main effects of several design variables on campaign availability, number of sorties failed, and number of vehicles lost. Each of the plots shows results from an analysis of the design space sampled using an orthogonal array with 14 factors and 29 levels (841 design points). The factors are the elements of $\mathbf{x}$ and $\boldsymbol{\lambda}^s$, and the levels are equally spaced stratifications of those elements. Orthogonal arrays allow the calculation of the factors' *main effects* on performance output, which is the effect of that factor averaged across the levels of all other factors. For example, the main effect of wing span, b, on campaign availability, at a level equal to 110 ft, is the average availability of all 14 design points with $b = 110$ ft. *Interaction effects* may also exist between the factors, but this is to a certain degree evident in the amount of dispersion between the points in the following figures, as a relatively large number

of levels was used. More on orthogonal arrays may be referenced in [54].

Figures 5-18 and 5-19 show the main effects of wingspan and maximum engine power on campaign availability. The wingspan effect is due primarily to its influence on aspect ratio ($\mathcal{R} = b^2/S$), thus there is a known interaction with wing area, S. Regardless, one can still observe the general trend that increasing wingspan improves availability across most of its design interval. There is a much more distinct trend in the effect of maximum engine power, which may be thought of as the engine size. In general, the larger engine helps increase availability up to a maximum power of about 160 Hp, after which availability reverses trend and starts to decrease. More detailed inspection of the performance state space shows that, in the lower region, the larger engine prevents several state performances from falling below the mission abort airspeed. As the engine continues to increase in size and weight, however, the first level failure of the outboard engine results in large enough moments that the ailerons and rudder can no longer trim for steady cruising flight at altitude. Once this threshold crossing is broad enough that the majority of design geometries have fallen from the *degraded* to *abort* state, the trend tapers off near the high end of the engine power range.

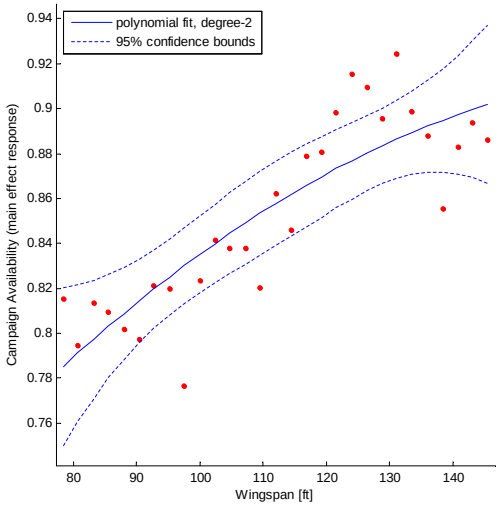

Figure 5-18: Main effect of wingspan on campaign availability

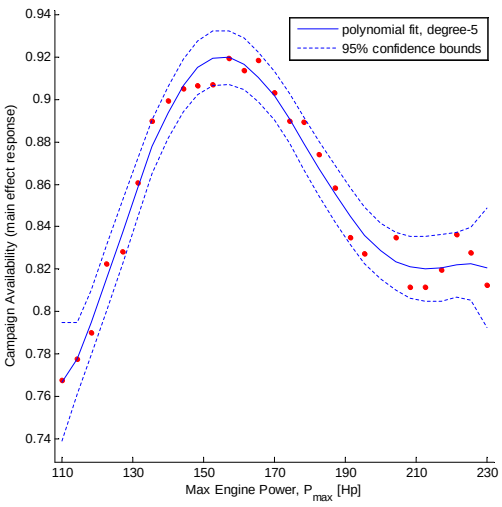

Figure 5-19: Main effect of max engine power on campaign availability

Figures 5-20 and 5-21 show the effects of wing sweep on the total number of sorties failed and the total number of vehicles lost over the 5-year campaign. Although the aircraft is of a different size and thrust ratio as that of *Scenario I*, the trends in wing sweep here are analogous to those observed in the ultra long duration vehicle. Specifically, a slight amount of wing sweep, on the order of ten to fifteen degrees, acts to improve multistate performance. Above this, the worsening drag characteristics associated with higher sweep begin to outweigh improvements in lateral stability. In Fig. 5-20, this trend presents itself as a minimum in total sorties failed, while in *Scenario I* it was evident in the resulting design progression. Of interest is that the number of total vehicles *lost* in Fig. 5-21 starts to increase at a wing sweep five degrees lower than that of the increase in Fig. 5-20. This indicates that, while the best wing sweep for minimizing entry into a *failed* state (which includes both *loss* and *abort* states) is between ten to fifteen degrees, keeping it nearer to ten will increase chances of entering into an *abort* state instead of crossing directly from *degraded* to *loss*.

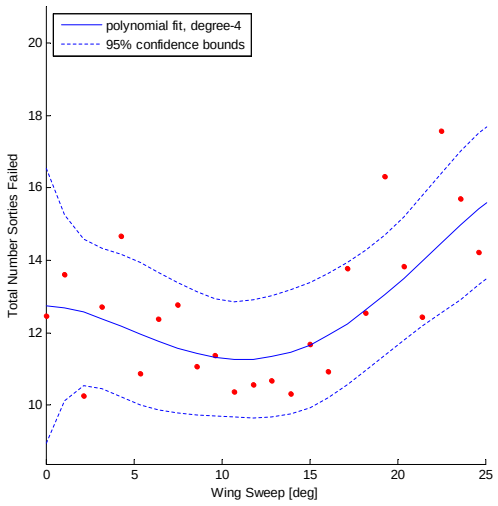

Figure 5-20: Main effect of wing sweep on total sorties failed

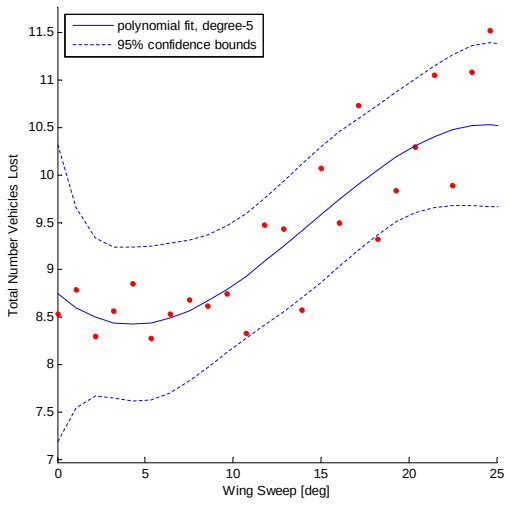

Figure 5-21: Main effect of wing sweep on total vehicles lost

Finally, Fig. 5-22 displays the main effect of engine power on total number of vehicles lost. This trend is distinctly different from that in Fig. 5-19. While campaign availability reached a maximum at a certain engine size, the number of vehicles lost

does not reverse trend throughout the entire design interval. This occurs, in general, because the increased engine size is enough to initiate departure from acceptable mission performance, but not enough to cause an increase in aircraft loss rate.

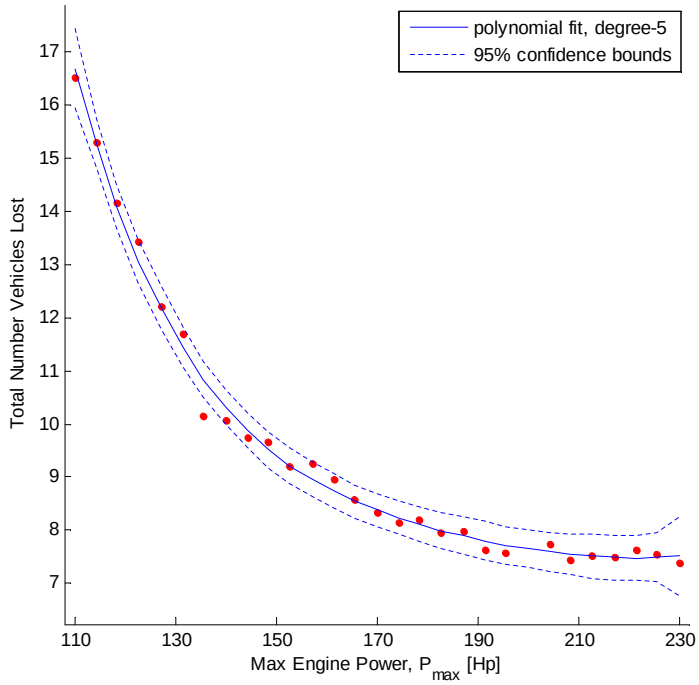

Figure 5-22: Main effect of max engine power on total number of vehicles lost

5.7 Case Summary

This case study demonstrated the multistate analysis and design methodology as applied to two long endurance UAV scenarios. In the first scenario, Pareto analysis and Design of Experiment (DOE) techniques were used to show the progression of 'best' design geometries within an a) nominal design performance space, b) performance space allowing only variation of failure rates, c) performance space allowing only variation of the static design vector, and d) a performance space allowing a full multistate variation of both. The best design was then further improved via a constrained optimization using the surrogate availability function introduced in Chapter 4. The second scenario demonstrated how multistate performance of the vehicle system can be used to determine campaign level performance metrics. Systematic exploration of

the design space illustrated the main effects of several important design variables on campaign outputs such as availability and number of sorties failed and vehicles lost.

Several extremely important findings resulted from the above analyses. These are summarized below:

- Each of the performance design spaces stemming from a), b), c), and d) above had distinctly unique shapes and boundaries. Such uniqueness was initially suggested by the opposing trends in design sensitivities of the Super King Air example in Chapter 2, and further confirmed through visual representation of the entire design space in this chapter (Figures 5-9 through 5-13).

- The nominally designed aircraft was characterized by a design point lying extreme opposite of the non-dominated Pareto points for maximum system availability (Fig. 5-11). This emphasizes the importance of considering multistate performance in the design of long duration systems where availability is a critical requirement. The nominally designed system may actually result in *lower* system availability.

- The achievable improvement in availability via static design variables was nearly as large as that made via component failure rates (Fig. 5-13). From the perspective of reliability analysis, this is significant due to the fact that improvements in reliability are nearly always sought after in the space of $\boldsymbol{\lambda}^{\boldsymbol{s}}$ rather than affecting G_K^s through changes to static design variables, $\mathbf{x}$. This leaves a large region of the performance space potentially unexplored.

- Perhaps most importantly, the inclusion of both $\mathbf{x}$ and $\boldsymbol{\lambda}^{\boldsymbol{s}}$ in the design analysis allowed a region of system availability to be reached that was unobtainable via the independent variation of either one (Fig. 5-13). Furthermore, the resulting design had a distinctly different shape from the nominally designed NASA baseline system (see Fig. 5-23 for a summary comparison of geometries).

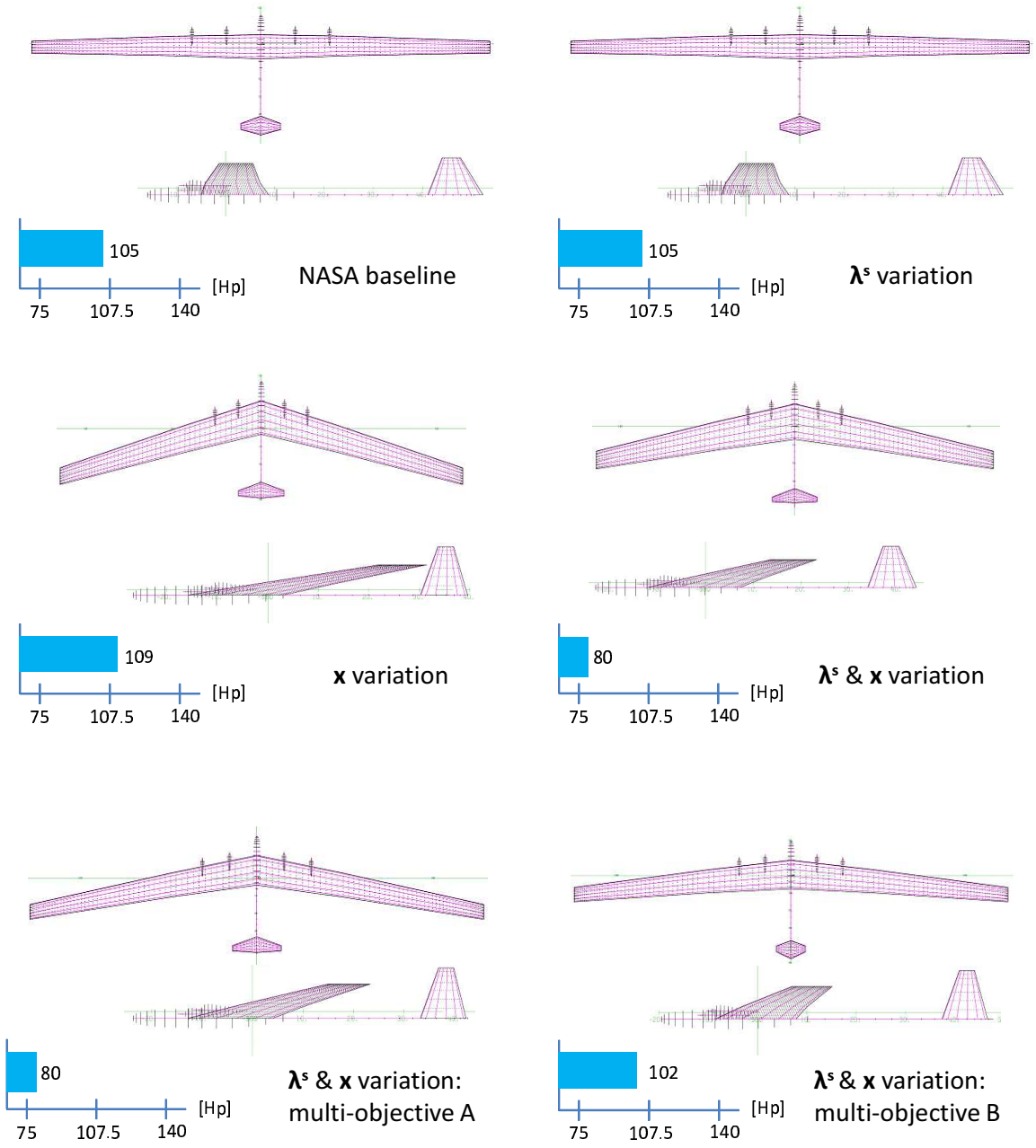

Figure 5-23: Summary of UAV Aircraft Geometries from *Scenario I*

- Finally, examination of campaign level metrics derived from system level vehicle performance demonstrated application of the methodology to systems with shorter mission durations. Main effects of static design variables on these higher level metrics showed unique trends that would not be found outside of the multistate analysis and design method. These include:
  - The leveling out of the max engine power vs. campaign availability trend in Fig. 5-19 near the high end of the power range. In a nominal state analysis for endurance, this trend would continue its negative slope as increasing engine size results in higher energy consumption and increasing mass.
  - The concave shape of the wing sweep vs. sorties failed trend in Fig. 5-20. In a nominal state analysis, best endurance would occur with zero wing sweep and have a continuous negative slope towards the high end of the wing sweep range.
  - The constant negative slope of the max engine power vs. vehicles lost trend in Fig. 5-22. For nominal endurance, the trend in max engine power would have a positive slope (improve endurance) near the low end of the power range, reach an optimum, and then have a continuously negative slope (decrease endurance) as the max engine power increased.

Specific results of the *Scenario I* analysis showed that the combined multistate approach demonstrated improvement in system availability of 11%, at a 3% lower cost, when compared to the baseline aircraft designed for nominal performance. Variation of component failure rates or static design variables alone showed improvement of only 6.5%. Furthermore, when considering multiple objectives of system availability, expected performance, nominal performance, and cost, the combined approach was still able to achieve an 11% improvement in availability, with only a 4.5% decrease in nominal performance, albeit at a small 6% increase in aircraft flyaway cost.

Chapter 6

Case Study - III: Lubrication System for a Geared Turbofan Engine

This chapter extends the methodology by demonstrating application of multistate analysis and design to a lower level aerospace subsystem. The case study is the lubrication system for a high bypass ratio geared turbofan (GTF) engine in the 20,000- to 30,000-lbf thrust class. Whereas traditional turbofan engines have a fixed shaft connecting the fan with the low-pressure turbine and compressor, the GTF engine has a fan drive gear system that couples the fan to the low pressure spool, allowing both the fan and the compressor to operate at more efficient wheel speeds. This has advantages of improving fuel efficiency and reducing noise levels, but results in a more complex and operationally critical lubrication system.

The lubrication subsystem is modeled for a single set of time-variant operational parameters, representing the typical mission profile of an airline passenger jet. A Pareto optimum solution is taken from the output space of expected oil temperature versus cooling surface size. This serves as the baseline for sensitivity analysis and improvement of expected availability via Pareto fronts calculated using the surrogate function for E_A. The goal of this case study is to quantify how specific changes to the lubrication system's design might improve the robustness of its performance

across several modes of failure, and to demonstrate the methodology such that it may be extended to a more detailed multistate analysis given higher fidelity tools and models available to engine industry experts. Results were favorable, showing that when compared to the traditional, nominal case design as a baseline, performing the multistate design analysis improves the overall lubrication system availability by as much as 22% over a 500-hour maintenance interval.

6.1 The Geared Turbofan Engine Concept

The underlying principle of the GTF engine, shown in Fig. 6-1, is to further increase bypass ratio over current designs in order to improve propulsive efficiency (specific fuel consumption), decreasing noise and hopefully weight at the same time. The above is achieved by reducing fan speed through a gearbox to allow higher low-pressure compressor (LPC) and turbine (LPT) speeds and efficiencies. This generally leads to a larger fan for the same thrust demand, where the final outcome is a high bypass ratio turbofan engine with low thrust-specific-fuel-consumption (TSFC) and lower specific thrust [71]. Along with the low bypass jet velocity comes low jet noise [88], and because of the correspondingly slow fan speed, the fan emitted sound pressure level is lower.

The geared turbofan engine concept has existed in smaller class turbofan engines for several decades (e.g. Honeywell TFE731), where loading of the gear-box was kept at relatively benign levels due to low thrust output. Only recently have improvements in technology and materials made such gearing systems viable on high thrust engines used by medium- and long-haul airliners such as the Boeing 777 or the Airbus A320. Even so, many engine manufacturers remain reluctant to invest in the technology due to perceived concerns about engine maintainability and system complexity, often on the part of aircraft manufacturers or the airlines themselves. A recent study done at MIT found that the integration of the fan drive gear system (FDGS) into the turbofan engine does in fact drive a significant increase in complexity of supporting systems, specifically on the performance and integration of the lubrication system [95].

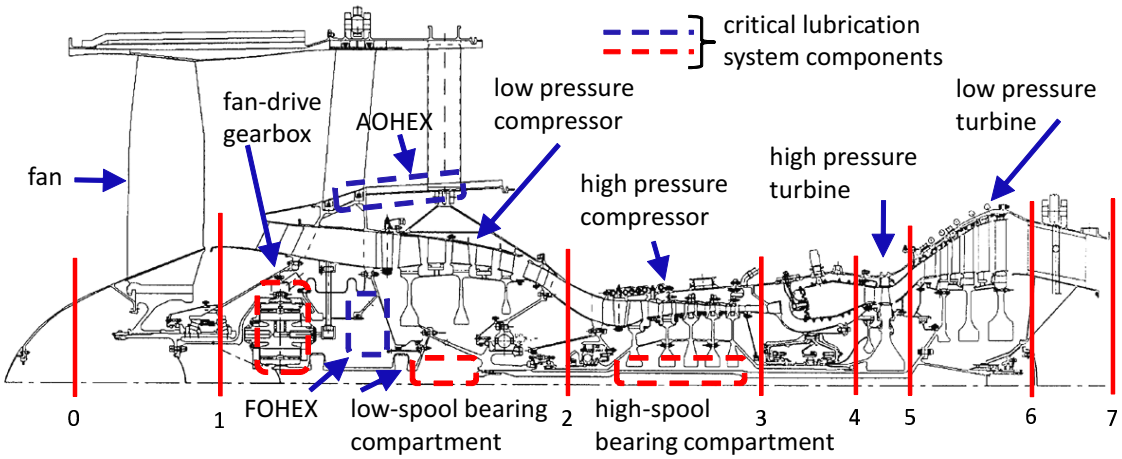

Figure 6-1: Cut-away of a dual-spool geared turbofan engine showing critical lubrication system components

6.2 Step 1 - Requirements Definition and Concept of Operations

The operational concept for the lubrication system stems directly from its function within the GTF engine. It is the critical system supplying lubricating oil to the gear and bearing compartments affixed to the turbine and compressor shafts. The main components of the lubrication system are the air-oil heat exchanger (AOHEX), the fuel-oil heat exchanger (FOHEX), the fan drive gear system (FDGS), and the low and high-spool bearing compartments. These are denoted by the dashed lines in Fig. 6-1.

The lubrication system's performance is driven by the maximum temperatures allowed on gear and bearing compartments, and by the target oil mass flow rates to which these compartments are designed.[1] Limits for these come from discussion with engineers from a major U.S. engine manufacturer, with the values in Table 6.1 general enough as to not disclose proprietary data.

[1]In lubrication design, there is typically an optimum flow rate associated with best lubrication and heat extraction. The compartment geometries are designed for this flow rate and are considered fixed in this study, as they are at a much lower level of design detail.

Table 6.1: Requirements summary for GTF lubrication system

Component:	Oil Temperature	Oil Mass Flow Rate
High Bearing Compartment	$\leq$ 350 deg F	$\dot{m}_{design} \pm 10\%$
Low Bearing Compartment	$\leq$ 350 deg F	$\dot{m}_{design} \pm 20\%$
Fan Drive Gear System	$\leq$ 350 deg F	$\dot{m}_{design} \pm 20\%$

6.3 Step 2 - Preliminary Analysis of Failure Modes

As the second step in the multistate design process, a preliminary Failure Mode and Effect Analysis was performed, based on the knowledge of at least one professional engineer having extensive experience with GTF engine lubrication systems. This resulted in the consideration of three main failure modes: the failure of the FDGS auxiliary oil pump, the failure of the oil seal in the FOHEX, and the failure of a main oil pump. There are other failures that could be modeled, but these are enough to demonstrate effectiveness of the methodology, and result in eight states that must be analyzed at each design point. The general effects of the failures are given below:

- *FDGS auxiliary oil pump*: This results in a significant reduction in the oil mass flow rate through the FDGS, and a corresponding increase in the mass flows through the high and low bearing compartments. As these are nominally designed for target mass flow rates in order to keep temperature down, the perturbations of flow rate result in increased temperature in each of the bearing and gear compartments.

- *Oil seal in FOHEX*: As fuel mixes with oil flow throughout the system, lubricity of the oil decreases causing an overall increase in temperature in each of the compartments. This might be offset by designing for more flow through the AOHEX or increasing the size of the main oil pump.

- *Failure of a main oil pump*: This models the failure of one of two oil pumps operating in series on the main oil line and results in an overall reduction in mass flow rate through the entire system.

Table 6.2 summarizes the above failure modes in the context of the FMEA.

Table 6.2: Summary of preliminary FMEA for the GTF lubrication system

Component	Function	Failure Mode	Effect	Failure Rate [1/hr]	Mitigation
mainline pump	provide pressure	partial inop	50% press. loss	1/5000	n/a
auxiliary pump	provide pressure	inop	FDGS press. loss	1/5000	increase FDGS flow
FOHEX seal	prevent contamination	fuel leak	loss in lubricity	1/2500	increase AOHEX flow

The transition rate vector is $\boldsymbol{\lambda}^s = [\lambda_{main}\ \lambda_{aux}\ \lambda_{seal}]$, denoting the respective component failure rates shown in Table 6.2. These are taken from airline data on aircraft maintenance planning found in Tozan, et al. [108]

6.4 Step 3 - System and Performance Classification

Step 3 classifies the system according to its level of analysis, and determines whether the performance metric is *dynamic* or *static*. The lubrication system study considers only the lower, single system level, although an extension to multiple engine, phased operation is conceivable. Performance output are the oil temperatures of the system components, as well as the overall average system oil temperature. These temperatures are functions of the time-varying load on the engine and the corresponding variations in oil mass flow throughout the system. Thus, the responses are *dynamic* and the performance analysis accomplished through simulation, with an appropriate controller in place to regulate oil flow through the FDGS. This is described further in the following section.

6.5 Step 4 - Modeling and Simulation

The lubrication system, as shown in Fig. 6-2, was constructed in MATLAB's Simscape® software to as closely resemble a GTF engine's oil system as possible. This was ac-

complished with input from the engine manufacturer and is intended to be detailed enough to provide accurate results without infringing upon proprietary information.

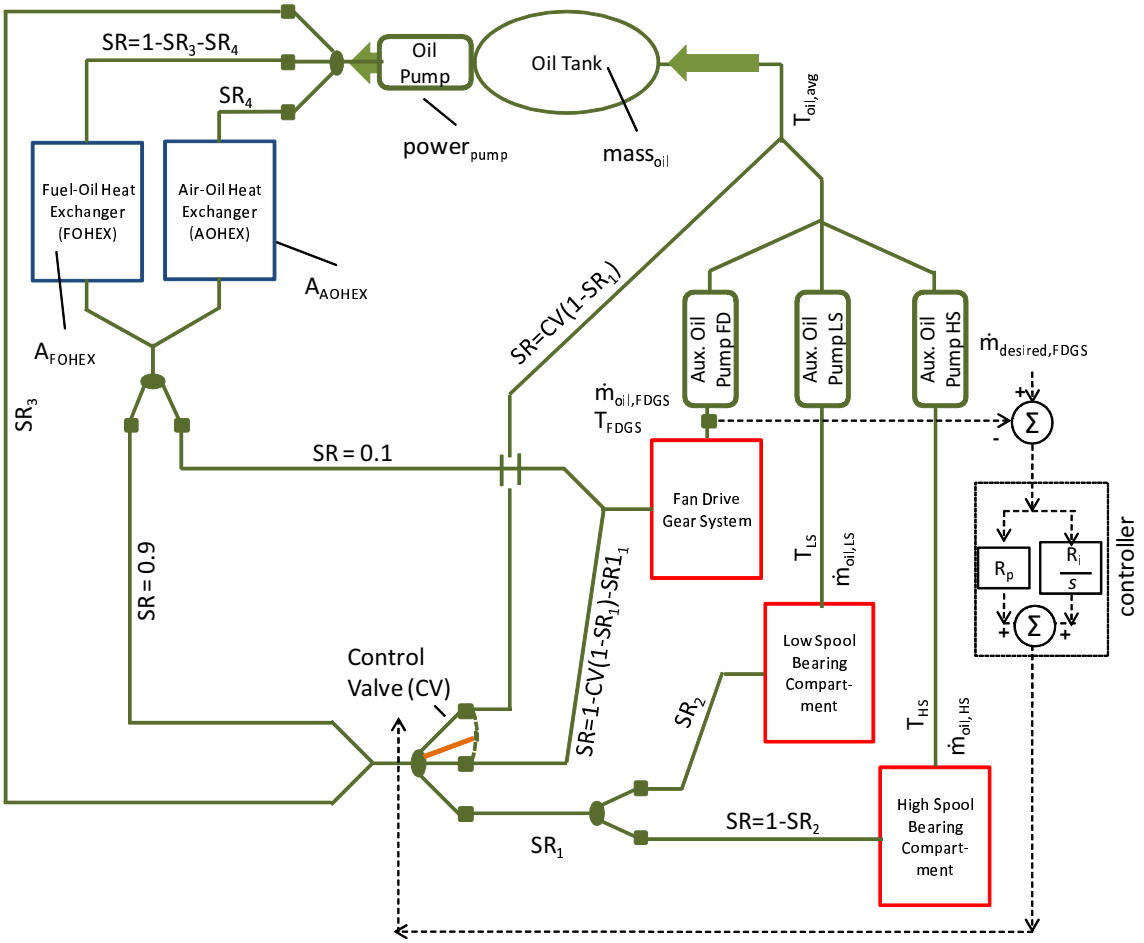

Figure 6-2: Geared turbofan engine lubrication system as modeled in MATLAB's Simscape

Oil mass flow ($\dot{m}_{oil}$) is modeled as a source stemming from the main oil pump series just downstream of the oil tank in Fig. 6-2. This mass flow varies as both a function of engine RPM (spool speed), during simulation, and the pump size. Downstream of the oil pump, the flow splits into three separate lines, with one flowing to the AOHEX, one to the FOHEX, and a bypass path in place for the event in which one of the heat exchangers fails. After the heat exchangers, the flow splits again with a bypass allowing a minimum of oil to reach the critical FDGS. On the main line, a controller operates a bypass valve regulating oil to the FDGS in order to maintain

a target flow rate, minimizing the temperature in the fan drive gear system and diverting a small amount of bypass oil back to the tank. Auxiliary oil pumps located downstream of each of the bearing compartments and the FDGS ensure that positive oil pressure is maintained at the compartment exits, preventing oil from pooling in the corresponding bearing housings or gearing. Mass flow through each of the oil line segments varies according to the inverse of its size ratio (SR).

Although it is necessary to model the system in Simscape to correctly characterize oil temperature variation with time and thermal mass, analytic equations for the steady state mass flow rates through the main component lines are relatively straightforward. These are given in Eqns. 6.1 - 6.4 and lend insight into the mass flow dependencies on the system architecture.

$$\dot{m}_{oil,HS} = \dot{m}_{oil} SR_1 (1 - SR_2)(0.1 SR_3 + 0.9) \tag{6.1}$$

$$\dot{m}_{oil,LS} = \dot{m}_{oil} SR_1 SR_2 (0.1 SR_3 + 0.9) \tag{6.2}$$

$$\dot{m}_{oil,FDGS} = \dot{m}_{oil}(1 - CV(1 - SR_1) - SR_1)(0.1 SR_3 + 0.9) + 0.1(1 - SR_1) \tag{6.3}$$

$$\dot{m}_{oil,CVbypass} = \dot{m}_{oil} CV (1 - SR_1)(0.1 SR_3 + 0.9) \tag{6.4}$$

The Simscape model generates time-variant output for a number of performance parameters. It takes as input a single flight profile, given in matrix form where row-oriented parameters vary as a function of time across the columns. These flight profiles may be cruise, takeoff, landing, or any other type of maneuver for which the engine can be modeled in GasTurb11 [64], a medium- to high-fidelity, commercially used engine design software, developed under coordination with MTU Aero Engines in Germany. For the study presented here, a geared turbofan engine was first designed in GasTurb11 for optimal cruise conditions in an operationally representative cruise-climb profile (35k ft to 42k ft altitude at Mach 0.82). The output from this engine/profile are the parameters listed in the profile parameter set shown in Fig. 6-3. This provides, from the perspective of the oil system, the typical operational parameters to which the lubrication system must be designed.

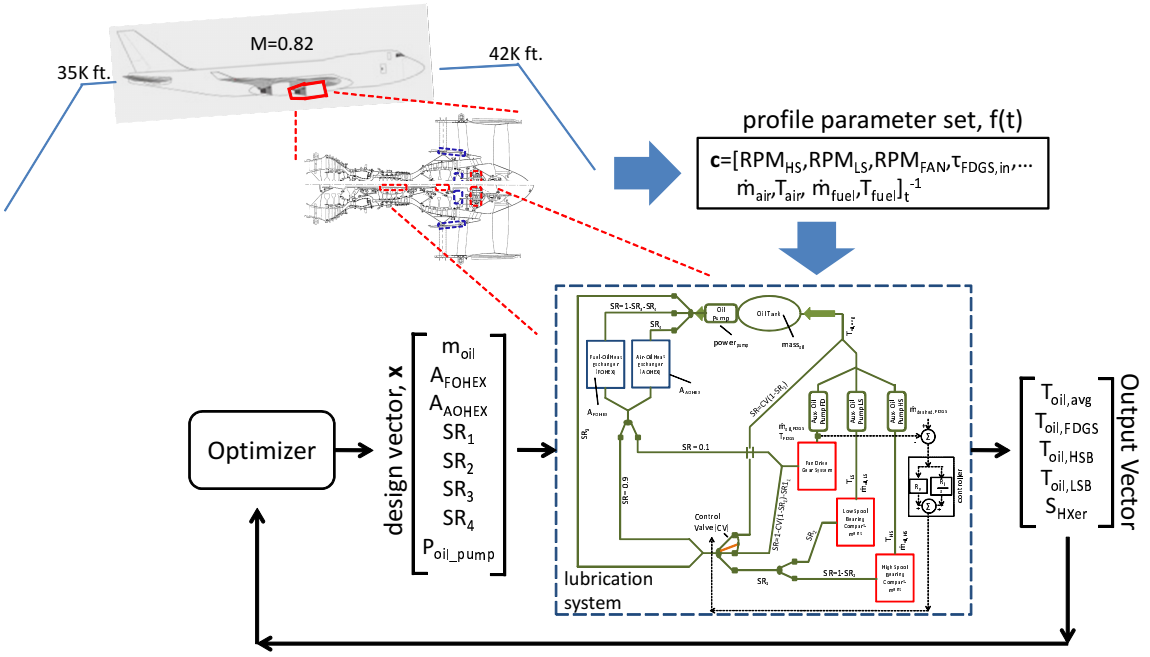

Figure 6-3: Baseline (nominal) optimization flow

The baseline nominal case optimization follows the flow depicted in Fig. 6-3, where Eqn. 6.5 shows the formal, single objective optimization problem:

$$
\begin{aligned}
\textit{given} \quad & \text{parameter set, } \mathbf{c}\text{, controller gains, } \mathbf{r} \\
& \mathbf{c} = [RPM_{HS}, RPM_{LS}, RPM_{FAN}, \tau_{FDGS,in}, \dot{m}_{air}, T_{air}, \dot{m}_{fuel}, T_{fuel}]_t \\
& \mathbf{r} = [R_p, R_i] \\
\textit{minimize} \quad & J(\mathbf{x}, \mathbf{r}, \mathbf{c}) = T_{oil,avg}(\mathbf{x}, \mathbf{r}, \mathbf{c}) \\
& \mathbf{x} = [m_{oil}, A_{AOHEX}, A_{FOHEX}, SR_1, SR_2, SR_3, SR_4, P_{pump}] \\
s.t. \quad & x_{i,LB} \leq x_i \leq x_{i,UB}, \qquad i = 1, 2, ..., 8
\end{aligned}
\tag{6.5}
$$

The multistate problem is significantly more complex in construction and execution, namely because the lubrication system analysis must be executed for several failed modes of operation in addition to the nominal case. A description of this setup is given in the next section.

The oil system presents a meaningful design problem involving trade-offs between the lubrication and temperature requirements of each of the bearing compartments

and the FDGS, the size of the air and fuel heat exchangers required to maintain operating oil temperature, and the oil flow rate supplied by the engine and oil pump. The bearing and gear compartments are typically designed to specifications that result in a minimum operating temperature occurring at a specific oil mass flow rate. Thus the overall system must provide these target flow rates, which are different for each of the components, while at the same time managing flow rates to the air and oil heat exchangers in order to maximize heat extraction.

6.6 Step 5 - Markov Analysis

A good description of the general multistate problem setup and Markov analysis is found Chapters 3, 4, and 5, therefore the following focuses on the multistate formulation issues specific to the GTF lubrication system.

Given that the state performances, G^s_K, do not depend on the order of failure, the symmetric Markov chain requires only eight states, as shown in Fig. 6-4.

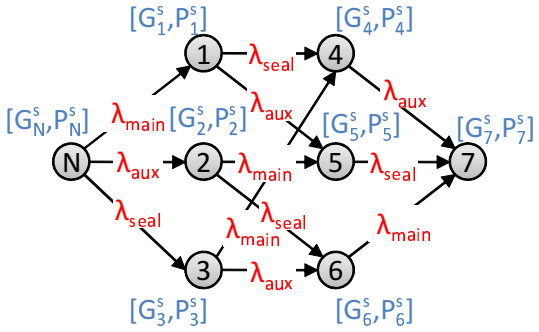

Figure 6-4: GTF lubrication system Markov formulation

The solution to the above chain yields the state probabilities, $P^s_{K,1,..,7}$, corresponding to the nominal state, N, and each of the failed states, 1 through 7. The probability set, $\breve{\mathbf{P}}^{\mathbf{s}}$, and state performance set, $\breve{\mathbf{G}}^{\mathbf{s}}$, are computed at each iteration in the multistate optimization process shown in Fig. 6-5.

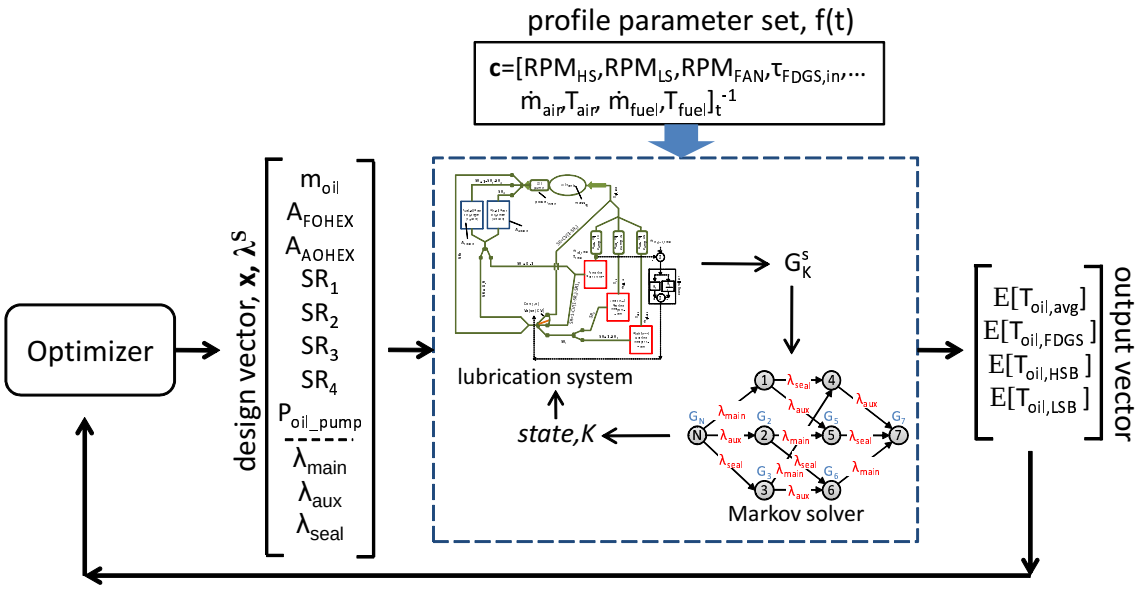

Figure 6-5: GTF multistate optimization flow

Equation 6.6 gives the formal multistate optimization statement:

$$
\begin{aligned}
&\textit{given} \quad \text{parameter set, } \mathbf{c}\text{, controller gains, } \mathbf{r} \\
&\qquad \mathbf{c} = [RPM_{HS}, RPM_{LS}, RPM_{FAN}, \tau_{FDGS,in}, \dot{m}_{air}, T_{air}, \dot{m}_{fuel}, T_{fuel}]_t \\
&\qquad \mathbf{r} = [R_p, R_i] \\
&\textit{minimize} \quad -E_G(\mathbf{x}, \boldsymbol{\lambda}^{\boldsymbol{s}}, \mathbf{r}, \mathbf{c}) = -\sum_{K=N}^{7} P_K^s(\boldsymbol{\lambda}^{\boldsymbol{s}}) T_{oil,avg,K}(\mathbf{x}, \mathbf{r}, \mathbf{c}) \quad \textit{or} \\
&\qquad -\tilde{S}_{E_A}(\mathbf{x}, \boldsymbol{\lambda}^{\boldsymbol{s}}, \mathbf{r}, \mathbf{c}) = -\sum_{K=N}^{7} P_K^s(\boldsymbol{\lambda}^{\boldsymbol{s}}) \{ \frac{b}{b^{(max[1+(350-T_K(\mathbf{x},\mathbf{r},\mathbf{c})),1])}} \} \\
&\qquad \mathbf{x} = [m_{oil}, A_{AOHEX}, A_{FOHEX}, SR_1, SR_2, SR_3, SR_4, P_{pump}] \\
&\qquad \boldsymbol{\lambda}^{\boldsymbol{s}} = [\lambda_{main}, \lambda_{aux}, \lambda_{seal}] \\
&s.t. \quad x_{i,LB} \leq x_i \leq x_{i,UB}, \quad i = 1, 2, ..., 8 \\
&\qquad \lambda_{i,LB}^s \leq \lambda_i^s \leq \lambda_{i,UB}^s, \quad i = 1, 2, 3
\end{aligned}
\tag{6.6}
$$

In Chapter 5, a cost was associated with increasing the MTBF of any particular component, and this was incorporated into the overall UAV system cost model. For the lubrication system study, however, the cost model was not readily available

(although it is generally available to the manufacturer). The result is that including the component failure rates as variables in Eqn. 6.6 above will nearly always result in failure rates being driven to their lower limits. Nevertheless, these variables were included in the sensitivity analyses of Section 6.7.1, which allows direct comparison between failure rate driven sensitivities and those driven by the static design variables, even in the absence of cost.

6.7 Step 6 - Analysis and Visualization of Results

Step 6 presents the results according to a logical process intended to highlight the differences between the traditional, nominal design solution and the multistate solution. First, a Pareto optimal solution for the nominal case is taken from the Pareto front in Fig. 6-9 (this chart will be described further at the end of the section). This is chosen as Point 5 from the nominal front, which occurs just before further increases in heat exchanger size become ineffective in reducing system oil temperature. Next, this point is examined in Figs. 6-6, 6-7, and 6-8, from a multistate perspective, to illustrate the behavior of performance and sensitivities under the influence of numerous failure states. Finally, Pareto fronts are constructed using the multistate system expected performance and availability for time periods of 100- and 500-hrs respectively, time periods which might be experienced between instances of scheduled maintenance on various geared turbofan engines. The final results demonstrate significant improvement in expected availability between the nominal case design point and the multistate design points.

The important design variables, $\mathbf{x}$, for the lubrication system shown in Fig. 6-2, are given in Table 6.3 along with the upper and lower limits used in the design optimization described in the next section. Output of the analysis is the average oil temperature, the temperature of the oil in the bearing compartments and the FDGS, and the size of the air and fuel heat exchangers.

In this case study, the number of states is low enough to individually observe the outputs of G_K^s for several different design perturbations. This provides insight into

Table 6.3: Lubrication system design variables

Design Variables	$\mathbf{m_{oil}}$ [kg]	$\mathbf{A_{AOHEX}}$ [m^2]	$\mathbf{A_{FOHEX}}$ [m^2]	$\mathbf{SR_1}$ [nd]	$\mathbf{SR_2}$ [nd]	$\mathbf{SR_3}$ [nd]	$\mathbf{SR_4}$ [nd]	$\mathbf{P_{pump}}$ [kW]
$\mathbf{x_{lb}}$	50	0.5	0.5	0.35	0.1	0.05	0.05	0.3
$\mathbf{x_{init}}$	55	1	1	0.5	0.5	0.2	0.55	1
$\mathbf{x_{ub}}$	60	1.3	1.3	0.95	0.8	0.9	0.8	1.5

how the performance thresholds interact with design changes on a state-specific basis, as shown through the quad-plots of Fig. 6-6.

Each quadrant of the plot is a representation of two critical system temperatures. These are chosen from the system average oil temperature, T_{avg}, high bearing oil temperature, T_{hb}, low bearing temperature, T_{lb}, and the fan drive gear system temperature, T_{fdgs}. The pairing of temperatures in each quadrant is for purposes of illustration, helping to spread out the points along two axes instead of one, without affecting temperature magnitude representation. Note that the scales in each quadrant are increasing positive outward from 200 to 500 degrees Fahrenheit.

In each quadrant are 17 design points, made by taking the nominal design point as baseline and perturbing each of the eight design variables in Table 6.3 by $\pm$ 10%. The blue dashed lines are the location of the nominal design point. The red dashed lines indicate the operationally critical temperature of 350 deg F.

As one would hope, in the nominal state, the baseline design as well as each of the perturbed designs is located well within the safe region for each of the temperature metrics. In the case of State 1, however, the baseline design remains under limits for the FDGS, low bearing, and average system oil temperatures, but far exceeds the limit for the high bearing temperature. This is due to the fact that the high bearing oil temperature is much more sensitive to reductions in oil flow than the other components.

Also of interest is that some of the designs in the upper right quadrant of State 1 span the critical temperature limit for T_{avg}. This indicates an area where small changes to design variables other than component failure rates can affect the system's availability, which depends on the crossing of a performance limit threshold. In the case of State 1, these changes promote a crossing from the baseline to an unsafe area

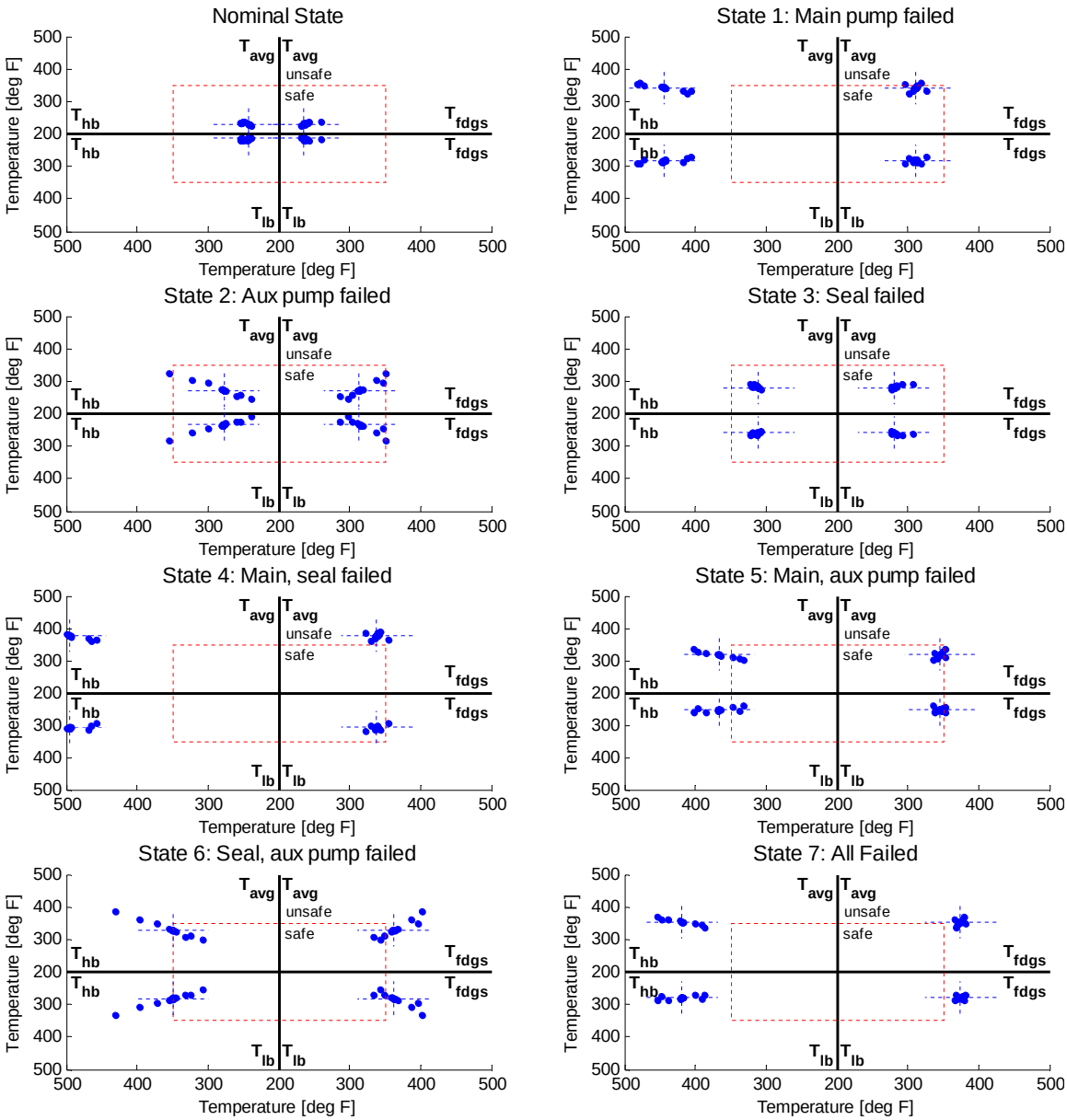

Figure 6-6: Quad-plots of oil temperatures

of operation, but in States 5 and 6, one observes cases where the baseline exists in the unsafe region and changes to any one of several design variables move the system back into the safe region. The most compelling example is State 6, where the nominal design point lies nearly on the limit for each of the temperature criteria, and several design changes are possible which simultaneously move each of the temperatures towards center.

6.7.1 Design Sensitivities

Insight into how one accomplishes this is provided by examining the design's sensitivity to changes in both static design variables (those given in Table 6.3) and component failure rates. Figures 6-7 and 6-8 show exactly this, where sensitivity of expected performance and expected availability are plotted for three separate cases: the nominal case, a 100-hr time period, and a 500-hr time period.

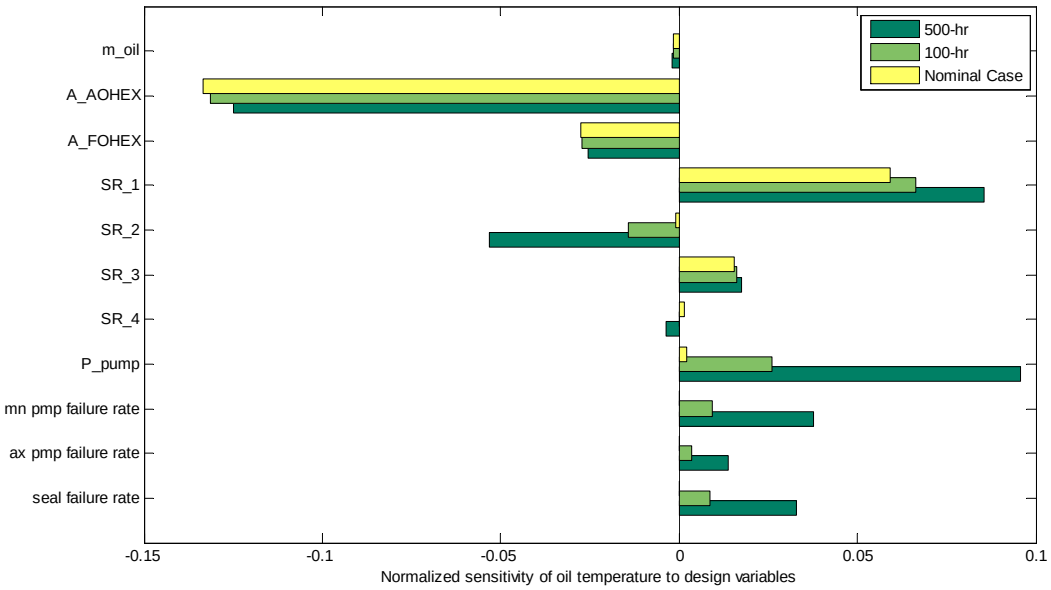

Figure 6-7: Expected performance sensitivity (avg. oil temperature)

Figure 6-7 shows the system's expected overall oil temperature variation with changes to design variables and component failure rates. Since a lower temperature is desirable, negative sensitivities indicate improvement. The low sensitivity to oil mass (m_{oil}) was anticipated since the simulation was carried out over an entire cruise segment, allowing ample time for temperatures to stabilize. The small positive effect that does exist is a result of the variation in thermal mass heating and cooling rates picked up by the simulation. Of special interest in this chart is that several of the design variables, such as the area of the air-oil heat exchanger (A_{AOHEX}), the size ratio of the low and high-spool feed line (SR_1), and the max power of the main pump

(P_{pump}) have a greater effect on the overall expected performance than do changes in the component failure rates. Additionally, although small in magnitude, increasing the size ratio of the feed line to the AOHEX (SR_4) actually hurts performance in the nominal case, but helps it in the 500-hr multistate case. This is because the increased size disrupts the on-design balance of heat extraction between the AOHEX and FOHEX in the nominal state, while in the off-nominal states where the FOHEX seal has failed, the increased size improves flow to the AOHEX, thus improving system cooling.

Figure 6-8 shows the same sensitivities as in Fig. 6-7, but for expected availability instead of expected performance. Since expected availability is not defined for the short time-span, nominal case scenario, here only the 100-hr and 500-hr analyses are shown. The data indicate that, in general, significant improvements to availability may be made by increasing the cooling area of the AOHEX, decreasing the size ratio of line 1, or increasing that of line 2. These trends correlate closely with those of Fig. 6-7 (note that availability improves when it is increasing, while expected performance, measured as temperature, improves when it is decreasing).

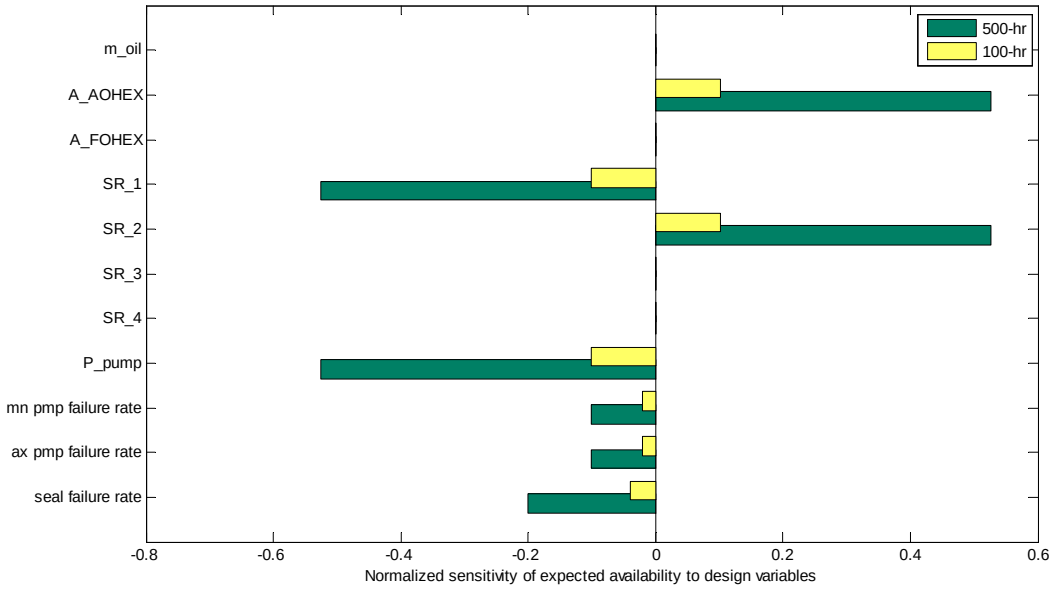

Figure 6-8: Expected availability sensitivity (oil temperature criterion)

6.7.2 Analysis of Pareto Fronts

Using Eqn. 6.6 (with fixed component failure rates) and a Normal Boundary Intersect (NBI) algorithm, the multistate Pareto fronts in Fig. 6-9 were constructed for average system oil temperature vs. oil cooling system size. In the case of the nominal front, only the nominal state oil temperature was included in the objective function (Eqn. 6.5), while the 100-hr and 500-hr fronts include all state temperatures, weighted by the Markov probabilities resulting from the solution to the Markov chain in Fig. 6-4. Solution time for each point on the nominal front was approximately 1.25 hours on an Intel Quad i7 2.8GHz CPU and 3.5-4 hours for the multistate fronts. Fortunately, the NBI method is easily modified for parallel computation and the total time to generate the fronts was greatly reduced by distributing across multiple processors.

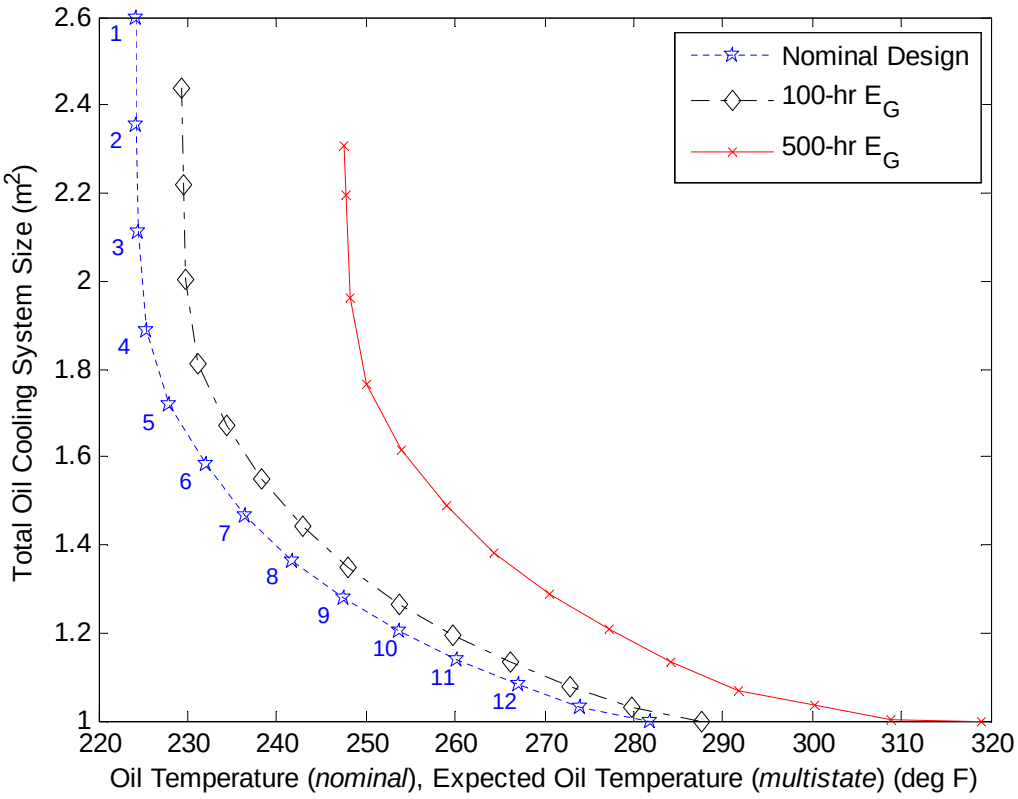

Figure 6-9: Comparison of nominal and multistate Pareto fronts

As expected, the two multistate fronts shift to the right, due to the inclusion of the failure states that have higher temperatures and higher probability of occurring as the period of time increases. However, measurable improvement is realized when comparing the expected *availability* of the best design point taken from the nominal front (Point 5) to those of the best multistate designs, as shown in Fig. 6-10. Point 5, analyzed for the 100-hr time period, has $E_{A,N}^{100}$=0.923, while the 100-hr multistate design is 2% better with an availability of 0.942. The percent gain for the 500-hr analyses is even larger, at 10%. These are significant improvements, considering that they do not include the effect of decreasing component failure rates and were achieved merely by affecting the system's architectural design.

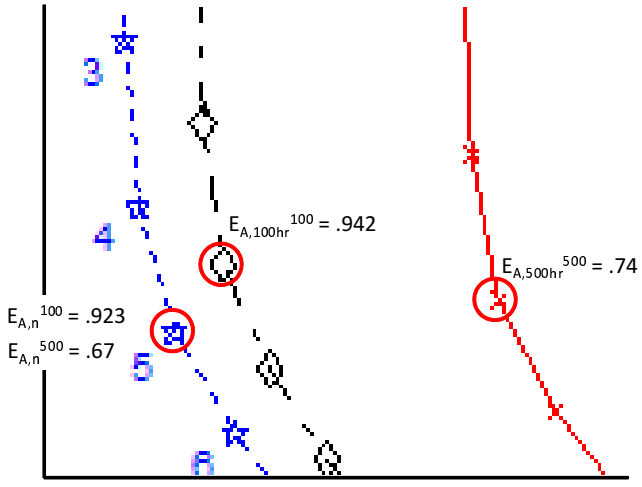

Figure 6-10: Blow-up of expected performance Pareto fronts showing improvement in expected availability

The sensitivity plots in Figs. 6-7 and 6-8 indicated that availability and expected performance were positively correlated for the lubrication system study. To determine whether further improvements to E_A were possible, Pareto fronts for system *availability* vs. oil cooling system size were constructed using the NBI algorithm with the surrogate function for availability, $\tilde{S}_{E_A}$. Figure 6-11 shows results for these Pareto fronts, along with the exact values of availability for each design point.

Unlike the Pareto front estimations shown for the UAV case study in Fig. 5-13, of Chapter 5, Fig. 6-11 shows the lubrication system availability breaking into three

distinct levels across the range of cooling system sizes. This is due to a couple of reasons, mostly the fact that the lubrication study involves many less states (eight vs. sixty-four in the former), and that the design space for this lower level system is less complex than that of the UAV system. The lowest availability levels are E_A=0.67 and E_A=0.923 for the 500-hr and 100-hr intervals, respectively. This lowest level is populated by the design points in which only the nominal state achieves acceptable performance.

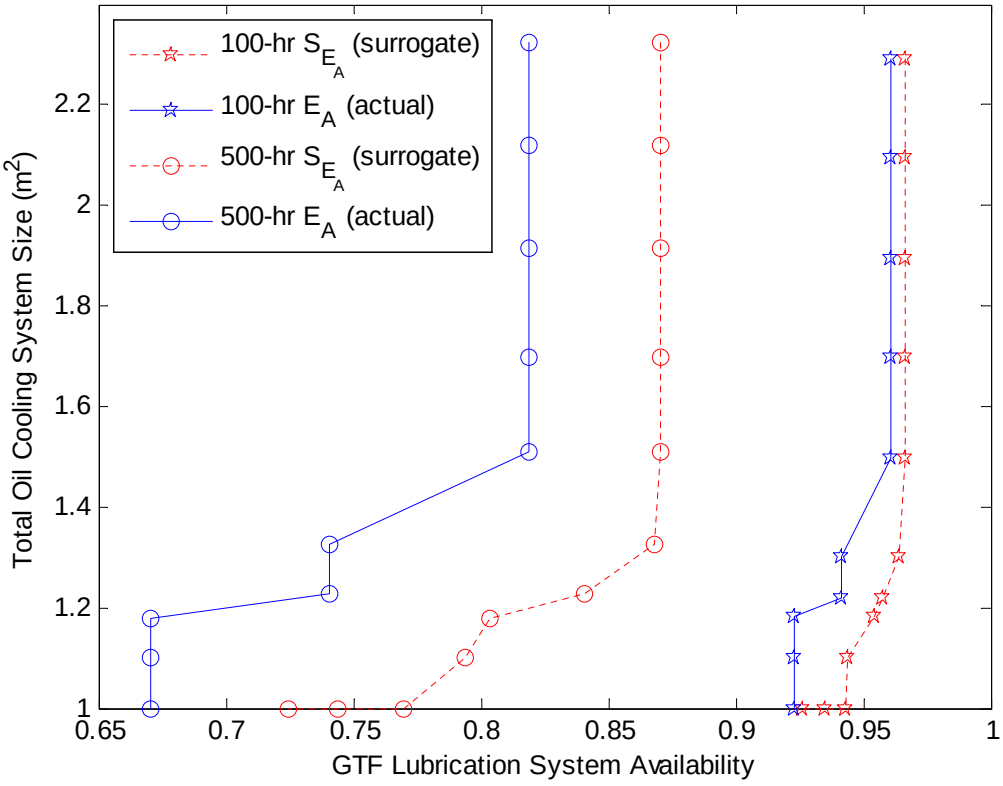

Figure 6-11: Comparison of surrogate function and actual availability Pareto fronts

The next highest level of availability has E_A=0.741 and E_A=0.942 for the two time intervals. These are design points in which both the nominal state and State 2 (aux pump failure) maintain acceptable temperatures. They are also the levels achieved by the best expected performance design points of Fig. 6-10. Finally, the highest level of availability is characterized by E_A=0.819 and E_A=0.961. It occurs

as State 2 leaves the acceptable set and State 3 (FOHEX seal failure) enters (note that $P_3^s > P_2^s$). These values of availability represent improvements of 22.2% for the 500-hr case, and 4.1% for the 100-hr case, when compared to the values of availability resulting from the nominal design optimization.

In general, the surrogate function for availability satisfactorily modeled the trends for actual availability. The smoothing term base (see Eqn.6.6) was b=10 for the 500-hr interval and b=50 for the 100-hr interval, as these were determined through experimentation to provide the best results. The 100-hr interval required less smoothing than did the 500-hr interval because the degree of change between availability levels was much smaller. The different bases are also evident in the difference between magnitudes of actual and surrogate results for each respective time interval. In both cases, however, the trends in exact availability are in agreement.

Finally, the Normal Boundary Intersect (NBI) method for Pareto front determination is very unforgiving in regions where the front is concave. Therefore, some of the convergence criteria were relaxed on the point optimizations in order to prevent extraordinarily long run times. The point spacing on the $\tilde{S}_{E_A}$ fronts are somewhat less than uniform in certain areas as a result. This did not significantly affect the E_A fronts. In fact, some of the points on the front for exact availability would not have been found without the smoothing provided by the surrogate function.[2]

6.8 Case Summary

This chapter applied multistate analysis and design to the lubrication system of a geared turbofan engine. Where previous case studies demonstrated the methodology on higher level aircraft systems, this study focused on a lower level subsystem, demonstrating that, even with a less complex design space and fewer states, significant improvements can be made to the system's availability through static design variables alone. Additionally, shorter analysis times allowed computation of full Pareto fronts

[2]The points that would not have been found are the ones lying to the left of a straight line drawn between the points for maximum and minimum cooling system size, as the NBI algorithm [33] only searches in a direction of combined improvement w.r.t. (to the right of) the intersect line.

for expected availability using the surrogate function introduced in Chapter 4.

The following points summarize key findings from this case study:

- Even in the simpler design space characterized by the lubrication subsystem, sensitivity of expected performance to changes in static design variables varied significantly between the nominal case and two multistate scenarios of differing time duration (Fig. 6-7). In one case, the sign of the sensitivity even reverses trend. The impact of this is that, designing for best performance in the nominal scenario, while affecting availability only through component failure rates, will likely result in an inferior multistate design.
- The surrogate function for availability, $\tilde{S}_{E_A}$, proved effective within a gradient-based algorithm for generation of Pareto fronts. Although convergence in some areas of the approximated front led to very long optimization times, the function was still able to generate an accurate representation of the Pareto front for actual availability.
- Variation of static design variables alone led to improvement of subsystem availability by 22% over a time duration of 500-hrs (Fig. 6-11). When considering oil system cooling size as a representation of cost, and adjusting accordingly, the best Pareto solution still resulted in an improvement of 10%. These gains are promising and suggest that further analysis with a more detailed model for cost and performance would be beneficial to the engine manufacturer.

Chapter 7

Conclusions

This final chapter begins by summarizing key results of the thesis. It draws together major findings and conclusions arising from the three central case studies, and uses these to develop some general principles for early-phase multistate analysis and design. Finally, areas for future research are suggested, with a short summary of progress-to-date in those directions.

7.1 Summary

The thesis lays a foundation for the in-depth and comprehensive exploration of complex, multistate, early-phase design spaces. Advances in design optimization, computing power (including parallel processing), and certain reliability analysis techniques enable this endeavor, whereas in the past it has remained prohibitively challenging. The research integrates, refines, and tests these methodologies on several case studies with high-dimensional performance state spaces.

The first chapter presents the compelling argument that, given current levels of technology in component reliability, operators must accept the fact that ultra long endurance systems, as demonstrated in Fig. 1-1, will likely *not* remain in their nominal state of operation throughout their service duration. Thus, design practices that focus on this state, even in the earliest phases, will result in suboptimal systems. This is verified through results in all three case studies, including the design sensitivities of

Fig. 3-10 and Fig. 6-7, for the twin-engine aircraft and geared turbofan engine, and most dramatically through Fig. 5-11, for the ultra long endurance UAV.

With the above motivation, Chapter 2 further develops the case for including effects of static design variables, component failure rates, and control variables in the multistate design loop. It defines multistate in the context of the present research, placing scope within the appropriate rung of an extended hierarchy of system state change (Fig. 2-6). This hierarchy sets the bounds on all possible considerations of state within the context of system design, encompassing the search space potentially achievable as design technology and computational ability advance.

The twin-engine aircraft study in Chapter 3 takes the first step into this search space, demonstrating that the multistate performance behavior of a well-known and validated aircraft system clearly exhibits itself in design sensitivities driven by both static design variables *and* component failure rates. The performance model developed for the study is non-trivial and of significant fidelity, including elements for dynamic control of the aircraft system at each design point. It has been developed from simulation algorithms over ten years in the making [18] (see Appendix A), and subsequently validated by real world flight test data. Results from this first case study have also been recommended for publication in [1].

The lessons and experience gained from above are used to develop a generalized methodology for multistate analysis and design in the fourth chapter (Fig. 4-1). The methodology begins by identifying a broadened set of multistate requirements early in the design process and performing a preliminary analysis of failure modes to define the state transition rate vector, $\boldsymbol{\lambda}^{s}$, in advance of multistate computational analysis. Computational analysis then departs from traditional methods by integrating Markov state analysis directly into the design loop. This includes processes for determining multistate output as a function of static design variables, $\mathbf{x}$, component failure rates, $\boldsymbol{\lambda}^{s}$, and controller gains, $\mathbf{r}$, depending on the dynamics of the performance metric. The output of this is often a multi-objective performance space, defined by expected performance, nominal performance, system availability, and cost. The final step of the methodology outlines several techniques for visualizing this performance output

space, all of which are demonstrated throughout the thesis case studies. The above framework involves use of several tools from Multidisciplinary Design Analysis and Optimization (MDAO), as well as the thesis developed supporting methods of multi-layer Markov analysis and a surrogate function for system availability (both of which are described in the last sections of Chapter 4). Figure 7-1 maps the use of these techniques to the thesis case studies.

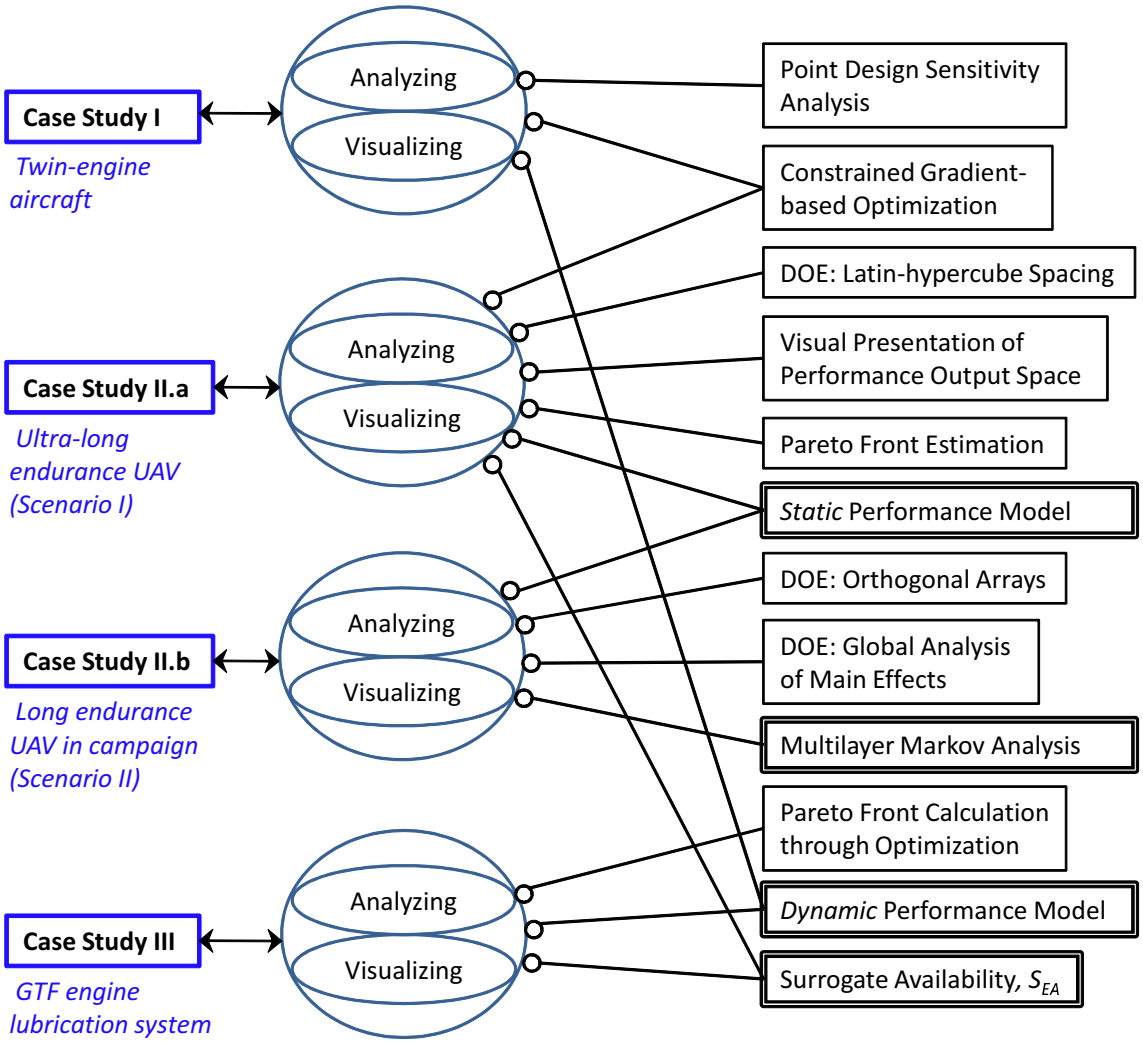

Figure 7-1: Object-Process Diagram mapping of methods and techniques to case applications, double borders indicate supporting objects developed in thesis

The fifth chapter introduces the long endurance UAV case study, broken into its two scenarios in Fig. 7-1 for ease of depiction. *Scenario I* of this case is an ultra long

endurance UAV with a mission duration of three months aloft. Here, a full analysis of the DOE sampled design space for differing combinations of independent variables shows clear distinction between each of the performance output spaces arising from: a) component failure rate variation, b) static design variable variation, and c) combined variation of both. The overlay plot in Fig. 5-13 portrays this best, depicting a region of improved performance resulting from c), above, that is unachievable through either a) or b). *Scenario II* is the case of a one-to-two day duration vehicle, involved in a 5-year multi-sortie campaign requiring omnipresence over the mission area. This scenario makes use of the multilayer Markov analysis technique to extend vehicle level performance metrics to the campaign level. The design space is systematically sampled via an orthogonal array and main effects of aircraft design variables on attrition and sortie abort rates are plotted, showing an observable and measurable link between the two.

Finally, Chapter 6 moves from the higher aircraft system level down to the lubrication subsystem of a geared turbofan engine. The multistate methodology proves effective on this lower level system as well, taking advantage of the computationally cheaper performance analysis to broadly demonstrate use of the surrogate availability function, $\tilde{S}_{E_A}$, across a range of gradient-based optimizations. While results of this study showed less of a trade-off between expected performance and availability, due to the simpler interaction between failure states, these metrics were still more sensitive to changes in many of the static design variables than they were to changes in component failure rates (Fig 6-7 and Fig. 6-8). Additionally, when compared to the nominal case design, significant improvement in subsystem availability was realized through variation of static design variables alone.

To conclude the thesis summary, the contributions of this research are outlined below:

- **The central multistate analysis and design methodology.** This includes the novel integration of Markov state analysis into the early-phase design loop as shown in Fig. 4-1, of Chapter 4. Initial feasibility of the methodology is demonstrated in Chapter 3, and it is successfully applied in Chapters 5 and 6.

- **Demonstration of the cost and benefits, in the form of design trade-offs, associated with a multistate design approach as compared to pure reliability analysis or the nominal design approach.** This is most clearly shown in the results of Chapter 5, Fig. 5-13 and Tables 5.4, 5.5, and 5.6. It is also observable in the design sensitivities of case studies in Chapter 3 and Chapter 6.

- **A multilayer approach, using Markov analysis, for translating single sortie vehicle level metrics into measures of multistate campaign performance.** The process for multilayer Markov analysis is described in Section 4.2.1, of Chapter 4, including a detailed example problem. It is applied in Section 5.6.2, of Chapter 5. Data linking vehicle static design variables to campaign level metrics for attrition, failed sorties, and availability are found in Figs. 5-19 through 5-22.

- **A surrogate function for system availability that allows the otherwise piecewise-constant metric to be optimized via gradient-based optimization algorithms.** The function is first introduced in Section 4.2.2, of Chapter 4. It is successfully used in Chapter 5 in the constrained gradient-based optimization of Eqn. 5.5, with results in Fig. 5-15. It is again used in Chapter 6 to generate the Pareto fronts of Fig. 6-11.

7.2 Major Findings and General Principles in Multistate Analysis and Design

The above section highlighted three central case studies: the twin-engine aircraft (Chapter 3), the long endurance UAV (Chapter 5), and the geared turbofan engine lubrication system (Chapter 6). This section focuses in more detail on the major findings from those case studies, some of which are evident from the results, and others which were more implicitly evident through the process of examination itself. Several general principles are then suggested for consideration in future multistate

analysis and design endeavors.

The major findings, in order of what the author considers most significant to least significant, are given below:

1. *Each of the output spaces for the ultra long endurance UAV system availability had distinctly unique shapes and boundaries*, depending on whether they were formed by: a) component failure rate variation, b) static design variable variation, or c) combined variation of both. The availability obtained by variation of both was unachievable through variation of either independently. Those solutions generated via component failure rates came at the expense of higher cost with no effect on nominal performance, while those generated via static design variables came at the expense of lower nominal performance with much lower overall cost. The combined design space struck a balance between the two *and* significantly extended the increase in system availability.

2. *Results from all three case studies showed that small changes in static design variables may be used to improve system availability and expected performance.* Furthermore, these sensitivities were quantifiable. In the case of the twin-engine aircraft, the shifts were a result of improvement in stability and control characteristics brought about by a larger control surface. With the UAV, there was broad improvement across numerous states resulting from the lower required trim moments of a slightly increased wing sweep. The lubrication system solution achieved improvement by increasing the size ratio of an oil line that improved cooling in the most likely failure state.

3. *In general, there were competing objectives between system availability and nominal performance, and to a lesser degree between system availability and expected performance.* This is shown most directly through the Pareto front estimations in the UAV case study, with emphasis on the fact that the nominally designed aircraft was characterized by a design point lying extreme opposite of the non-dominated Pareto points for maximum system availability. The competing trend between system availability and expected performance was much weaker

in the lubrication system study, noting that the best choice for expected performance was also near the best choice for system availability. This is explained by the following. To a certain degree, availability and expected performance will rise together, as both attempt to better distribute performance, G_K^s, across their weighted objective formulations. As more and more state thresholds, W, are crossed, however, expected performance continues to push all G_K^s up, while availability only pushes those G_K^s up that have not achieved W. Thus, a highly optimized availability will pull the extra few percent of improvement from the performance surpluses of states in the *acceptable* set, thus decreasing expected performance. In the case of the simpler lubrication system, there were many less surpluses to be exploited than in the more complex UAV case. This emphasizes the importance of performing a multi-objective analysis for systems in which both performance and availability are important.

4. *The extension of Markov analysis to the campaign level in the UAV study showed a clear relationship between vehicle static design variables and the higher level metrics of sorties* failed *and* lost. Many of these showed unique trends arising not only from vehicle performance behavior, but also from the passage of states between the varying degrees of acceptance categories. The same wing sweep effect described in Finding #2 was also observed here.

5. *The surrogate function for system availability was effective in guiding the path towards improved E_A, even when the actual and surrogate values of availability were not in close agreement.* In the UAV case study, this function was used to improve availability from an initial design point that was already quite close to the final solution. The required smoothing was minimal and the surrogate approximation value was nearly equal to that of the actual value. In the lubrication system study, the function was used across a broader Pareto front, requiring much more smoothing. As a result, the surrogate value was significantly higher than the actual value. The exact Pareto front, however, was accurate. Since the function is intended to model the *shape* of the availability

output space, and not its *value*, this behavior is expected. In fact, the value of surrogate availability should always be higher than exact availability, in all but the case where exact availability is equal to 1.0. This is because the surrogate function includes within its summation a fraction of every state's performance deficiency, while the exact availability function does not (see Eqn. 4.12 and Fig. 4-9 in Chapter 4).

The above findings assist in developing some general principles concerning multistate analysis and design in the early-phase development of complex systems. The first of these relates to the issue of trade-offs discussed in Finding #3, and is succinctly stated as:

> **The general multistate problem is also a multi-objective one with competing trade-offs between nominal performance, system availability, expected performance, and cost.**

The degree of these trade-offs will depend on the system under investigation and the nature of the objective performance metric. Typically, cost will rise strongly with nominal performance, but if means of improving multistate performance are weighted heavily towards the component failure rates, expected performance and availability may also correlate strongly with cost.

The amount of competition between expected performance and system availability will depend in the factors discussed in Finding #3. Specifically, if the individual state performances within the set, $\check{\mathbf{G}}^{\mathbf{s}}$, have gradients that vary to a large degree in magnitude and sign, a highly optimized availability will result in lower expected performance. On the other hand, if the sensitivities are aligned, where a direction of improvement for one state results in improvement for all, this will not be the case.

Finally, stating that improved expected performance (or availability) will always come at the expense of decreased nominal performance is incorrect. This is akin to saying that strengthening a constraint in an optimization problem will automatically result in a lower value of the objective function. If the constraint is active, it will result in a more limited optimum, but this activity will change throughout the design

space, in the same way as do state performances. It is probably safe to say that increasing expected performance will result in a lower nominal performance *near its optimum*, but even this does not always have to be true. If the gradients are aligned or strongly functions of differing design variables, they may move together or remain stationary.

The second principle makes a statement about the types of systems to which multistate analysis and design is best suited. It is given as:

> **The systems benefiting most from multistate analysis and design are systems with long operational durations and little opportunity for maintenance or repair, and systems involved in multi-system operations where costs of downtime and system loss are high.**

The above is not meant to preclude other types of systems from the methodology, but to assist in determining whether the extra effort of multistate performance analysis is worth it. For instance, the first type of system could just as easily read "systems with short operational durations and frequent maintenance opportunity, but very poor reliability of components." Such systems, however, are rarely encountered in modern aerospace design.[1]

There is one additional qualifier that should be mentioned regarding the above principle. The degree of applicability to these types of systems may, in some cases, depend on whether or not the system can afford to operate in other than the fully nominal state. One unique instance where this comes into play is that of commercial airliners. The concept of knowingly operating in a mechanically degraded state for an extended period of time may not be acceptable with a full load of passengers. This means that regardless of design changes to improve multistate performance, in actual operation one would not fully realize the improvement in availability or expected performance. The airliner would simply land as soon as possible. Although improvements would show up in terms of changes to the *acceptable/unacceptable* probability

[1] This is not necessarily the case for other industries, say, for instance, oil platforms.

distribution, i.e. the probability of entering the *unacceptable* performance set would decrease, the airline may be more interested in simply decreasing the transition rate out of the nominal state. Given their relatively short flight times and extremely tight margins on fuel efficiency, even a very small decrease in nominal performance may not be worth the decrease in risk of experiencing *unacceptable* performance.

Having stated this, there is, to the contrary, at least one documented example that suggests airlines might accept off-nominal operation if it can be shown that an acceptable safety margin still exists. In the 1990's, Draper Laboratories worked with a major engine manufacturer to show that the probability of engine failure remained below an acceptable threshold in the face of a partially failed engine controller [5]. The engine fitted with this Full Authority Digital Engine Controller (FADEC) was then allowed to continue revenue generating operations until the next scheduled maintenance period. In 1993, the Federal Aviation Administration circulated a policy letter (revised in 2001) allowing operators to deviate from Master Minimum Equipment Lists (MMELs) when fitted with such FADEC systems [49]. One should, of course, also note that the effects of such partial failures would not be observable by revenue generating passengers.

The third principle stems from Finding #1 and relates to the difference between using failure rates or static design variables to affect multistate performance:

> **Using component failure rates to increase availability or expected performance will tend to increase direct system cost, while using static design variables for the same can either increase or decrease this cost.**

Although this does not apply to operation and maintenance costs, which may very well decline over the system's lifetime, in most cases a higher MTBF component will not be cheaper than a lower MTBF component (and still provide the same functionality). On the other hand, the static design variables typically enter the cost function on the basis of manufacturing difficulty, material properties, etc. It is entirely possible that considering off-nominal states in the design formulation may actually result in

a cheaper design, especially in cases where the design backs off from its optimum nominal design as a result.

The final principle is simple, but perhaps not obvious:

In multistate system design, time often plays the role of both objective and constraint.

This is specifically true in the case of multistate long endurance systems, where the objective performance metric is to stay in operation as long as possible. As the improving design lengthens this period of operation, the probability distribution of performance begins migrating from the nominal state into the failure states. The result is a constraining effect on expected performance and availability as a mere result of the improved endurance. Simply put, the longer the system's endurance, the longer the period between maintenance opportunities, and the higher the chance of experiencing failures. This applies to shorter duration systems as well, although often the objective in such systems is not endurance but some other measure of performance.

Although this last principle seems to be common sense, it is a fact that many designers not familiar with reliability analysis might overlook. By the time the design makes it to the reliability engineers, it has already passed the point where useful improvement to the system's availability may be effected through static design variables. This is, hopefully, one of the key issues that the thesis has successfully addressed.

7.3 Future Research

There are a couple of areas most in need of advancement for further support of multistate analysis and design. One deals with the high computational burden associated with the multistate performance space. A promising solution to this problem is the use of state performance mapping to approximate off-nominal output spaces with that of the nominal. Modest work in this area has already begun as part of this research.

The goal of the performance mapping approach is to reduce computational effort required for evaluation of $G^s_{N+1,\ldots,M}(\mathbf{x})$ by exploiting similarities between the nominal

$G^s_N(\mathbf{x})$ and the off-nominal $G^s_{N+1,\ldots,M}(\mathbf{x})$ performance spaces. In many cases, for instance where a failure causes a simple change in motive resistance (drag), these performance spaces shift or stretch but, in general, retain very similar shapes. The mappings are obtained by solving the following problem:

$$\begin{aligned} &given \;\; \text{design vector } \mathbf{x}, \text{and response spaces } G^s_N, G^s_{N+1,\ldots,M} \\ &find \;\; \text{mappings } \; H_{N+1,\ldots,M} : G^s_N(H_{N+1,\ldots,M}(\mathbf{x})) \approx G^s_{N+1,\ldots,M}(\mathbf{x}) \\ &where \;\; H_{N+1,\ldots,M} \triangleq \underset{H_{N+1,\ldots,M}}{\text{argmin}} \sum_{j=1}^{L} \|G^s_N(H_{N+1,\ldots,M}(\mathbf{x^j})) - G^s_{N+1,\ldots,M}(\mathbf{x^j})\|^2 \\ &for \;\; L \text{ test points and } M-1 \text{ off-nominal states} \end{aligned} \tag{7.1}$$

Each off-nominal state corresponds to a unique mapping, as depicted in Fig. 7-2.

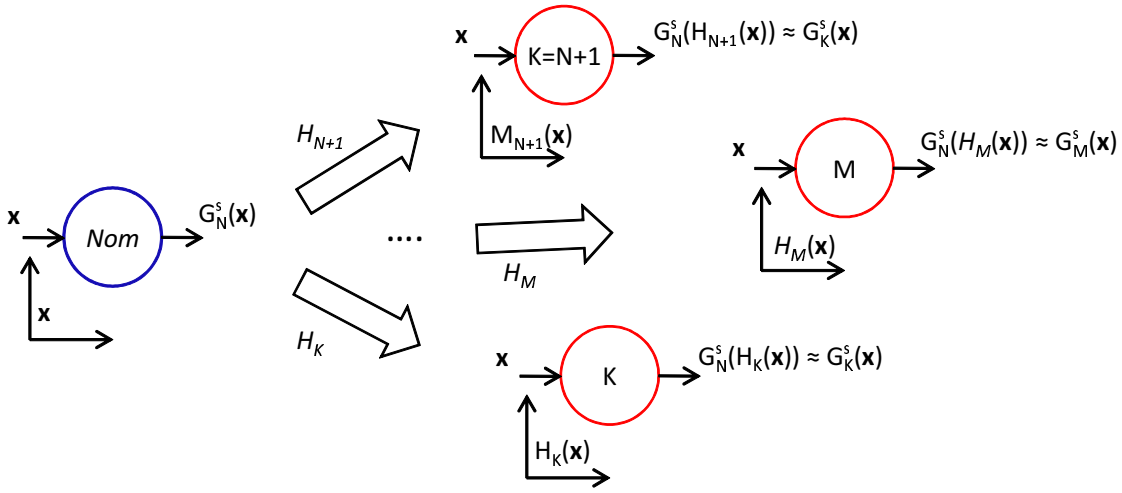

Figure 7-2: State performance space mapping

The minimization in Eqn. 7.1 searches only in G^s_N, but is performed for each of the $M-1$ off-nominal states. Therefore, much computational efficiency is gained by fitting a densely populated response surface to G^s_N and using it for all of the $M-1$ minimizations. Kriging surfaces [99] are particularly good for this because of the fact that they are exact at each of the test points. Ensuring that the test points j (relatively few) for each of the off-nominal states are a subset of the test points (relatively many) used in the Kriging surface fit should provide the best minimization

results.

The above approach was tested on the multistate Gaussian function described in Appendix D in order to demonstrate that the process shows increased computational efficiency for a relatively simple case with only two design variables. Four scenarios were run, each with M=64 states and L=30 test points. These scenarios were intended to determine:

1. Total number of function evaluations required to perform state performance mapping in Eqn. 7.1 *without* response surface modeling.
2. Total number of function evaluations required to perform state performance mapping in Eqn. 7.1 *with* response surface modeling of the nominal state.
3. Total number of function evaluations required to solve the optimization of Eqn. 4.9 in Chapter 4, but for expected performance instead of availability. This was performed *without* response surface modeling or performance mapping.
4. Total number of function evaluations required to do 3. above *with* response surface modeling and performance mapping.

A Kriging surface was used for all cases with a response surface. Enough points were used in the fitting of this surface that the minimization in Eqn. 7.1 was able to find the exact mapping parameters (which were known), thus there was negligible accuracy lost due to the surface approximation and the expected performance minima (- maxima) from 3. and 4. were nearly identical. Results were promising, and are given in Table 7.1.

There are two important observations to make from Table 7.1. First, the approach can significantly improve computational efficiency. The comparison between 3. and 4. shows over a 60% reduction in total required function evaluations to obtain nearly identical solutions for the optimization minima. Second, comparison between 1. and 2. shows that this improvement would be impossible without use of the response surface.

Table 7.1: Summary of state performance mapping results for the multistate Gaussian function

Scenario	# of function evaluations			
	Kriging formation	nominal state	off-nominal states	total
1.	n/a	97,760	1890	97,560
2.	900	0	1260	2160
3.	n/a	126	5698	5824
4.	900	0	1260	2160

Inspiration for this performance mapping approach came from the research area of multi-fidelity optimization, where space mapping is used to merge the optimization of low and high fidelity analysis models (see [13, 14, 28]). The two characteristics that make the state performance mapping unique are that Eqn. 7.1 must be solved $M-1$ times to obtain mappings for each of the off-nominal states, and that none of the states are necessarily cheaper to calculate than the other, as they are in the case of multi-fidelity analysis. This is the reason why the response surface is beneficial (which is not used in the multi-fidelity case). The main computational burden in Eqn. 7.1 comes from having to calculate G_N^s, $M-1$ times.

Although the preliminary analysis above shows promise for the approach, there is a tremendous amount of work that remains in order to fully prove its merit. This includes:

- Testing on a real-world problem where the form of the mapping function is not known *a priori*, as it is in the case of the Gaussian function.
- Determining the limits on M and L, outside of which the approach loses its computational benefit.
- Using the derivative of the mapping functions to estimate the off-nominal state Jacobians without directly calculating them. This can then be used to assist in the characterization of multistate systems, according to the degree of variability between gradients of individual state outputs (described further below).
- Dealing with the issue of design space boundaries, which arises as a result of

some mappings requiring analysis beyond the original, nominal state design space.

A second area recommended for future work involves further characterizing multistate systems according to the individual behaviors of their states. This will help to better understand and predict the multistate performance trade-offs discussed in Finding #3. Systems with a large degree of variability between gradients of individual state outputs should exhibit larger trade-offs between nominal and expected performance, and between availability and expected performance. The degree of this opposition will be evident through the sensitivities in the multistate Jacobian, defined here as,

$$\nabla \breve{\mathbf{G}}^{\mathbf{s}} = \begin{bmatrix} \frac{\delta G_1^s}{\delta x_1} & \frac{\delta G_2^s}{\delta x_1} & \cdots & \frac{\delta G_M^s}{\delta x_1} \\ \frac{\delta G_1^s}{\delta x_2} & \frac{\delta G_2^s}{\delta x_2} & \cdots & \frac{\delta G_M^s}{\delta x_2} \\ \vdots & \vdots & \ddots & \vdots \\ \frac{\delta G_1^s}{\delta x_{n_x}} & \frac{\delta G_2^s}{\delta x_{n_x}} & \cdots & \frac{\delta G_M^s}{\delta x_{n_x}} \end{bmatrix} \tag{7.2}$$

for n_x design variables and $K = M$ states.

As previously mentioned, it may be possible to efficiently determine this matrix via performance mapping, or at least estimate it to a degree that allows predictions to be made about the relative shapes of the state output spaces. Absent this, it is still possible to directly calculate gradients at predetermined DOE points. In both cases, the gradient information may then be used to pinpoint states that most conflict with the nominal, or to gain a general understanding of the performance trade-offs resulting from the multistate analysis.

As a final note on future work, there is one additional area where the methodology described in this thesis might be used to push the envelope on performance and cost. That is, namely, using multistate design to identify unnecessary design attributes and eliminate them from the system in order to either save cost or improve overall expected performance. Consider the design of a system composed of elements A, B, and C. If the multistate design and analysis methodology can show that when B and C fail, it is still possible to design with A such that the system achieves nominal or

near-nominal performance, it may be possible to go one step further and redesign the system with A to absorb the functions of B and C, thus eliminating them.

In truth, instances such as this have already occurred in aerospace design, but never from the probabilistic context of multistate analysis and design. The Northrop B-2 bomber is a flying wing configuration that accomplishes lateral control through split ailerons rather than a conventional tail. Although driven by the requirement to have the smallest radar signature possible, the lack of a tail also significantly reduces structural weight. Coaxial rotor helicopters achieve high lift through the use of counter rotating propellers mounted on the same shaft structure. An added benefit is that the torque generated from these main propellers can be used to accomplish the same stability normally afforded by the tail rotor, thus eliminating the requirement for an additional propeller on the tail.

The above examples have two things in common. First, they are enabled by high powered computing. As this continues to increase, there are many performance gains to be made from areas that have not traditionally been considered feasible options. Secondly, they both require decisions to be made regarding the system's geometric design before the system is fielded. The probabilistic elements of multistate analysis and design should prove very effective in predicting what these decisions should be.

Appendix A

6-DoF Multistate Aircraft Model

The twin-engine aircraft model used in the analysis of Chapter 3 is the product of a larger multistate aircraft performance tool that resulted from this research. Although flight simulation is the ultimate performance output of this higher fidelity conceptual design routine, *pseudo*-instantaneous performance analysis may also be accomplished by trimming for desired flight conditions across a very short time span. This technique was effectively used in determination of the *reachability* criterion described at the end of Chapter 3, using an optimization similar to that in Eqn. 3.6 to trim.

When using as a design tool for the conceptual or early-primary design stage, it is not possible to know exact mass properties of every design variation, and it is inherently impossible to flight-test validate each of the design points. Thus, the accuracy of the performance analysis will be partially limited by these conceptual level estimates, even though the accuracy of the simulation output is likely higher than typical conceptual level design.[1]

Nonetheless, there are two other advantages that make this multistate performance tool desirable. The first is that it automates the translation of typical conceptual level design variables such as wingspan, aspect ratio, tail geometry, etc., into the full set of aerodynamic properties output by AVL. These are then defined as internal properties in the flight simulation, such that they can be updated at every time step,

[1]For the case of the Super King Air, these limitations were partially offset by comparing the baseline design to several flight test data points and making sure that the models agreed.

if desired. The second is that failures can be input into the analysis during runtime, and dynamic effects of the resulting performance may be approximated. Ultimately, the author intends to use this as part of a conceptual aircraft design curriculum, where students design and size their aircraft based on top-level mission requirements, and are then able to personally fly what they have designed in the full 6-DoF flight simulator within a matter of minutes.

A.1 Mass and Inertias

Aircraft mass properties, including exact values for individual moments of inertia, mass, and centers of gravity for each of the aircraft components, can be entered directly into the performance simulation module. When executed as part of the design loop, however, a separate mass properties module calculates the mass of each of these values using empirically based equations from Brandt et al. [25] and Roskam [92]. These are mass estimations commonly used in conceptual level design, and take, for instance, the form of Eqn. A.1 for wing mass [92].

$$m_{wing} = 0.033S\frac{n_{max}^{0.2}\mathcal{R}^{1.8}(1+\lambda)^{0.5}}{(t/c)^{0.7}cos\ \Lambda_{LE}} \tag{A.1}$$

The standard practice for using such estimates is to verify that output is valid for the type of aircraft being designed (through comparison to already existing aircraft), and adjust the appropriate factors accordingly. In the case of the Super King Air, the component estimates were verified and adjusted (i.e., the leading coefficient of Eqn. A.1) against the exact data given in [37] for the Beech Model 200, as well as against weight and balance sheets for operational USAF C-12's.

The research developed code calculates inertias for each of these components by volumetrically discretizing them into smaller divisions, computing the divisional centers of gravity, and summing the discretized inertias, according to formulae such as Eqn. A.2.

$$I_{xx,comp} = \sum m_i(y_{i,c.g.}^2 + z_{i,c.g.}^2) \tag{A.2}$$

where

$$m_i = \forall_i \ * \ f_i D \tag{A.3}$$

and f_i is a weighting factor on component density, D, such that it satisfies,

$$D = \frac{\sum f_i D}{\#\text{ divisions}} = \frac{m_{comp}}{\sum \forall_i} \tag{A.4}$$

This provides I_{xx}, I_{yy}, I_{zz}, and I_{xz} for the wing, tail, fuselage, etc. The parallel axis theorem is then used to calculate total inertias for the aircraft. Comparison to the actual inertias in [37] for the Beech 200 showed that this method was very accurate, given proper component weights. Where discrepancies existed, the weighting factor, f_i, was easily adjusted to control component density distributions, until inertias matched. In general, the products of inertia, I_{xy} and I_{yz}, are neglected when the aircraft has symmetry of mass and geometry about these axes (as most do).

A.2 Aerodynamic Forces and Moments

All lift-affected aerodynamics are computed through Athena Vortex Lattice (AVL), which employs an extended vortex lattice model for lifting surfaces and a slender body model for fuselages and nacelles. Documentation is extensive and is found in [8]. As AVL input files are cumbersome and require significant work to correctly construct, a pre-processing routine was developed that takes general aircraft design variables and geometry as input, and gives the appropriate AVL input file as output. The AVL output is then post-processed into a format that can be passed directly to the modified JSBSim flight simulator. This enables AVL to be directly integrated into the design loop for any desired flight condition.

There are two methods used to complete the drag polar with the addition of non-lift-induced drag (a.k.a. parasite drag, C_{D_o}). The first is to simply supply AVL with a known value of C_{D_o} from flight test for the appropriate flight conditions and configuration. This will be accurate for the baseline aircraft. A second method, which proves very accurate for subsonic conditions [25], is to use an estimate based

on drag data for similar aircraft under the concept of an *equivalent skin-friction drag coefficient*, C_{fe}, defined in:

$$C_{D_o} = C_{fe}\frac{S_{wet}}{S} \tag{A.5}$$

There is a large database of values for C_{fe} for several classes of aircraft in [86, 91]. The advantage of the second method is that both S and S_{wet} are functions of aircraft geometry, thus C_{D_o} can be calculated for differing design points. In the twin-engine aircraft case, the above two methods were combined, using the flight test value for the baseline aircraft to provide C_{fe}, such that Eqn. A.5 could then be used for the perturbed design points.

In addition to overall aircraft lift and drag characteristics, control derivatives for the aileron, rudder, and elevator are computed in AVL and used as input to the flight simulation routine. The process is to compute each of these derivatives for a range of angles-of-attack (in the Super King Air case, this was -4° to 14°) at the target maneuver flight conditions for each design geometry. This entire range is then read into the flight simulation code as a look-up table, and accessed depending on control inputs at each time step. If maneuver flight conditions vary enough that the control derivatives are no longer valid, the look-up table format is extensible to multiple dimensions, where data points between pre-computed AVL flight conditions can be rapidly interpolated. This has little to no effect on (simulation) run-time as all of the simulation takes place within a C^{++} executable and is extremely fast. This property of the core JSBSim code makes it extremely powerful as a tool for performance analysis.

A.3 Performance Simulation Through JSBSim

JSBSim [18] is an open-sourced, GNU licensed collection of 6-DoF flight simulation libraries written in C^{++}. It has been under development by dozens of engineers for over ten years. Input to JSBSim is typically done through a front-end *.xml* input file, where the aircraft's characteristic parameters are read in once at the onset of the simulation and then control inputs are treated as dynamic properties updated several times per second during run-time. Mills [76] began work on the basic implementation

of a MATLAB S-Function over three years ago and work for this thesis picked up from his work, making modifications to the flight simulation engine itself. The resulting updates focused on two areas:

- Bypassing the standard *.xml* input file so that aircraft characteristics are read directly from geometry, mass, and aerodynamics modules
- Rewriting and recompiling the source code such that all aircraft design variables are defined as time dependent inputs within the simulation executable

This enables the effects of aircraft design variables to be treated as dynamic properties in the same way as control inputs, such that they can be varied as a functions of time during the execution of the flight model in Simulink. It makes possible the rapid evaluation of a wide range of aircraft performance parameters for a nearly limitless number of aircraft configurations, including simulation of failure states, e.g. loss of actuators and engine failures. Additionally, it makes possible the in-flight physical reconfiguration of the aircraft, whether that be due to a failure (such as loss of vertical stabilizer) or variation of wing geometry (i.e. sweep, aspect ratio). If a more traditional analysis is desired, the variables are simply held fixed throughout the simulation.

There are over 70 C^{++} classes that make up JSBSim, as shown in the hierarchy of Fig. A-1. These classes fall into several categories, including *math*, *input/output*, *initialization*, *model*, and *basic*. In order to facilitate the modeling of arbitrary vehicle configurations, the framework is based around flexible object oriented modeling for the propulsion system, aerodynamic characteristics, control system, and ground reaction mechanisms. The JSBSim input set, as defined within the multistate design loop, is given in Fig. A-2, where all of the aerodynamic coefficients come from AVL. The output set is found in Fig. A-3. This is actually only a subset of possible outputs, but encompasses the typical 6-DoF output vector $[U, V, W, P, Q, R, \phi, \theta, \psi, pos_N, pos_E, h]$. In practice, both input and output are row oriented matrices with the number of columns equal to the number of time-steps within the simulation.

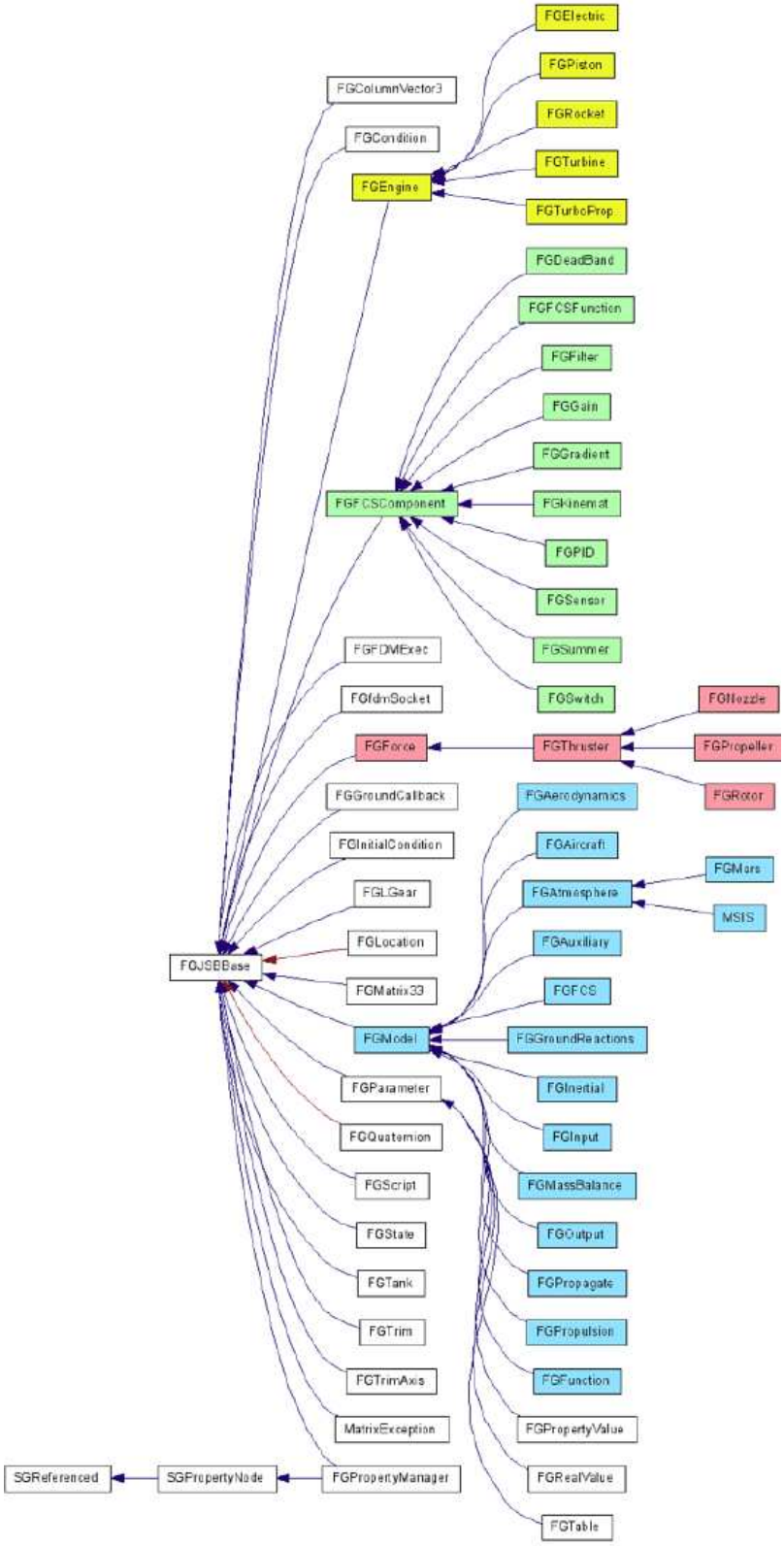

Figure A-1: JSBSim class hierarchy [19]

Variable	Description	Units		Variable	Description	Units
$P_{throttle}$	throttle position	[0,1]		$C_{L,@\alpha=4^\circ}$	lift coefficient for drag polar at target flight altitude	n/a
$P_{aileron}$	left aileron position	[0,1]		$C_{L,@\alpha=6^\circ}$	lift coefficient for drag polar at target flight altitude	n/a
$P_{elevator}$	elevator position	[0,1]		$C_{L,@\alpha=8^\circ}$	lift coefficient for drag polar at target flight altitude	n/a
P_{rudder}	rudder position	[0,1]		$C_{L,@\alpha=10^\circ}$	lift coefficient for drag polar at target flight altitude	n/a
P_{engine}	engine mixture	[0,1]		$C_{L,@\alpha=12^\circ}$	lift coefficient for drag polar at target flight altitude	n/a
$P_{magneto}$	magneto position	[0,1]		$C_{L,@\alpha=14^\circ}$	lift coefficient for drag polar at target flight altitude	n/a
P_{flap}	flap position	[0,1]		$C_{D,@\alpha=-4^\circ}$	drag coefficient for drag polar at target flight altitude	n/a
P_{gear}	gear position	[0,1]		$C_{D,@\alpha=-2^\circ}$	drag coefficient for drag polar at target flight altitude	n/a
$C_{L,\delta flap}$	change in lift coefficient due to flap deflection	n/a		$C_{D,@\alpha=0^\circ}$	drag coefficient for drag polar at target flight altitude	n/a
$C_{L,\delta elevator}$	change in lift coefficient due to elevator deflection	n/a		$C_{D,@\alpha=2^\circ}$	drag coefficient for drag polar at target flight altitude	n/a
$C_{D,\delta flap}$	change in drag coefficient due to flap deflection	n/a		$C_{D,@\alpha=4^\circ}$	drag coefficient for drag polar at target flight altitude	n/a
$C_{D,\delta elevator}$	change in drag coefficient due to elevator deflection	n/a		$C_{D,@\alpha=6^\circ}$	drag coefficient for drag polar at target flight altitude	n/a
$C_{l\beta}$	change in rolling-moment coefficient with sideslip angle	n/a		$C_{D,@\alpha=8^\circ}$	drag coefficient for drag polar at target flight altitude	n/a
C_{lp}	change in rolling-moment coefficient with roll rate	n/a		$C_{D,@\alpha=10^\circ}$	drag coefficient for drag polar at target flight altitude	n/a
C_{lr}	change in rolling-moment coefficient with yaw rate	n/a		$C_{D,@\alpha=12^\circ}$	drag coefficient for drag polar at target flight altitude	n/a
$C_{l,\delta aileron}$	change in rolling-moment coefficient with aileron deflection	n/a		$C_{D,@\alpha=14^\circ}$	drag coefficient for drag polar at target flight altitude	n/a
$C_{l,\delta rudder}$	change in rolling-moment coefficient with rudder deflection	n/a		S_{wing}	wing area	ft^2
$C_{m\alpha}$	change in pitching-moment coefficient with angle-of-attack	n/a		b_{wing}	wing span	ft
$C_{m,\delta elevator}$	change in pitching-moment coefficient with elevator deflection	n/a		c_{wing}	wing chord	ft
C_{mq}	change in pitching-moment coefficient with pitch rate	n/a		S_{ht}	horizontal tail area	ft^2
$C_{m,\delta flap}$	change in pitching-moment coefficient with flap deflection	n/a		l_{ht}	horizontal tail arm	ft
$C_{n\beta}$	change in yawing-moment coefficient with sideslip angle	n/a		S_{vt}	vertical tail area	ft^2
C_{nr}	change in yawing-moment coefficient with yaw rate	n/a		l_{vt}	vertical tail arm	ft
$C_{n,\delta rudder}$	change in yawing-moment coefficient with rudder deflection	n/a		$x_{a.c.}$	aircraft aerodynamic center, x-coordinate	in
$C_{n,\delta aileron}$	change in yawing-moment coefficient with aileron deflection	n/a		$y_{a.c.}$	aircraft aerodynamic center, y-coordinate	in
$C_{Y\beta}$	change in side-force coefficient with sideslip angle	n/a		$z_{a.c.}$	aircraft aerodynamic center, z-coordinate	in
C_{Yp}	change in side-force coefficient with roll rate	n/a		$x_{c.g.\cdot}$	aircraft center-of-gravity, x-coordinate	in
$C_{Y,\delta rudder}$	change in side-force coefficient with rudder deflection	n/a		$y_{c.g.\cdot}$	aircraft center-of-gravity, y-coordinate	in
$C_{Y,\delta aileron}$	change in side-force coefficient with aileron deflection	n/a		$x_{c.g.\cdot}$	aircraft center-of-gravity, z-coordinate	in
$C_{L,@\alpha=-4^\circ}$	lift coefficient for drag polar at target flight altitude	n/a		I_{xx}	moment of inertia about x-axis	$sl*ft^2$
$C_{L,@\alpha=-2^\circ}$	lift coefficient for drag polar at target flight altitude	n/a		I_{yy}	moment of inertia about y-axis	$sl*ft^2$
$C_{L,@\alpha=0^\circ}$	lift coefficient for drag polar at target flight altitude	n/a		I_{zz}	moment of inertia about z-axis	$sl*ft^2$
$C_{L,@\alpha=2^\circ}$	lift coefficient for drag polar at target flight altitude	n/a		W_G	aircraft gross weight	lb

Figure A-2: Performance simulation input set

Variable	Description	Units
U	velocity along x-axis	ft/s
V	velocity along y-axis	ft/s
W	velocity along z-axis	ft/s
P	roll rate	rad/s
Q	pitch rate	rad/s
R	yaw rate	rad/s
Long	geographic longitude	deg
Lat	geographic latitude	deg
h_{GEO}	geodetic altitude	ft
Φ	roll angle	rad
θ	pitch angle	rad
Ψ	yaw angle	rad
h	altitude	ft
α	angle-of-attack	rad
β	angle-of-sideslip	rad
n	vertical acceleration	ft/s^2
α_{dot}	angular acceleration about y-axis	rad/s^2
β_{dot}	angular acceleration about z-axis	rad/s^2
M	Mach number	n/a
V_C	calibrated airspeed	knots
V_E	equivalent airspeeed	knots
P_{eng1}	engine power	Hp
P_{eng2}	engine power	Hp
N1	engine rpm	rev/min
N2	engine rpm	rev/min
FF	fuel flow rate	lbm/hr

Figure A-3: Performance simulation output subset

Finally, Figs. A-4 and A-5 show two time histories for the Super King Air baseline geometry performance output.

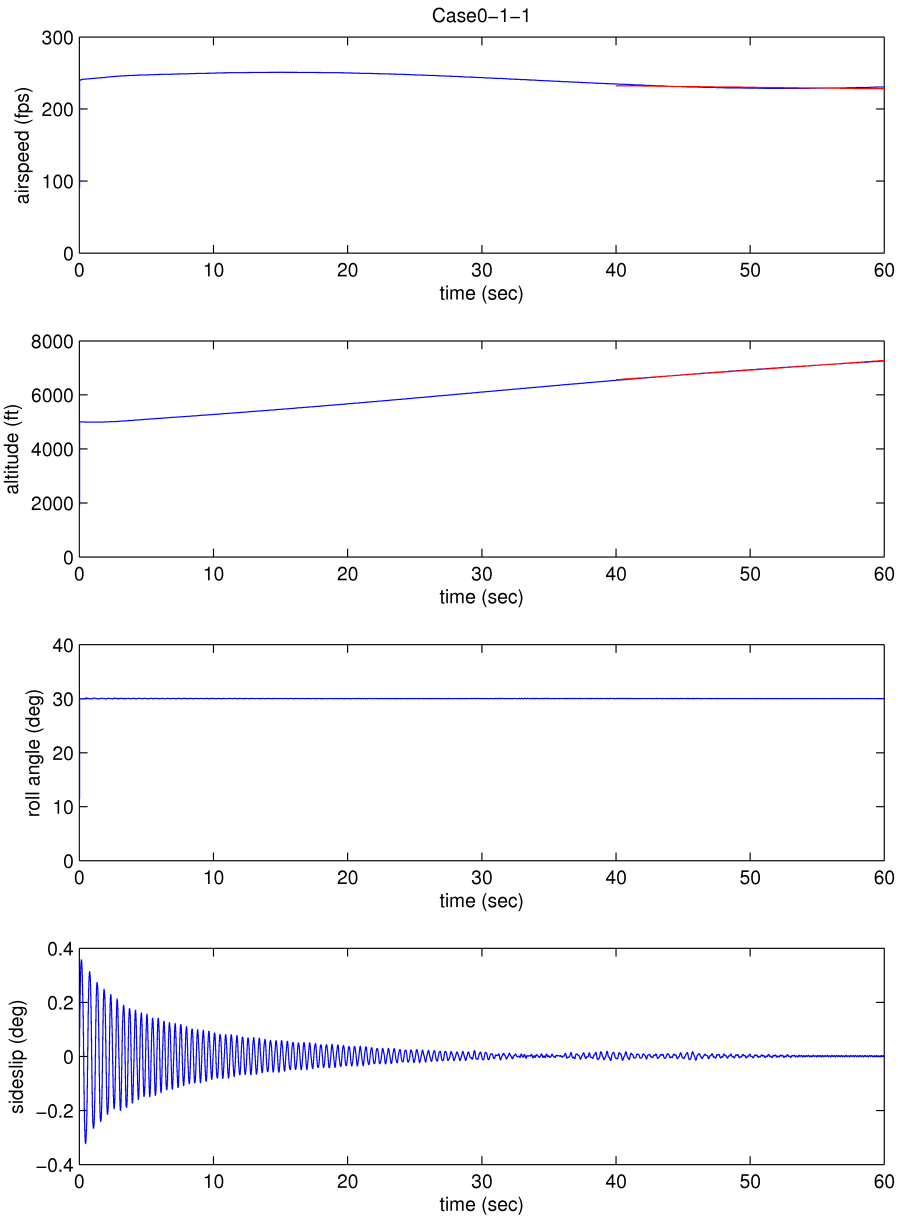

Figure A-4: Super King Air output for nominal state, baseline geometry

In Fig. A-4, the small oscillation in sideslip angle is the result of a numerical interaction with some relatively high gains on the controller. The magnitude, at its largest, is only ± 0.3 degrees and it does not affect overall output in any way. For the failure case shown in Fig. A-5, the controller has a harder time handling both bank

and sideslip with only the rudder, but eventually manages to dampen out the longer period oscillations.

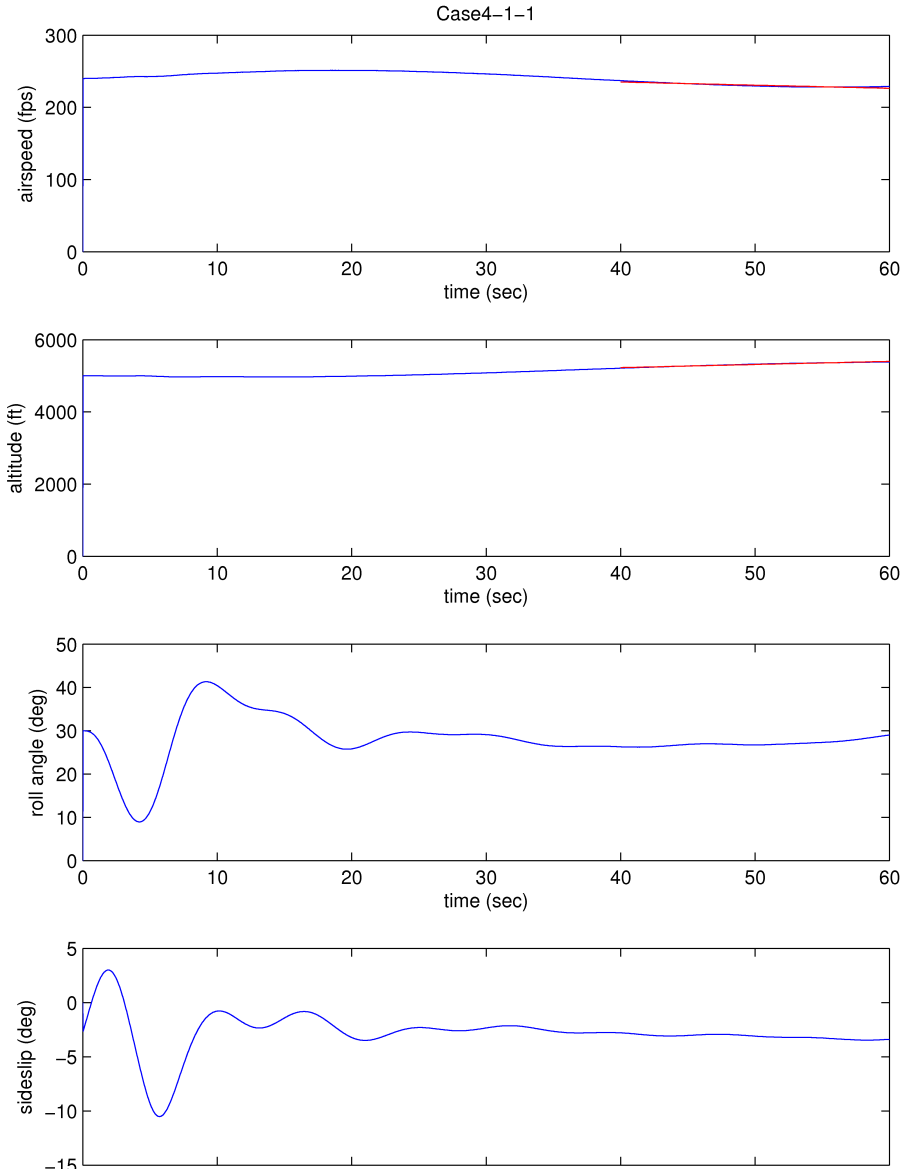

Figure A-5: Super King Air output for baseline geometry, left engine and ailerons failed

A.4 Controls

JSBSim also incorporates the ability to build up entire flight control systems using series of components to model filters, switches, summers, gains, sensors, etc. This was how the PID controller in Fig. 3-7, of Chapter 3, was constructed, where the gains were defined as design variables within the design loop. Although the multistate performance model is executed as part of an S-function, and thus has all of the traditional Simulink controllers at its disposal, allowing the flight simulator to perform these tasks was several orders of magnitude faster since all sensing and feedback was performed internally within the C^{++} executable. In either case, however, it was verified that the results were the same.

A.5 Propulsion

The propulsion module takes the form of engine and thruster decks within JSBSim. It supports piston, turbine, rocket, and electric engine force, moment, and fuel consumption calculations. For the vehicle's desired thrust mechanism, the engine model (e.g. turboprop) is coupled with the thruster definition (e.g. propeller) to model the aircraft's overall thrust characteristics. The basic power output of the engine as a function of altitude and airspeed comes from the engine deck in the form of a look-up table. Effects of the propeller are integrated into this model by using specification tables for thrust and power coefficient as a function of advance ratio and blade-angle (in the case of variable pitch propellers). Additional effects that can be modeled include gyroscopic effects due a spinning drive shaft and propeller, and P-factor. P-factor is a phenomenon that occurs in a climbing aircraft due to the fact that the downward arcing propeller blade has a higher angle of attack relative to wind velocity than the upward arcing blade, and thus higher thrust. In an aircraft with clockwise spinning propellers, this results and yawing moment to the left. P-factor is approximated in JSBSim by shifting the point of application of the thrust vector over the propeller disk as a function of α (angle-of-attack).

Appendix B

Twin-engine Aircraft Reachability Analysis

****

In Appendix B only, the term *state*, unless capitalized and followed by a number, refers to state in the context of a continuous state-space in controls theory, rather than the discrete performance-based states used throughout the rest of the thesis. Additionally, x refers to the state vector rather than the static design vector, in order to conform with traditional controls theory nomenclature.

****

The purpose of the reachability analysis is ensure that the results of the worst performing states were not merely due to an inappropriate selection of gains for the specified control system, but that they truly were unachievable, given the system configuration. One means of doing this was a careful formulation of the gain optimization given in Eqn. 3.6, examination of the resulting post-optimality criterion, and comparison of results from multiple starting points within the design space, all of which indicated the best possible solution had been obtained. As a second means of

verification, a comparison of system *reachability* was made between satisfactory and non-satisfactory geometries, a full discussion of which is provided below.

The state-space system described by

$$\begin{aligned} \dot{\mathbf{x}} &= A\mathbf{x} + B\mathbf{u} \\ \mathbf{y} &= C\mathbf{x} + D\mathbf{u} \end{aligned} \tag{B.1}$$

in which $\mathbf{x}(t) \in \mathbb{R}^n$ is the state vector, $\mathbf{u}(t) \in \mathbb{R}^m$ is the input vector, and $\mathbf{y}(t) \in \mathbb{R}^p$ is the output vector, is termed *reachable* if a control input can be selected to drive the system from any initial state to any final state in time t. This solves the problem of determining whether it is possible, given the current system configuration, of reaching the desired final state. The are many techniques available for solving the *reachability* problem for discrete time, one of which is the formation and analysis of the *reachability matrix*, which is defined as

$$Z = [B|AB|A^2B|...|A^{n-1}B] \in \mathbb{R}^{nxnm} \tag{B.2}$$

If and only if the matrix Z has full rank n is the system *reachable*. This characteristic arises from the nature of the system zeros, which may be divided into three categories: *input-decoupling* zeros, *output-decoupling* zeros, and *transmission* zeros. Only the *input-decoupling* zeros will be discussed here as they are most relevant to the *reachability* problem, but the reader is directed to [7] and [89] for a full treatment of the topic.

The above mentioned zeros for a multiple-input multiple-output (MIMO) system can be derived from the Rosenbrock system matrix, given in the Laplace domain as

$$F(s) = \begin{bmatrix} sI - A & B \\ C & D \end{bmatrix} \tag{B.3}$$

The *input-decoupling* zeros are the values of s where the upper block matrix (describing the input coupling) of Eqn. B.3, given below as Eqn. B.4,

$$F_{upper}(s) = [sI - A|B] \in \mathbb{R}^{n\text{x}(n+m)} \tag{B.4}$$

has rank less than n. This occurs when multiple paths exist to the same system output or alternate physical mechanisms result in competing output components [101]. The existence of *input-decoupling* zeros means that control effectiveness is unachievable with the given set of inputs. Furthermore, *reachability* is equivalent to the absence of *input-decoupling* zeros.

Eqns. B.2 and B.4 provide a convenient means for verifying the performance of the worst performing states as reported in Section 3.3. As an example, consider the results shown in State 4 of Fig. 3-9. Here, Eqns. B.2 and B.4 were used to determine the *reachability* of the baseline geometry system as compared to the low tail height geometry system, where the baseline geometry performance fell well within the safe region, while the low tail height geometry was the leftmost point outside of the it.

The initial step in this process was to construct the state-matrix A, the control-matrix B, and the output-matrix C (the feed-forward matrix D was null). This was accomplished using an *interior-point* optimization algorithm acting on the state derivatives to trim the aircraft model as close as possible to the desired flight conditions for both geometries. The model was then linearized about these points using an algorithm adapted from Stevens and Lewis [101], in order to obtain two distinct, geometry-specific sets of (A, B, C). Although only A and B are needed for the evaluation of Eqn. B.2, C was used to find the system zeros from Eqn. B.3 for the rank evaluation of Eqn. B.4. For State 4, the state vector consisted of $[U, V, W, P, Q, R, \phi, \theta, \psi, pos_N, pos_E, h]$ (following notation from the standard equations of motion), while the input vector was $[\delta_{elevator}, \delta_{rudder}]$ with output of $[P, R, \phi, \psi]$, recalling that for State 4 the ailerons and left engine were failed.

Results showed a distinct difference in the degree of *reachability* for the two geometries. The rank of Z from Eqn. B.2 for the baseline geometry was 12 (full rank

since $n = 12$), indicating a *reachable* system. For the low tail geometry, the rank dropped to 11 for the same tolerances, indicating an *unreachable* system and implying the existence of one or more input-decoupling zeros. Further examination of the system zeros and subsequent evaluation of $F_u(s)$ from Eqn. B.4 showed the presence of one input-decoupling zero near the origin for the low tail geometry and confirmed the absence of input-decoupling zeros for the baseline geometry system. Thus, the analysis confirmed that, in cases where the simulation resulted in unsatisfactory state performance, this was truly due to the physical configuration of the system, and not to the inappropriate selection of controller gains.

Appendix C

Sorting Algorithm for Multilayer Markov Analysis

The following algorithm is used to sort and bin probabilities resulting from the Vehicle Markov Model (VMM), based on the sortie performance thresholds, such that they may be aggregated into Sortie Equivalent Markov Model (SEMM) probabilities (Section 4.2.1, Chapter 4). The algorithm specifically applies to a model with four performance categories, *nominal(N)*, *degraded(D)*, *abort(A)*, and *loss(L)*, but could be extended to additional categories if necessary. This extension would simply require additional tiers of performance categorization, being sure to include the code within the **while** loop for downstream categories that are spanned by multiple levels of failure.

Inputs: Probability set from Vehicle Markov Model, $\breve{\mathbf{P}}^{\mathbf{VMM}}$; Performance set from Vehicle Markov Model, $\breve{\mathbf{G}}^{\mathbf{VMM}}$; Index set of previous Vehicle Markov Model states, $\mathbf{S}_{\mathbf{prev}}^{\mathbf{VMM}}$, the elements of which comprise the states from which each state arrives; and Sortie Equivalent Markov Model performance thresholds $\mathbf{W} = [W_{min,N}\ W_{min,D}\ W_{min,A}]$. Each of the above are size M^{VMM}, except for $\mathbf{W}$

Outputs: Probability set for Sortie Equivalent Markov Model, $\breve{\mathbf{P}}^{\mathbf{SEMM}}$

Initialize variables
declare $\mathbf{I_N}$, $\mathbf{I_D}$, $\mathbf{I_A}$, $\mathbf{I_L}$, $\mathbf{I_{NA}}$, $\mathbf{I_{DA}}$, $\mathbf{I_{NL}}$, $\mathbf{I_{DL}}$, $\mathbf{I_{NAL}}$, $\mathbf{I_{DAL}}$, $\mathbf{c}$, m, n, q, r

Check that nominal state achieves nominal performance
if $G^{VMM}(1) < W_{min,N}$
    display "error, nominal performance not met"
end if

PERFORM TOP-TIER PERFORMANCE CATEGORIZATION
$m = n = q = r = 1$
for $i = i...M^{VMM}$
    if $G^{VMM}(i) \geq W_{min,N}$
        $I_N(m) = i$
        $m = m + 1$
    else if $G^{VMM}(i) \geq W_{min,D}$
        $I_D(n) = i$
        $n = n + 1$
    else if $G^{VMM}(i) \geq W_{min,A}$
        $I_A(q) = i$
        $q = q + 1$
    else
        $I_L(r) = i$
        $r = r + 1$
    end if
end for

PERFORM 2ND-TIER PERFORMANCE CATEGORIZATION:
Determine which abort states come from nominal or degraded states
$m = n = 1$
for $i = 1...number\ of\ elements\ in\ \mathbf{I_A}$
    if $S_{prev}^{VMM}(I_A(i)) \in \mathbf{I_N}$
        $I_{NA}(m) = I_A(i)$
        $m = m + 1$
    else if $S_{prev}^{VMM}(I_A(i)) \in \mathbf{I_D}$
        $I_{DA}(n) = I_A(i)$
        $n = n + 1$
    end if
end for

Check for abort states that come from other abort states and add to correct path
$c = 1$
while *number of elements in* $\mathbf{c} > 0$, **do**
    $\mathbf{c} = \mathbf{I_A} \backslash \{\mathbf{I_{NA}}\ \mathbf{I_{DA}}\}$ *(the excluded set)*
    for $i = 1...number\ of\ elements\ in\ \mathbf{c}$
        if $S_{prev}^{VMM}(c(i)) \in \mathbf{I_{NA}}$

$I_{NA}(m) = c(i)$
$m = m + 1$
else if $S_{prev}^{VMM}(c(i)) \in \mathbf{I_{DA}}$
$I_{DA}(n) = c(i)$
$n = n + 1$
end if
end for
end while

Determine which loss states come from nominal or degraded states
$m = n = 1$
for $i = 1...number\ of\ elements\ in\ \mathbf{I_L}$
if $S_{prev}^{VMM}(I_L(i)) \in \mathbf{I_N}$
$I_{NL}(m) = I_L(i)$
$m = m + 1$
else if $S_{prev}^{VMM}(I_L(i)) \in \mathbf{I_D}$
$I_{DL}(n) = I_L(i)$
$n = n + 1$
end if
end for

PERFORM 3RD-TIER PERFORMANCE CATEGORIZATION:
Determine which loss states come from nominal→abort or degraded→abort paths
$m = n = 1$
for $i = 1...number\ of\ elements\ in\ \mathbf{I_L}$
if $S_{prev}^{VMM}(I_L(i)) \in \mathbf{I_{NA}}$
$I_{NAL}(m) = I_L(i)$
$m = m + 1$
else if $S_{prev}^{VMM}(I_L(i)) \in \mathbf{I_{DA}}$
$I_{DAL}(n) = I_L(i)$
$n = n + 1$
end if
end for

FORM PROBABILITY SET, $\breve{\mathbf{P}}^{\mathbf{SEMM}}$
(subscripts correspond to states in SEMM, Fig. 4-6, Chapter 4)

$$P_N^{SEMM} = \sum_i P^{VMM}(I_N(i))$$

$$P_D^{SEMM} = \sum_i P^{VMM}(I_D(i))$$

$$P_{A_1}^{SEMM} = \sum_i P^{VMM}(I_{NA}(i))$$

$$P_{L_1}^{SEMM} = \sum_i P^{VMM}(I_{NL}(i))$$

$$P_{L_2}^{SEMM} = \sum_i P^{VMM}(I_{DL}(i))$$

$$P_{A_2}^{SEMM} = \sum_i P^{VMM}(I_{DA}(i))$$

$$P_{L_3}^{SEMM} = \sum_i P^{VMM}(I_{NAL}(i))$$

$$P_{L_4}^{SEMM} = \sum_i P^{VMM}(I_{DAL}(i))$$

$$\breve{\mathbf{P}}^{\mathbf{SEMM}} = [P_N^{SEMM}\ P_D^{SEMM}\ P_{A_1}^{SEMM}\ P_{L_1}^{SEMM}\ P_{L_2}^{SEMM}\ P_{A_2}^{SEMM}\ P_{L_3}^{SEMM}\ P_{L_4}^{SEMM}]$$

Appendix D

A Gaussian Test Function for Multistate Performance Modeling

Referenced in Chapters 4 and 7, a Gaussian test function of the form,

$$\begin{aligned} G_K^s(\mathbf{x}) =& (1 - 0.4u_K^1(\mathbf{x}))^2 e^{-(0.4u_K^1(\mathbf{x}))^2 - (u_K^2(\mathbf{x})+1)^2} \\ &... - 10(4u_K^1(\mathbf{x}) - 0.5u_K^2(\mathbf{x})^4) e^{-(0.4u_K^1(\mathbf{x}))^2 - u_K^2(\mathbf{x})^2} \\ &... - e^{-(4u_K^1(\mathbf{x})-2)^2 - u_K^2(\mathbf{x})} - 0.3(0.8u_K^1(\mathbf{x}) + u_K^2(\mathbf{x})) \end{aligned} \tag{D.1}$$

shown in Fig. D-1, was modified to model nominal and off-nominal states.

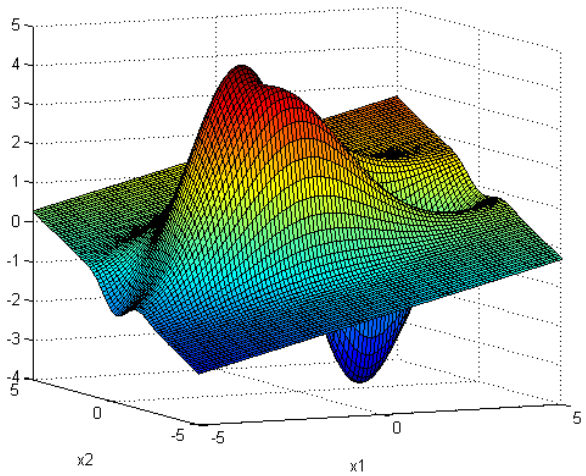

Figure D-1: Plot of the Gaussian test function (nominal state)

This was accomplished by defining $\mathbf{u_K}$ as shown in Eqn. D.2:

$$\mathbf{u_K}(\mathbf{x}) = \begin{bmatrix} \alpha_K^1 & 0 \\ 0 & \alpha_K^2 \end{bmatrix} \begin{bmatrix} x^1 \\ x^2 \end{bmatrix} + \begin{bmatrix} \gamma_K^1 \\ \gamma_K^2 \end{bmatrix},$$

$$\textit{where} \qquad \boldsymbol{\alpha_K} = \begin{bmatrix} 1+f \\ 1-a-bc \end{bmatrix}_K, \tag{D.2}$$

$$\textit{and} \qquad \boldsymbol{\gamma_K} = \begin{bmatrix} b+e \\ b+d/(1-c) \end{bmatrix}_K$$

The 'mode' vector $[a\ b\ c\ d\ e\ f]_K$ is defined as:

$$\begin{bmatrix} a \\ b \\ c \\ d \\ e \\ f \end{bmatrix}_K^T = \begin{bmatrix} 0.6 \\ 0.5 \\ 0.5 \\ 1.5 \\ -1.5 \\ 1.4 \end{bmatrix}^T \begin{bmatrix} \{0,1\} & 0 & 0 & 0 & 0 & 0 \\ 0 & \{0,1\} & 0 & 0 & 0 & 0 \\ 0 & 0 & \{0,1\} & 0 & 0 & 0 \\ 0 & 0 & 0 & \{0,1\} & 0 & 0 \\ 0 & 0 & 0 & 0 & \{0,1\} & 0 \\ 0 & 0 & 0 & 0 & 0 & \{0,1\} \end{bmatrix}_K \tag{D.3}$$

The above equations model a multistate system with six modes of failure, corresponding to $[a\ b\ c\ d\ e\ f]$ and the diagonal elements of the right hand matrix in Eqn. D.3. These diagonal elements are 0 when the represented element is functional and 1 when it has failed. When the diagonal consists of all zeros, $\mathbf{u_K}(\mathbf{x}) = \mathbf{x}$, and the function is in its 'nominal' state as displayed in Fig. D-1. All of the other possible permutations correspond to the 63 off-nominal states. These states are essentially modeled by a shifting and stretching of the performance space via the mechanisms in Eqns. D.2 and D.3. Plots of four 'off-nominal' states are shown in Figs. D-2 through D-5 on the following page. The starred points are representations of Kriging surfaces mapped from the nominal state, as described in Chapter 7.

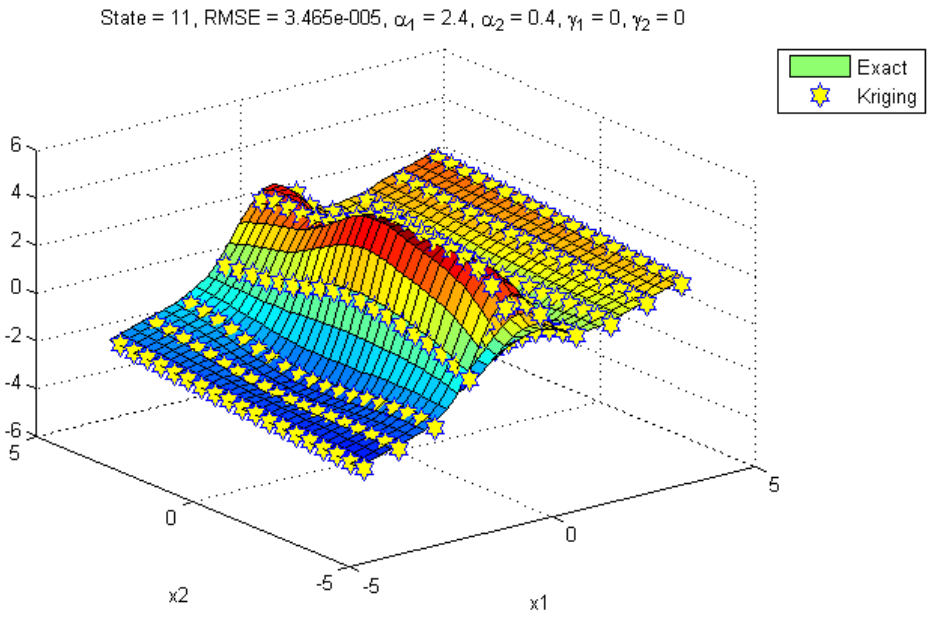

Figure D-2: Plot of the Gaussian test function (off-nominal with 'a' and 'f' failed)

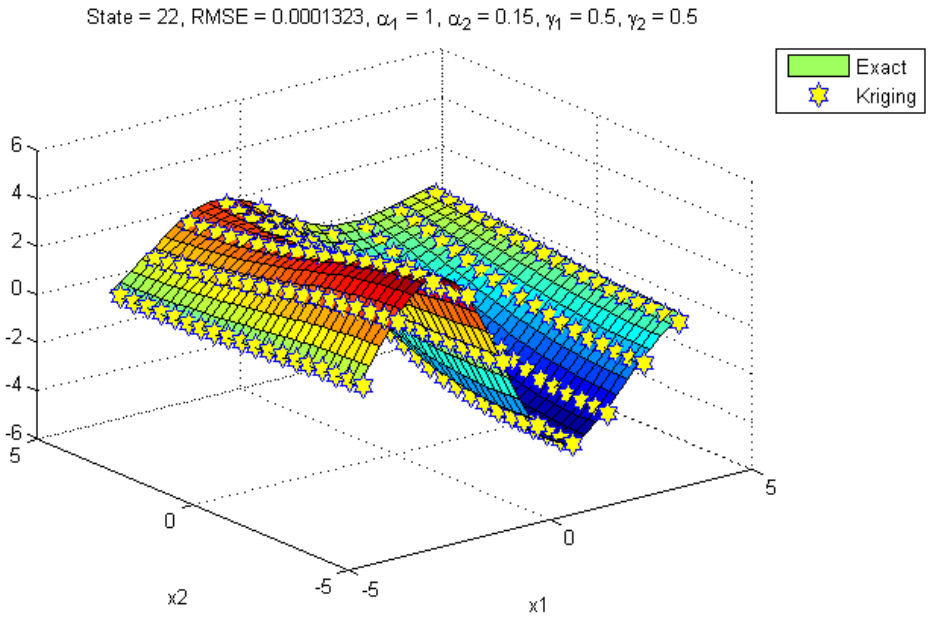

Figure D-3: Plot of the Gaussian test function (off-nominal with 'a' 'b' and 'c' failed)

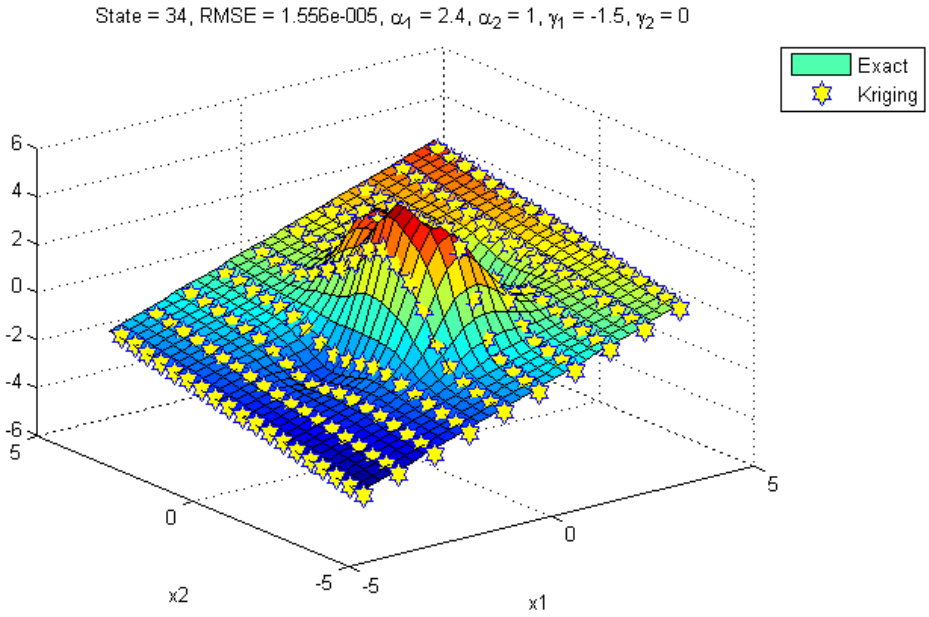

Figure D-4: Plot of the Gaussian test function (off-nominal with 'e' and 'f' failed)

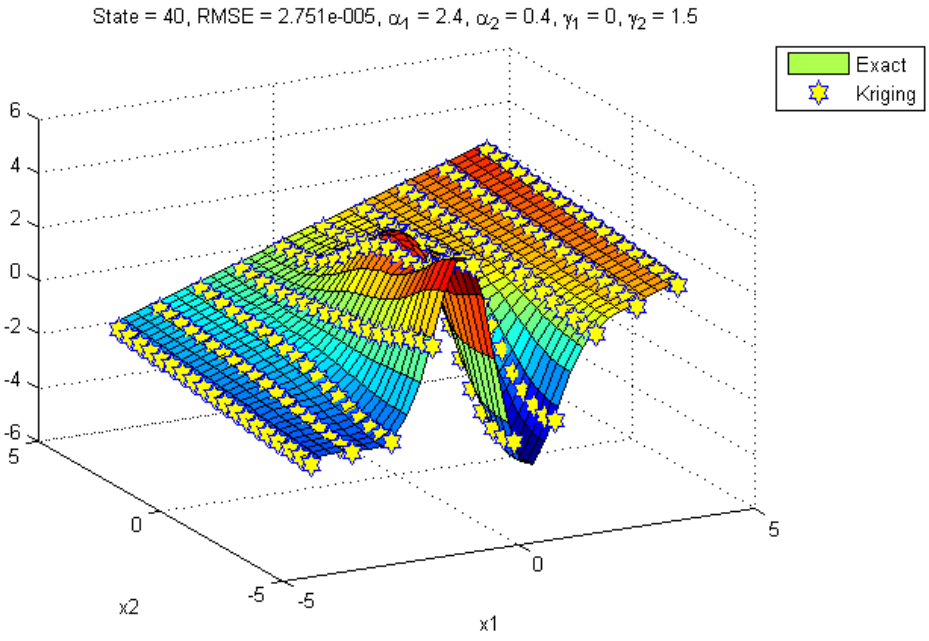

Figure D-5: Plot of the Gaussian test function (off-nominal with 'a' 'd' and 'f' failed)

Appendix E

Multistate Modeling for the Long Endurance UAV

The multistate performance model for both scenarios of the long endurance UAV generally executes according to the iterative processes given in Fig. 5-6, of Chapter 5. The modules used to define the aircraft are similar to those used in the twin-engine aircraft model, but with the mass properties module being updated to reflect current technology used in lighter weight, high aspect ratio UAVs. These corrections were made according to the mass data given in the NASA study of [83]. The modeling of thrust and energy consumption was also adjusted accordingly, depending on whether the aircraft was using traditional combustible fuel or the LH_2-PEM fuel cells.

The trim algorithm represented by the innermost loop of Fig. 5-6 was constructed using the methods found in a very early, but extremely thorough, publication of Roskam [90], and in Grasmeyer [51]. The Grasmeyer publication was a NASA study, contracted in 1998, to determine engine-out constraints based on estimation of stability and control derivatives. These derivatives can be used in the characterization an aircraft's equilibrium about or along any one of its axes, such as that in Eqn. E.1,

$$C_{y_{\delta_a}}\delta_a + C_{y_{\delta_r}}\delta_r + C_{y_\beta}\beta + C_L sin\ \phi - \frac{T sin\ \epsilon}{qS} = -\frac{Y_{ext}}{qS} \tag{E.1}$$

which is the sideforce equation, derived from the 6-DoF equations of motion, as found

in many textbooks. The $sin\ \epsilon$ terms are included for the general case in which thrust may be vectored at an angle ϵ. The yawing moment and rolling moment equations are given in Eqns. E.2 and E.3,

$$C_{n_{\delta_a}}\delta_a + C_{n_{\delta_r}}\delta_r + C_{n_\beta}\beta + \frac{T sin\ \epsilon}{qS} = \frac{(T_R l_{e,R} - T_L l_{e,L}) cos\ \epsilon}{qS\bar{c}} \tag{E.2}$$

$$C_{l_{\delta_a}}\delta_a + C_{l_{\delta_r}}\delta_r + C_{l_\beta}\beta - \frac{T sin\ \epsilon}{qS}\frac{z_{vt}}{\bar{c}} = -\frac{L_{ext}}{qS\bar{c}} \tag{E.3}$$

where $T = T_R + T_L$. Sign convention above follows that depicted in Fig. E-1, with the z-axis positive downwards and the positive y-axis out the right wing.

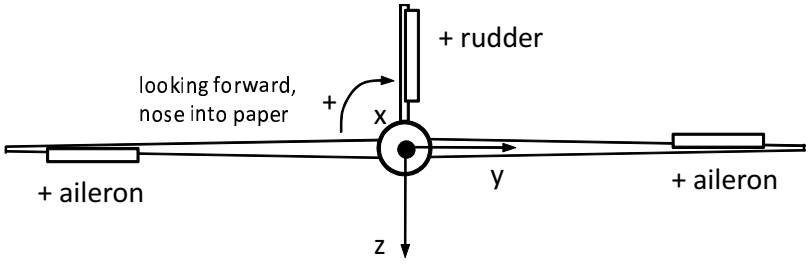

Figure E-1: UAV model sign convention

The multistate trim algorithm is more complex than that in [51], as it is used as part of a broader range of performance determination, and involves more unknowns than those required for calculation of engine-out constraints. It is based on the principle that Equations E.1 through E.3 are satisfied through three possible control inputs: rudder deflection, δ_r, aileron deflection, δ_a, and throttle control through variation of thrust, T_R and T_L. It assumes that the thrust vector angle, ϵ, is zero. If the external forces and moments, Y_{ext} and L_{ext}, are also assumed to be zero, and the control derivatives are estimated through the techniques in [90] or through aerodynamics solvers such as AVL, the remaining unknowns are the sideslip angle, β, and the bank angle, ϕ.

This leaves three equations with, at most, five unknowns,[1] for any given set of flight conditions defined by $q = 0.5\rho V^2$. Fortunately, some safe assumptions allow

[1]Total thrust, T, is equal to drag in straight, level flight. Thus, for a given flight condition, the moment created by the differential thrust is the only thrust related unknown.

the extra two unknowns to be computationally solved for through iteration. The first assumption is that the smallest possible control surface deflection should be used to counter any moments generated by engine loss. This accounts for the first unknown, allowing alternate iteration on δ_r and δ_a for a fixed thrust differential, starting from zero degrees and stopping when the force and moment equations are satisfied, or max deflections have been reached.

The second assumption is that for the above aircraft, trimmed using control surfaces, any beneficial reduction in the thrust differential must result in a higher cruise altitude. Figure E-2 shows this trend for the state with an inoperative inboard engine and failed rudder.

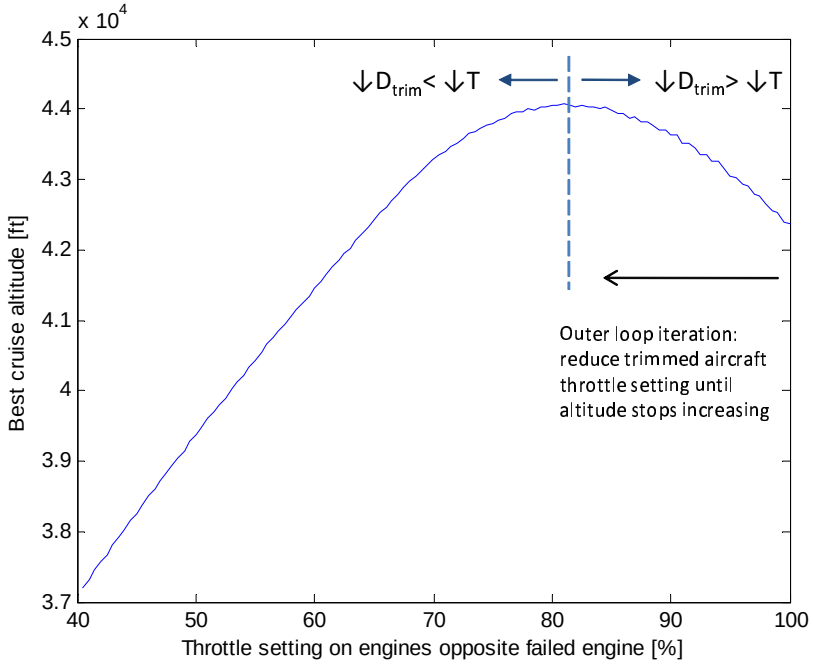

Figure E-2: Variation of best cruise altitude (at end of cruise-climb) with throttle setting for aircraft with failed inboard engine and rudder

The optimum throttle setting in Fig. E-2 arises from the fact that the flight conditions entering the trim algorithm are those for minimum power required at altitude (found by solving Eqn. 5.2, in Chapter 5). In other words, every point on the throttle-altitude line is constrained by Eqn. 5.2. Throttle reduction of the operating

engines must be accompanied by a reduction in trim drag greater in magnitude than the resulting loss in total thrust, in order to be 'improving.' Given the constraint of Eqn. 5.2, this will show up as an increase in cruise altitude, when reducing from 100% throttle. Therefore, the complete trim process is to inner loop iterate on control deflections (increasing) until moments are zero, and outer loop iterate on throttle (decreasing) until cruise altitude stops increasing. This results in the best trimmed cruise performance for the engine-out scenario.

In practice, there is one additional iteration that occurs between the inner and outer loops discussed above. This is an iteration on altitude required to satisfy Eqn. 5.2, which is a function of both a Mach number *and* altitude. The solution to this is to select a low altitude, solve for the Mach number required to satisfy Eqn. 5.2, shown below in Eqn. E.4,

$$M_{cr} = \frac{\sqrt{2W}}{\sqrt{\rho S}(a\pi e\text{Æ}3C_{D_o})} \tag{E.4}$$

and then increase altitude incrementally until the design required Mach number at altitude is reached, or thrust becomes limited at altitude.[2] The implicit result is that every performance output is already calculated at the best possible cruise conditions, corresponding to the minimum power required and the highest altitude.

Sample results for the baseline long endurance UAV are provided in Fig. E-3 and Fig. E-4. Although spread across separate figures on two pages, they compose a single design point for 64 states. The deflection, sideslip, and bank angles are those required to trim the aircraft in the appropriate engine-out scenario.

[2]Both density, ρ, and the speed of sound, a, are decreasing functions of altitude. Since they are located in the denominator of Eqn. E.4, the best cruise Mach number increases with altitude.

	Nom State	State 2	State 3	State 4	State 5	State 6	State 7	State 8
Failed	0	1	2	3	4	5	6	1,2
Alt [ft]	50240	47420	42020	39820	50240	50240	LOSS	39620
M_cruise	0.3799	0.33938	0.30351	0.28788	0.3799	0.3799	--	0.27499
V [KTAS]	217.765	194.536	173.976	165.017	217.765	217.765	--	157.629
Rud_df [deg]	0	0	-18.6	-25.2	0	0	--	-22.2
Ail_df [deg]	0	0	-0.2976	-5.40706	0	0	--	-0.28558
Beta [deg]	0	0	0.34209	-3.69896	0	0	--	0.35552
Bank [deg]	0	0	-3.6	-8.4	0	0	--	-4
Cn_residual	0	0	-3.77E-05	-0.00031	0	0	--	-1.97E-05
Range [nm]	9079.69	8070.51	8429.93	7570.36	9079.69	9079.69	LOSS	7593.26
	State 9	State 10	State 11	State 12	State 13	State 14	State 15	State 16
Failed	1,3	1,4	1,5	1,6	2,3	2,4	2,5	2,6
Alt [ft]	34460	47420	47420	LOSS	LOSS	37700	42020	LOSS
M_cruise	0.24386	0.33938	0.33938	--	--	0.27437	0.30351	--
V [KTAS]	139.783	194.536	194.536	--	--	157.273	173.976	--
Rud_df [deg]	-25.2	0	0	--	--	0	-16.3	--
Ail_df [deg]	-8.23948	0	0	--	--	-2.35276	0	--
Beta [deg]	-6.3372	0	0	--	--	-1.96442	-0.22993	--
Bank [deg]	-9.8	0	0	--	--	-1.65	-3.6	--
Cn_residual	-0.00045	0	0	--	--	-6.12E-05	0.00036	--
Range [nm]	6008.53	8070.51	8070.51	LOSS	LOSS	8221.73	8433.6	LOSS
	State 17	State 18	State 19	State 20	State 21	State 22	State 23	State 24
Failed	3,4	3,5	3,6	4,5	4,6	5,6	1,2,3	1,2,4
Alt [ft]	31360	38700	LOSS	50240	LOSS	LOSS	LOSS	35080
M_cruise	0.23639	0.28104	--	0.3799	--	--	--	0.2474
V [KTAS]	135.503	161.099	--	217.765	--	--	--	141.813
Rud_df [deg]	0	-22.85	--	0	--	--	--	0
Ail_df [deg]	-3.73883	0	--	0	--	--	--	-2.27916
Beta [deg]	-3.15428	-0.02593	--	0	--	--	--	-1.93848
Bank [deg]	-2.65	-4.8	--	0	--	--	--	-1.5
Cn_residual	-7.07E-05	0.0007	--	0	--	--	--	-0.00011
Range [nm]	7933.6	8432.96	LOSS	9079.69	LOSS	LOSS	LOSS	7468.98
	State 25	State 26	State 27	State 28	State 29	State 30	State 31	State 32
Failed	1,2,5	1,2,6	2,3,4	2,3,5	2,3,6	3,4,5	3,4,6	4,5,6
Alt [ft]	39620	LOSS	LOSS	LOSS	LOSS	30680	LOSS	LOSS
M_cruise	0.27499	--	--	--	--	0.23189	--	--
V [KTAS]	157.629	--	--	--	--	132.923	--	--
Rud_df [deg]	-19.85	--	--	--	--	0	--	--
Ail_df [deg]	0	--	--	--	--	0	--	--
Beta [deg]	-0.22893	--	--	--	--	0	--	--
Bank [deg]	-4	--	--	--	--	0	--	--
Cn_residual	0.00039	--	--	--	--	0	--	--
Range [nm]	7596.84	LOSS	LOSS	LOSS	LOSS	8562.44	LOSS	LOSS

Figure E-3: Multistate data from baseline long endurance UAV *Scenario II*, States N-32; 1-cowl, 2-eng3, 3-eng4, 4-rudder, 5-aileron, 6-elevator

	State 33	State 34	State 35	State 36	State 37	State 38	State 39	State 40
Failed	1,5,6	2,5,6	3,5,6	1,3,4	1,4,5	1,3,5	2,4,6	2,4,5
Alt [ft]	LOSS	LOSS	LOSS	28580	47420	35260	LOSS	35180
M_cruise	--	--	--	0.21318	0.33938	0.24859	--	0.25775
V [KTAS]	--	--	--	122.632	194.536	142.496	--	147.748
Rud_df [deg]	--	--	--	0	0	-24.5	--	0
Ail_df [deg]	--	--	--	-4.66947	0	0	--	0
Beta [deg]	--	--	--	-4.00469	0	-0.10338	--	0
Bank [deg]	--	--	--	-3.1	0	-4.8	--	0
Cn_residual	--	--	--	-3.22E-05	0	0.00021	--	0
Range [nm]	LOSS	LOSS	LOSS	7021.21	8070.51	7621.54	LOSS	8493.25
	State 41	State 42	State 43	State 44	State 45	State 46	State 47	State 48
Failed	1,4,6	1,3,6	1,2,3,4	1,2,3,5	1,2,3,6	1,2,4,5	1,2,4,6	1,2,5,6
Alt [ft]	LOSS	LOSS	LOSS	LOSS	LOSS	32760	LOSS	LOSS
M_cruise	--	--	--	--	--	0.23353	--	--
V [KTAS]	--	--	--	--	--	133.865	--	--
Rud_df [deg]	--	--	--	--	--	0	--	--
Ail_df [deg]	--	--	--	--	--	0	--	--
Beta [deg]	--	--	--	--	--	0	--	--
Bank [deg]	--	--	--	--	--	0	--	--
Cn_residual	--	--	--	--	--	0	--	--
Range [nm]	LOSS	LOSS	LOSS	LOSS	LOSS	7679.11	LOSS	LOSS
	State 49	State 50	State 51	State 52	State 53	State 54	State 55	State 56
Failed	1,3,4,5	1,3,4,6	1,3,5,6	1,4,5,6	2,4,5,6	2,3,5,6	2,3,4,6	2,3,4,5
Alt [ft]	28220	LOSS	LOSS	LOSS	LOSS	LOSS	LOSS	LOSS
M_cruise	0.21116	--	--	--	--	--	--	--
V [KTAS]	121.69	--	--	--	--	--	--	--
Rud_df [deg]	0	--	--	--	--	--	--	--
Ail_df [deg]	0	--	--	--	--	--	--	--
Beta [deg]	0	--	--	--	--	--	--	--
Bank [deg]	0	--	--	--	--	--	--	--
Cn_residual	0	--	--	--	--	--	--	--
Range [nm]	7758.06	LOSS	LOSS	LOSS	LOSS	LOSS	LOSS	LOSS
	State 57	State 58	State 59	State 60	State 61	State 62	State 63	State 64
Failed	3,4,5,6	1,2,3,4,5	1,2,3,4,6	1,2,3,5,6	1,2,4,5,6	1,3,4,5,6	2,3,4,5,6	1,2,3,4,5,6
Alt [ft]	LOSS	LOSS	LOSS	LOSS	LOSS	LOSS	LOSS	LOSS
M_cruise	--	--	--	--	--	--	--	--
V [KTAS]	--	--	--	--	--	--	--	--
Rud_df [deg]	--	--	--	--	--	--	--	--
Ail_df [deg]	--	--	--	--	--	--	--	--
Beta [deg]	--	--	--	--	--	--	--	--
Bank [deg]	--	--	--	--	--	--	--	--
Cn_residual	--	--	--	--	--	--	--	--
Range [nm]	LOSS	LOSS	LOSS	LOSS	LOSS	LOSS	LOSS	LOSS

Figure E-4: Multistate data from baseline long endurance UAV *Scenario II*, States 33-64; 1-cowl, 2-eng3, 3-eng4, 4-rudder, 5-aileron, 6-elevator

Bibliography

[1] J. Agte, N. Borer, and O. de Weck. Multistate design approach to the analysis of performance robustness for a twin-engine aircraft. *Journal of Aircraft* (recommended for publication pending minor revisions), March 2011. 38, 176

[2] J. Agte and K. Cohen. First order effects of new technology on a high altitude long endurance (HALE) unmanned aerial vehicle (UAV). In *Proceedings of the 46th AIAA Aerospace Sciences Meeting and Exhibit*, Reno, Nevada, 2008. 124, 132, 136

[3] J. Agte, O. de Weck, J. Sobieski, P. Arendsen, A. Morris, and M. Spieck. MDO: assessment and direction for advancement – an opinion of one international group. *Structural and Multidisciplinary Optimization*, 40(1):17–33, 2010. 49, 50

[4] N. Alexandrov. Editorial - multidisciplinary design optimization. *Optimization and Engineering*, 6(1):5–7, 2005. 49

[5] D. F. Allinger, P. S. Babcock, and R. F. LaPrad. The role of time-limited dispatch operation in fault tolerant flight critical control systems. AGARD Advisory Report No. 281, May 1990. 184

[6] C. Almeder. A hybrid optimization approach for multi-level capacitated lot-sizing problems. *European Journal of Operational Research*, 200(2):599–606, 2010. 51

[7] P. J. Antsaklis and A. J. Michel. *A Linear Systems Primer*. Birkhauser, Boston, MA, 2007. 204

[8] AVL. Athena vortex lattice solver. http://web.mit.edu/drela/Public/web/avl/, Accessed July 2011. 72, 193

[9] P. S. Babcock IV. Channelization: the two-fault tolerant attitude control function for the space station freedom. *Aerospace and Electronics Systems Magazine (IEEE)*, 11(5):9–22, 1996. 32, 47, 77

[10] P. S. Babcock IV, G. Rosch, and J. J. Zinchuk. An automated environment for optimizing fault-tolerant systems designs. In *Proceedings of the (1991) Annual Reliability and Maintainability Symposium (IEEE)*, pages 360–367, January 1991. 48

[11] P. S. Babcock IV and J. J. Zinchuk. Fault-tolerant design optimization: Application to an underwater vehicle navigation system. In *Proceedings of the (1990) Symposium on Autonomous Underwater Vehicle Technology (IEEE/OES)*, pages 34–43, June 1990. 47

[12] R. J. Balling and J. Sobieszczanski-Sobieski. Optimization of coupled systems: A critical overview of approaches. *AIAA Journal*, 34(1):6–17, 1996. 50

[13] J. W. Bandler, Q. X. Cheng, S. A. Dakroury, A. S. Mohamed, M. H. Bakr, K. Madsen, and J. Sondergaard. Space mapping - the state of the art. *IEEE Transactions on Microwave Theory and Techniques*, 52(1):337–361, 2004. 188

[14] J. W. Bandler, A. S. Mohamed, M. H. Bakr, K. Madsen, and J. Sondergaard. EM-based optimization exploiting partial space mapping and exact sensitivities. *IEEE Transactions on Microwave Theory and Techniques*, 50(12):2741–2750, 2002. 188

[15] A. Banks, J. Vincent, and C. Anyakoha. A review of particle swarm optimization. part ii: hybridisation, combinatorial, multicriteria and constrained optimization, and indicative applications. *Natural Computing*, 7(1):109–204, 2008. 51

[16] R. E. Barlow and A. S. Wu. Coherent systems with multi-state components. *Mathematics of Operations Research*, 3(4):275–281, 1978. 44

[17] J. F. M. Barthelemy and J. Sobieszczanski-Sobieski. Optimum sensitivity derivatives of objective functions in nonlinear programming. *AIAA Journal*, 21:913–915, 1983. 51

[18] J. Berndt and A. de Marco. Progress on and usage of the open source flight dynamics model software library, JSBSim. In *Proceedings of the (2009) AIAA Modeling and Simulation Technologies Conference*, August 2009. 72, 176, 194

[19] J. S. Berndt. JSBSim Reference Manual. http://jsbsim.sourceforge.net/JSBSimReferenceManual.pdf, Accessed July 2011. 196

[20] U. N. Bhat and G. K. Miller. *Elements of Applied Stochastic Processes*. John Wiley and Sons, Inc., Hoboken, NJ, 2002. 59

[21] L. Blackmore. *Robust Execution for Stochastic Hybrid Systems*. PhD dissertation, Massachusetts Institute of Technology, Department of Aeronautics and Astronautics, 2007. 31, 47

[22] W. R. Blischke and D. N. P. Murthy. *Reliability - Modeling, Prediction, and Optimization*. Wiley, New York, 2000. 54

[23] N. K. Borer, I. R. Claypool, W. D. Clark, J. J. West, R. G. Odegard, K. M. Somervill, and N. H. Suzuki. Model-driven development of reliable avionics architectures for lunar surface systems. Technical report, IEEE Aerospace Conference, Big Sky, Montana, March 2010. 77

[24] J. Braman, R. Murray, and D. Wagner. Safety verification of a fault tolerant reconfigurable autonomous goal-based robotic control system. In *Proceedings of the 2007 IEEE/RSJ International Conference on Intelligent Robots and Systems*, October 2007. 47

[25] S. A. Brandt, R. J. Stiles, J. J. Bertin, and R. Whitford. *Introduction to Aeronautics: A Design Perspective, second edition*. American Institute of Aeronautics and Astronautics, Reston, VA, 2004. 71, 87, 129, 192, 193

[26] F. W. Burcham and C. G. Fullerton. Controlling crippled aircraft - with throttles. NASA/TM-104238, 1991. 46

[27] F. W. Burcham, T. A. Maine, C. G. Fullerton, and L. D. Webb. Development and flight evaluation of an emergency digital flight control system using only engine thrust on an F-15 airplane. Technical report, NASA, Edwards, CA, September 1996. 46

[28] J. P. Castro, G. A. Gray, A. Giunta, and P. D. Hough. Developing a computationally efficient dynamic multilevel hybrid optimization scheme using multifidelity model interactions. SAND2005-7498, Sandia National Laboratories, 2005. 188

[29] K. Chang. Panel wants deep space, not landings as U.S. goal. *The New York Times*, page A16, July 31, 2009. 27

[30] A. Cozzola and J. L. Dolce. High-altitude, long-endurance airships for coastal surveillance. NASA/TM-2005-213427, February 2005. 27

[31] N. A. Creech, T. A. Burton, P. Cuadra, A. D. Harder, R. L. Odom, and J. S. Wisecup. C-12C parameter estimation, USAF TPS Technical Information Memorandum. Technical report, U.S. Air Force Test Pilot School, Edwards AFB, CA, March 2010. 74, 87

[32] DARPA. Broad Agency Announcement (BAA) Vulture II. Defense Advanced Research Projects Agency TTO, October 2009. 26, 78

[33] I. Das and J. Dennis. Normal-boundary intersection - a new method for generating pareto optimal points multicriteria optimization problems. *SIAM Journal on Optimization*, 8(3):631–657, 1998. 104, 173

[34] O. de Weck and K. Willcox. Introduction to multidisciplinary system design optimization. Lesson 1 Lecture Notes - Course 16.888, Spring 2010. 52

[35] Department of Defense. Military standard: Procedures for performing a failure mode, effects and criticality analysis. MIL-STD-1629A, November 1980. 98

[36] Department of Transport. The status of commercial passenger operations in turbine powered single engine aeroplanes. Technical report, Australian Bureau of Air Safety Investigation, Information Paper SAB/IP/93/4, December 1993. 27, 83

[37] Department of Transportation. Hawker Beechcraft Model 200 Type Certificate Data Sheet No. A24CE. Technical report, Federal Aviation Administration Regulatory and Guidance Library, March 2002. 73, 192, 193

[38] DoD. Acquisition strategy guide, 4th edition. Technical report, Defense Systems Management College Press, Fort Belvoir, VA, 1999. 96

[39] A. D. Dominguez-Garcia. *An Integrated Methodology for the Performance and Reliability Evaluation of Fault-Tolerant Systems*. PhD dissertation, Massachusetts Institute of Technology, Department of Electrical Engineering and Computer Science, May 2007. 32, 48

[40] A. D. Dominguez-Garcia, J. G. Kassakian, J. E. Schindall, and J. J. Zinchuk. An integrated methodology for the dynamic performance and reliability evaluation of fault-tolerant systems. *Journal of Reliability Engineering and System Safety*, 93(11):1628–1649, 2008. 48

[41] Dov Dori. *Object-Process Methodology: a Holistic Systems Paradigm*. Springer, 2002. 36

[42] G. Dorini. Performing pareto set membership tester for sets of points in k-dimensions. Matlab File Exchange, June 2007. 137

[43] M. A. Dornheim. Research pilot devises rules of thumb for engine-only control of disabled aircraft. *Aviation Week and Space Technology*, page 43, June 24, 1991. 46

[44] J. Dubbeldam and F. Redig. Multilayer markov chains with applications to polymers in shear flow. *Journal of Statistical Physics*, 125(1):229–247, 2006. 105

[45] J. Dugan, S. Bavuso, and M. Boyd. Dynamic fault fault-tree models for fault-tolerant computer systems. *IEEE Transactions on Reliability*, 41(3):363–377, 1992. 48

[46] D. Dvorak, M. Indictor, M. Ingham, R. Rasmussen, and M. Stringfellow. A unifying framework for systems modeling, control systems design, and system operation. In *Proceedings of the IEEE Conference on Systems, Man, and Cybernetics*, October 2005. 46

[47] E. El-Neweihi, F. Proschan, and J. Sethuraman. Multistate coherent systems. *Journal of Applied Probability*, 15(4):675–688, 1978. 44

[48] A. Elfes, S. S. Bueno, M. Bergerman, E. C. de Paiva, and J. G. Ramos Jr. Robotic airships for exploration of planetary bodies with an atmosphere: Autonomy challenges. *Autonomous Robots*, 14(2-3):147–164, March 2003. 27

[49] FAA. Policy for time limited dispatch (TLD) of engines with full authority digital engine controls (FADEC) systems. FAA Policy Letter ANE-1993-33.28TDL-R1, June 2001. 184

[50] F. Z. Feng, Y. H. Kim, and B. Yang. Applications of hybrid optimization techniques for model updating of rotor shafts. *Structural and Multidisciplinary Optimization*, 32(1):65–75, 2006. 51

[51] J. Grasmeyer. Stability and control derivative estimation and engine-out analysis. VPI-AOE-254, Virginia Tech, January 1998. 131, 215, 216

[52] R. T. Haftka and H. Adelman. Recent developments in structural sensitivity analysis. *Structural and Multidisciplinary Optimization*, 1:137–151, 1989. 51

[53] Headquarters Department of the Army. Operator's manual for Army C-12C/D/T aircraft. Technical report, Department of the Army, available at emilitarymanuals.com, September 2001. 73

[54] A. S. Hedayat, N. J. A. Sloane, and J. Stufken. *Orthogonal Arrays - Theory and Applications*. Springer, New York, NY, 1999. 51, 103, 149

[55] R. A. Howard. *Dynamic Probabilistic Systems: Volume I, Markov Models*. Dover Publications, 2007. 60

[56] A. Hoyland and M. Rausand. *System Reliability Theory*. John Wiley and Sons, New York, NY, 1994. 48

[57] Moire Inc. Cost and business model analysis for civilian UAV missions. prepared for the National Aeronautics and Space Administration, NASA, 2004. 132

[58] M. D. Ingham, R. D. Rasmussen, M. B. Bennett, and A. C. Moncada. Engineering complex embedded systems with state analysis and the mission data system. *AIAA Journal of Aerospace Computing, Information and Communication*, 2(12):507–536, 2005. 46

[59] T. Jin, L. Xing, and Y. Yu. A hierarchical markov reliability model for data storage systems with media self-recovery. *International Journal of Reliability, Quality & Safety Engineering*, 18(1):25–41, 2011. 105

[60] A. Mishkin R. Rasmussen T. Starbird J.R. Morris, M. Ingham. Application of state analysis and goal-based operations to a MER mission scenario. AIAA 2006-5981, AIAA International Conference on Space Operations, Rome, Italy, June 2006. 46

[61] I. Y. Kim and O. L. de Weck. Adaptive weighted-sum method for multi-objective optimization - a new method for Pareto front generation. *Structural and Multidisciplinary Optimization*, 31(2):105–116, 2006. 104

[62] J. P. C. Kleijnen. *Design and Analysis of Simulation Experiments*. Springer, New York, NY, 2010. 51, 103, 137

[63] G. Kreisselmeier and R. Steinhauser. Systematic control design by optimizating a vector performance index. In *Proceedings of the International Federation of Active Controls Symposium on Computer-Aided Design of Control Systems*, Zurich, Switzerland, 1979. 116

[64] J. Kurzke. Gasturb11 for design performance of gas turbine engines. Software, GasTurb11 Laboratory Package, 2009. 161

[65] G. Labinaz, M. M. Bayoumi, and K. Rudie. A survey of modeling and control of hybrid systems. *Annual Reviews in Control*, 21(1):79–92, 1997. 47

[66] NASA Jet Propulsion Laboratory. Mission data system - state analysis. http://mds.jpl.nasa.gov/, accessed July 2011. 31, 46

[67] G. Levitin and A. Lisnianski. A new approach to solving problems of multi-state system reliability optimization. *Quality and Reliability Engineering International*, 17(2):93–104, 2001. 44, 66

[68] H. Li and B. C. Williams. Generalized conflict learning for hybrid discrete/linear optimization. In *Proceedings of the 11th International Conference on Principles and Practices of Constraint Programming (CP-05)*, pages 415–429, September 2005. 47

[69] A. Lisnianski and G. Levitin. *Multi-State System Reliability*, volume 6 of *Series on Quality, Reliability & Engineering Statistics*. World Scientific, Singapore, 2003. 31, 45, 54, 55, 59, 112

[70] A. Lisnianski, G. Levitin, H. Ben-Haim, and D. Elmakis. Power system structure optimization subject to reliability contraints. *Electric Power Systems Research*, 39(2):145–152, 1996. 45

[71] F. J. Malzacher, J. Gier, and F. Lippl. Aerodesign and testing of an aeromechanically highly loaded lp turbine. *Journal of Turbomachinery*, 128(4):643–649, 2006. 156

[72] K. F. Man, K. S. Tang, and S. Kwong. *Genetic Algorithms: Concepts and Design, 3rd Edition*. Springer-Verlag, London, United Kingdom. 51

[73] Y. Massim, A. Zeblah, R. Meziane, M. Benguediab, and A. Ghouraf. Optimal design and reliability evaluation of multi-state series-parallel power systems. *Nonlinear Dynamics*, 40(4):309–321, 2005. 45

[74] J. Matson. Unfree spirit - NASA's mars rover appears stuck for good. *Scientific American*, 302(4):16, March 2010. 26

[75] A. Mettas. Reliability allocation and optimization for complex systems. In *Proceedings of the Annual IEEE Reliability and Maintainability Symposium*, Los Angeles, CA, January 2000. 132

[76] Brian Mills. DIY Drones: Profile of Brian Mills. http://diydrones.ning.com/profile/BrianMills, Accessed July 2011. 72, 194

[77] J. D. Murchland. *Fundamental Concepts and Relations for Reliability Analysis of Multistate Systems*. Reliability and Fault Tree Analysis, Theoretical, and Applied Aspects of System Reliability. SIAM, 1975. 44

[78] NASA. *NASA Systems Engineering Handboook*. NASA Center for Aerospace Information, Hanover, MD, 2007. 96

[79] NASA. Icebridge: an airborne mission for earth's polar ice. http://www.nasa.gov/mission_pages/icebridge/, Accessed July 2011. 123

[80] NASA. ICESat - cryoshperic sciences. http://icesat.gsfc.nasa.gov/icesat/, Accessed July 2011. 122

[81] National Transportation Safety Board. Annual review of aircraft accident data - U.S. air carrier operations calendar year 2006. Technical report, NTSB/ARC-10/01, December 2006. 27, 83

[82] US Navy. NAVAIR acquisition guide. Technical report, Department of Defense, 2009. 96

[83] C. L. Nickol, M. D. Guynn, L. L. Kohout, and T. A. Ozoroski. High altitude long endurance uav analysis of alternatives and technology requirements development. NASA/TP-2007-214861, March 2007. 124, 136, 215

[84] Office of the Secretary of Defense. Unmanned aerial vehicle reliability study. Technical report, Department of Defense, Washington, D.C., February 2003. 27, 83, 125, 126, 127

[85] V. Pareto and S. Schwier. *Manual of Politcal Economy*. Kellag, New York, NY, 1971. 103

[86] D. P. Raymer. *Aircraft Design: A Conceptual Approach, third edition*. American Institute of Aeronautics and Astronautics, Reston, VA, 1999. 131, 194

[87] A. Reibman and M. Veeraraghavan. Reliability modeling: An overview for system designers. *IEEE Computer*, 24(4):49–57, 1991. 48

[88] C. Riegler and C. Bichlmaier. The geared turbofan technology opportunities, challenges, and readiness status. In *Proceedings of the 1st CEAS European Air and Space Conference*, Berlin, Germany, September 2007. 156

[89] H. H. Rosenbrock. *State-space and Multivariable Theory*. Wiley Interscience Division, New York, NY, 1970. 204

[90] J. Roskam. *Methods for Estimating Stability and Control Derivatives of Conventional Subsonic Airplanes*. Roskam Aviation and Engineering Corporation, Kansas, 1971. 131, 215, 216

[91] J. Roskam. *Airplane Design Part VI*. Roskam Aviation and Engineering Corp., Ottawa, KS, 1990. 194

[92] J. Roskam. *Airplane Design Part VIII*. Roskam Aviation and Engineering Corp., Ottawa, KS, 1990. 71, 192

[93] R. A. Rutenbar. Simulated annealing algorithms: An overview. *IEEE Circuits and Devices Magazine*, 5(1):19–26, 1989. 51

[94] P. S. Schenker, P. Pirjanian, B. Balaram, K. S. Au, A. Trebi-Ollennu, T. L. Huntsberger, H. Aghazarian, B. A. Kennedy, E. T. Baumgartner, K. lagnemma, A. Rzepniewski, S. Dubowsky, P. C. Leger, D. Apostolopoulos, and G. T. McKee. Reconfigurable robots for all terrain exploration. *Proceedings of SPIE*, 4196(2000):454–468, 2000. 27

[95] K. Sinha, D. James, and J. Agte. Multidisciplinary design optimization of a high bypass ratio geared turbofan engine. Final report - Course 16.888, Massachusetts Institute of Technology, Cambridge, MA, May 2010. 156

[96] M. Smotherman and K. Zemoudeh. A non-homogeneous markov model for phased-mission reliability analysis. *IEEE Transactions on Reliability*, 38(5):585–590, December 1989. 48

[97] J. Sobieszczanski-Sobieski. Sensitivity of complex, internally coupled systems. *AIAA Journal*, 28(1):153–160, 1990. 51

[98] J. Sobieszczanski-Sobieski and R. T. Haftka. Multidisciplinary aerospace design optimization: survey of recent developments. *Structural and Multidisciplinary Optimization*, 14(1):1–23, 1997. 49

[99] M. Stein. *Interpolation of Spatial Data - Some Theory for Kriging*. Springer, New York, 1999. 186

[100] M. Steinberg. Historical overview of research in reconfigurable flight control. *Proceedings of the Institution of Mechanical Engineers*, 219(4):263–275, 2005. 45

[101] B. L. Stevens and F. L. Lewis. *Aircraft Control and Simulation*. Wiley Interscience Division, New York, NY, 1992. 205

[102] D. V. Stewart. The design structure matrix - a method for managing the design of complex systems. *IEEE Transactions on Engineering Management*, 28(3):71–74, 1981. 51

[103] T. Ozoroski, M. Guynn, and C. Nickol. Quick look feasibility study for an unmanned aerial vehicle ice surveillance mission. NASA viewgraphs, NASA Langley Research Center, June 2007. 123

[104] H. A. Taboada, J. F. Espiritu, and D. W. Coit. MOMS-GA: A multi-objective multi-state genetic algorithm for system reliability optimization design problems. *IEEE Transactions on Reliability*, 24(1):182–191, 2008. 45

[105] N. P. Tedford and J. Martins. On the common structure of MDO problems: a comparison of architectures. AIAA 2006-7080, 11th AIAA/ISSMO Multidisciplinary Analysis and Optimization Conference, Portsmouth, VA, September 2006. 49

[106] S. Thompson and J. Agte. C-12C aerodynamic model evaluation, USAF TPS Memorandum. Technical report, U.S. Air Force Test Pilot School, Edwards AFB, CA, April 2001. 73

[107] J. Till, S. Engell, S. Panek, and O. Stursberg. Applied hybrid system optimization: An empirical investigation of complexity. *Control Engineering Practice*, 12(10):1291–1303, 2004. 47

[108] M. Tozan, A. M. Al-Garni, A. Z. Al-Garni, and A. Jamal. Failure data analysis for aircraft maintenance planning. In *Proceedings of the 2004 Aircraft Engineering Symposium*, Jeddah, Saudi Arabia, December 2004. 159

[109] S. Tsach, A. Peled, D. Penn, and D. Touitou. The CAPECON program: Civil applications and economical effectivity of potential UAV configurations. In *Proceedings of the 3rd AIAA Unmanned Unlimited Technical Conference, Workshop, and Exhibit*, Chicago, Illinios, September 2004. 132

[110] I. Ushakov. The method of generalized generating sequences. *European Journal of Operational Research*, 125(2):675–688, 2000. 44

[111] D. G. Ward and J. F. Monaco. System identification for retrofit reconfigurable control of an f/a-18 aircraft. *Journal of Aircraft*, 42(1):63–72, 2005. 46

[112] J. West, I. Claypool, N. Borer, and R. Odegard. LSS lunar habitat avionics modeling study - Task 3 final report, reliability and performance implications of the use of commercial grade components. NASA/JSC Contract NNJ06HC37C, Draper Laboratory, 2009. 132

[113] J. G. Ziegler and N. B. Nichols. Optimum settings for automatic controllers. *Transactions of the A.S.M.E.*, 64:759–768, 1942. 80